Copyright Undertaking

HIGH SENSITIVITY SPECTROSCOPIC GAS SENSING WITH HOLLOW-CORE OPTICAL FIBERS

YAN ZHAO

PhD

The Hong Kong Polytechnic University

2022

The Hong Kong Polytechnic University

Department of Electrical Engineering

High Sensitivity Spectroscopic Gas Sensing with Hollow-core Optical Fibers

Yan Zhao

A thesis submitted in partial fulfillment of the requirements for

the degree of *Doctor of Philosophy*

September 2021

CERTIFICATE OF ORIGINALITY

I hereby declare that this thesis is my own work and that, to the best of my knowledge and belief, it reproduces no material previously published or written, nor material that has been accepted for the award of any other degree or diploma, except where due acknowledgement has been made in the text.

(Signed)

Yan Zhao (Name of student)

Abstract

Trace gas sensing is of importance in many areas including environmental and air-pollution monitoring, industrial process control and safety, and medical breath analysis. Among various kinds of gas sensing methods, laser absorption spectroscopy (LAS) offers advantages in sensitivity and selectivity as well as non-contact real-time measurement. Traditional LAS, including tunable diode LAS, cavity-enhanced LAS and photoacoustic LAS, uses a bulk multi-pass gas cell or resonating optical cavity. The size of gas cell and the need for careful optical alignment and/or cavity locking limit the application of traditional LAS in a real-world environment.

Hollow-core fiber (HCF) has been proved to be an efficient platform for light-gas interaction. With HCFs, compact gas cells can be made, which reduces gas consumption as well as benefits space-limited applications. HCF-based gas cells can be integrated with fiber-based components to provide advantages such as remote sensing and multi-point interrogation. However, since the first demonstration of HCF-based LAS in 2004, its sensitivity has long remained in tens of parts per million (ppm) level, which is insufficient for many precision applications. In 2015, the first HCF-based laser gas sensor with parts per billion (ppb) level sensitivity was demonstrated with photothermal spectroscopy (PTS). In this thesis, we explore several methods to further improve the sensitivity of HCF-based PTS gas sensors, and apply HCFs to stimulated Raman spectroscopy to detect gases with weak or no strong absorption in the operating wavelength range.

A straightforward way to improve the sensitivity of PTS is to increase the optical pump power level. For this, we developed an intracavity PTS system by placing a HCF gas cell inside a fiber ring laser cavity. The intracavity laser power was shown to be significantly higher than the laser output power. With a 0.62-m-long photonic bandgap HCF (PBG-HCF), we realize a sensitivity of 176 ppb acetylene in nitrogen. We build a model to study the PTS in the fiber ring laser. Theoretical study shows that the sensitivity of intracavity PTS can be further enhanced to ppb level by reducing the optical loss inside the laser cavity.

Apart from increasing the pump power level, the gas detection sensitivity may be improved by reducing the system noise level. As an interferometric gas sensing method, part of the noises of PTS comes from the optical interferometer. We discovered that an in-fiber modal interferometer with a dual-mode anti-resonant HCF (AR-HCF) gives a much better signal-to-noise ratio (SNR). A gas sensing method named mode-phase-difference PTS (MPD-PTS) is demonstrated. The photothermal effect is measured by the phase difference between the two optical modes in the AR-HCF. The common-mode noise is greatly reduced and hence the

MPD-PTS shows a much higher SNR. A multi-physics model is built to investigate the robustness of the dual-mode interferometer. Simulation shows that the sensitivity of MPD-PTS to environmental temperature and pressure perturbations is reduced by two orders of magnitude when compared to the previous HCF-based PTS. By using a 4.67-m-long AR-HCF, the sensitivity of tracing acetylene reaches parts per trillion (ppt) level with 3630-s integration time.

HCFs are made of fused silica, which is not good at confining heat. The heat generated by optical absorption quickly dissipated into the environment via the silica claddings. Hence, we investigated another subsequent effect of optical absorption: photoacoustic effect. The large acoustic impedance mismatch between the silica and air makes HCF a good acoustic resonator. A gas sensing method named photoacoustic Brillouin spectroscopy (PABS) is then demonstrated. A theoretical model is built to understand the acoustic-optical interaction and the thermodynamics in the HCF. The shifting boundary of the silica capillary of AR-HCF introduces an additional change of refractive index of the optical mode. With a 0.3-m-long AR-HCF, a sensitivity of 8-ppb acetylene in nitrogen has been demonstrated. Isotope detection at low pressures and characterization of the fiber microstructure have also been realized by PABS. Theoretical simulation shows that the sensitivity of PABS can be further enhanced by several orders of magnitude by using specially designed optical fibers.

For gases with no strong optical absorption such as hydrogen, Raman spectroscopy provides a solution for tracing them. The small air-core of HCF provides a perfect platform for light-gas interaction with high optical intensity, which enables highly efficient stimulated Raman scattering (SRS). We demonstrated a point hydrogen sensor and a distribution hydrogen sensor based on stimulated Raman gain spectroscopy of the $S_0(0)$ transition of hydrogen. With a 15-m-long PBG-HCF, a sensitivity of 20 ppm hydrogen has been demonstrated. By using backward SRS with a pulsed laser, distributed hydrogen sensing is demonstrated with a 2.7-m spatial resolution and a sensitivity of 833 ppm hydrogen over a length of 100 meters. The response time of the distributed hydrogen sensor is less than 60 s. Distributed pressure sensing is also demonstrated by decoding the Raman linewidth.

SRS process also generates heat, which may be exploited for gas detection. The indirect measurement of SRS via the generated heat would provide a higher gas sensing sensitivity because we could allow more pump photons to transform into Stokes photons without saturating the PD. We demonstrated Raman spectroscopy in an AR-HCF by detecting the SRS-induced photothermal phase modulation by using a setup similar to the MPD-PTS, which is named Raman photothermal interferometry. A theoretical model is built to investigate the SRS-induced photothermal effect in HCFs. Theoretical simulation shows that

part of the temperature change generated by SRS can be measured by the phase difference between two optical modes in the AR-HCF. The broad transmission band of AR-HCF enables the use of the $Q_1(1)$ transition of hydrogen, which greatly enhances the heat generated by SRS. By using a 3.9-m-long AR-HCF, a sensitivity of 3.2 ppm hydrogen has been demonstrated at a pressure of 6 bar.

Acknowledgements

First, I would like to express my sincere thanks to my supervisor Prof. Wei Jin for his continuous guidance and support. The meeting and discussion with him enlighten me to overcome the difficulties in my PhD study. His open mind, knowledge and patience are indispensable for the process of producing a published result from inspiration or accidental discovery.

Then I would like to give my special thanks to Dr. Fan Yang and Dr. Yun Qi. It is from the discussion and talk with them that I found my original curiosity for research in my PhD study.

I would like to thank my colleagues Dr. Hoi Lut Ho, Dr. Yuechuan Lin, Dr. Haihong Bao, Dr. Yanzhen Tan, Dr. Chao Wang, Dr. Shoulin Jiang, Dr. Congzhe Zhang, Dr. Haipeng Luo, Mr. Pengcheng Zhao, Mr. Feifan Chen, Miss Han Gao, Miss Yingzhen Hong for the useful discussion and kind help.

I would also like to acknowledge Prof. Yingying Wang, Dr. Shoufei Gao and Dr. Michael Frosz for kindly providing us the hollow-core fibers.

Finally, we would like to thank my parents for their love and support.

Publications Arising from the Thesis

Journal articles

1. Zhao, P., **Zhao, Y.**, Bao, H., Ho, H. L., Jin, W., Fan, S., ... & Wang, P. (2020). Mode-phase-difference photothermal spectroscopy for gas detection with an anti-resonant hollow-core optical fiber. *Nature Communications*, *11*(1), 1-8.

2. **Zhao, Y.**, Qi, Y., Ho, H. L., Gao, S., Wang, Y., & Jin, W. (2021). Photoacoustic Brillouin spectroscopy of gas-filled anti-resonant hollow-core optical fibers. *Optica*, *8*(4), 532-538.

3. Qi, Y., **Zhao, Y.**, Bao, H., Jin, W., & Ho, H. L. (2019). Nanofiber enhanced stimulated Raman spectroscopy for ultra-fast, ultra-sensitive hydrogen detection with ultra-wide dynamic range. *Optica*, *6*(5), 570-576.

4. Yang, F*., **Zhao, Y*.**, Qi, Y., Tan, Y. Z., Ho, H. L., & Jin, W. (2019). Towards label-free distributed fiber hydrogen sensor with stimulated Raman spectroscopy. *Optics Express*, *27*(9), 12869-12882.

5. **Zhao, Y.**, Jin, W., Lin, Y., Yang, F., & Ho, H. L. (2018). All-fiber gas sensor with intracavity photothermal spectroscopy. *Optics Letters*, *43*(7), 1566-1569.

Conference articles

1. **Zhao, Y.**, Jin, W., & Yang, F. (2018, September). Optomechanical sensing of hydrogen based on Brillouin scattering in gas in a hollow-core photonic crystal fiber. In *Optical Fiber Sensors* (p. WE1). Optical Society of America.

2. Yang, F., **Zhao, Y.**, Qi, Y., Tan, Y., Ho, H. L., & Jin, W. (2018, September). Label-free distributed hydrogen sensing with stimulated Raman scattering in hollow-core fibers. In *Optical Fiber Sensors* (p. TuE4). Optical Society of America.

3. Qi, Y., **Zhao, Y.**, Bao, H., Jin, W., Ho, H. L., & Luo, H. (2018, September). Nano-taper enhanced stimulated Raman gain spectroscopy for high sensitivity hydrogen detection. In *Optical Fiber Sensors* (p. FA3). Optical Society of America.

Table of Contents

Abstract I

Acknowledgements IV

Publications Arising from the Thesis V

Table of Contents VI

List of Figures IX

List of Tables XIV

List of Acronyms XV

List of Symbols XVIII

Chapter 1 Introduction **1**

1.1. Background 1

1.2. Literature review 2

1.3. Motivation of this work 3

1.4. Outline 5

Reference of Chapter 1 6

Chapter 2 Basic principles **12**

2.1. Absorption spectroscopy of gases 12

2.2. Raman spectroscopy of gases 19

2.3. Wavelength modulation spectroscopy 25

2.4. Photothermal and photoacoustic spectroscopy 27

2.5. Hollow-core fibers 30

2.6. Conclusion 31

Reference of Chapter 2 31

Chapter 3 PTS and PAS in gas-filled HCFs **34**

3.1. Photothermal and photoacoustic effects in gas-filled HCFs 34

3.1.1 Heat source 35

3.1.2. Heat conduction 37

3.1.3. Thermo-viscous acoustics 40

3.2. Perturbation theory of optical mode in HCFs 42

3.3. Probe the photothermal and photoacoustic effects with optical interferometers 46

3.3.1. Fiber optical interferometers 46

3.3.2. Noise of fiber optical interferometer with HCFs 49

3.4. Conclusion 52

Reference of Chapter 3 52

Chapter 4 Sensitivity enhancement of PTS in HCFs 54

4.1. Intracavity PTS with HCF 54

4.1.1. Configuration of the fiber ring laser 54

4.1.2. Gas detection experiment 57

4.1.3. Theoretical sensitivity of intracavity PTS for gas detection 60

4.2. MPD-PTS with HCF 62

4.2.1. Theory of MPD-PTS with AR-HCF 62

4.2.2. Sensitivity of MPD to external temperature and pressure 68

4.2.3. Experiment and discussion 71

4.3. Conclusion 74

Reference of Chapter 4 75

Chapter 5 Photoacoustic Brillouin spectroscopy with HCFs 78

5.1. Previous work of PAS for gas sensing 78

5.2. Principle of PABS with gas-filled HCFs 78

5.2.1. Acoustic mode and optical mode in HCFs 78

5.2.2. Excitation of acoustic mode 80

5.3. Experiment of PABS 87

5.3.1. Experiment setup 87

5.3.2. Phase calibration of the probe light 89

5.3.3. Measurement of the thermal relaxation time 90

5.3.4. Basic experiments of PABS 91

5.3.5. Spectroscopy of the microstructure of HCFs 93
5.3.6. Spectroscopy of acetylene 97
5.4. Discussion about the potential of PABS.. 98
5.5. Conclusion.. 103
Reference of Chapter 5... 104
Chapter 6 Raman spectroscopy of hydrogen with HCFs..................................107
6.1. SRG spectroscopy of hydrogen 107
6.1.1. Principle of SRG spectroscopy with HCFs 107
6.1.2. Hydrogen sensing with forward SRS 109
6.1.3. Distributed hydrogen sensing with backward SRS 111
6.1.4. Discussion of SRG spectroscopy.. 120
6.2. Raman photothermal spectroscopy.. 121
6.2.1. Principle of RPTS in HCFs 122
6.2.2. MPD-RPTS in AR-HCFs 123
6.2.3. Experiment and result.. 130
6.2.4. Discussion of RPTS.. 136
6.3. Conclusion.. 139
Reference of Chapter 6... 140
Chapter 7 Conclusions and future works 144
7.1. Conclusions 144
7.2. Future works.. 145

List of Figures

Figure 2.1. The energy level diagram of IR active molecules.

Figure 2.2. Molecular rotational modes.

Figure 2.3. The absorption coefficient of acetylene.

Figure 2.4. The normalized absorption coefficient for different gases under atmospheric condition.

Figure 2.5. The energy level diagram of Raman scattering.

Figure 2.6. The definition of the Raman scattering plane and polarizations.

Figure 2.7. The Raman gain coefficient of $Q_1(1)$ for different pump wavelengths, pressures, and polarizations.

Figure 2.8. The harmonic coefficients with different modulation depth.

Figure 2.9. Process of photothermal/photoacoustic effect.

Figure 2.10. Excitation state relaxation of rovibrational levels.

Figure 2.11. Schematic diagram of HCFs.

Figure 3.1. Schematic diagram of HCFs for simulation.

Figure 3.2. The temperature change and 3-dB cut-off frequency of PTS with different core size.

Figure 3.3. The temperature change and 3-dB cut-off frequency of PTS with different thermal conductivity.

Figure 3.4. The temperature change and 3-dB cut-off frequency of PTS with different heat capacity.

Figure 3.5. The geometry and boundary of single-ring AR-HCF.

Figure 3.6. Acoustic modes in an AR-HCF with their frequency f and quality factor Q_A.

Figure 3.7. Schematic diagram of optical interferometers.

Figure 3.8. The relative noise spectrum of PD, LIA and the fiber laser.

Figure 4.1. The configuration of fiber ring laser with HCF.

Figure 4.2. Optical self-delayed heterodyne measurement setup.

Figure 4.3. PSD measured by the self-delayed heterodyne at two moments.

Figure 4.4. The output power versus 980-nm pump power.

Figure 4.5. The spectrum and optical power of the fiber ring laser.

Figure 4.6. The experiment setup of an IC-PT gas sensor.

Figure 4.7. The second harmonic signal with different intracavity power.

Figure 4.8. Theoretical analysis of the intracavity photothermal gas sensor.

Figure 4.9. The transmission spectrum and the optical mode of AR-HCF used in the experiment.

Figure 4.10. The optical modes in the AR-HCF.

Figure 4.11. The basic principle of MPD-PTS.

Figure 4.12. Modulation coefficient k^* as a fucntion of second harmoinc frequency.

Figure 4.13. PT modulation coefficient k^* as a fucntion of η for different combinations of LP_{01} and LP_{11} modes of pump and probe beam.

Figure 4.14. The model for numerically calculating the phase sensitivity to external perturbations.

Figure 4.15. The experiment setup for MPD-PTS.

Figure 4.16. The optical property of the AR-HCF gas cell.

Figure 4.17. The experiment result with 1 ppm acetylene.

Figure 5.1. The SEM of AR-HCF and the acoustic modes in the fiber.

Figure 5.2. The geometry used for simulation and the optical modes supported by the fiber.

Figure 5.3. The absorption coefficient of acetylene with different pressures.

Figure 5.4. The transient response of the pressure and the temperature.

Figure 5.5. The modal interference induced periodical distribution of harmonic heat source $\tilde{Q}$, density change $\tilde{\rho}$, and displacement of capillary $\tilde{w}$.

Figure 5.6. The calculated phase modulation of PABS.

Figure 5.7. The experiment setup of PABS.

Figure 5.8. The homemade HCF gas cell.

Figure 5.9. The measured interferogram of the modal interferometer.

Figure 5.10. The transient response of thermal relaxation and thermal conduction in AR-HCF.

Figure 5.11. The PABS spectrum due to the photoacoustic effect and the force.

Figure 5.12. The PABS spectrum with different LP_{11} modes of the probe light.

Figure 5.13. The PABS spectrum with different states of the fiber.

Figure 5.14. The PABS spectrums of 30-cm-long AR-HCFs filled with 10 mbar pure C_2H_2.

Figure 5.15. The pressure dependence of the Brillouin spectrum measured by PABS with different AR-HCFs.

Figure 5.16. Phase modulation due to different acoustic mode with different gas pressures.

Figure 5.17. The experiment and simulation of PABS spectrum.

Figure 5.18. PABS of different HCFs at a pressure of 1 bar.

Figure 5.19. Results of gas detection experiment with fiber A filled with 106 ppm C_2H_2 balanced with nitrogen at a pressure of 1 bar.

Figure 5.20. The geometry of the dual-nano web-like fibers and its acoustic mode.

Figure 5.21. The optical mode and the heat source of dual nanoweb fiber.

Figure 5.22. The simulation of phase modulation with dual nanoweb fiber.

Figure 5.23. The geometry of a designed nanoweb fiber for PABS.

Figure 5.24. The pump field, heat source and the acoustic mode.

Figure 5.25. The simulation of phase modulation with designed dual nanoweb fiber.

Figure 6.1. HC-1550-06 fiber used for hydrogen sensing.

Figure 6.2. The experiment setup of point fiber hydrogen sensor.

Figure 6.3. Performance of the point hydrogen sensor with a 15-m-long PBG-HCF gas cell.

Figure 6.4. Distributed hydrogen sensing with backward SRS in a PBG-HCF.

Figure 6.5. Experimental setup for distributed hydrogen sensing.

Figure 6.6. SRG trace along a 100-m-long PBG-HCF.

Figure 6.7. Experiment results of dynamic range and linearity.

Figure 6.8. Experiment result for testing the spatial resolution.

Figure 6.9. Measured backward Raman linewidth and line-shift at 296 K.

Figure 6.10. Results of distributed gas pressure measurement.

Figure 6.11. Monitoring the gas filling and purging process.

Figure 6.12. The basic principle of Raman PTS.

Figure 6.13. The AR-HCF used for RPTS.

Figure 6.14. The phase modulation in RPTS with only the LP_{01} mode.

Figure 6.15. The weighted temperature change at modulation frequencies of 1 kHz and 10 kHz.

Figure 6.16. The distribution of the heat sources of RPTS.

Figure 6.17. The integrated heat source along the fiber.

Figure 6.18. RPT modulation coefficient of all three distributions of heat source.

Figure 6.19. The RPT modulation coefficient.

Figure 6.20. The pressure dependence of RPTS.

Figure 6.21. The experiment setup of RPTS.

Figure 6.22. The feedback locking of the probe laser.

Figure 6.23. The 2-nd harmonic phase modulation at different frequencies.

Figure 6.24. The 2-nd harmonic wave with different optical powers.

Figure 6.25. The 2-nd harmonic wave with respect to the product of pump power and Stokes power.

Figure 6.26. The measured vibrational band of pure hydrogen.

Figure 6.27. The Allan plot for analysis of the sensitivity of RPTS.

Figure 6.28. PSD of the noise in the system.

Figure 6.29. The transmission spectrum of the SMF-HCF-SMF structure.

Figure 6.30. The Raman linewidth and the Raman gain coefficient of the rotational and vibrational band of pure hydrogen.

List of Tables

Table 2.1. The fundamental vibrational transition of linear molecules.

Table 2.2. Vibrational modes and their wavenumber of C_2H_2.

Table 2.3 Polarization dependent Raman cross-section.

Table 2.4. The vibrational relaxation time of gases.

Table 4.1. Detection limit of different PBG-HCF gas sensors.

Table 4.2. Parameters used for simulation.

Table 4.3. Comparison between several spectroscopic laser gas sensors

Table 5.1. Parameters of AR-HCF estimated from SEM.

Table 5.2. Parameters used for acoustic simulation.

Table 6.1. The overlap integral $S_{\upsilon\zeta}$.

Table 6.2. The overlap integral $S_{\sigma\upsilon\zeta\eta}$.

Table 6.3. Coefficients A and B at room temperature (298 K).

List of Acronyms

ASE	amplified spontaneous emission
AOM	acousto-optic modulator
AR-HCF	anti-resonant hollow-core fiber
BPD	balanced photodetector
CC	current controller
CCD	charge-coupled device
CERPAS	cantilever-enhanced resonant photoacoustic spectroscopy
CRDS	cavity ringdown spectroscopy
CT-AR-HCF	conjoined tube anti-resonant hollow-core fiber
CTF	conjoined tube hollow-core fiber
DAQ	data acquisition
DAS	direct absorption spectroscopy
DFB	distributed feedback
DM	dichroic mirror
ECDL	external cavity diode laser
EDF	erbium doped fiber
EDFA	erbium doped fiber amplifier
ESA	electric spectrum analyzer
FEM	finite element method
FS	frequency shifter
FWHM	full-width at half-maximum
HCF	hollow-core fiber
HWHM	half-width at half-maximum
IC-PT	intracavity photothermal

IM	intensity modulator
IR	infrared
ISO	isolator
LAS	laser absorption spectroscopy
LIA	lock-in amplifier
MPD	mode phase difference
NEA	noise equivalent absorbance
NEC	noise equivalent concentration
NICE-OHMS	noise-immune cavity-enhanced optical heterodyne molecular spectroscopy
OA-ICOS	off-axis integrated cavity output spectroscopy
OC	optical circulator
OF-CEAS	optical feedback cavity-enhanced absorption spectroscopy
OSA	optical spectrum analyzer
PABS	photoacoustic Brillouin spectroscopy
PAS	photoacoustic spectroscopy
PBG-HCF	photonic bandgap hollow-core fiber
PC	polarization controller
PD	photodetector
PE	photoelastic effect
PF	pump filter
PS	polarization scrambler
PSD	power spectrum density
PTI	photothermal interferometry
PTS	photothermal spectroscopy
PZT	piezoelectric transducer

RHS	right hand side
RI	refractive index
RMS	root-mean-square
RPT	Raman photothermal
RPTS	Raman photothermal spectroscopy
SB	shifting boundary
SEM	scanning electron microscopy
SMF	single mode fiber
SNR	signal-to-noise ratio
SRG	stimulated Raman gain
SRL	stimulated Raman loss
SRS	stimulated Raman scattering
TC	temperature controller
TDLAS	tunable diode laser absorption spectroscopy
TF	tunable filter
TTFMS	two-tone frequency modulation spectroscopy
VRT	vibrational relaxation time
WDM	wavelength division multiplexer
WMS	wavelength modulation spectroscopy
ppb	parts per billion
ppm	parts per million
ppt	parts per trillion

List of Symbols

α_A	absorption coefficient of gas
$\alpha_{\rho\sigma}$	polarizability tensor of molecule
α_P	isobaric coefficient of thermal expansion of gas
$\boldsymbol{\alpha_T}$	thermal expansion coefficient of solid
B_v	rotational harmonic wavenumber
β_T	isothermal compressibility of gas
γ_e	electrostrictive constant
γ_r	ratio of specific heat capacity
γ_D	Doppler HWHM linewidth
γ_L	Lorentzian HWHM linewidth
γ_{air}	air-broadening coefficient of gas molecule
γ_{self}	self-broadening coefficient of gas molecule
$\Delta\nu_R$	FWHM Raman linewidth
ΔN_{fi}	density difference between the initial state i and the final state f
c_0	speed of light in the vacuum
c_s	speed of sound in gas
C	concentration of absorptive gas
$\boldsymbol{C_T}$	compliance tensor of solid
c_P	isobaric specific heat capacity of gas
D_v	rotational anharmonic constant
ε	absolute electric permittivity
ε_r	relative electric permittivity
$\boldsymbol{\epsilon_S}$	strain tensor

E_Y	Young's modulus
$\boldsymbol{\sigma_S}$	stress tensor
f_D	Doppler lineshape function
f_L	Lorentzian lineshape function
f_V	Voigt lineshape function
g_R	Raman gain coefficient
η_0	dynamic viscosity
η_B	bulk viscosity
η_H	efficiency of heat generation
h	Planck's constant
$\hbar$	reduced Planck's constant
κ	thermal conductivity
k_B	Boltzmann constant
k^*	phase modulation coefficient
k_{PA}^*	photoacoustic phase modulation coefficient
k_R^*	Raman photothermal phase modulation coefficient
M	molar mass of the molecule
N_A	Avogadro constant
N_u	number density of molecules in the upper energy level
Q_A	acoustic quality factor
Q_R	molecular coherence
S_i	spectral line intensity
$\boldsymbol{S_T}$	stiffness tensor of solid
τ_1	depopulation time of molecular coherence
τ_2	dephasing time of molecular coherence

τ_V	vibrational relaxation time
ν_e	vibrational harmonic wavenumber
ν_r	Poisson’s ratio
w_R	difference of occupational probability
χ_e	vibrational anharmonic constant

Chapter 1 Introduction

1.1. Background

Gas detection is of importance in many areas including environmental and air-pollution monitoring, industrial process control, and medical breath analysis [1-4]. Quantitative gas detection has been achieved by gas chromatography [5], semiconductor or electrochemical gas sensors and pellistors [6, 7]. Gas chromatography offers both high sensitivity and selectivity by separating different gas components with metal or glass tubing. However, the gas separating process precludes it from real-time measurement. Compared with gas chromatography, semiconductor and electrochemical gas sensors, and pellistors are low in cost and small in size and yet they still provide good sensitivity down to ppm or ppb level. However, they suffer from problems such as cross-sensitivity, zero-drift and limited lifetimes.

Gas sensing based on optical absorption or Raman scattering offers advantages of high sensitivity and selectivity, and non-contact real-time measurement. Optical gas sensing is a fast-growing field that benefits from the development of lasers. It maybe be divided into two categories: those that directly measure the change of laser intensity or scattering intensity, such as tunable diode laser absorption spectroscopy (TDLAS) [8] and Raman spectroscopy [9]; and those that measure the subsequent effects of laser absorption or Raman scattering, such as photoacoustic spectroscopy (PAS) and photothermal spectroscopy (PTS) [10, 11]. Modern optical gas spectroscopy is usually combined with laser modulation techniques including wavelength modulation, frequency modulation and intensity modulation. The modulation of laser upshifts the detection signal to a frequency of a few kilohertz to hundreds of megahertz, where the '1/f' noise is smaller. Gas cells including multi-pass, resonant cavity and other types are an important part of optical gas spectroscopy that can improve detection sensitivity by increasing the optical interaction length.

Among the optical gas spectroscopic methods that directly measures the optical absorption, noise-immune cavity-enhanced optical heterodyne molecular spectroscopy (NICE-OHMS) is the most sensitive method that could provide sensitivity at ppt level [12, 13]. By using an optical cavity with very high finesse, NICE-OHMS provides an optical interaction length of a few kilometers. However, limited by the saturation power of photodetector (PD), the input laser power of these methods is only at a level of a few milliwatts, which prevents further improvement of their sensitivity. Besides, these high-finesse cavities need careful optical alignment which makes it a challenge to use them in harsh environments.

Gas spectroscopy that measures the subsequent effect of optical absorption can offer good sensitivity even with a short optical interaction length. These methods do not directly measure the laser power at the wavelength of optical absorption. Hence, the laser power can be up to a few watts and that is one of the reasons why they offer good sensitivity. For example, PAS and PTS measure, respectively, the acoustic wave and refractive index (RI) change due to optical absorption. The acoustic wave could be detected by a microphone and the RI change can be detected by using optical interferometer. For PAS, different types of microphones are designed to improve the sensitivity on the acoustic detection: such as quartz-tuning fork [14], cantilever-type microphone [15], microphone based on optical fiber tips [16], etc. The acoustic wave generated by optical absorption can also be enhanced by using an acoustic resonating cavity for better sensitivity [17].

For traditional optical gas spectroscopy, bulk gas cells such as Herriott-type multi-pass gas cells, resonant type gas cells with high finesse are used. For these gas cells which realize long optical path lengths, careful adjustment or complex locking method is needed and it would be hard to maintain their performance over a long-time in a real-world environment. Hollow-core fibers (HCFs), since invented in the 1990s, have been proved to be a good platform for light-gas interaction over a long distance [18]. HCFs could be used to improve the performance of the traditional spectroscopies including PTS, PAS, Raman spectroscopy, etc. HCF-based gas cells could also be easily integrated with single-mode fiber to provide advantages such as compactness, multi-point interrogation, and remote sensing.

1.2. Literature review

The spectroscopic gas sensor with HCFs was firstly reported by Hoo et al. in 2004 [19]. They demonstrated gas diffusion measurement with direct absorption spectroscopy (DAS) of acetylene (C_2H_2) by using a photonic bandgap HCF (PBG-HCF). And later in the same year, Ritari et al. reported the PBG-HCF-based spectroscopic gas sensing of C_2H_2, hydrogen cyanide (HCN) and methane (CH_4) [20]. Since then, gas sensing with PBG-HCFs has been demonstrated with gases such as C_2H_2, CH_4, ethylene (C_2H_6), oxygen (O_2) [21-27]. However, for a long time, the sensitivity of HCF-based spectroscopic gas sensors remained in tens of ppm level, which is insufficient for many practical applications.

In 2015, the first HCF-based high sensitivity gas sensor was reported with PTS by Jin et al. [28]. Ppb level sensitivity of C_2H_2 was demonstrated with a 10-m-long PBG-HCF by using photothermal interferometry (PTI). PTI measures the phase modulation of a probe beam due to the absorption of a modulated pump beam. The photothermal phase modulation amplitude is proportional to the gas concentration, the power of pump, and the length of HCFs [28].

Later, for a faster response time of gas sensing, a Fabry-Perot PTI gas sensor with a 2-cm-long PBG-HCF was demonstrated and achieved a response time less than 19 s [29]. The dynamics of photothermal effect in PBG-HCF is also studied by Lin et al. [30]. To achieve higher sensitivity of gas sensing with HCFs, methods such as cavity enhancement [31] and mid-infrared (IR) pump [32] are also used. By using PTI, the sensitivity of HCF gas sensor was improved by three orders of magnitude when compared with those HCF gas sensors based on DAS.

For gases such as hydrogen (H_2) and nitrogen (N_2) that only have weak or no optical absorption, Raman spectroscopy is an alternative method for tracing them. Besides, the high optical intensity in HCFs improves the efficiency of Raman scattering. Raman gas sensor with HCFs has been demonstrated with stimulated Raman scattering (SRS) and spontaneous Raman scattering, respectively. Sensing of different gases such as H_2, O_2, N_2, CH_4, carbon dioxide (CO_2), and nitrous oxide (N_2O) has been reported [33-36]. In 2014, based on spontaneous Raman scattering with PBG-HCF, Hanf et al. demonstrated a high sensitivity hydrogen gas sensor with a sensitivity of 5 ppm H_2 using a nitrogen-cooled charge-coupled device (CCD) [36].

Brillouin scattering is another important phenomenon of nonlinear scattering in optical fibers. It has been firstly reported by Ippen et al. in 1972 [37] and has long been used for distributed sensing [38]. In optical fibers, Brillouin scattering occurs both in the backward and in the forward direction. Forward Brillouin scattering (FBS) or guided acoustic-wave Brillouin scattering was first reported in single-mode fiber by Shelby et al. in 1985 [39]. Since then, FBS has been observed in multi-core fibers [40], solid-core photonic crystal fibers [41-43], and integrated silicon waveguides [44], and has been exploited for sensing [45-48], coherent information processing [49], optical amplification [50] and lasing [51], frequency comb generation [43], mode-locked lasers [52], etc. Recently, Brillouin scattering in HCFs has also been studied [53-58]. Yang et al. first reported intense backward Brillouin scattering in PBG-HCF and it was used for lasing and distributed temperature sensing [57]. However, at atmospheric pressure, FBS is extremely weak in HCFs, and no useful application has been reported.

1.3. Motivation of this work

So far, HCF-based PTS (or PTI) gas sensors have demonstrated ppb level detection sensitivity. It is natural to ask whether we can further increase the sensitivity of HCF-based gas sensors? Can we achieve comparable or even higher sensitivity compared with other advanced technologies such as TDLAS, cavity-enhanced absorption spectroscopy (CEAS), and NICE-OHMS?

One way to enhance the sensitivity of PTS is to use a higher pump power level. For this, we proposed to place a HCF gas cell inside a fiber ring laser cavity to fully utilize the laser power, which is named intracavity PTS. We conducted theoretical modeling, built a fiber ring laser, and conducted gas detection experiments with intracavity PTS.

Another way to improve the sensitivity is to reduce the detection noise of PTS. As an interferometric gas sensing method, parts of the noise of PTS come from the optical interferometer. We studied different types of interferometers such as Mach-Zehnder, Fabry-Perot, Sagnac and the noise is more or less at the same level. By exploiting the unique mode property of HCFs, we proposed to detect the phase difference between different guided optical modes due to gas absorption. This technique is termed mode-phase-difference PTS (MPD-PTS). We carried out comprehensive modeling for MPD-PTS in HCFs and conducted gas detection experiments. We found that MPD-PTS provides a much better signal-to-noise ratio (SNR) compared with the traditional PTS.

HCF, which is made of fused silica, is not good at confining heat. The heat generated by optical absorption quickly dissipated into the environment via the silica claddings, and hence the PT phase modulation amplitude is relatively small. Therefore, we seek another subsequent effect of optical absorption: the photoacoustic effect. The large acoustic impedance mismatch between the silica and the air makes HCF a good acoustic resonator, which could enhance the amplitude of phase modulation. A gas sensing method called photoacoustic Brillouin spectroscopy (PABS) is hence proposed by employing the FBS induced by the photoacoustic effect. We carried out comprehensive modeling for the acoustic-optical interaction and the thermodynamics in HCFs, conducted gas detection experiments. The PABS could be used not only for gas detection but also for characterization of the HCF microstructures.

For gases with weak or no optical absorption such as hydrogen, Raman spectroscopy provides a solution for tracing them. HCF is a good platform for Raman spectroscopy due to its small mode area and perfect overlap between optical field and gases, which enhances the detection sensitivity. We proposed and demonstrated a hydrogen gas sensor by measuring the forward stimulated Raman gain (SRG) and a distribution hydrogen gas sensing system by measuring the backward SRG.

By combining Raman spectroscopy with PTS, we demonstrated, for the first time to our knowledge, a Raman PTS (RPTS) hydrogen sensor. RPTS measures the strength of Raman scattering indirectly by detecting the phase modulation due to heat generation associated with

SRS. RPTS could provide higher sensitivity for detecting hydrogen because we could allow more pump photons to transform into Stokes photons without saturating the PD. We carried out comprehensive modeling for RPTS in HCFs and conducted gas detection experiments with a dual-mode fiber interferometer.

1.4. Outline

The thesis is organized as follows:

In Chapter 1, the background and the development of HCF-based gas sensors are reviewed. Fiber gas sensors with HCFs by using DAS, PTS, and Raman spectroscopy are introduced. The Brillouin scattering in optical fibers and its application are briefly reviewed.

In Chapter 2, the principles of spectroscopic gas sensing, including optical absorption spectroscopy, stimulated Raman spectroscopy, wavelength modulation spectroscopy (WMS), PTS, and PAS are reviewed. A brief introduction of HCFs is also presented.

In Chapter 3, the principles of PTS and PAS with HCFs are studied theoretically, including the photothermal and photoacoustic effects in HCFs, and the optical interferometers for detecting the photothermal and photoacoustic effects.

In Chapter 4, the sensitivity enhancement methods for PTS are presented, including intracavity PTS and MPD-PTS. For intracavity PTS, experiments of detecting C_2H_2 are demonstrated. The potential and limitations of this method are also discussed with theoretical modeling. For MPD-PTS, the mechanism of sensitivity enhancement with MPD is explained with comprehensive modeling. Experiments of tracing C_2H_2 are demonstrated with high sensitivity.

In Chapter 5, PABS with HCFs is studied. The mechanism of sensitivity enhancement for gas detection by photoacoustic effect and FBS are explained. The spectroscopy of C_2H_2, as well as spectroscopy of the microstructure of HCFs, are demonstrated experimentally. The potential for higher sensitivity gas sensing with PABS is also discussed with comprehensive modeling.

In Chapter 6, the gas sensing methods with stimulated Raman spectroscopy in HCFs are presented, including SRG spectroscopy and RPTS. For SRG spectroscopy with HCFs, experiments of tracing H_2 are demonstrated with high sensitivity as well as the capability of distributed sensing. For RPTS, the mechanism of gas detection by SRS induced photothermal effect is described. Experiments of tracing H_2 with high sensitivity are demonstrated. The potential of H_2 sensing with RPTS is also discussed with theoretical modeling.

In Chapter 7, the works in this thesis are summarized and the future work along this direction is suggested.

Reference of Chapter 1

1. Martin, P. A. (2002). Near-infrared diode laser spectroscopy in chemical process and environmental air monitoring. *Chemical Society Reviews*, *31*(4), 201-210.
2. Risby, T. H., & Solga, S. F. (2006). Current status of clinical breath analysis. *Applied Physics B*, *85*(2), 421-426.
3. Vogler, D. E., & Sigrist, M. W. (2006). Near-infrared laser based cavity ringdown spectroscopy for applications in petrochemical industry. *Applied physics B*, *85*(2), 349-354.
4. Willer, U., Saraji, M., Khorsandi, A., Geiser, P., & Schade, W. (2006). Near-and mid-infrared laser monitoring of industrial processes, environment and security applications. *Optics and Lasers in Engineering*, *44*(7), 699-710.
5. McNair, H. M., Miller, J. M., & Snow, N. H. (2019). *Basic gas chromatography*. John Wiley & Sons.
6. Fergus, J. W. (2007). Materials for high temperature electrochemical NO_x gas sensors. *Sensors and Actuators B: Chemical*, *121*(2), 652-663.
7. Yamazoe, N. (1991). New approaches for improving semiconductor gas sensors. *Sensors and Actuators B: Chemical*, *5*(1-4), 7-19.
8. Werle, P. O., Mücke, R., & Slemr, F. (1993). The limits of signal averaging in atmospheric trace-gas monitoring by tunable diode-laser absorption spectroscopy (TDLAS). *Applied Physics B*, *57*(2), 131-139.
9. Weber, A. (Ed.). (2012). *Raman spectroscopy of gases and liquids* (Vol. 11). Springer Science & Business Media.
10. Bialkowski, S. E. (1996). *Photothermal spectroscopy methods for chemical analysis* (Vol. 177). John Wiley & Sons.
11. Harren, F. J., & Cristescu, S. M. (2006). Photoacoustic spectroscopy in trace gas monitoring. *Encyclopedia of Analytical Chemistry: Applications, Theory and Instrumentation*, 1-29.
12. Ye, J., Ma, L. S., & Hall, J. L. (1998). Ultrasensitive detections in atomic and molecular physics: demonstration in molecular overtone spectroscopy. *JOSA B*, *15*(1), 6-15.
13. Foltynowicz, A., Schmidt, F. M., Ma, W., & Axner, O. (2008). Noise-immune cavity-enhanced optical heterodyne molecular spectroscopy: Current status and future potential. *Applied Physics B*, *92*(3), 313.

14. Kosterev, A. A., Bakhirkin, Y. A., Curl, R. F., & Tittel, F. K. (2002). Quartz-enhanced photoacoustic spectroscopy. *Optics Letters*, *27*(21), 1902-1904.

15. Koskinen, V., Fonsen, J., Roth, K., & Kauppinen, J. (2008). Progress in cantilever enhanced photoacoustic spectroscopy. *Vibrational Spectroscopy*, *48*(1), 16-21.

16. Cao, Y., Jin, W., Ho, H. L., & Ma, J. (2013). Miniature fiber-tip photoacoustic spectrometer for trace gas detection. *Optics Letters*, *38*(4), 434-436.

17. Miklós, A., Hess, P., & Bozóki, Z. (2001). Application of acoustic resonators in photoacoustic trace gas analysis and metrology. *Review of Scientific Instruments*, *72*(4), 1937-1955.

18. Cregan, R. F., Mangan, B. J., Knight, J. C., Birks, T. A., Russell, P. S. J., Roberts, P. J., & Allan, D. C. (1999). Single-mode photonic band gap guidance of light in air. *Science*, *285*(5433), 1537-1539.

19. Hoo, Y. L., Jin, W., Ho, H. L., Ju, J., & Wang, D. N. (2005). Gas diffusion measurement using hollow-core photonic bandgap fiber. *Sensors and Actuators B: Chemical*, *105*(2), 183-186.

20. Ritari, T., Tuominen, J., Ludvigsen, H., Petersen, J. C., Sørensen, T., Hansen, T. P., & Simonsen, H. R. (2004). Gas sensing using air-guiding photonic bandgap fibers. *Optics Express*, *12*(17), 4080-4087.

21. Cubillas, A. M., Silva-Lopez, M., Lazaro, J. M., Conde, O. M., Petrovich, M. N., & Lopez-Higuera, J. M. (2007). Methane detection at 1670-nm band using a hollow-core photonic bandgap fiber and a multiline algorithm. *Optics Express*, *15*(26), 17570-17576.

22. Magalhaes, F., Carvalho, J. P., Ferreira, L. A., Araújo, F. M., & Santos, J. L. (2008, October). Methane detection system based on wavelength modulation spectroscopy and hollow-core fibres. In *SENSORS, 2008 IEEE* (pp. 1277-1280). IEEE.

23. Hoo, Y. L., Liu, S., Ho, H. L., & Jin, W. (2010). Fast response microstructured optical fiber methane sensor with multiple side-openings. *IEEE Photonics Technology Letters*, *22*(5), 296-298.

24. Lehmann, H., Bartelt, H., Willsch, R., Amezcua-Correa, R., & Knight, J. C. (2011). In-line gas sensor based on a photonic bandgap fiber with laser-drilled lateral microchannels. *IEEE Sensors Journal*, *11*(11), 2926-2931.

25. Li, X., Liang, J., Lin, S., Zimin, Y., Zhang, Y., & Ueda, T. (2012). NIR spectrum analysis of natural gas based on hollow-core photonic bandgap fiber. *IEEE Sensors Journal*, *12*(7), 2362-2367.

26. Nwaboh, J. A., Hald, J., Lyngsø, J. K., Petersen, J. C., & Werhahn, O. (2013). Measurements of CO_2 in a multipass cell and in a hollow-core photonic bandgap fiber at 2 μm. *Applied Physics B*, *110*(2), 187-194.

27. Munzke, D., Böhm, M., & Reich, O. (2015). Gaseous oxygen detection using hollow-core fiber-based linear cavity ring-down spectroscopy. *Journal of Lightwave Technology*, *33*(12), 2524-2529.

28. Jin, W., Cao, Y., Yang, F., & Ho, H. L. (2015). Ultra-sensitive all-fibre photothermal spectroscopy with large dynamic range. *Nature Communications*, *6*(1), 1-8.

29. Yang, F., Tan, Y., Jin, W., Lin, Y., Qi, Y., & Ho, H. L. (2016). Hollow-core fiber Fabry–Perot photothermal gas sensor. *Optics Letters*, *41*(13), 3025-3028.

30. Lin, Y., Jin, W., Yang, F., Ma, J., Wang, C., Ho, H. L., & Liu, Y. (2016). Pulsed photothermal interferometry for spectroscopic gas detection with hollow-core optical fibre. *Scientific Reports*, *6*(1), 1-12.

31. Tan, Y., Jin, W., Yang, F., Qi, Y., Zhang, C., Lin, Y., & Ho, H. L. (2017). Hollow-core fiber-based high finesse resonating cavity for high sensitivity gas detection. *Journal of Lightwave Technology*, *35*(14), 2887-2893.

32. Li, Z., Wang, Z., Yang, F., Jin, W., & Ren, W. (2017). Mid-infrared fiber-optic photothermal interferometry. *Optics Letters*, *42*(18), 3718-3721.

33. Buric, M. P., Chen, K. P., Falk, J., & Woodruff, S. D. (2008). Enhanced spontaneous Raman scattering and gas composition analysis using a photonic crystal fiber. *Applied Optics*, *47*(23), 4255-4261.

34. Yang, X., Chang, A. S., Chen, B., Gu, C., & Bond, T. C. (2013). High sensitivity gas sensing by Raman spectroscopy in photonic crystal fiber. *Sensors and Actuators B: Chemical*, *176*, 64-68.

35. Doménech, J. L., & Cueto, M. (2013). Sensitivity enhancement in high resolution stimulated Raman spectroscopy of gases with hollow-core photonic crystal fibers. *Optics Letters*, *38*(20), 4074-4077.

36. Hanf, S., Bögözi, T., Keiner, R., Frosch, T., & Popp, J. (2015). Fast and highly sensitive fiber-enhanced Raman spectroscopic monitoring of molecular H_2 and CH_4 for point-of-care diagnosis of malabsorption disorders in exhaled human breath. *Analytical Chemistry*, *87*(2), 982-988.

37. Ippen, E. P., & Stolen, R. H. (1972). Stimulated Brillouin scattering in optical fibers. *Applied Physics Letters*, *21*(11), 539-541.

38. Horiguchi, T., Shimizu, K., Kurashima, T., Tateda, M., & Koyamada, Y. (1995). Development of a distributed sensing technique using Brillouin scattering. *Journal of Lightwave Technology*, *13*(7), 1296-1302.

39. Shelby, R. M., Levenson, M. D., & Bayer, P. W. (1985). Guided acoustic-wave Brillouin scattering. *Physical Review B*, *31*(8), 5244.

40. Diamandi, H. H., London, Y., & Zadok, A. (2017). Opto-mechanical inter-core cross-talk in multi-core fibers. *Optica*, *4*(3), 289-297.

41. Dainese, P., Russell, P. S. J., Wiederhecker, G. S., Joly, N., Fragnito, H. L., Laude, V., & Khelif, A. (2006). Raman-like light scattering from acoustic phonons in photonic crystal fiber. *Optics Express*, *14*(9), 4141-4150.

42. Dainese, P., Russell, P. S. J., Joly, N., Knight, J. C., Wiederhecker, G. S., Fragnito, H. L., ... & Khelif, A. (2006). Stimulated Brillouin scattering from multi-GHz-guided acoustic phonons in nanostructured photonic crystal fibres. *Nature Physics*, *2*(6), 388-392.

43. Kang, M. S., Nazarkin, A., Brenn, A., & Russell, P. S. J. (2009). Tightly trapped acoustic phonons in photonic crystal fibres as highly nonlinear artificial Raman oscillators. *Nature Physics*, *5*(4), 276-280.

44. Shin, H., Qiu, W., Jarecki, R., Cox, J. A., Olsson, R. H., Starbuck, A., ... & Rakich, P. T. (2013). Tailorable stimulated Brillouin scattering in nanoscale silicon waveguides. *Nature Communications*, *4*(1), 1-10.

45. Antman, Y., Clain, A., London, Y., & Zadok, A. (2016). Optomechanical sensing of liquids outside standard fibers using forward stimulated Brillouin scattering. *Optica*, *3*(5), 510-516.

46. Chow, D. M., Yang, Z., Soto, M. A., & Thévenaz, L. (2018). Distributed forward Brillouin sensor based on local light phase recovery. *Nature Communications*, *9*(1), 1-9.

47. Bashan, G., Diamandi, H. H., London, Y., Preter, E., & Zadok, A. (2018). Optomechanical time-domain reflectometry. *Nature Communications*, *9*(1), 1-9.

48. Pang, C., Hua, Z., Zhou, D., Zhang, H., Chen, L., Bao, X., & Dong, Y. (2020). Opto-mechanical time-domain analysis based on coherent forward stimulated Brillouin scattering probing. *Optica*, *7*(2), 176-184.

49. Shin, H., Cox, J. A., Jarecki, R., Starbuck, A., Wang, Z., & Rakich, P. T. (2015). Control of coherent information via on-chip photonic–phononic emitter–receivers. *Nature Communications*, *6*(1), 1-8.

50. Kittlaus, E. A., Shin, H., & Rakich, P. T. (2016). Large Brillouin amplification in silicon. *Nature Photonics*, *10*(7), 463-467.

51. Otterstrom, N. T., Behunin, R. O., Kittlaus, E. A., Wang, Z., & Rakich, P. T. (2018). A silicon Brillouin laser. *Science*, *360*(6393), 1113-1116.

52. Pang, M., Jiang, X., He, W., Wong, G. K. L., Onishchukov, G., Joly, N. Y., ... & Russell, P. S. J. (2015). Stable subpicosecond soliton fiber laser passively mode-locked by gigahertz acoustic resonance in photonic crystal fiber core. *Optica*, *2*(4), 339-342.

53. née Zhong, W. E., Stiller, B., Elser, D., Heim, B., Marquardt, C., & Leuchs, G. (2015). Depolarized guided acoustic wave Brillouin scattering in hollow-core photonic crystal fibers. *Optics Express*, *23*(21), 27707-27714.

54. Renninger, W. H., Shin, H., Behunin, R. O., Kharel, P., Kittlaus, E. A., & Rakich, P. T. (2016). Forward Brillouin scattering in hollow-core photonic bandgap fibers. *New Journal of Physics*, *18*(2), 025008.

55. Renninger, W. H., Behunin, R. O., & Rakich, P. T. (2016). Guided-wave Brillouin scattering in air. *Optica*, *3*(12), 1316-1319.

56. Koehler, J. R., Köttig, F., Trabold, B. M., Tani, F., & Russell, P. S. J. (2018). Long-lived refractive-index changes induced by femtosecond ionization in gas-filled single-ring photonic-crystal fibers. *Physical Review Applied*, *10*(6), 064020.

57. Yang, F., Gyger, F., & Thévenaz, L. (2020). Intense Brillouin amplification in gas using hollow-core waveguides. *Nature Photonics*, *14*(11), 700-708.

58. Iyer, A., Xu, W., Antonio-Lopez, J. E., Correa, R. A., & Renninger, W. H. (2020). Ultra-low Brillouin scattering in anti-resonant hollow-core fibers. *APL Photonics*, *5*(9), 096109.

Chapter 2 Basic principles

In this chapter, we introduce the basic knowledge required for spectroscopic gas sensing with HCFs. The principles of optical absorption spectroscopy and stimulated Raman spectroscopy are presented; followed by the basics of WMS, PTS, PAS, and HCFs.

2.1. Absorption spectroscopy of gases

Gas molecules are made of atoms bonded to each other. Similar to a dumbbell connected by a spring, the molecule can vibrate or rotate at a given frequency called natural frequency, which is typically in the frequency range of IR light. For those vibrational or rotational modes that change the dipole moment of molecules near the equilibrium position, IR light can be absorbed in these frequencies, named IR active.

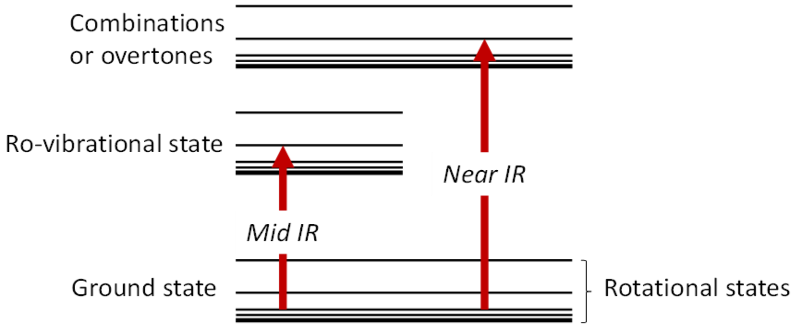

Figure 2.1. The energy level diagram of IR active molecules.

Quantum mechanics states that the energy of molecule can only be in a series of discrete values, termed the energy level. The energy of a gas molecule is the sum of the electronic, vibrational, rotational, nuclear and transitional components. IR light cannot excite an electronic transition for ordinary gas molecules. In the IR region, we concern on the vibrational and rotational components of molecules (rovibrational transitions). There are mainly four kinds of physical processes: absorption, spontaneous emission, non-radiative relaxation, and stimulated emission. The first three processes are closely related to photothermal process and absorbance of the gas sample. The stimulated emission is hard to observe in rovibrational transitions due to the short lifetime of the energy level.

The incoming photons with a specific frequency can be absorbed by the molecule when the energy of the incident photon equals the energy gap between the upper energy level and the lower energy level of the molecule, termed absorption. The molecules in the upper energy level can transit to a lower energy level without emitting a photon, termed as non-radiative relaxation. The energy is transformed into the translational energy of the molecule and increases the temperature of the sample on the macroscopic scale. Figure 2.1 shows a schematic diagram of IR absorption spectroscopy. For example, the rovibrational modes of common molecules, such as CH_4, C_2H_2 and H_2O, lie in the mid IR range. Besides, the vibrational and rotational modes can also form overtone or combination bands, which commonly lie in the near IR. The IR absorption spectrum (or IR spectroscopy) is sensitive to the bond structure of the molecule and can be the fingerprint of molecules. By absorbing a photon, the molecule is pumped to a higher energy level. The rotational quantum number of the molecule will change by -1, +1, or 0, referring to the P-branch, R-branch or Q-branch, respectively. The excited molecules then return to the ground state via complex de-excitation channels. Most of the absorbed energy will be released via non-radiative relaxation and heat or acoustic waves can be generated during this process. We will introduce this process in detail in Section 2.4.

Vibrational modes and rotational modes refer to the periodic physical motion of molecules. For a linear multi-atom molecule with N atoms, there are 3N modes in total (3N degrees of freedom). Three transitional modes represent the direction of movement of molecules, and two or three (for linear molecules or nonlinear molecules) rotational modes. From this point of view, we call vibrational modes and rotational modes the internal modes, which represent the internal molecular motions. Therefore, there are 3N-5 vibrational modes for linear molecules and 3N-6 vibrational modes for nonlinear molecules. In IR spectroscopy, the frequency of rovibrational modes is usually described by the inverse of wavelength, namely wavenumber. The wavenumber of vibrational modes is approximately from 400 cm^{-1} to 4000 cm^{-1}. Take hydrogen halide and molecular hydrogen as an example, as we show in Table 2.1, the stiffness of these chemical bonds is similar because Chlorine (Cl) and Bromine (Br) are both halogens. The wavenumber of fundamental vibrational modes varies because the masses of these molecules are different. The ability of attracting electrons is different between halogen and hydrogen, which makes the hydrogen halide a permanent dipole. This enables the IR absorption of the fundamental vibrational modes. However, for molecules like H_2, the same atoms which form the molecule make H_2 a non-permanent dipole. Hence, hydrogen is hard to detect using traditional IR absorption spectroscopy.

Table 2.1. The fundamental vibrational transition of linear molecules.

Molecule	Wavenumber (*cm*$^{-1}$)
HCl	2658
HBr	2439
H_2	4342

The vibrational model of a diatomic molecule is not exactly a harmonic oscillator. The wavenumber of a vibrational mode of diatomic molecule can be described by [1]

$$G_e(v) = \nu_e\left(v + \frac{1}{2}\right) - \nu_e\chi_e\left(v + \frac{1}{2}\right)^2 \tag{2.1}$$

where ν_e is the vibrational harmonic wavenumber, v the vibrational quantum number and χ_e is the vibrational anharmonic constant. The subscript e in Eq. (2.1) refers the electronic quantum number. The electronic energy level is assumed to be in the ground state for IR absorption spectroscopy. The wavenumber of a rotational mode can be described by

$$F_v(J) = B_vJ(J+1) - D_vJ^2(J+1)^2 \tag{2.2}$$

where B_v is the rotational harmonic wavenumber and D_v is the rotational anharmonic constant. The subscript v in Eq. (2.2) refers the vibrational quantum number. In a classical view, the rotational anharmonic constant represents that the centrifugal force pulls the atoms apart when the molecule rotates. The wavenumber of rovibrational mode is the sum of vibrational term $G_e(v)$ and the rotational term $F_v(J)$. The wavenumber of rovibrational mode can be directly related to the energy by using

$$E_{vR}(v,J) = hc_0\big(G(v) + F_v(J)\big) \tag{2.3}$$

where h is the Planck's constant and c_0 is the speed of light in the vacuum. The dissociation energy of a chemical bond is much higher than the vibrational energy, and both of which are much higher than the rotational energy. Take hydrogen chloride (HCl) as an example, the dissociation energy of HCl bond is 420 *kJ/mol*, the harmonic vibrational energy gap is 35 *kJ/mol* and the rotational energy gap is 0.25 *kJ/mol* [2].

For a linear molecule, take nitrogen as an example, there are two degenerate rotational modes with the same wavenumber as shown in Figs. 2.2(a) and (b). However, there is no rotational mode like Fig. 2.2(c) existed because the molecule is rotational symmetric along the spin axis. For a nonlinear molecule like H_2O, there are three independent rotational modes with different rotational wavenumber. As we shown in Figs. 2.2(d)-(f), these rotational modes have different moment of inertia, which makes them different in rotational wavenumber.

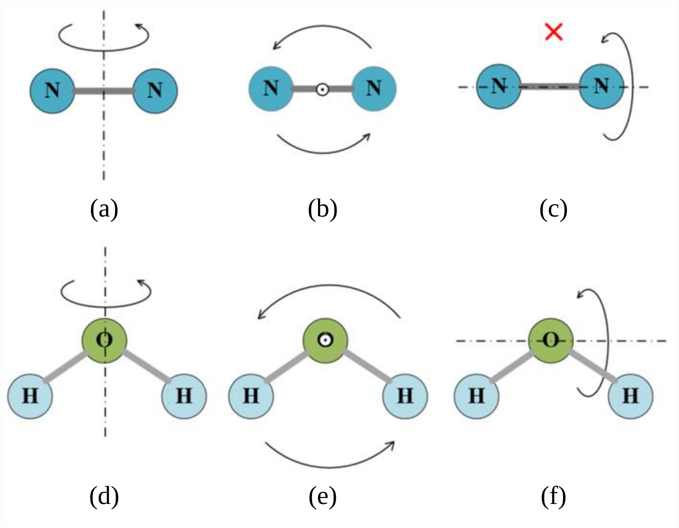

Figure 2.2. Molecular rotational modes.

Every chemical bond of a molecule can vibrate symmetrically or asymmetrically. Although the discussion above is about diatomic molecules, C_2H_2 molecule is similar to a diatomic molecule, which can be regarded as a linear molecule. As shown it Table 2.2, there are seven vibrational modes in total for C_2H_2 [3]. The bending modes and the wagging modes have two degeneracies because the molecule can vibrate in two orthogonal directions.

Table 2.2. Vibrational modes and their wavenumber of C_2H_2.

Vibrational Modes		$G_0(v)(cm^{-1})$
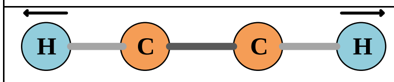	Symmetric C-H stretching, v_1	3476
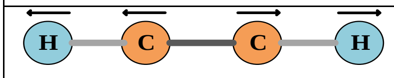	Symmetric C-C stretching, v_2	2181
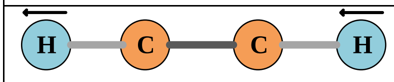	Asymmetric C-H stretching, v_3	3423
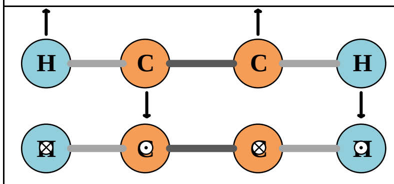	H-C-C-H bending, v_4	805
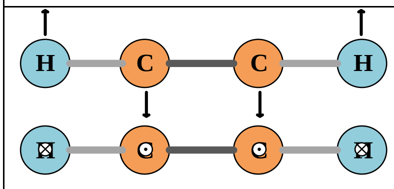	H-C-C-H wagging, v_5	929

These fundamental vibrational modes can couple together to form a complex vibration of the molecule. In the view of IR spectroscopy, the intense fundamental absorption band will be accompanied by several weaker bands at the multiple fundamental wavenumbers and at the sum of two fundamental wavenumbers, namely, overtone and combination bands.

Take C_2H_2 as an example, a combination band of C_2H_2 is the $\nu_1 + \nu_3$ band located near 6714 cm^{-1}. The molecule can also rotate about an axis as we discussed above and thus have a series of quantized rovibrational transitions. The dipole selection rule for this band is $\Delta J = \pm 1$, termed as the so-called P-branch ($\Delta J = -1$) and R-branch ($\Delta J = +1$):

$$\nu_{-1}(J) = \nu_1 + \nu_3 - (B_0 + B_1)J - (B_0 - B_1)J^2 \tag{2.4}$$

$$\nu_{+1}(J) = \nu_1 + \nu_3 + (B_0 + B_1)(J+1) - (B_0 - B_1)(J+1)^2 \tag{2.5}$$

where B_0 and B_1 refers to the rotational harmonic wavenumber in the ground vibrational state and in the excited vibrational state, respectively. The anharmonic constant can also be included in Eqs. (2.4) and (2.5) for higher accuracy.

Experimentally, the absorption by the gas molecules can be measured by the attenuation of the IR light. The transmitted intensity of light I_0' described by Beer-Lambert law is

$$I_0' = I_0 \exp(-\alpha_A(\nu)L) \tag{2.6}$$

where I_0 is the intensity of incident light, α_A in cm^{-1} the absorption coefficient of gas molecules at a given wavenumber ν, and L the length of absorptive medium. However, the absorption coefficient varies with the pressure p, temperature T, and other parameters such as the components of gas mixture. The absorption of molecules is more generally described by the spectral line intensity S_i at a given temperature T. The absorption coefficient can be calculated using the parameters provided by the HITRAN database [4]:

$$\alpha_A(\nu) = S_i N f_V(\nu) \tag{2.7}$$

$$N = \frac{pC}{k_B T} \tag{2.8}$$

where N is the molecule density per unit volume in $molecule/cm^3$, $f_V(\nu)$ the Voigt lineshape function in cm^{-1}, C the gas concentration of the absorptive gas, and k_B is the Boltzmann constant. The spectral line intensity S_i in $cm/molecule$ is defined by the area of the lineshape per molecule per unit volume. For most large molecules like C_2H_2, CH_4, etc., the Voigt profile is sufficient to describe the lineshape accurately. The line profile can also be more accurately described by other models like Rautian profile, Hartmann-Tran model, etc. [5] to account for the speed-dependent lineshape or collision-induced velocity changes (so called

Dicke narrowing [6]).The Voigt lineshape function is a convolution of the Lorentzian lineshape function f_L and the Doppler lineshape function f_D:

$$f_V(\nu) = \int_{-\infty}^{-\infty} f_L(\nu - \xi) f_D(\xi) d\xi \tag{2.9}$$

$$f_L(\nu) = \frac{1}{\pi} \frac{\gamma_L}{\gamma_L^2 + (\nu - \nu_i)^2} \tag{2.10}$$

$$f_G(\nu) = \sqrt{\frac{\ln 2}{\pi \gamma_D^2}} \exp\left(-\frac{(\nu - \nu_i)^2 \ln 2}{\gamma_D^2}\right) \tag{2.11}$$

where γ_L and γ_D are, respectively, the Lorentzian linewidth and the Doppler linewidth at half-width and half-maximum, and ν_i is the wavenumber of the absorption line. In the application of gas sensing, the pressure shift of the absorption line is ignored and the buffer gas is assumed to be air or nitrogen. Hence, the air-broadening coefficient is used in the calculation. The pressure and temperature dependent linewidths are calculated by

$$\gamma_D = \frac{\nu_i}{c_0} \sqrt{\frac{2 N_A k_B T \ln 2}{M}} \tag{2.12}$$

$$\gamma_L = \left(\frac{T_{ref}}{T}\right)^{n_{air}} \left[\gamma_{air}(1 - C) + \gamma_{self} C\right] p \tag{2.13}$$

where N_A is Avogadro constant, M the molar mass of the molecule, $T_{ref} = 296\,K$ the reference temperature, n_{air} the exponential coefficient of the temperature dependence, γ_{air} and γ_{self} are respectively the air-broadening coefficient and the self-broadening coefficient of the gas molecule.

Here we can calculate the spectrum of C_2H_2 at the $\nu_1 + \nu_3$ band by using the data from HITRAN database. The P-branch and R-branch of acetylene $\nu_1 + \nu_3$ are shown in Fig. 2.3(a). A real spectrum of the absorption band is slightly different from the theoretical band calculated from Eqs. (2.4) and (2.5) due to the isotopes, overtone absorption band, etc. The different line intensity between even rotational quantum number and odd rotational quantum number is because of the nuclear spin degeneracy of hydrogen atom. The nuclear spin degeneracy for even J states is 1 and for odd J states is 3.

Equations (2.7)-(2.13) give a complex nonlinear dependence of α_A on the gas concentration. Under the atmospheric condition (i.e., $T \approx T_{ref}$, $p = 1\ atm$), the Doppler broadening and the absorption due to the neighboring absorption line can be ignored. The absorption coefficient of P(13) absorption line with different concentrations in air is shown in Fig. 2.3(b). The blue curve shows the absorption coefficient calculated from Eq. (2.7). And under the small gas concentration approximation ($C \ll 1$), the self-broadening can be ignored. Then we have a linear approximation of α_A on the gas concentration at the line center ν_i:

$$\alpha_A(\nu_i) = \frac{S_i p C}{\pi \gamma_{air} k_B T} \tag{2.14}$$

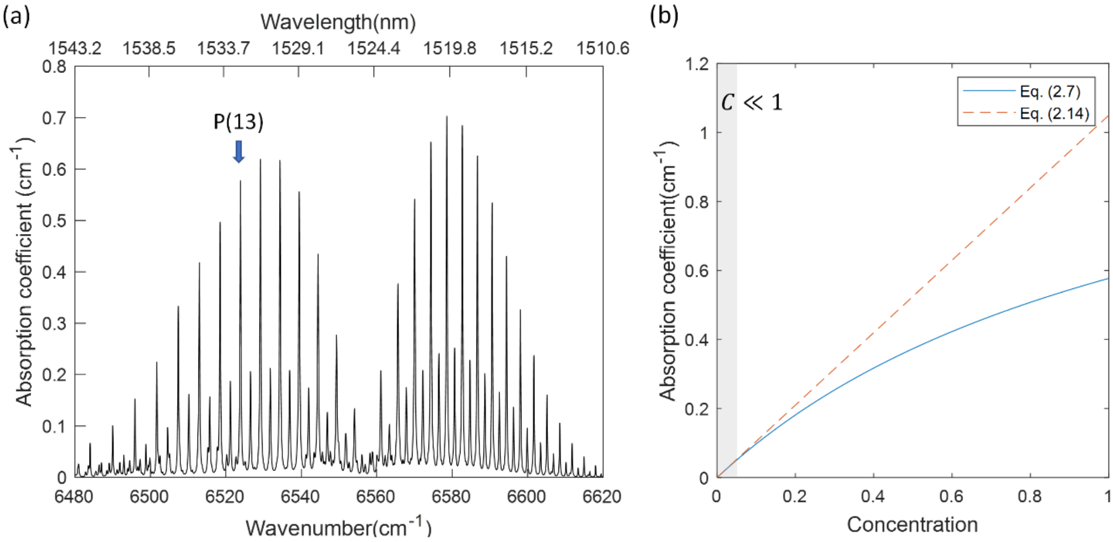

Figure 2.3. The absorption coefficient of acetylene. (a) the $\nu_1 + \nu_3$ combination band of C_2H_2 at atmospheric condition. (b) The absorption coefficients for P(13) line calculated from Eqs. (2.7) and (2.14).

The red dashed curve in Fig. 2.3(b) shows the absorption coefficient calculated from Eq. (2.14). This approximation is only accurate for gas concentration much smaller than unity. The line center ν_i of absorption line of gas is also an important parameter when we design a system for gas detection. For example, under the atmospheric condition and the small gas concentration approximation, the normalized absorption coefficients (α_A/C) of different gases in the near IR and mid-IR range is shown in Fig. 2.4. For C_2H_2, the fundamental ν_3 band in the mid-IR is much stronger than the $\nu_1 + \nu_3$ band in the near IR as indicated by the blue arrows.

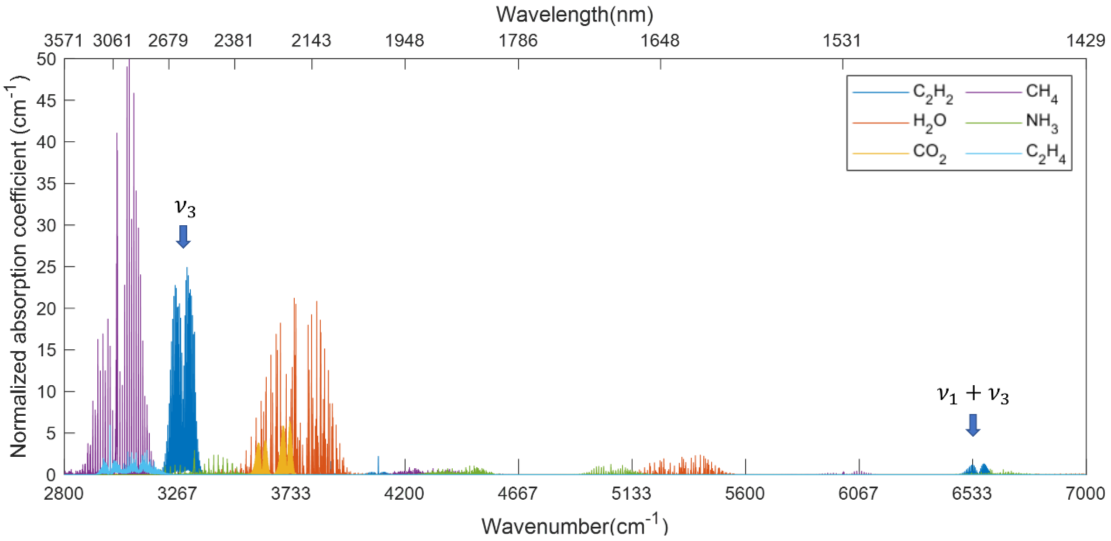

Figure 2.4. The normalized absorption coefficient using Eq. (2.14) for different gases under atmospheric condition.

2.2. Raman spectroscopy of gases

Raman scattering is an inelastic scattering process which the scattered light is upshifted or downshifted by a fixed frequency. The molecule is excited from an initial state to a final state. And the frequency shift is equal to the frequency difference between the initial state and the final state. From a classical view, the excited molecule can vibrates near its equilibrium position and changes its polarizability, corresponding to a Raman active vibrational mode. For the combination or overtone of the modes, they can also be Raman active but are typically much weaker than the fundamental modes. In the scope of this thesis, we only discuss the rovibrational Raman scattering with the ground electronic state. As shown in Fig. 2.5, an incident pump can be scattered to a lower frequency called Stokes and excite the gas molecule to a rovibrational state. Meanwhile, the pump can also be scattered to a higher frequency called anti-Stokes and de-excite the gas molecule from a rovibrational state to a lower energy state. These two processes are, respectively, named Stokes and anti-Stokes Raman scattering. The process of Raman scattering becomes stimulated when the pump power is sufficiently high or an additional Stokes/anti-Stokes beam is incident.

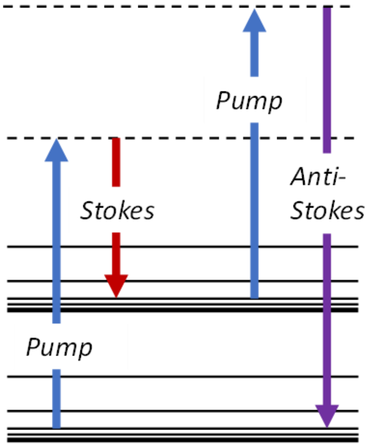

Figure 2.5. The energy level diagram of Raman scattering

We begin with a very simple case when only two plane waves (pump and Stokes) are involved. In the steady state, the Raman gain coefficient is related to the spontaneous Raman scattering cross-section σ' by [7]

$$g_R = \frac{2c_0^2}{h\nu_S^3}\frac{\Delta N_{fi}}{\pi\Delta\nu_R}\sigma'(\theta;\hat{p}_S,\hat{p}_P) \tag{2.15}$$

where ν_S is the frequency of Stokes light, $\Delta\nu_R$ the Raman linewidth (full-width at half-maximum, FWHM), and ΔN_{fi} is the density difference between the initial state i and the final state f. The Raman scattering cross-section is related to the scattering angle (θ) and the polarizations ($\hat{p}_S$ and $\hat{p}_P$) of Stokes light and pump light. Figure 2.6 shows a schematic diagram of the Raman scattering, where $\hat{e}_S$ and $\hat{e}_P$ show the propagation direction of the Stokes and the pump, respectively.

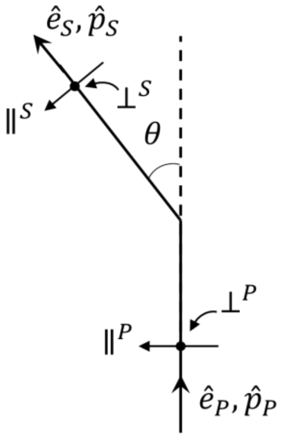

Figure 2.6. The definition of the Raman scattering plane and polarizations [8].

The Raman cross-section in *cm²/sr* is related to an isotropic average of the polarizability tensor $\alpha_{\rho\sigma}$ in the laboratory coordinate by [8]

$$\sigma'(\theta;\hat{p}_S,\hat{p}_P)=\left(\frac{2\pi\nu_S}{c_0}\right)^4\langle\left(\alpha_{\rho\sigma}\right)_{fi}^2\rangle \tag{2.16}$$

where the bracket $\langle\ldots\rangle$ refers to an isotropic average over all directions. It is straightforward to make an isotropic average since the Raman scattering is related to polarizability of free rotating molecules. In our concern of Raman scattering in HCFs, the scattering angle is taken to be 0 or π, which refers to the forward or backward Raman scattering. For example, for backward Raman scattering,

$$\sigma'(\pi;\Vert^S,\perp^P)=\left(\frac{2\pi\nu_S}{c_0}\right)^4\langle\left(\alpha_{xy}\right)_{fi}^2\rangle \tag{2.17}$$

$$\sigma'(\pi;\perp^S,\perp^P)=\left(\frac{2\pi\nu_S}{c_0}\right)^4\langle\left(\alpha_{yy}\right)_{fi}^2\rangle \tag{2.18}$$

The subscripts x,y,z refers the three axes of the coordinates. The symbol $\Vert^S$ or $\perp^P$ refer to the polarization of light which is parallel or perpendicular to the plane with a normal vector of $\hat{e}_S\times\hat{e}_P$ (the Raman scattering plane). Because the axes can be chosen arbitrarily, all isotropic averages with the same type are equal. For example, $\langle\left(\alpha_{xy}\right)_{fi}^2\rangle=\langle\left(\alpha_{yz}\right)_{fi}^2\rangle$ and $\langle\left(\alpha_{yy}\right)_{fi}^2\rangle=\langle(\alpha_{xx})_{fi}^2\rangle$. Therefore, the cross-sections are equal for forward and backward Raman scattering with the same linear polarizations.

Table 2.3 Polarization dependent Raman cross-section [8].

Branch	Δv	ΔJ	$\sigma'(0;\perp^S,\perp^P)$[a]	$\sigma'(0;\Vert^S,\perp^P)$	$\sigma'(0;R^S,R^P)$[b]	$\sigma'(0;R^S,L^P)$
S₀(J)	0	+2	$\frac{4}{45}b_{J+2,J}\gamma_{00}^2$	$\frac{1}{15}b_{J+2,J}\gamma_{00}^2$	$\frac{1}{45}b_{J+2,J}\gamma_{00}^2$	$\frac{2}{15}b_{J+2,J}\gamma_{00}^2$
S₁(J)	+1		$\frac{4}{45}b_{J+2,J}\gamma_{10}^2$	$\frac{1}{15}b_{J+2,J}\gamma_{10}^2$	$\frac{1}{45}b_{J+2,J}\gamma_{10}^2$	$\frac{2}{15}b_{J+2,J}\gamma_{10}^2$
Q₁(J)	+1	0	$a_{10}^2+\frac{4}{45}b_{J,J}\gamma_{10}^2$	$\frac{1}{15}b_{J,J}\gamma_{10}^2$	$a_{10}^2+\frac{1}{45}b_{J,J}\gamma_{10}^2$	$\frac{2}{15}b_{J,J}\gamma_{10}^2$
Rayleigh	0	0	$a_{00}^2+\frac{4}{45}b_{J,J}\gamma_{00}^2$	$\frac{1}{15}b_{J,J}\gamma_{00}^2$	$a_{00}^2+\frac{1}{45}b_{J,J}\gamma_{00}^2$	$\frac{2}{15}b_{J,J}\gamma_{00}^2$

a. The factor $(2\pi\nu_S/c_0)^4$ has been omitted;

b. R and L refer to the right and left hand circular polarization;

c. The Placzek-Teller b factor are $b_{J,J}=\frac{J(J+1)}{(2J-1)(2J+3)}$ and $b_{J+2,J}=\frac{3(J+1)(J+2)}{2(2J+1)(2J+3)}$.

However, in the above formula we need to know the isotropic average for every specific initial state i and final state f, which is lack of versatility. The initial and final states can both be a rovibrational energy level. Actually, the contribution of rotational level to the Raman cross-section can be evaluated by introducing a molecule-fixed irreducible polarizability tensor [8]. The rotation-vibration interaction is ignored in the intensity calculation of Raman scattering. We summarize the Stokes Raman cross-section of the S-branch and Q-branch of diatomic molecule in Table 2.3.

In Table 2.3, the subscript of the polarizability refers to the final vibrational quantum number and the initial vibrational quantum number. For diatomic molecule, the mean polarizability a and the anisotropy γ can be regard as a function of the vibrational coordinate q to the first order:

$$a = a_{00} + \left(\frac{\partial a}{\partial q}\right)_0 q \tag{2.19}$$

$$\gamma = \gamma_{00} + \left(\frac{\partial \gamma}{\partial q}\right)_0 q \tag{2.20}$$

Then

$$a_{fi} = \langle v^f|a|v^i\rangle = a_{00}\langle v^f|v^i\rangle + \left(\frac{\partial a}{\partial q}\right)_0 \langle v^f|q|v^i\rangle \tag{2.21}$$

$$\gamma_{fi} = \langle v^f|\gamma|v^i\rangle = \gamma_{00}\langle v^f|v^i\rangle + \left(\frac{\partial \gamma}{\partial q}\right)_0 \langle v^f|q|v^i\rangle \tag{2.22}$$

The ‘bra-ket’ notation refers to the overlap integral of the vibrational wave function. The overlap integral in Eqs. (2.21) and (2.22) can be evaluated using harmonic assumption. A special case is when both $\Delta v = v^f - v^i$ and ΔJ are zero. The scattering cross-section here actually describes the Rayleigh scattering. Rayleigh scattering has long been used to measure the mean polarizability and the anisotropy of gas molecules [9-10]. And it shows a good agreement with the polarizability measured by the pure rotational Raman scattering. It needs to be noted here that the polarizability is also dependent on the frequency of pump light ν_P and the frequency of electronic states of the molecule. Empirical formula is usually used to describe the pump frequency dependence of polarizability.

The Raman scattering of different scattering angle sometimes shares the same cross-section. This is because they are related to the same isotropic average of the polarizability tensor. For linear polarization and circular polarization, the relationship are listed below:

$$\sigma'(\pi; \perp^S, \perp^P) = \sigma'(0; \perp^S, \perp^P) \tag{2.18}$$

$$\sigma'(\pi; \|^S, \perp^P) = \sigma'(0; \|^S, \perp^P) \tag{2.19}$$

$$\sigma'(\pi; R^S, R^P \ or \ L^P) = \sigma'(0; L^S, R^P \ or \ L^P) \tag{2.20}$$

Equations (2.18)-(2.20) show that the cross-sections of forward and backward spontaneous Raman scattering only depend on the relative polarization between pump and Stokes light. However, for SRS, the backward Raman gain coefficient is usually smaller than the forward one due to the Doppler broadening.

Here we use the *$Q_1(1)$* transition of molecule hydrogen with a Raman frequency shift of $\nu_R = 4155\ cm^{-1}$ as an example. The Raman linewidth of molecule hydrogen is pressure dependent. At low pressures, the linewidth is limited by the Doppler broadening. As pressure increases, under the influences of both Dick narrowing [6] and collisional broadening, the linewidth reaches its minimum and then further increases. The Dick narrowing can be accounted by using Rautian profile [11]. However, for simplicity, the linewidth of the *$Q_1(1)$* transition is usually given by an empirical formula [12]

$$\Delta\nu_R^f = \frac{309}{\rho} + 51.8\rho \tag{2.21}$$

where $\Delta\nu_R^f$ describes the forward Raman linewidth in *MHz*, ρ is the density in amagats. The error of this formula increases as the gas density decreases. It is accurate for density larger than 1 *amagat*. By using Eqs. (2.15), (2.21) and Table 2.3, and considering the wavelength dependence of polarizability, the forward Raman gain coefficient (in *cm/W*) for parallel linear polarizations of pump and Stokes at room temperature (298 *K*) is given by [7]

$$g_R = \frac{9.37 \times 10^6 \left(52\rho/\Delta\nu_R^f\right)(K_B/0.658)(\nu_P - 4155)}{(7.19 \times 10^9 - \nu_P^2)^2} \tag{2.22}$$

where K_B is the Boltzmann population factor equal to 0.658 at 298 *K* for $J = 1$ rotational level of hydrogen and ν_P is the pump wavenumber in cm^{-1}. The wavelength dependence, polarization dependence, and pressure dependence of Raman gain coefficient calculated from Eq. (2.22) and Table 2.3 are shown in Fig. 2.7. The Raman gain coefficient is higher for shorter wavelengths of pump light. For vibrational Raman transitions like *$Q_1(1)$*, the Raman gain coefficient reaches the maximum with parallel linear polarizations of pump and Stokes.

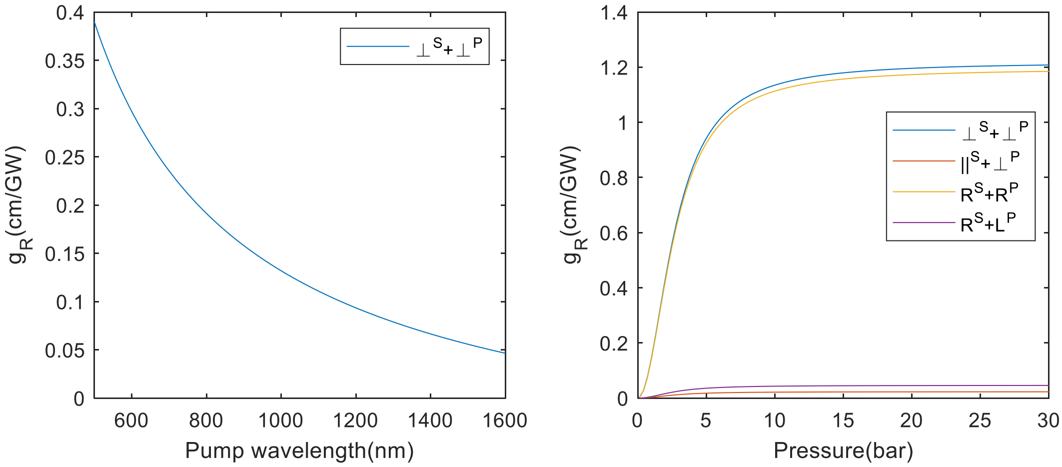

Figure 2.7. The Raman gain coefficient of $Q_1(1)$ for different pump wavelengths, pressures, and polarizations.

Then we summarize the main conclusions of SRS using a semi-classic approach. For further details, readers may refer to [13-16]. In the semi-classical approach, the molecule is considered as a two-level system and the state of the molecules is described by the density matrix. The diagonal elements of the density matrix and the off-diagonal elements describe, respectively, the occupational probabilities (in other words, the population of molecules) and the coherence of the two energy states.

Considering a simple situation when only the fundamental mode of the pump field E_P and the Stokes field E_S are involved, the molecular coherence Q_R and the difference of occupational probability w_R between the two energy level are described by the Maxwell-Bloch equations:

$$\frac{\partial Q_R}{\partial t}+\frac{Q_R}{\tau_2}=\frac{i}{4}\kappa_1 E_P E_S^* q_P q_S^* w_R \tag{2.23}$$

$$\frac{\partial w_R}{\partial t}+\frac{w_R-w_{R,0}}{\tau_1}=Im\{\kappa_1 Q_R^* E_P E_S^* q_P q_S^*\} \tag{2.24}$$

where $q_l=\exp\left(-j\beta_l z\right)$ is the phase term of optical field, $\beta_l=2\pi n_l/\lambda_l$ the propagation constant of the optical mode l, and κ_1 is a coefficient which represents the strength of Raman gain. The time constant τ_1 and τ_2 are phenomenologically the dephasing time of the molecular coherence and the relaxation time of the excited molecule. At thermal equilibrium, $w_{R,0}=-1$. For the forward Raman scattering, the evolution of pump and Stokes amplitude can be calculated by

$$\left(\frac{\partial}{\partial z}+\frac{n_P}{c_0}\frac{\partial}{\partial t}\right)E_P=-i\kappa_2\frac{\omega_P}{\omega_S}Q_R^* E_S q_S q_P^* \tag{2.25}$$

$$\left(\frac{\partial}{\partial z}+\frac{n_S}{c_0}\frac{\partial}{\partial t}\right)E_S = -i\kappa_2 Q_R^* E_P q_P q_S^* \tag{2.26}$$

where $n_{P,S}$ are the mode indices of the pump and Stokes fields. By calculating the steady-state Raman gain factor g_R, the coefficients κ_1 and κ_2 can be expressed as

$$\kappa_1 = \sqrt{\frac{2g_R c_0^2 \varepsilon_0^2}{Nh(\nu_P - \nu_R)\tau_2}} \tag{2.27}$$

$$\kappa_2 = \frac{Nh(\nu_P - \nu_R)\kappa_1}{2\varepsilon_0 c_0} \tag{2.28}$$

where ε_0 the absolute electric permittivity in the vacuum. The above equations can also be applied when multiple optical fields (e.g., anti-Stokes and high-order scattering light) are involved.

By making several assumptions, the Maxwell-Bloch equations can be reduced to simple coupled equations of pump and Stokes lights. First, since we are tracing gases in low concentrations, the Raman gain $g_R I_P z$ is much smaller than 1. Second, the modulation frequency of pump or Stokes laser is in the range of a few kilohertz. Hence, the molecular coherence satisfies that $\partial Q_R/\partial t \ll Q_R/T_2$. Last, SRS is operated at the steady-state regime. Under these assumptions, the intensity change of pump and Stokes lights can be described by

$$\frac{\partial I_P}{\partial z} = -\frac{\nu_P}{\nu_S} g_R I_P I_S \tag{2.29}$$

$$\frac{\partial I_S}{\partial z} = g_R I_P I_S \tag{2.30}$$

where $I_{P,S} = \varepsilon_0 c_0 n_{P,S} \left|E_{P,S}\right|^2/2$ is the optical intensity of pump or Stokes. Equations (2.29) and (2.30) are sufficient to describe SRS in most applications of tracing gas. Exceptions such as RPTS will be discussed detailly in Chapter 6.

2.3. Wavelength modulation spectroscopy

Laser spectroscopy usually uses modulation techniques such as wavelength modulation, frequency modulation and intensity modulation to improve its sensitivity. The modulation techniques shift the signal to a higher frequency with a lower noise. In this section, we introduce WMS which is used in our experiments. The optical frequency (or wavelength) is sinusoidally modulated as

$$\nu = \bar{\nu}(1 + me^{j\omega t}) \tag{2.31}$$

where $m = \delta\nu/\bar{\nu}$ is the modulation depth and $\bar{\nu}$ is the mean optical frequency of the modulated light over a modulation period. The absorption coefficient (or Raman gain coefficient) with a Lorentzian lineshape is expressed as

$$\alpha_A(\nu) = \alpha_{A,i}\frac{1}{1+[(\nu-\nu_i)/\gamma_L]^2} \tag{2.32}$$

where $\alpha_{A,i}$ is the absorption coefficient at the center of an absorption line ν_0. By inserting Eq. (2.31) into Eq. (2.32) and expand it as harmonic series, we have [17]

$$\alpha_A(\bar{\nu}) = \alpha_{A,i}Re\left\{H_0 + \sum_{n=1}^{\infty} H_n\, e^{-jn\omega t}\right\} \tag{2.33}$$

$$H_0(\bar{\nu}) = \frac{1}{\pi}\int_0^{\pi}\frac{1}{1+[(\bar{\nu}-\nu_i)/\gamma_L \ + mcos(\vartheta)]^2}d\vartheta \tag{2.34}$$

$$H_n(\bar{\nu}) = \frac{2}{\pi}\int_0^{\pi}\frac{\cos{(n\vartheta)}}{1+[(\bar{\nu}-\nu_i)/\gamma_L + mcos(\vartheta)]^2}d\vartheta \quad (n \geq 1) \tag{2.35}$$

where H_0 and H_n are the harmonic coefficients which describe the harmonic waveforms. A complex notation is used in Eq. (2.33) and in the remaining chapters, and only the real component has the physics meaning. From now on, the function '$Re\{\}$' is omitted for clarity.

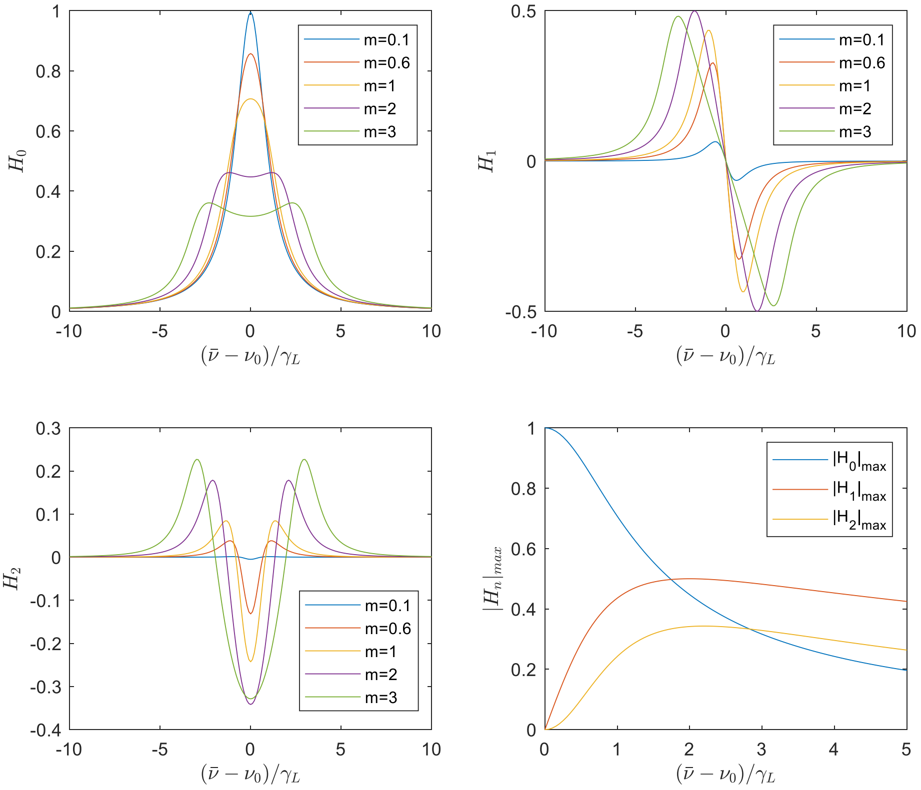

Figure 2.8. The harmonic coefficients with different modulation depth.

Figure 2.8 shows calculated the harmonic coefficients with different modulation depth. The even orders of harmonic coefficients reach their maximum at the center of the absorption line. For the second harmonic wave, the second harmonic coefficient at the line center reaches its maximum with a modulation depth of $m \approx 2.2$ and then slowly drops when further increase the modulation depth.

The process of harmonics generation is a nonlinear process that should be carefully considered when we study any subsequent physical processes of optical absorption (or Raman scattering). For instance, a second-order harmonic heat source will be generated by wavelength modulation. We will discuss this in the next chapter.

2.4. Photothermal and photoacoustic spectroscopy

PTS and PAS refer to a group of high-sensitivity gas tracing methods by measuring subsequent temperature change or pressure change due to optical absorption. The basic principle of the photothermal and photoacoustic processes is demonstrated by Fig. 2.9.

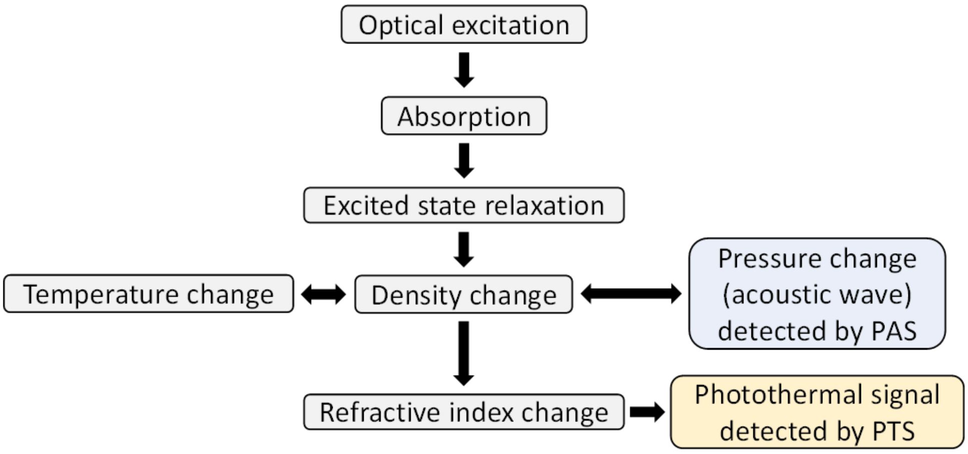

Figure 2.9. Process of photothermal/photoacoustic effect [18].

The incident pump light centered at an absorption line of the target gas is partially absorbed by the gas molecule. Part of the molecules is pumped to the upper rovibrational level from a pure rotational level. Then through a series of fast or slow excited state relaxation processes, molecules at the upper rovibrational level return to the pure rotational levels with a canonical distribution (or Boltzmann distribution). The relaxation processes cause local heating and generate thermal expansion which induces a pressure change or acoustic wave. The acoustic wave can then be detected by a microphone, which is the principle of PAS. Besides, the local heating results in temperature change, causing RI change of the gas. The change of RI can be measured by a probe light, which is the principle of PTS.

Then we introduce the basic processes of non-radiative relaxation [18]. As shown in Figs. 2.10(a) and (b), before the absorption of light, there are molecules in a series of pure rotational levels on the ground vibrational level in canonical distribution. As the pump photons being absorbed by the gas molecules, molecules in one of the rotational levels are excited to an upper rovibrational level, leaving a hole in its original rotational level. The rotation to rotation (R-R) relaxation in the ground vibrational level happens immediately to fill the hole caused by optical excitation. And also, R-R relaxation happens on the excited vibrational level, making the molecules redistributed in canonical distribution on the excited vibrational level. These R-R relaxations accompany with the rotation to translation (R-T) and translation to rotation (T-R) processes. The accompanying R-T and T-R processes can generate or consume translational energy. If the energy of the excited rotational state is larger than $k_B T$, translational energy will be generated during the redistribution of excited rotational levels. Otherwise, translational energy is consumed in this process. Typical relaxation time constant of R-R and R-T (or T-R) for small molecules at room temperature and standard atmospheric pressure are about 10^{-10} s and 10^{-8} s.

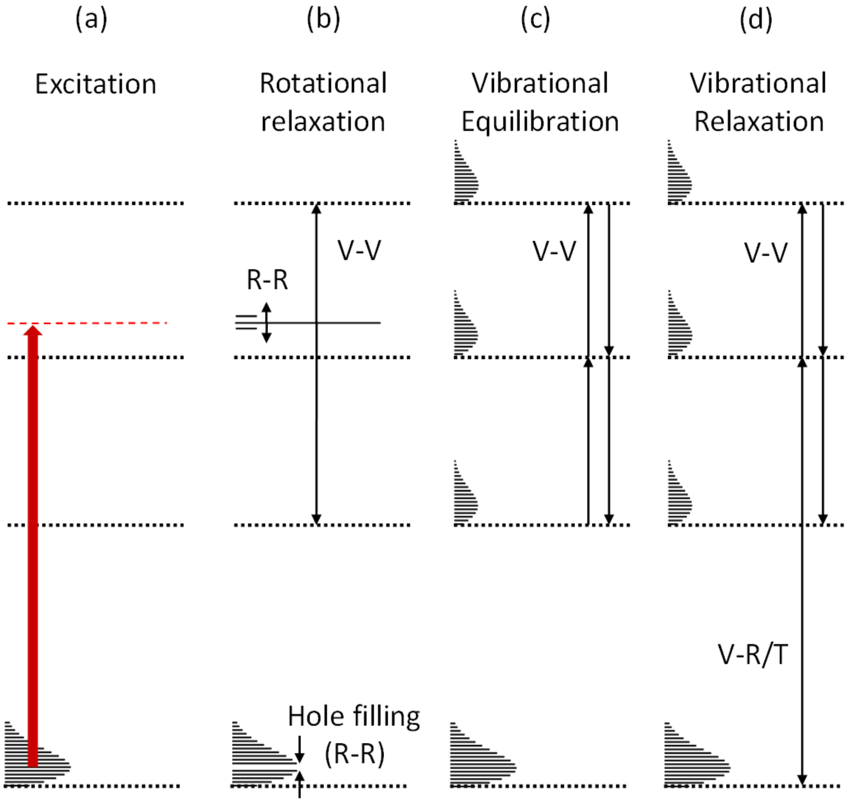

Figure 2.10. Excitation state relaxation of rovibrational levels [18].

Following this, the vibration to vibration (V-V) processes take place. Before returning to the ground state, V-V relaxation will result in a quasi-equilibrium at all vibrational levels as shown in Fig. 2.10(c). The typical relaxation time constant of V-V process is 10^{-8} s. Finally, the excited vibrational levels return to the ground state by vibration to rotation (V-R) and vibration to translation (V-T) process as we demonstrated in Fig. 2.10(d). V-R/T process is the bottleneck of the excitation-state relaxation. For common polyatomic molecules, they have a typical relaxation time constant of 10^{-6} s.

Table 2.4. The vibrational relaxation time of gases.

Gas-Buffer gas	$p\tau_V(atm \cdot s)$
C_2H_2-C_2H_2	1.0×10^{-7}
C_2H_2-Ne	2.9×10^{-6}
C_2H_2-Ar	2.0×10^{-6}
H_2-H_2	3.4×10^{-4}
H_2-Ne	1.5×10^{-4}
H_2-Ar	6.5×10^{-3}
CO-H_2	9.3×10^{-5}
CO-He	3.0×10^{-3}

One needs to note that the relaxation time of V-R/T process (vibrational relaxation time, VRT) might vary significantly for different gases or in different gas mixtures. For gases at room temperature (296 *K*), the product of the gas pressure (p) and VRT (τ_V) can be viewed as a constant:

$$p\tau_V = const. \tag{2.36}$$

For example, Table 2.4 shows VRT of some gases. For C_2H_2, VRT is about a few hundred nanoseconds [19]. For hydrocarbons which have many vibrational modes, VRT is usually much shorter than those molecules only have one vibrational mode (e.g. H_2 [20], CO [21], O_2, etc.).

The V-R/T process determines the speed of heat generation through non-radiative relaxation. Hence, the VRT is of importance for PTS and PAS. Although the relaxation of excited rovibrational states is a complex process, it is a good approximation to treat it as a two-level system with a time constant of τ_V. The efficiency of heat generation at a given angular frequency ω can be approximated as

$$\eta_H = \frac{1}{\sqrt{1 + (\omega\tau_V)^2}} \tag{2.37}$$

2.5. Hollow-core fibers

HCFs refer to a class of optical fibers that guide light in a hollow core. According to the light guiding mechanism, HCFs can be categorized into two types: photonic bandgap HCF (PBG-HCF) and anti-resonant HCF (AR-HCF). The schematic diagrams of HCFs are shown in Fig. 2.11.

Figs. 2.11(a) and (b) show the 7-cell and 19-cell PBG-HCFs that guide the light by photonic bandgaps [22, 23]. PBG-HCFs can be easily coiled to smaller diameters (e.g., a few centimeters) with a small additional loss, which enables compact fiber gas sensors. However, in the aspect of gas sensing, PBG-HCFs have two main disadvantages: first, PBG-HCFs usually have a transmission window of a few hundred nanometers, which is insufficient for vibrational Raman spectroscopy or multi-gases detection that needs a broadband transmission; second, the cladding modes and high-order modes of the fiber limit the sensitivity of PBG-HCF-based interferometry gas sensors.

Figs. 2.11(c-f) shows several types of AR-HCFs [24-26]. The light guiding mechanism can be explained by using the principle of anti-resonant reflecting optical waveguide [27]. The silica thin layers surrounding the air core act as a Fabry-Perot resonator. The anti-resonance of the thin layers greatly reduces the overlap between the air-core mode and the silica cladding mode. This prohibits the air-core mode to channel out through its coupling with the silica cladding mode continuum, which is called inhibited-coupling [28]. Compared with PBG-HCFs, AR-HCFs have a much broader transmission window and better mode purity. However, the bending loss of these fibers is usually larger than that of PBG-HCFs.

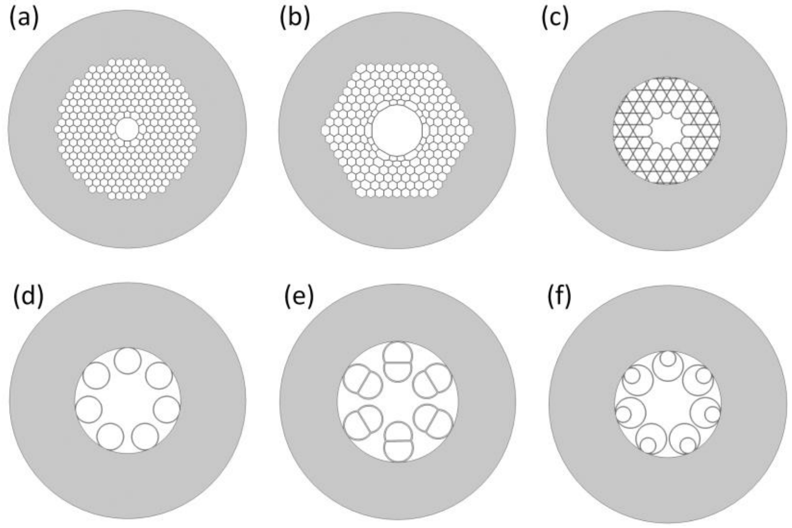

Figure 2.11. Schematic diagram of HCFs. (a) 7-cell PBG-HCF. (b) 19-cell PBG-HCF. (c) Kagome HCF. (d) Single-ring AR-HCF. (e) Conjoined-tube AR-HCF. (f) Nested nodeless AR-HCF.

2.6. Conclusion

We have introduced the basic principles of optical gas sensing based on either absorption spectroscopy or Raman spectroscopy. Several techniques to achieve high sensitivity, i.e., WMS, PTS and PAS are presented. The different types of HCFs that may be used in the experiment are also presented. This will form the foundation for the remaining chapters.

Reference of Chapter 2

1. Banwell, C. N. (1972). *Fundamentals of molecular spectroscopy*.
2. Steinfeld, J. I. (2012). *Molecules and radiation: An introduction to modern molecular spectroscopy*. Courier Corporation.
3. Colthup, N. (2012). *Introduction to infrared and Raman spectroscopy*. Elsevier.
4. Rothman, L. S., Gordon, I. E., Babikov, Y., Barbe, A., Benner, D. C., Bernath, P. F., ... & Wagner, G. (2013). The HITRAN2012 molecular spectroscopic database. *Journal of Quantitative Spectroscopy and Radiative Transfer*, *130*, 4-50.
5. Tennyson, J., Bernath, P. F., Campargue, A., Császár, A. G., Daumont, L., Gamache, R. R., ... & Polyansky, O. L. (2014). Recommended isolated-line profile for representing high-resolution spectroscopic transitions (IUPAC Technical Report). *Pure and Applied Chemistry*, *86*(12), 1931-1943.
6. Dicke, R. H. (1953). The effect of collisions upon the Doppler width of spectral lines. *Physical Review*, *89*(2), 472.
7. Bischel, W. K., & Dyer, M. J. (1986). Wavelength dependence of the absolute Raman gain coefficient for the Q(1) transition in H_2. *JOSA B*, *3*(5), 677-682.
8. Long, D. A. (2002). *The Raman effect: a unified treatment of the theory of Raman scattering by molecules*. Wiley.
9. Bridge, N. J., & Buckingham, A. D. (1966). The polarization of laser light scattered by gases. *Proceedings of the Royal Society of London. Series A. Mathematical and Physical Sciences*, *295*(1442), 334-349.
10. Bogaard, M. P., Buckingham, A. D., Pierens, R. K., & White, A. H. (1978). Rayleigh scattering depolarization ratio and molecular polarizability anisotropy for gases. *Journal of the Chemical Society, Faraday Transactions 1: Physical Chemistry in Condensed Phases*, *74*, 3008-3015.
11. Rautian, S. G., & Sobel'man, I. I. (1967). The effect of collisions on the Doppler broadening of spectral lines. *Soviet Physics Uspekhi*, *9*(5), 701.
12. Bischel, W. K., & Dyer, M. J. (1986). Temperature dependence of the Raman linewidth and line shift for the Q(1) and Q(0) transitions in normal and para-H_2. *Physical Review A*, *33*(5), 3113.

13. Boyd, R. W. (2020). *Nonlinear Optics*. Academic press.

14. Mridha, M. (2018). *Ultraviolet Raman Scattering in Hollow-Core Photonic Crystal Fiber* (Doctoral dissertation, Friedrich-Alexander-Universität Erlangen-Nürnberg (FAU)).

15. Bauerschmidt, S. T., Novoa, D., & Russell, P. S. J. (2015). Dramatic Raman gain suppression in the vicinity of the zero dispersion point in a gas-filled hollow-core photonic crystal fiber. *Physical Review Letters*, *115*(24), 243901.

16. Raymer, M. G., & Walmsley, I. A. (1990). III The quantum coherence properties of stimulated Raman scattering. *Progress in Optics, 28,* 181-270.

17. Arndt, R. (1965). Analytical line shapes for Lorentzian signals broadened by modulation. *Journal of Applied Physics, 36*(8), 2522-2524.

18. Bialkowski, S. E. (1996). *Photothermal spectroscopy methods for chemical analysis* (Vol. 177). John Wiley & Sons.

19. Häger, J., Krieger, W., Rüegg, T., & Walther, H. (1980). Vibrational relaxation of acetylene and acetylene–rare-gas mixtures. *The Journal of Chemical Physics*, *72*(8), 4286-4290.

20. Dove, J. E., & Teitelbaum, H. (1974). The vibrational relaxation of H2. I. Experimental measurements of the rate of relaxation by H_2, He, Ne, Ar, and Kr. *Chemical Physics*, *6*(3), 431-444.

21. Millikan, R. C., & White, D. R. (1963). Systematics of vibrational relaxation. *The Journal of chemical physics*, *39*(12), 3209-3213.

22. Smith, C. M., Venkataraman, N., Gallagher, M. T., Müller, D., West, J. A., Borrelli, N. F., ... & Koch, K. W. (2003). Low-loss hollow-core silica/air photonic bandgap fibre. *Nature*, *424*(6949), 657-659.

23. Mangan, B. J., Farr, L., Langford, A., Roberts, P. J., Williams, D. P., Couny, F., ... & Russell, P. S. J. (2004, February). Low loss (1.7 dB/km) hollow core photonic bandgap fiber. *In Optical Fiber Communication Conference* (p. PD24). Optical Society of America.

24. Benabid, F., Knight, J. C., Antonopoulos, G., & Russell, P. S. J. (2002). Stimulated Raman scattering in hydrogen-filled hollow-core photonic crystal fiber. *Science*, *298*(5592), 399-402.

25. Gao, S. F., Wang, Y. Y., Ding, W., Jiang, D. L., Gu, S., Zhang, X., & Wang, P. (2018). Hollow-core conjoined-tube negative-curvature fibre with ultralow loss. *Nature Communications*, *9*(1), 1-6.

26. Poletti, F. (2014). Nested antiresonant nodeless hollow core fiber. *Optics Express*, *22*(20), 23807-23828.

27. Litchinitser, N. M., Abeeluck, A. K., Headley, C., & Eggleton, B. J. (2002). Antiresonant reflecting photonic crystal optical waveguides. *Optics Letters*, *27*(18), 1592-1594.

28. Debord, B., Amsanpally, A., Chafer, M., Baz, A., Maurel, M., Blondy, J. M., ... & Benabid, F. (2017). Ultralow transmission loss in inhibited-coupling guiding hollow fibers. *Optica*, *4*(2), 209-217.

Chapter 3 PTS and PAS in gas-filled HCFs

In this chapter, we present the principles of PTS and PAS in gas-filled HCFs. Firstly, we study the photothermal and photoacoustic effects in HCFs, including the heat generation, heat conduction, and thermo-viscous acoustics. Secondly, we investigate the mechanisms of optical phase modulation in HCFs induced by the gas density change, shifting boundary effect, and photoelastic effect. At last, we study different types of fiber optical interferometers and the noise in these interferometers.

3.1. Photothermal and photoacoustic effects in gas-filled HCFs

The non-radiative relaxation of excited molecules generates heat and subsequently results in temperature change. The change of local temperature will also lead to local expansion or contraction of the gas. This process generates a pressure wave (acoustic wave) that propagates at the speed of sound. The generation of temperature change and acoustic wave by optical absorption are named photothermal effect and photoacoustic effect, respectively. These two effects can be described by a set of hydrodynamic equations that describe the pressure, density, and temperature of the gas. The conservation laws of mass, momentum, and energy of gas result in the complex Navier-Stokes equations. For optical spectroscopy, the gas sample can be viewed as continuous fluid if the mean free path of molecule is much smaller than the optical wavelength. At atmospheric conditions, the mean free path of common gases is less than 100 *nm*. The continuum approximation greatly simplifies the calculation. Under some circumstances, the Navier-Stokes equations can be reduced to simple equations such as heat conduction equation and the pressure acoustic equation. In HCFs, the hydrodynamics should be carefully evaluated to study the problem appropriately.

In the scope of tracing gases, the change of pressure (p), density (ρ), temperature (T) and velocity ($\boldsymbol{u}$) can be regarded as small perturbations from the equilibrium:

$$T = T_0(\boldsymbol{r}) + T_1(\boldsymbol{r}, t) \tag{3.1}$$

$$\rho = \rho_0(\boldsymbol{r}) + \rho_1(\boldsymbol{r}, t) \tag{3.2}$$

$$p = p_0(\boldsymbol{r}) + p_1(\boldsymbol{r}, t) \tag{3.3}$$

$$\boldsymbol{u} = \boldsymbol{u}_1(\boldsymbol{r}, t) \tag{3.4}$$

where the subscripts 0 and 1 refer to the equilibrium value and the first-order perturbation, respectively. The equilibrium velocity is assumed to be zero. The heat source can also be expressed as

$$Q = Q_0(\boldsymbol{r}) + Q_1(\boldsymbol{r}, t) \tag{3.5}$$

The parameters in Eqs. (3.1)-(3.4) are govern by the Navier-Stokes equations [1]. The equilibrium values are the solution of the steady-state equations and hence can be dropped from the equations. Then we have the first-order perturbation equations:

$$\frac{\partial \rho_1}{\partial t} + \nabla \cdot (\rho_0 \boldsymbol{u}_1) = 0 \tag{3.6}$$

$$\rho_0 \frac{\partial \boldsymbol{u}_1}{\partial t} = \nabla \cdot [-p_1 \boldsymbol{I} + \eta_0 (\nabla \boldsymbol{u}_1 + (\nabla \boldsymbol{u}_1)^T - \left(\frac{2}{3}\eta_0 - \eta_B\right)(\nabla \cdot \boldsymbol{u}_1)\boldsymbol{I}] \tag{3.7}$$

$$\rho_0 c_P \left(\frac{\partial T_1}{\partial t} + \boldsymbol{u}_1 \nabla T_0\right) - T_0 \alpha_P \left(\frac{\partial T_1}{\partial t} + \boldsymbol{u}_1 \cdot \nabla p_0\right) = \kappa \nabla^2 T + Q_1 \tag{3.8}$$

$$\rho = \rho_0 (\beta_T p - \alpha_P T) \tag{3.9}$$

where $\boldsymbol{I}$ is unit tensor, c_P the isobaric specific heat capacity, κ the thermal conductivity, η_0 the dynamic viscosity, and η_B is the bulk viscosity. The superscript T refers the transpose of the tensor. The isobaric coefficient of thermal expansion α_P and the isothermal compressibility β_T are defined as

$$\alpha_P = -\frac{1}{\rho_0} \frac{\partial \rho}{\partial T}\bigg|_{p_0} \tag{3.10}$$

$$\beta_T = \frac{1}{\rho_0} \frac{\partial \rho}{\partial p}\bigg|_{T_0} \tag{3.11}$$

Equations (3.6)-(3.9) can be solved numerically with commercial software. Among these thermodynamic variables, the density change is of our primary concern since it is the main contributor to the change of RI.

3.1.1 Heat source

Before the study of macroscopic state of gas in HCFs, we have a look at the heat source that causes the change of the state of gas. The heat source is the power generated by non-radiative relaxation per unit volume. For both photothermal and photoacoustic effects, it is an important source term that solely responsible for the temperature change and the generation of acoustic wave. In HCFs, due to the optical power is confined in a small hollow core, the heat source can have a very high power density. It can reach a level of MW/m^3, typically 4-5 orders of magnitude larger than that in free space. In PTS or PAS, the wavelength or intensity of the pump light is modulated to realize a low noise detection with a lock-in amplifier (LIA). The heat source consists of a background heat source Q_0 and harmonic heat sources $\tilde{Q}_n$:

$$Q = Q_0 + \sum_{n=1}^{\infty} \tilde{Q}_n \tag{3.12}$$

First, we introduce the heat source generated by the absorption with a Lorentzian lineshape. Assuming a two-level system, we have

$$\frac{dN_u}{dt} = \frac{\alpha_A I_P}{h\nu_P} - \frac{N_u}{\tau} \tag{3.13}$$

$$Q = h\nu_P \frac{N_u}{\tau} \tag{3.14}$$

where N_u is the number density of molecules in the upper energy level, $I_P = P_P|\psi_P|^2$ the optical intensity of pump beam, and τ is the relaxation time of the upper energy level, which is mainly determined by VRT as we have discussed in Chapter 2. By using Eqs. (3.13)-(3.14), we have

$$Q = P_P|\psi_P|^2\alpha_A\left(H_0 + \sum_{n=1}^{\infty} \frac{H_n e^{-j(n\omega t-\varphi_n)}}{\sqrt{(n\omega\tau)^2+1}}\right) \tag{3.15}$$

where ψ_P is the normalized electric field of the pump light that satisfies $\langle\psi_P, \psi_P\rangle = 1$ over the fiber cross-section, and $\varphi_n = arctan\,(n\omega\tau)$ is the phase difference between the pump light and the harmonic heat source $\tilde{Q}_n$. In Eq. (3.15), since $\langle\psi_P, \psi_P\rangle = 1$ over the fiber cross-section, the value of $|\psi_P|^2$ is on the order of $1/A_{eff}$, where A_{eff} is the effective area of the HCF.

For the heat source generated by SRS, only part of the energy is transformed into heat. In our case, the Raman gain $g_R I_P z$ is much smaller than 1 since we are tracing gases. SRS is operated in the steady state regime and the phase mismatch is ignored ($\beta_P - \beta_S \approx 0$). Recall Eqs. (2.23) and (2.34) in Chapter 2, we can arrive at a simple expression of the Raman heat source using

$$Q = h\nu_R N \frac{w_R - w_{R,0}}{2\tau_1} \tag{3.16}$$

and the intensity change of pump and Stokes lights are

$$\frac{\partial I_P}{\partial z} = -\frac{\nu_P}{\nu_S} g_R I_P I_S \tag{3.17}$$

$$\frac{\partial I_S}{\partial z} = g_R I_P I_S \tag{3.18}$$

Similar to the heat source due to optical absorption, we have a heat source due to SRS from Eqs. (3.16-3.18)

$$Q = P_P P_S |\psi_P \psi_S|^2 g_R \frac{\nu_R}{\nu_S} \left(H_0 + \sum_{n=1}^{\infty} \frac{H_n e^{-j(n\omega t - \varphi_n)}}{\sqrt{(n\omega\tau_1)^2 + 1}} \right) \tag{3.19}$$

Compared with the heat source due to optical absorption, the heat source due to SRS is more concentrated in the center of HCF due to the power four dependence of $|\psi_P \psi_S|^2$. We will revisit the Raman heat source later in Chapter 6.

3.1.2. Heat conduction

Approximated solutions of Eqs. (3.6)-(3.9) can be derived by using the Fourier-Laplace transform with some approximations [2]. The solutions can be divided into two modes: the thermal diffusion mode and the propagation acoustic mode. The propagation acoustic mode travels at the speed of sound and the thermal diffusion mode slowly spreads out due to heat conduction. In this section, we discuss about the thermal diffusion mode in HCFs. The thermal diffusion mode is described by the thermal diffusion equation:

$$\rho_0 c_P \frac{\partial T}{\partial t} - \kappa \nabla^2 T = Q \tag{3.20}$$

In this equation, only the temperature change is considered. Before calculation, we need to determine the boundary for heat conduction. HCFs usually consist of several functional layers as shown in Fig. 3.1(a): polymer coating, silica cladding, silica microstructures and air core. Ideally, all the layers of HCF and the surrounding air need to be included in simulation. However, we found that for most HCFs, it is a good approximation to treat the outer boundary of silica microstructure as an isothermal boundary. This approximation greatly simplifies our calculation. For instance, Figure 3.1(b) shows the scanning electron microscopy (SEM) of the central area of a PBG-HCF and a single-ring AR-HCF. For PBG-HCF, the boundary of the air core can be treated as an isothermal boundary, and we could only consider the thermal conduction of the filling gas. And for AR-HCF, the inner boundary of the solid silica cladding is treated as an isothermal boundary. Hence, we only need to consider the thermal conduction in the silica microstructures and in the air core.

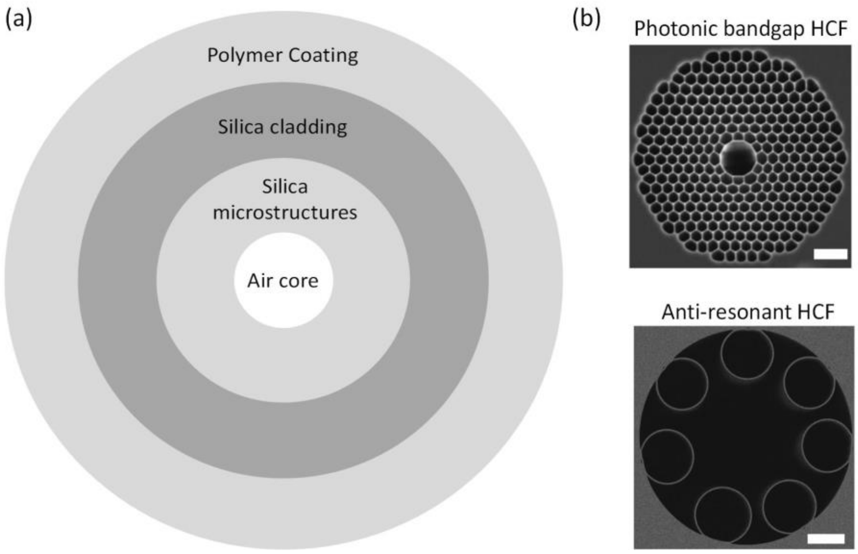

Figure 3.1. Schematic diagram of HCFs for simulation. (a) Model of HCFs. (b) SEM of PBG-HCF and AR-HCF. The white bar is 10 μm.

As we have discussed above, the thermodynamics we studied is linearized as small perturbations near the equilibrium. Hence, the harmonic heat source can be treated independently, and we can study Eq. (3.20) in the frequency domain:

$$j\omega\rho_0 c_P \tilde{T}_1 - \kappa\nabla^2\tilde{T}_1 = \tilde{Q}_1 \tag{3.21}$$

where $\tilde{T} = T_1 e^{j\omega t}$ and $\tilde{Q} = Q_1 e^{j\omega t}$ are the harmonic temperature field and the harmonic heat source.

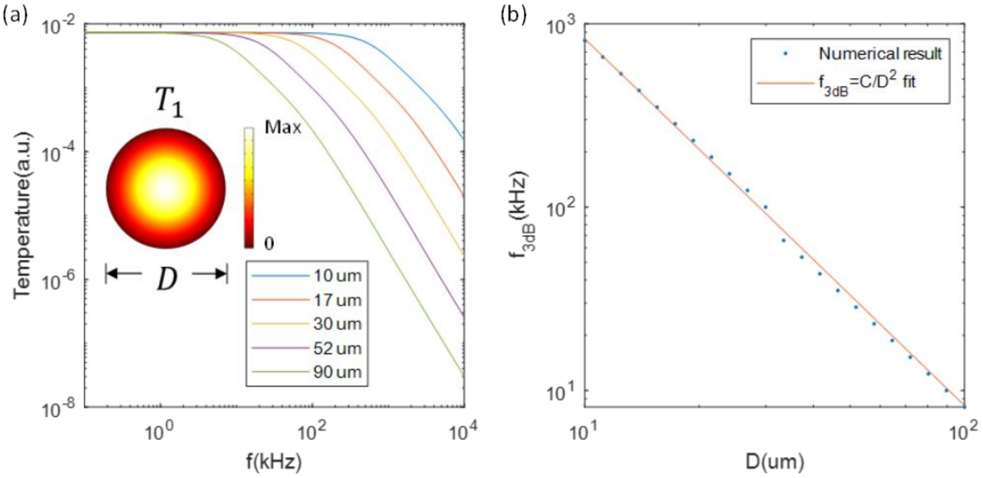

Figure 3.2. The temperature change and 3-dB cut-off frequency of PTS with different core size. (a) The frequency response of temperature at the center of air core. (b) The 3-dB roll-off frequency with different core diameter.

The core diameter of HCF is an important parameter for PTS. We take the PBG-HCF as an example and study the heat conduction in the air core with different core diameter D. For simplicity, the mode radius of the optical mode is approximated as $w_0 = D/3$ and thermal relaxation time is assumed to be much smaller than a harmonic period of heat source. As demonstrated in Fig. 3.2(a), temperature change at the center of air core saturates at low frequencies and decreases as we increase the frequency of heat source. The saturated temperature at low frequencies is the same for different core diameters. This is a useful result for us to select HCFs for PTS. The 3-dB roll-off frequency f_{3dB} for PTS of most HCFs is in the range of tens of kilohertz. At high frequencies, the speed of thermal conduction cannot catch up with the change of heat source and hence the amplitude of harmonic temperature change becomes smaller.

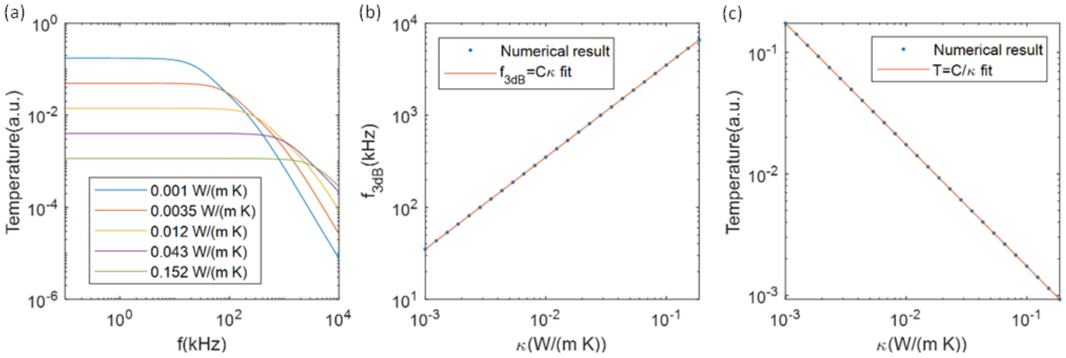

Figure 3.3. The temperature change and 3-dB cut-off frequency of PTS with different thermal conductivity. (a) The frequency response of temperature at the center of air core. (b) The 3-dB roll-off frequency with different thermal conductivity. (c) The temperature at the center of air core with different thermal conductivity.

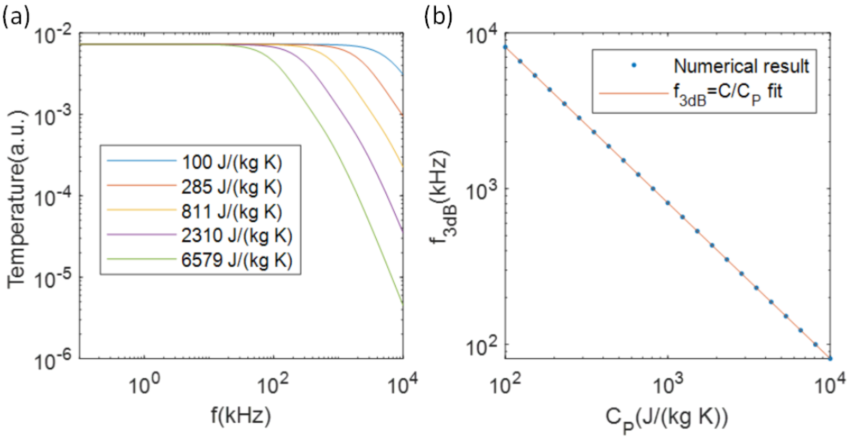

Figure 3.4. The temperature change and 3-dB cut-off frequency of PTS with different heat capacity. (a) The frequency response of temperature at the center of air core. (b) The 3-dB roll-off frequency with different isobaric heat capacity.

Although we can calculate the solution of Eq. (3.21) numerically, it would be helpful if we can have an empirical tendency of temperature at low frequencies and the 3-dB roll-off frequency. We numerically calculate the frequency response of temperature change with different core diameter D, thermal conductivity κ and isobaric specific heat capacity c_P of the filling gas. Figure 3.2(b) shows that f_{3dB} is inversely proportional to the square of core diameter. From Figs. (3.2)-(3.4) we can conclude an empirical formula of the maximum temperature change and the 3-dB roll-off frequency with an isothermal boundary condition:

$$T_{max} \propto \frac{1}{\kappa} \tag{3.22}$$

$$f_{3dB} \propto \frac{\kappa}{\rho_0 c_P D^2} \tag{3.23}$$

The exact formulas of Eqs. (3.22) and (3.23) depend on the exact profile of heat source. These two equations, the maximum temperature change at low frequencies is inversely proportional to the thermal conductivity. This is reasonable since for larger thermal conductivity, more heat is dissipated into the environment due to the thermal conduction of the filling gas. Although Eqs. (3.22) and (3.23) are derived from PBG-HCF, the empirical tendency is also applicable on other types of HCFs.

3.1.3. Thermo-viscous acoustics

In Section 3.1.2, we have discussed the thermal diffusion mode. Another approximated solution of the Navier-Stokes equations is the propagation acoustic mode. By ignoring the attenuation of acoustic wave, we have the homogeneous wave equation:

$$\frac{\partial^2 p}{\partial t^2} - c_s^2 \nabla^2 p = \frac{\alpha_P c_s^2}{c_P} \frac{\partial Q}{\partial t} \tag{3.24}$$

where c_s is the speed of sound. The wave equation describes the adiabatic process and the viscosity of gas is ignored. This equation is widely used in PAS and Brillouin spectroscopy. Traditional PAS uses bulk acoustic resonator and only a very small part of resonator is heated by the heat source. However, for HCFs, the heat source is almost overlapped with the resonator itself. For acoustic problem in small dimensions and situations that the heat conduction cannot be ignored, a thermo-viscous acoustic model is used to describe the acoustic wave. Hence, Eqs. (3.6)-(3.9) need to be used to calculate the acoustic problem in HCFs.

In HCFs, we also need to consider the vibro-acoustic coupling. The microstructure of HCFs is coupled with acoustic mode in the filling gas. Take single-ring AR-HCF as an example, the geometry used in the simulation is shown in Fig. 3.5. The fiber consists of seven silica capillaries and an air core. The displacement of silica capillary is described by the continuous linear elastic equation of solid [3]:

$$\rho_s \frac{\partial^2 \boldsymbol{w}}{\partial t^2} = \nabla \cdot \boldsymbol{\sigma_S} \tag{3.25}$$

$$\boldsymbol{\sigma_S} = \boldsymbol{S_T} \boldsymbol{\epsilon_S} = \boldsymbol{C_T} \frac{1}{2} [\nabla \boldsymbol{w} + (\nabla \boldsymbol{w})^T] \tag{3.26}$$

where ρ_S is the density of silica, $\boldsymbol{\sigma_S}$ the stress tensor, $\boldsymbol{\epsilon_S}$ the strain tensor, and $\boldsymbol{S_T}$ is the stiffness tensor, which is related to the is related to the Young's modulus and the Poisson's ratio of silica. The inner boundary of silica cladding is assumed to be rigid and the capillary is free to vibrate. The boundary condition ($b.c.$) is defined as

$$\frac{1}{\rho_0} \frac{\partial p}{\partial n} = \begin{cases} 0 & on\ A_R \\ -\dfrac{\partial^2 (\boldsymbol{w} \cdot \hat{n})}{\partial t^2} & on\ A_F \end{cases} \tag{3.27}$$

$$b.c. of\ solid = \begin{cases} \boldsymbol{w} = 0 & on\ A_R \\ \boldsymbol{\sigma_S} \cdot \hat{n} = -p\hat{n} & on\ A_F \end{cases} \tag{3.28}$$

where $\hat{n}$ is the normal vector on the outer boundary of capillary, A_R and A_F refer to the rigid boundary and the free boundary of silica. Equations (3.27) and (3.28) describe the boundary condition for the thermo-viscous acoustic equations in gas and the continuous linear elastic equation of solid, respectively. By using Eqs. (3.6)-(3.9) and Eqs. (3.25)-(3.28), we can solve the vibro-acoustic problem in the HCFs.

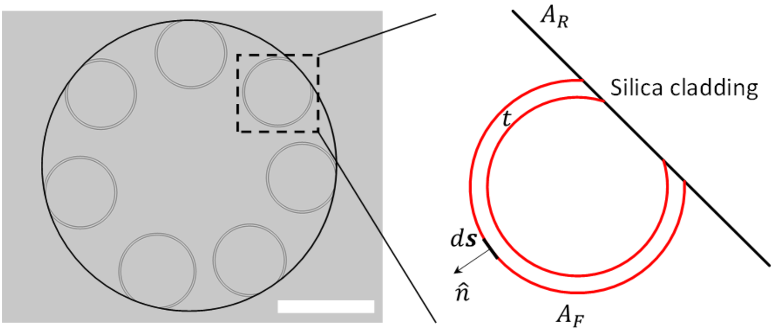

Figure 3.5. The geometry and boundary of single-ring AR-HCF. The white bar is 20 um.

For example, Fig. 3.6 demonstrates several acoustic modes supported by the AR-HCF in Fig. 3.5 calculated by finite element method (FEM). The acoustic modes can be numerically calculated with the above equations by setting the heat source as zero. The frequency of acoustic mode and its quality factor (Q_A) are also shown in the figure. The quality factor describes the damping rate of acoustic mode. It can be calculated by the ratio between the energy stored in the mode and energy loss in one acoustic cycle. The acoustic mode in AR-HCF consists of an air mode in the air core and a capillary mode in the silica capillaries. The air mode is described by the density change (ρ_1) and the capillary mode is described by the displacement of capillary ($\boldsymbol{w}$). Figures 3.6(a-c) shows the first-order radial air mode (R_{01}), the first-order two-lobes radial air mode (R_{11}) and the second-order radial air mode (R_{02}). For the air modes, the coupling with the capillary modes and uneven silica boundary makes the air modes quite lossy. The acoustic quality factors are usually less than 10 as we shown in Fig. 3.6(a-c). Compared with the air mode, the capillary modes show higher acoustic quality factor of a few hundred. Figures 3.6(d-f) show the first-order and the second-order in-plane bending modes of the capillary. Because the sizes of the capillary are slightly different, there are several bending modes with the same order for different capillaries. At atmospheric pressure, the acoustic quality factor of capillary mode is limited by the air damping. The photoacoustic effect in HCFs are studied in detail in Chapter 5.

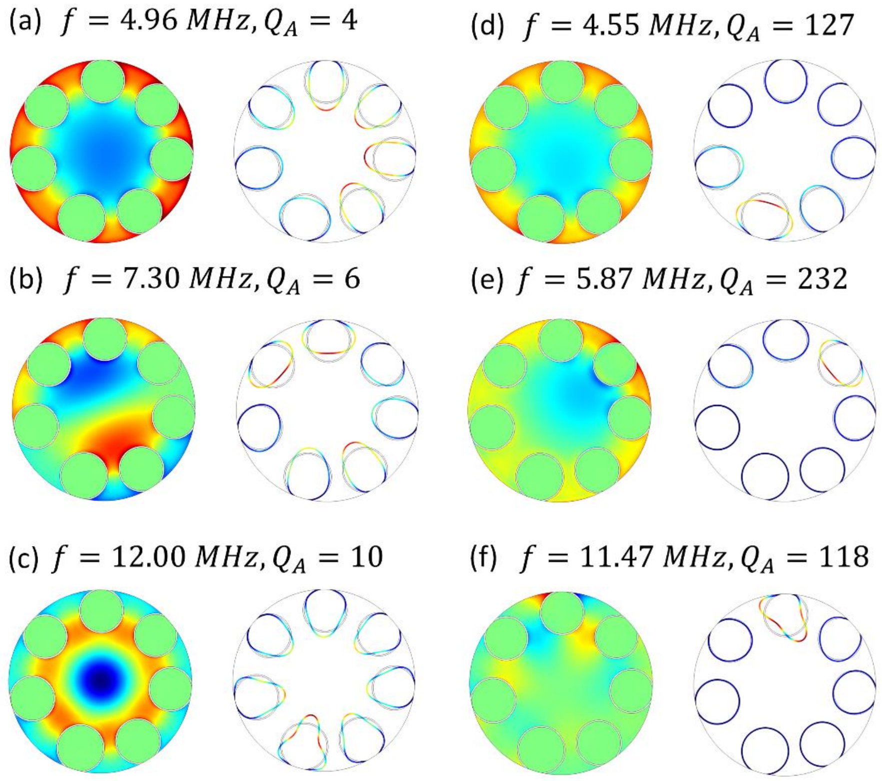

Figure 3.6. Acoustic modes in an AR-HCF with their frequency f and quality factor Q_A.

3.2. Perturbation theory of optical mode in HCFs

In HCFs, the change of thermodynamic parameters due to photothermal or photoacoustic effects has almost the same profile along the fiber. Hence, it is efficient to use an optical mode to probe the photothermal and photothermal effects via the perturbation of mode index. The vector wave equation in terms of the propagation constant β is [4]

$$(\nabla_t^2 + n^2k^2 - \beta^2)\boldsymbol{E}_m = -(\nabla_t + i\beta\hat{z})\boldsymbol{E}_{t,m} \cdot \nabla_t \ln n^2 \tag{3.29}$$

where the subscript t stands for the transverse component and n is the profile of RI on the fiber cross-section. Equation (3.49) is not a Hermitian eigenproblem and the perturbation theory cannot be directly applied on it. People have tried to find a rigid perturbation theory for the propagation constant but the no universal expression was got [5]. However, Equation (3.43) can be reduced to a Hermitian eigenproblem with the weakly guiding approximation:

$$(\nabla_t^2 + n^2k^2)\boldsymbol{E}_{t,m} = \beta^2\boldsymbol{E}_{t,m} \tag{3.30}$$

which is simply the Helmholtz equation. This is a good approximation for HCFs because the optical field in or near the silica structure is very weak. Hence, the right-hand side of Eq. (3.29) can be approximated as zero. For Hermitian eigenproblem, the standard perturbation theory can be applied to determine the perturbation of the eigenvalue [6]. Equation (3.30) leads to a simple perturbation formula of the mode index n_m:

$$\frac{dn_m}{dx} = \frac{1}{2n_m}\frac{\langle \boldsymbol{E}_{t,m} \left| \frac{d\varepsilon_r}{dx} \right| \boldsymbol{E}_{t,m}\rangle}{\langle \boldsymbol{E}_{t,m} | \boldsymbol{E}_{t,m}\rangle} \tag{3.31}$$

For PTS or PAS, the perturbation of mode index consists of three parts:

$$\frac{dn_m}{dx} = \left.\frac{dn_m}{dx}\right|_{GD} + \left.\frac{dn_m}{dx}\right|_{PE} + \left.\frac{dn_m}{dx}\right|_{SB} \tag{3.32}$$

The change of gas density (GD), photoelasticity (PE), and shifting boundary (SB) have contribution to the change of mode index. The gas density and the photoelasticity account for the change of RI profile in the gas-filled region and in the silica region of HCFs, respectively. And the shifting boundary accounts for the change of mode index by the shifting of gas-silica boundary. The first and second terms of Eq. (3.32) can be calculated using Eq. (3.31) easily. However, for the last term of Eq. (3.32), $d\varepsilon/dx$ becomes infinite when accounting a shifting boundary. An anisotropic smoothing method is applied to solve this problem and it can be calculated as [7]

$$\left.\frac{dn_m}{dx}\right|_{SB} = \frac{1}{2n_m}\frac{\int ds \frac{d(\boldsymbol{w}\cdot\hat{n})}{dx}\left(\Delta\varepsilon_{r,12}\left|\hat{n}\times\boldsymbol{E}_{t,m}\right|^2 - \Delta\left(\varepsilon_{r,12}^{-1}\right)\left|\hat{n}\cdot\boldsymbol{E}_{t,m}\right|^2\right)}{\langle \boldsymbol{E}_{t,m} | \boldsymbol{E}_{t,m}\rangle} \tag{3.33}$$

where $\Delta\varepsilon_{12} = \varepsilon_1 - \varepsilon_2, \Delta(\varepsilon_{12}^{-1}) = \varepsilon_1^{-1} - \varepsilon_2^{-1}$ are the differential permittivity between the dielectric material. The integral is performed along the air-silica boundary. In AR-HCF, the integrals over the two air-silica boundary have opposite signs. This is because the representation of symbols 1 and 2 are exchanged on the inner/outer boundary. Then we discuss about the gas density change term in Eq. (3.32). The change of the dielectric constant is

$$\Delta\varepsilon_r = \left(\frac{\partial\varepsilon_r}{\partial\rho}\right)_T \Delta\rho + \left(\frac{\partial\varepsilon_r}{\partial T}\right)_\rho \Delta T \tag{3.34}$$

The second term due to the temperature change can be ignored with an error of about 2% [6]. The approximation indicates that PTS measures the density change induced by the temperature change. The temperature change itself has little influence on the RI of gas. For pressure acoustic model (i.e., Eq. (3.24)) as an adiabatic process, the density change can be expressed as $\Delta\rho = \Delta p / c_s^2$. For thermo-viscous acoustic model, the density change is described by Eq. (3.9). The change of relative electric permittivity is related to the density change by

$$\Delta\varepsilon_r = \frac{\gamma_e \Delta\rho}{\rho} \tag{3.36}$$

where γ_e is the electrostrictive constant is defined as

$$\gamma_e \equiv \left(\rho \frac{\partial\varepsilon_r}{\partial\rho}\right)_{\rho_0} = \frac{(n^2-1)(n^2+2)}{3} \tag{3.37}$$

where n is the refractive index of material (gas or solid). The electrostriction effect in gas is a tendency of gas compression by the presence of electric field. In another perspective, the gas compression (density change) will also lead to the change of electric permittivity of gas [4]. From Eqs. (3.31), (3.36), and (3.37) we have

$$\left.\frac{dn_m}{dx}\right|_{GD} = \frac{\gamma_e}{2n_m\rho_0} \frac{\langle \boldsymbol{E}_{t,m} \left| \frac{d\rho_1}{dx} \right| \boldsymbol{E}_{t,m} \rangle}{\langle \boldsymbol{E}_{t,m} | \boldsymbol{E}_{t,m} \rangle} \tag{3.38}$$

From now on, the superscript ‘(0)’ of unperturbed electric field is omitted for clarity.

Then we discuss about the photoelasticity of the silica capillary of HCF. The photoelasticity describes the change of RI of solid under mechanical deformation. The PE of isotropic material is described by [3]

$$\Delta\varepsilon_{ij}^{-1} = p_{ijkl} S_{kl} \tag{3.39}$$

where p_{ijkl} is the strain tensor and S_{kl} is the strain tensor. It can be expressed in a matrix format by

$$\Delta(\boldsymbol{\varepsilon_r}^{-1}) = -\frac{1}{n^4}\begin{bmatrix}\Delta\varepsilon_{xx}\\ \Delta\varepsilon_{yy}\\ \Delta\varepsilon_{zz}\\ \Delta\varepsilon_{zy}\\ \Delta\varepsilon_{xz}\\ \Delta\varepsilon_{yx}\end{bmatrix} = \begin{bmatrix} p_{11} & p_{12} & p_{12} & 0 & 0 & 0\\ p_{12} & p_{11} & p_{12} & 0 & 0 & 0\\ p_{12} & p_{12} & p_{11} & 0 & 0 & 0\\ 0 & 0 & 0 & p_{44} & 0 & 0\\ 0 & 0 & 0 & 0 & p_{44} & 0\\ 0 & 0 & 0 & 0 & 0 & p_{44}\end{bmatrix}\begin{bmatrix}S_{xx}\\ S_{yy}\\ S_{zz}\\ S_{zy}\\ S_{xz}\\ S_{yx}\end{bmatrix} \tag{3.40}$$

And the overlap integral of Eq. (3.40) is

$$\langle E_m|\Delta\varepsilon_r|E_m\rangle = \varepsilon_0 \iint dS[E_{x,m}^* \quad E_{y,m}^* \quad E_{z,m}^*]\begin{bmatrix}\Delta\varepsilon_{xx} & \Delta\varepsilon_{yx} & \Delta\varepsilon_{xz}\\ \Delta\varepsilon_{yx} & \Delta\varepsilon_{yy} & \Delta\varepsilon_{zy}\\ \Delta\varepsilon_{xz} & \Delta\varepsilon_{zy} & \Delta\varepsilon_{zz}\end{bmatrix}\begin{bmatrix}E_{x,m}\\ E_{y,m}\\ E_{z,m}\end{bmatrix} \tag{3.41}$$

Then, by using Eqs. (3.31), (3.40) and (3.41) we have,

$$\left.\frac{dn_m}{dx}\right|_{PE} = \frac{n_{silica}^4}{2n_m\langle \boldsymbol{E}_{t,m}|\boldsymbol{E}_{t,m}\rangle}\iint dS(\sum 2Re\{E_{i,t,m}^* E_{j,t,m}\}p_{44}\frac{dS_{ij}}{dx} + \sum \left|E_{i,t,m}\right|^2\left(p_{11}\frac{dS_{ii}}{dx} + p_{12}\left(\frac{dS_{jj}}{dx} + \frac{dS_{kk}}{dx}\right)\right)) \tag{3.42}$$

where i, j and k is the components of electric field in cartesian coordinate. At last, Eqs. (3.33), (3.38) and (3.42) are combined to determine the perturbation of mode index. We found that for HCFs, the perturbation theory based on Helmholtz equation is a good approximation. The relative error of using Eq. (3.31) is less than 2%.

For PTS in HCFs, we could only consider the temperature change and hence only Eq. (3.38) is used:

$$\left.\frac{dn_m}{dx}\right|_{GD} = -\frac{\gamma_e}{2n_m T_0}\frac{\langle \boldsymbol{E}_{t,m}\left|\frac{dT_1}{dx}\right|\boldsymbol{E}_{t,m}\rangle}{\langle \boldsymbol{E}_{t,m}|\boldsymbol{E}_{t,m}\rangle} \tag{3.39}$$

From Eq. (3.21) we know that the temperature change T_1 is linearly proportional to the amplitude of heat source. Hence, the phase modulation due to PT effect can be expressed as

$$\phi_1^{PTS} = -\frac{2\pi L}{\lambda_L}P_P\alpha_A\frac{\gamma_e}{2n_m T_0}\frac{\langle \boldsymbol{E}_{t,m}\left|\frac{dT_1}{dx}\right|\boldsymbol{E}_{t,m}\rangle}{\langle \boldsymbol{E}_{t,m}|\boldsymbol{E}_{t,m}\rangle} \tag{3.40}$$

where L is the length of HCF, λ_L the wavelength of probe light, and now dx represents the absorption of unit optical power. In Eq. (3.40), dT_1/dx can be solved numerically by

$$j\omega\rho_0 c_P\frac{dT_1}{dx} - \kappa\nabla^2 T_1\frac{dT_1}{dx} = |\psi_P|^2 \tag{3.41}$$

Equation (3.41) shows the phase modulation (or phase change) of PTS, which is proportional to the pump power P_P, the absorption coefficient α_A, and the electrostrictive constant ($\gamma_e \approx 2(n_0 - 1)$).

For PAS in HCFs, it is hard to find an analytical formula like Eq. (3.40). However, Eqs. (3.6-3.8) are linearized near the equilibrium, the phase modulation of PAS can be expressed as

$$\phi_1^{PAS} = \frac{2\pi L}{\lambda_L} P_P \alpha_A \left(\left.\frac{dn_m}{dx}\right|_{GD} + \left.\frac{dn_m}{dx}\right|_{SB} + \left.\frac{dn_m}{dx}\right|_{PE} \right) \tag{3.42}$$

We can also define a phase modulation coefficient as

$$k^* = \frac{|\phi_1|}{P_P \alpha_A L} \tag{3.43}$$

This coefficient is only related to the filling gas and the structure of HCF.

In summary, the photothermal and photoacoustic effects in HCFs can be probed by the perturbation of optical mode index. For PTS, the perturbation of mode index is mainly due to the temperature change. For PAS, the perturbation of mode index is due to the gas density change, the shifting boundary of the HCF microstructure, and the photoacoustic effect of silica.

3.3. Probe the photothermal and photoacoustic effects with optical interferometers

The phase modulation induced by the perturbation of mode index can be accumulated along HCFs and is used to determine the strength of photothermal or photoacoustic effects. To measure the phase modulation of probe light, an optical interferometer is employed to transform the phase modulation of light into intensity change.

3.3.1. Fiber optical interferometers

Four kinds of fiber optical interferometers are studied in this thesis: Mach-Zehnder interferometer, Fabry-Perot interferometer, Sagnac interferometer and fiber modal interferometer. The schematic diagram of them is shown in Fig. 3.7.

Figure 3.7(a) shows the schematic diagram of Mach-Zehnder interferometer. The probe is split into two arms and then combined. One of arm consists of a HCF. The optical power detected by PD is related to the phase difference between the two arms:

$$P = P_1 + P_2 + 2\sqrt{P_1 P_2}\cos\left(\phi_0 + \phi_1 e^{j\omega t}\right) \tag{3.44}$$

where $P_{1,2}$ are the optical power coupled into PD from the two arms. The phase difference between the two arms contains two parts, a background phase difference ϕ_0 mainly due to the different length of the two arms and a small phase modulation ϕ_1 ($\phi_1 \ll 1$) at frequency ω due to the photothermal and photoacoustic effects. The background phase difference is not only due to the length of arms, the environmental factors such as temperature and vibration also have influence on ϕ_1. For example, a temperature difference of 10 μK on the two arms will generate a background phase different ϕ_0 of about 0.07 rad/m at room temperature. Hence, for fiber Mach-Zehnder interferometer with meters-long optical arms, feedback locking technique is need to stabilize the interferometer at the working point. For our research, the working point is locked at the quadrature point of the interferometer. At the quadrature point, the optical power at PD is linear proportional to the photothermal or photoacoustic induced phase modulation.

Figure 3.7(b) shows the diagram of a fiber Fabry-Perot interferometer. It consists of a SMF-HCF-SMF structure. The reflected optical waves at the two HCF-SMF interfaces interference with each other and the power at PD can be expressed as

$$P \approx P_0 R\left[1 + \eta_c^2 + 2\eta_c \cos\left(\phi_0 + \phi_1 e^{j\omega t}\right)\right] \tag{3.45}$$

where P_0 is the incident power, R ($\approx$ 4%) the reflectivity at the HCF-SMF interface, and η_c is the coupling efficiency between HCF and SMF. In principle, the Fabry-Perot interferometer shown in Fig. 3.7(b) is more stable than the fiber Mach-Zehnder interferometer. This is because the RI of gas is very close to unity. For example, a temperature change of 10 μK will only cause a phase fluctuation of 80 $\mu rad/m$ in air. Hence, HCF-based Fabry-Perot interferometer can work even without external locking of the working point. The single-end structure of the HCF sensor head also makes this setup more economic in practical use.

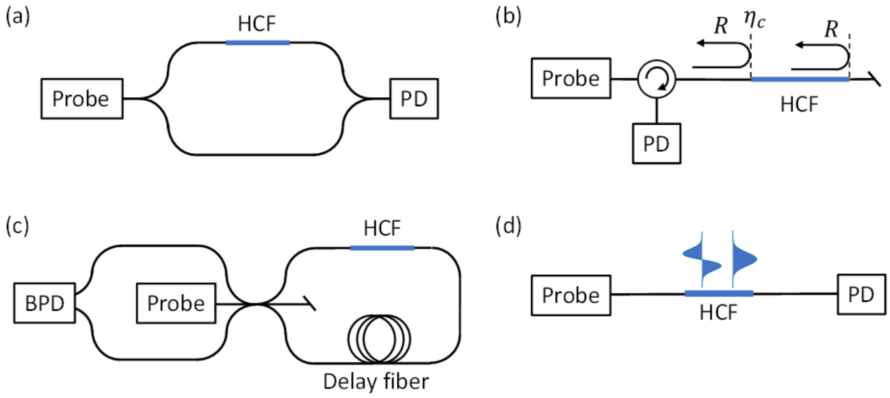

Figure 3.7. Schematic diagram of optical interferometers. (a) Mach-Zehnder interferometer; (b) Fabry-Perot interferometer; (c) Sagnac interferometer; (d) Fiber modal interferometer.

Figure 3.7(c) shows the schematic diagram of a fiber Sagnac interferometer. The probe light is split into two counter-propagated waves by a 3x3 coupler. Due to the delay fiber, the two counter-propagated waves experience phase modulation of HCF at different moments. The two waves then combine at the 3x3 coupler and are measured by a balanced PD (BPD). An advantage of Sagnac interferometer is that there is no static background phase difference ϕ_0. By using a 3x3 coupler and a BPD, the interferometer inherently works at the quadrature point of the interferometer. It can work without external locking techniques. For Sagnac interferometer shown in Fig. 3.7(c), the differential optical power at the BPD can be expressed as [8]

$$P_{diff} = \frac{2\sqrt{3}}{9} P_0 \sin\left(\eta_\omega \frac{\phi_1}{L_s} e^{j\left(\omega t+\omega L_t \frac{n}{2c}+\frac{\pi}{2}\right)}\right) \tag{3.46}$$

$$\eta_\omega = \frac{2c}{L_s \omega n}\left(\cos\left(\omega(L_t - 2L_s)\frac{n}{2c}\right) - \cos\left(\omega L_t \frac{n}{2c}\right)\right) \tag{3.47}$$

where L_s and L_t are the length of sensing HCF and the total length of optical fiber, respectively, n the RI of SMF, and η_ω is a frequency dependent coefficient. In the above calcuation, the length of fiber between the HCF and the coupler is assumed to be much smaller than the total length of optical fiber. Equation (3.57) can be further simplified if $L_s \ll c/\omega n$. This is usually satisfied for PTS using tens-meters of HCF. We have

$$\eta_\omega = 2\sin\left(\frac{\omega L_t n}{2c}\right) \tag{3.48}$$

For PTS, the detection frequency is usually fixed. Hence, the length of delay fiber is chosen to make η_ω maximum. In Eq. (3.58), η_ω approximates zero when ω is small. This explains why the Sagnac interferometer is intrinsically working at the quadrature point. A disadvantage of fiber Sagnac interferometer is the interference due to the backscattered light (e.g., Rayleigh scattering). Especially for PTS applications, the length of delay fiber can be several kilometers, which will result in more backscattered light. Although the its influence can be reduced by using broadband probe source, the sensitivity of fiber Sagnac interferometer is usually limited by the backscattered light.

Figure 3.7(d) shows the diagram of a fiber modal interferometer. The HCF supports two groups of optical modes (i.e., LP_{01}-like mode and LP_{11}-like mode). The modal interferometer consists of a SMF-HCF-SMF structure. The two optical modes experience a difference in the phase modulation in the HCF. The optical power at PD can be expressed as

$$P = P_{01} + P_{11} + 2\sqrt{P_{01}P_{11}}\cos\left(\phi_{0,01} - \phi_{0,11} + (\phi_{1,01} - \phi_{1,11})e^{j\omega t}\right) \tag{3.49}$$

where P_{01} and P_{11} are the optical power at the PD from LP_{01} mode and LP_{11} mode, respectively, and $\phi_{0,01}(\phi_{0,11})$, $\phi_{1,01}(\phi_{1,11})$ are the static background phase and the first-order phase perturbation of LP_{01} mode (LP_{11} mode). An advantage of fiber model interferometer is the common-mode-noise rejection. In other words, due to the orthogonality of optical modes, the phase difference between them are insensitive to uniform perturbations on the fiber. We will revisit the fiber modal interferometer in Chapter 4.

3.3.2. Noise of fiber optical interferometer with HCFs

Interferometric detection of photothermal and photoacoustic effects suffers from the noise in optical interferometers. The noise in interferometers is complicated and depends on the specific setup of the interferometer. Generally speaking, the source of noise comes from several aspects: first, the noise of lasers, including the intensity noise and the phase noise; second, the noise from the environment such as the vibration and temperature variation; third, the noise from electronic devices such as PD, LIA, piezoelectric transducer (PZT), etc.; last, the fundamental noise such as shot noise.

For a well-designed system, the noise from PD and LIA can usually be ignored. For example, Fig. 3.8 shows the relative noise to the carrier of a common sensing system. The PD is Nirvana Model 2017 from New Focus, the LIA is MFLI from Zurich Instruments, and the fiber laser is ConLAS-1550 from Connect Laser Technology. In frequency range of our concern (i.e., from a few kilohertz to several megahertz), the relative intensity noise (RIN) of the fiber laser is about -140 dBc/Hz and the relative noises of PD and LIA are about -150 dBc/Hz or lower. Hence, in the further discussion, we ignore the noise from PD and LIA.

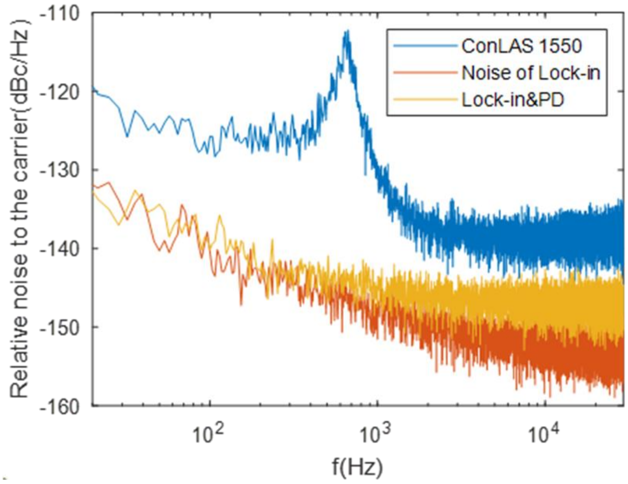

Figure 3.8. The relative noise spectrum of PD, LIA and the fiber laser.

As we have discussed in Section 3.2.1, the output power of the interferometer P_D has the form of

$$P_D = P_L + P_L \cos\left(\phi_0 + \phi_1 e^{j\omega t}\right) \tag{3.50}$$

where P_L is the probe power and $P_L/2$ is the power in one of the arm, which assumed to be the same in the two arms for simplicity. In Eq. (3.60), ϕ_0 is the phase difference between the two arms and is close to the quadrature point of the interferometer (e.g., $\phi_0 \approx \pi/2$). By using Taylor series and ignored the high-order terms and using Eq. (3.58), we have

$$P_D = P_L - P_L\left(\phi_0 - \frac{\pi}{2} + P_P k^* \alpha_{A,0} C L e^{j\omega t}\right) \tag{3.51}$$

where $\alpha_{A,0}$ is the absorption coefficient for pure gas calculated from Eq. (2.14), and $C(\ll 1)$ is the gas concentration. In Eq. (3.51), we ignore the relative phase between the pump power and the phase modulation (i.e., $\phi_1 = k^* P_P \alpha_{A,0} C L$). This is reasonable since we are measuring the amplitude of harmonic phase modulation with lock-in detection. The optical power can be expressed as

$$P_L = \bar{P}_L + \delta P_L(t) \tag{3.52}$$

$$P_P = \bar{P}_P + \delta P_P(t) \tag{3.53}$$

where $\bar{P}_{L,P}$ is the mean power and $\delta P_{L,P}(t)$ is the fluctuation of power. The root-mean-square (RMS) value of $\delta P_{L,P}$ can be estimated from the power spectrum density (PSD) $S_P(f)$ of the lasers [9]:

$$\frac{\delta P_{L,P}\big|_{RMS}}{\bar{P}_{L,P}} = \sqrt{S_{L,P}(f)\Delta f} \tag{3.54}$$

where $S_{L,P}(f)$ is the PSD of the relative intensity noise (RIN) of the laser, and Δf is the detection bandwidth. From Eqs. (3.61)-(3.63) and ignore the high-order terms, we have

$$P_D = \bar{P}_L + \delta P_L(t) - \bar{P}_L\left(\phi_0(t) - \frac{\pi}{2}\right) - \left(\bar{P}_L \bar{P}_P + \bar{P}_P \delta P_L(t) + \bar{P}_L \delta P_P(t)\right) k^* \alpha_{A,0} C L e^{j\omega t} \tag{3.55}$$

Quantitative analysis can be performed by calculated the spectrum density [10] of Eq. (3.55) and is out of the scope of this thesis. Here we analysis the noise in Eq. (3.55) qualitatively. In a real experiment setup $P_L \ll P_P$ and the phase modulation $k^* P_P \alpha_A L \ll 1$, hence, the intensity noise ($\delta P_P(t)$) from the pump laser has little influence on the output power. The noise is mainly comes from the intensity noise of the probe light ($\delta P_L(t)$). The term $\phi_0(t)$ contains the environmental perturbations such as temperature, pressure and vibration, noise from the

PZT (for Mach-Zehnder interferometer), and the phase noise of the probe laser. The phase noise is dominant in interferometers with unequal arms, such as Fabry-Perot interferometer. For interferometers with equal arms, such as Sagnac interferometer, modal interferometer, Mach-Zehnder interferometer, and etc., the influence of laser phase noise can be ignored.

Another source of noise is shot noise. The minimum detectable phase change limited by the shot noise can be expressed as [11]

$$\delta\phi_{shot} = \sqrt{\frac{2h\nu_L\Delta f}{\eta\bar{P}_D}} \tag{3.56}$$

where ν_L is the frequency of probe light, η the efficiency of PD and $\bar{P}_D$ is the average probe power received by PD. The shot noise can limit the performance of HCF-based gas sensor when the power received by PD is very small. This is often the case when the coupling loss between HCF and single mode fiber (SMF) is large.

From Eqs. (3.54) and (3.55), we can derive that the SNR limited by RIN of probe laser is

$$SNR_{RIN} = \frac{\bar{P}_L\bar{P}_P k^*\alpha_{A,0}CL}{\delta P_L(t)|_{STD}} \tag{3.57}$$

where STD refers to the standard deviation of the power fluctuation. When the mean value of $\delta P_L(t)$ is zero, the standard deviation is exactly its RMS value. Hence, Eq. (3.67) can be related to RIN of probe by

$$SNR_{RIN} = \frac{\bar{P}_P k^*\alpha_{A,0}CL}{\sqrt{S_L(f)\Delta f}} \tag{3.58}$$

We can also derive the SNR limited by the shot noise from Eq. (3.58) and Eq. (3.66):

$$SNR_{shot} = \bar{P}_P k^*\alpha_{A,0}CL\sqrt{\frac{\eta\bar{P}_D}{2h\nu_L\Delta f}} \tag{3.59}$$

The noise equivalent concentration (NEC) is defined as

$$NEC = \frac{C}{SNR} \tag{3.60}$$

We have the shot-noise-limited NEC and the RIN limited NEC:

$$NEC_{shot} = \frac{1}{\bar{P}_P k^*\alpha_{A,0}L}\sqrt{\frac{2h\nu_L\Delta f}{\eta\bar{P}_D}} \tag{3.61}$$

$$NEC_{RIN} = \frac{\sqrt{S_L(f)\Delta f}}{\bar{P}_P k^* \alpha_{A,0} L} \tag{3.62}$$

The above two equations are instructive for designing a HCF-based PTS gas sensor with high sensitivity. For example, the sensitivity can be improved by methods including improving the pump power and probe power, using longer fiber with higher phase modulation coefficient (k^*), using probe laser with lower intensity noise, tracing gases with stronger absorption line, etc.

3.4. Conclusion

The principles of PTS and PAS in HCFs are studied theoretically to pave the way for sensitivity enhancement. PTS, limited by the thermal conductivity of gas, has small signal at high frequencies and hence is usually operating in the frequency of tens of kilohertz. PAS provides better performance at high frequencies and will be detailed in Chapter 5. As an interferometric sensing method, the sensitivity of PTS/PAS in HCFs can be enhanced by improving the amplitude of photoacoustic/photothermal phase modulation or reducing the noise in optical interferometers. The photoacoustic/photothermal phase modulation can be increased by using higher pump power, and/or a longer length of HCF. The noise in interferometers can be reduced by using lasers with lower intensity/phase noise, detecting with narrower bandwidth, etc. This will be the basics for designing a photoacoustic/photothermal gas sensor with higher sensitivity.

Reference of Chapter 3

1. Blackstock, D. T. (2001). *Fundamentals of physical acoustics*.
2. McLennan, J. A. (1989). *Introduction to nonequilibrium statistical mechanics*. Prentice Hall.
3. Royer, D., & Dieulesaint, E. (1999). *Elastic waves in solids II: generation, acousto-optic interaction, applications*. Springer Science & Business Media.
4. Snyder, A. W., & Love, J. (2012). *Optical waveguide theory*. Springer Science & Business Media.
5. Skorobogatiy, M., Ibanescu, M., Johnson, S. G., Weisberg, O., Engeness, T. D., Soljačić, M., ... & Fink, Y. (2002). Analysis of general geometric scaling perturbations in a transmitting waveguide: fundamental connection between polarization-mode dispersion and group-velocity dispersion. *JOSA B*, *19*(12), 2867-2875.
6. Boyd, R. W. (2020). *Nonlinear optics*. Academic press.

7. Johnson, S. G., Ibanescu, M., Skorobogatiy, M. A., Weisberg, O., Joannopoulos, J. D., & Fink, Y. (2002). Perturbation theory for Maxwell's equations with shifting material boundaries. *Physical Review E*, *65*(6), 066611.

8. Kråkenes, K., & Bløtekjaer, K. (1989). Sagnac interferometer for underwater sound detection: noise properties. *Optics Letters*, *14*(20), 1152-1154.

9. Hui, R., & O'Sullivan, M. (2009). *Fiber optic measurement techniques*. Academic Press.

10. Goodman, J. W. (2015). *Statistical optics*. John Wiley & Sons.

11. Mazzoni, D. L., & Davis, C. C. (1991). Trace detection of hydrazines by optical homodyne interferometry. *Applied Optics*, *30*(7), 756-764.

Chapter 4 Sensitivity enhancement of PTS in HCFs

In this chapter, we present two methods to enhance the sensitivity of PTS. One way is to increase the pump power by placing a HCF gas cell inside a laser cavity, which is named intracavity PTS. Another way is to reduce the noise of interferometer by measuring the phase difference between two optical modes in a HCF, which is named as MPD-PTS.

4.1. Intracavity PTS with HCF

An important conclusion of Chapter 3 is the phase modulation of PTS is proportional to the power of pump. For lasers, only a small part of energy is coupled out of the laser cavity for use. It is a straightforward idea to put the HCF gas cell inside a laser cavity to obtain a higher pump power in the hollow core. Intracavity LAS has previously been demonstrated by placing a fiber-pigtailed micro-optic gas cell inside a laser cavity [1-3] and they detect the power change at the laser output. The output spectrum is very sensitive to the intracity gas absorption when the laser was operating near the lasing threshold but the performance was unstable. In this section, we present the first demonstration of an all-fiber intracavity photothermal (IC-PT) gas sensor by placing a photonic bandgap-HCF (PBG-HCF) gas cell inside a fiber laser cavity. This offers a solution to enhance the phase modulation of PTS since the intracavity light intensity could be significantly higher than the laser output.

4.1.1. Configuration of the fiber ring laser

For gas detection applications, it is preferred to use a narrow linewidth laser with fast tuning and modulation capability. In practice, it is hard to realize a fiber ring laser with the ability of fast tuning with a large tuning range (e.g., tens of GHz). This is due to the relatively long length of fiber cavity. Several configurations, including using highly stretchable fiber Bragg grating [4], acousto-optic filter [5], and external injection locking [6], have been used to achieve fast tuning of fiber ring laser. In our experiment, we use external injection locking to realize WMS with fiber ring laser.

Figure 4.1(a) shows a simplified configuration of the erbium-doped fiber ring laser (EFRL). An erbium-doped fiber (EDF) is pumped by a 980-nm pump source. The fast tuning and the large tuning range are realized by using a seed distributed feedback (DFB) laser. We use a tunable filter (TF) centered at the absorption line of target gas (i.e., acetylene) to filter out the unwanted longitudinal modes in the laser cavity. However, it can be replaced by a circulator and a fiber Bragg grating to reduce the cavity loss. Figure 4.1(b) shows the configuration of the HCF gas cell. It consists of a PBG-HCF fusion spliced to two standard SMFs (SMFs).

Micro-channels are fabricated on the PBG-HCF [7] for the purpose of gas filling and the HCF gas cell is sealed in a gas chamber.

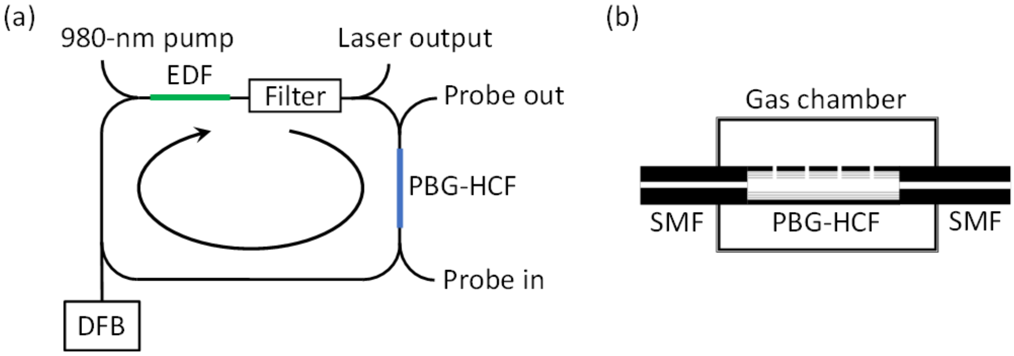

Figure 4.1. The configuration of fiber ring laser with a HCF gas cell placed in the laser cavity. (a) The simplified model of fiber ring laser. (b) Configuration of the HCF gas cell.

The optical power reaches the equilibrium when the optical gain of EDF equals the loss of the laser cavity. Considering the gain saturation of EDF, the optical loss of the cavity needs to be as small as possible to obtain a high intracavity laser power. The total loss of the cavity is about 10 dB, and the main loss comes from the coupling loss between SMF and PBG-HCF and the filter.

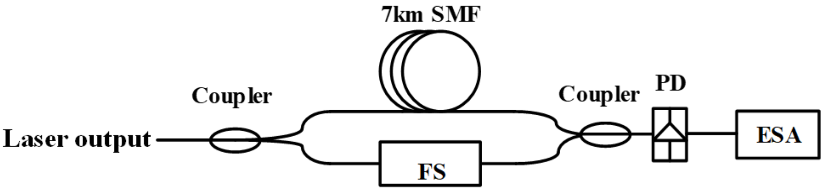

Figure 4.2. Optical self-delayed heterodyne measurement setup.

An important parameter of laser is its linewidth. A basic method to measure the linewidth of laser is the self-heterodyne measurement, which was first proposed by T. Okoshi et al. [8]. By using an acousto-optic modulator (AOM) as a frequency shifter (FS), and using a long delay fiber to form an Mach-Zehnder interferometer, the linewidth of the laser can be measured directly through the output of interferometer. The data is analyzed by an electric spectrum analyzer (ESA). When the delay time is shorter than the coherent time of laser or comparable to it, the output signal shows some sideband and ripples, and a delta function will appear in the center of the frequency shift. Under this condition, we can also determine the linewidth of the laser by curve fitting [9]. One needs to note that ‘1/f’ noise has a considerable impact on the measurement while use short delay time. In the experiment, the linewidth of DFB seed laser is about 2 MHz and the linewidth of fiber ring cavity is believed to be much narrower than that of the DFB laser. This is due of the long length of the laser cavity used in our experiment.

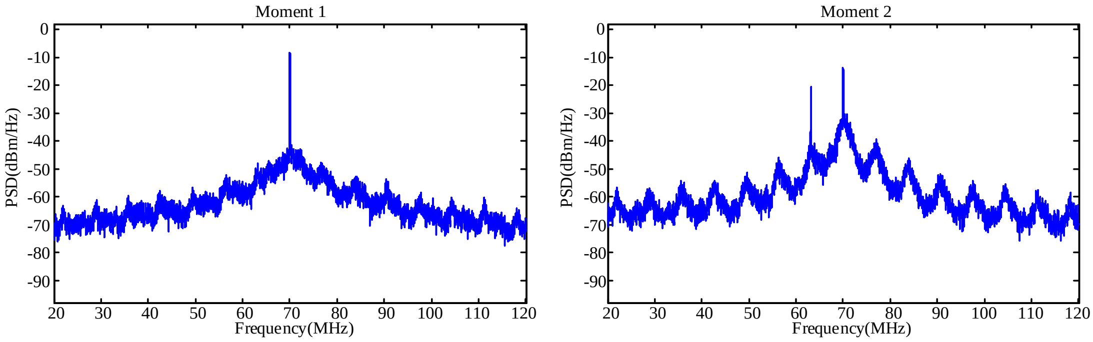

Figure 4.3. PSD measured by the self-delayed heterodyne at two moments.

As shown in Fig. 4.2, we use a simple self-heterodyne setup to measure the linewidth of our laser. The result of the measurement is shown in Fig. 4.3. The sidebands and the delta function indicate the coherent length of laser is longer than the length of delay fiber. The laser cavity is not stable as indicating by the jitter of the delta function. Although the fiber ring laser is not operated at single frequency, the effective linewidth considering the jitter of laser mode is still much smaller than the linewidth of absorption line (about 4.6 GHz for the absorption line we measured). The frequency spacing of the delta function reflects the longitudinal mode spacing of the fiber ring laser, which is about 6.9 MHz.

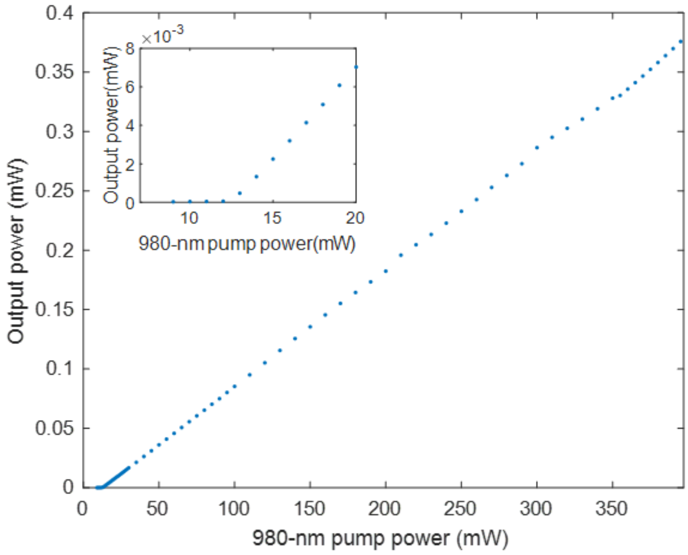

Figure 4.4. The output power versus 980-nm pump power. The inset shows the output power near the threshold.

Then we measure the output power at the output port of laser. As shown in Fig. 4.4, the threshold of the laser is about 12 mW. The output power is almost linearly proportional to the pump power. We also measure the output spectrum of the laser at different wavelength. The laser spectrum measured by an optical spectrum analyzer (OSA) is shown in Fig. 4.5(a). The linewidth of laser is smaller than the resolution of OSA. The output power is stable when we tune the wavelength across the absorption line as we shown in Fig. 4.5(b).

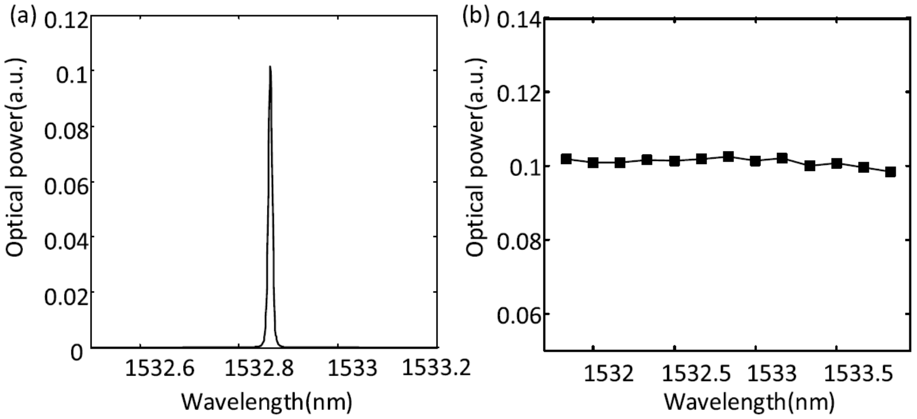

Figure 4.5. The spectrum and optical power of the fiber ring laser. (a) The laser spectrum measured by an OSA. (b) The output power at different wavelengths.

4.1.2. Gas detection experiment

As we have shown in Fig. 4.6, the system setup consists of two part: the intracavity pump system and the Sagnac interferometer. The system uses two wavelength division multiplexers (WDMs) to combine the pump system and the Sagnac interferometer. The wavelength of the seed laser is at 1532.83 nm, which is the P(13) absorption line of the $\nu_1 + \nu_3$ band of C_2H_2. The wavelength of the probe laser source (PLS) is at 1553.33 nm. The LIA generates a 25-kHz sinusoid signal to drive the current of DFB laser. Then DFB laser inputs as a seed laser into the fiber ring cavity. A filter is used in the cavity to suppress the amplified spontaneous emission (ASE) noise and represses the self-oscillating of the fiber ring cavity. The wavelength of the fiber ring laser is modulated periodically and generates a sinusoid modulated phase change in the PBG-HCF that can be measured by the Sagnac interferometer. The stability of pump laser (fiber ring laser) is not single longitudinal mode as we have discussed in Chapter 4.1.1, and this will be the main reason for the noise in the system. The HCF (HC-1550-02 from NKT Photonics) is fused with SMFs. Twenty microchannels are drilled along the HCF by using a femtosecond laser and the fiber is then sealed in a gas chamber.

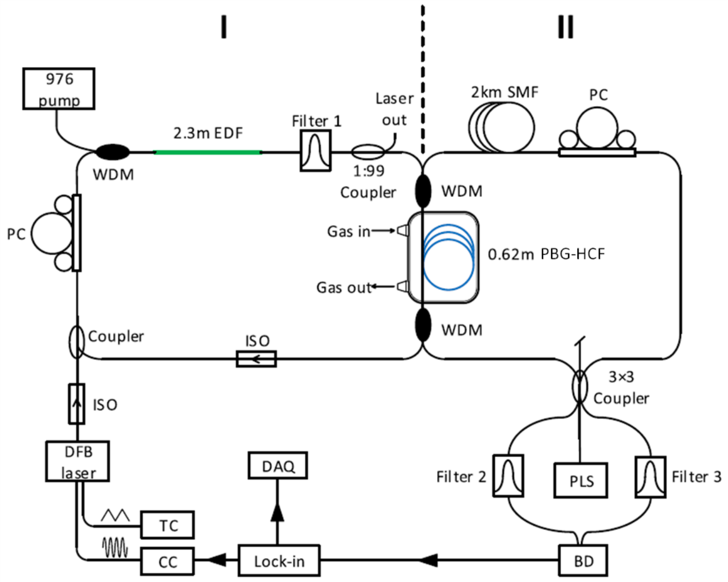

Figure 4.6. The experiment setup of an IC-PT gas sensor. It consists of two parts: a fiber ring laser as pump unit and a Sagnac interferometer as probe unit.

The probe laser source is from a superluminescent diode, filtered to a spectral width of about 1 nm and amplified by an EDF amplifier (EDFA). The use of such a light source, significantly reduces the coherent length of the laser and hence the noise due to interference of the reflection/scattering light. The wavelength of probe centers around 1553.33 nm. The SMF fiber loop in the Sagnac interferometer is about 2 km, giving a proper loop frequency of about 49 kHz. The two filters before the balanced detector pass the probe light but suppress ASE of the EDFA and residual pump from the fiber ring laser. At last, a LIA (SR830 from Stanford Research System) is used to measure the second harmonic output of Sagnac interferometer.

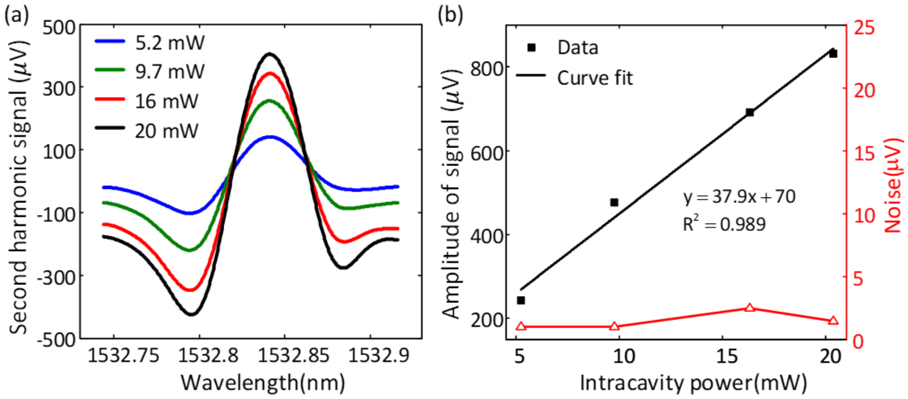

Figure 4.7. The second harmonic signal with different intracavity power. (a) The second harmonic signal at different intracavity power. (b) The amplitude of second harmonic wave. The amplitude of second harmonic wave is defined by the difference between the maximum and the minimum.

Figure 4.7 shows the measurement result with 100 ppm acetylene in nitrogen. The amplitude of second harmonic signal is linear proportional to the intracavity power. The noise of the system is measured by detuning the pump light away from the absorption line (i.e., 1532.65 nm). But the noise in the system keeps in the same level as we increase the pump power. Therefore, the sensitivity of the gas sensor can be further improved by increasing the pump power. We determine the NEC by measuring the standard deviation of the noise. With the time constant of LIA set to 1 second, the NEC is about 176 ppb, corresponding to a noise equivalent absorbance (NEA) about 1.1×10^{-5} for a given probe power of 50 μW; this corresponds to a normalized noise equivalent absorption of $1.2 \times 10^{-8}\ cm^{-1}W/\sqrt{Hz}$. A comparison to the result of other gas sensors based on PBG-HCF is summarized in Table 4.1. The performance of the IC-PT gas sensor is about 1 order of magnitude better than the sensors based on DAS and WMS.

Table 4.1. Detection limit of different PBG-HCF gas sensors.

Gas cell	Method	NEC(ppm)	NEA*
5.1-m PBG-HCF [10]	DAS	10(C_2H_2)	8.2×10^{-4}
13.7-cm PBG-HCF [11]	WMS	158(CH_4)	2.5×10^{-4}
10-m PBG-HCF [12]	PTS	0.002(C_2H_2)	2.3×10^{-6}
0.62-m PBG-HCF (our work)	IC-PT	0.176(C_2H_2)	1.3×10^{-5}

*NEA were calculated from NEC and line strength from HITRAN database [13].

Several factors limit the performance of the IC-PT gas sensor. First of all, the total loss of the fiber ring laser limits the intracavity laser power. In our system, the total loss is estimated to be 10 dB. This gives a maximum intracavity power of 20 mW with an EDF pump power of 200 mW. The cavity loss includes the coupling loss between the SMF and HC-1550-02 fiber, the loss of filter, and the loss of WDMs. The loss of a typical fusing splicing joint between SMF and HC-1550-02 fibers is ~2 dB [14, 15]. Recent research shows that trapping a nanospike in a PBG-HCF can achieve a high coupling efficiency of 87.8% [16].

Second, the erbium fiber ring laser in our experiment is not a single longitudinal mode laser. The fiber ring laser of our system have several longitudinal modes and mode hopping may occur during the wavelength modulation. Single longitudinal mode fiber ring laser with tuning capability is still under active research. Several works have involved in the building of EFRLs with wavelength tunability and research of the transient response of EFRLs have been reported [4-6]. Theoretical calculation shows that the mode build-up time of an EFRL is on the order of milliseconds but could be further reduced to the order of microseconds through nonlinear loss [17, 18]. Using a seeded injection laser could significantly reduce the mode build-up time because the optical mode builds up from seeded photons other than ASE photons.

Third, the HC-1550-02 fiber used in our experiment is actually not a true SMF. It supports several high order modes and results in a different optical loss at a different wavelength. The laser cavity is sensitive to the cavity loss and hence the mode interference would have a serious impact on the laser performance when the laser is wavelength modulated. The impact due to mode interference could be reduced by using HCFs that suppress the high order modes (for example, the single-ring anti-resonance hollow core fiber that suppresses high order modes [19]).

4.1.3. Theoretical sensitivity of intracavity PTS for gas detection

To investigate the potential theoretical performance of IC-PT gas sensor, we build a simplified model to calculate the intracavity power and the shot-noise limited sensitivity. The model is shown in Fig. 4.8(a). The EDF is considered as a two-level system and the intracavity laser power could be described by [20]

$$P_{in} = \eta\left(P_p^{in} - P_p^{th}\right) \tag{4.1}$$

$$\eta = \frac{\varepsilon_1 \delta_1 \kappa_1}{1 - e^{-\gamma_t}}\left(1 - \exp\left(-\alpha_P L + \frac{P_S^S}{P_P^S}(\alpha_S L + \gamma_t)\right)\right) \tag{4.2}$$

$$P_P^{th} = \frac{h\nu_P P_S^S(\alpha_S L + \gamma_t)}{1 - \exp\left(-\alpha_P L + \frac{P_S^S}{P_P^S}(\alpha_S L + \gamma_t)\right)} \tag{4.3}$$

$$\gamma = -\ln(\varepsilon_1 \varepsilon_2 \delta_1 \delta_2 \kappa_1) \tag{4.4}$$

$$P_{P,S}^S = \frac{A_{eff}}{\Gamma_{P,S}\tau\left(\sigma_{P,S}^e + \sigma_{P,S}^a\right)} \tag{4.5}$$

where $\alpha_{P,S}$ represents the absorption coefficient of EDF at the pump (P) or signal (S) wavelength, $\Gamma_{P,S}$ the overlap integral of the optical mode and dopant ions, A_{eff} the effective doping area, $\sigma_{P,S}^e$, $\sigma_{P,S}^a$ the emission and absorption cross-section, $P_{P,S}^S$ the saturation coefficient, τ the upper state lifetime and L is the length of EDF, P_P^{th} the pump threshold of the 976-nm diode laser, and γ_t is the total round trip loss of the ring cavity. δ_1 represents the optical loss from the EDF output to output coupler including the splicing loss between EDF and SMF and the component inserted (e.g., optical filter). κ_1 is the coupling ratio of the output coupler. δ_2 represents the optical loss after the light coming out of the HCF and before it enters the EDF again. $\varepsilon_{1,2}$ represent the coupling loss between the PBG-HCF and SMF. Figure. 4.8(b) shows the theoretical intracavity power calculated with the different optical loss. It shows that reducing the optical loss of the cavity could improve the intracavity power. With the state-of-the-art optical components and the best coupling method between SMF and PBG-HCF, the highest intracavity power is demonstrated in Fig. 4.8(b) with the blue line.

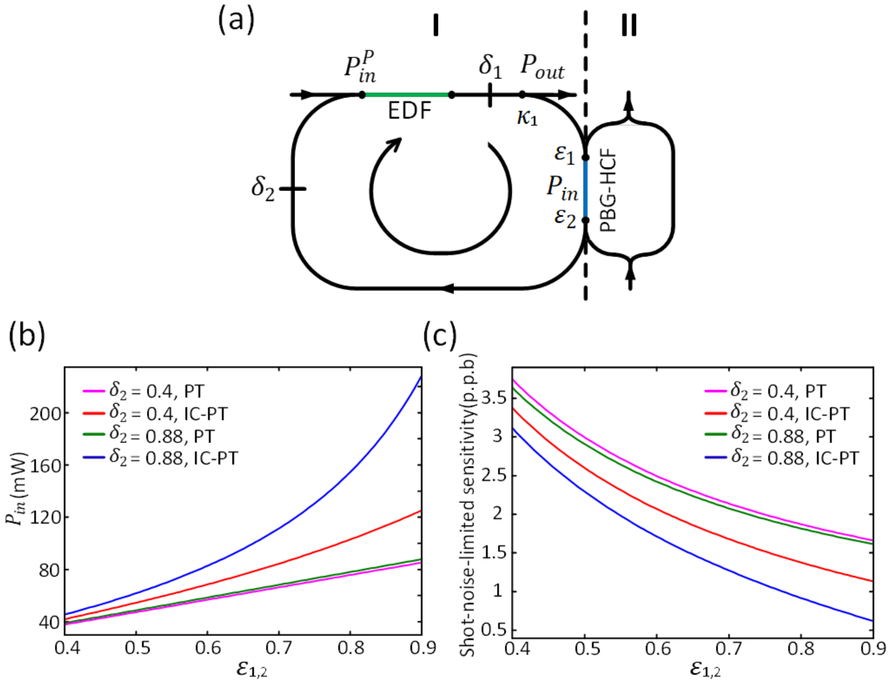

Figure 4.8. Theoretical analysis of the IC-PT gas sensor. I: the pump section. II: the phase detection section. P_{in}*: power inside the PBG-HCF.* P_{out}*: laser output power.* P_P^{in}*: the 976-nm diode laser power at the input of the EDF.*

We investigate the shot-noise-limit sensitivity of our gas sensor by considering the performance limited by the shot-noise-limit sensitivity of a Mach-Zehnder interferometer [21]

$$\delta\phi_{min} = \sqrt{\frac{2h\nu_L B}{\xi P_L}} \tag{4.6}$$

where ν_L, P_L are the frequency and power of probe light, B the detection bandwidth of LIA, ξ the quantum efficiency of PD. Considering that the 2f-detection deteriorates the shot-noise-limited sensitivity by a factor of ~4 [22], the shot-noise limited detection sensitivity is expressed as

$$C_{min} = \frac{4\delta\phi_{min}}{k^{*}\alpha_A P_{in} L} \tag{4.7}$$

For the P(13) absorption line of C_2H_2 around 1532.83 nm, the peak absorption coefficient is $\alpha_A = 1.051\ cm^{-1}$ at room temperature (296.15 K) and 1 atm. For the NKT's HC-1550-02 fiber, k^* is about 1.12 $rad\ cm\ mW^{-1}\ m^{-1}$ [12]. The detection bandwidth B is assumed to be 0.094 Hz corresponding to the 1s-time constant of LIA with a filter slope of 18 dB/Oct. As shown in Fig. 4.8(c), theoretical study shows, by reducing the loss of fiber ring laser cavity, the sensitivity can be enhanced to ppb level with the same length of HCF. The shot-noise-limited sensitivity is enhanced by a factor of 2.6 comparing the IC-PT method with the photothermal method with the same 980-pump power of EDF. Further, reduce the optical loss ($\delta_1, \delta_2, \varepsilon_1$, etc.) can further improve the enhancement factor.

4.2. MPD-PTS with HCF

In PTS, the ultimate sensitivity is limited by the shot noise at the PD. However, it is usually hard to reach the shot-noise limit because of the noisy environment as well as other noises associated with interferometric detection. Generally speaking, a fiber optic interferometer is more robust against the environment noise when the two interference beams travel in the same fiber. In this section, we demonstrate a new method of PTS by employing the unique dual-mode property of an AR-HCF, which is named MPD-PTS.

4.2.1. Theory of MPD-PTS with AR-HCF

As shown in Fig. 4.9, the single-ring AR-HCF supports two groups of optical mode: LP_{01}-like mode and LP_{11}-like mode. The intensity field observed by a mode field analyzer is shown in Figs. 4.9(b) and (c). The transmission spectrum of the fiber covers from 800 nm to 1700 nm. The inset of Fig. 4.9(a) shows the SEM of AR-HCF. It consists of seven capillaries with a diameter of ~14 μm and a thickness of ~370 nm. The inner diameter of the silica cladding is about 190 μm.

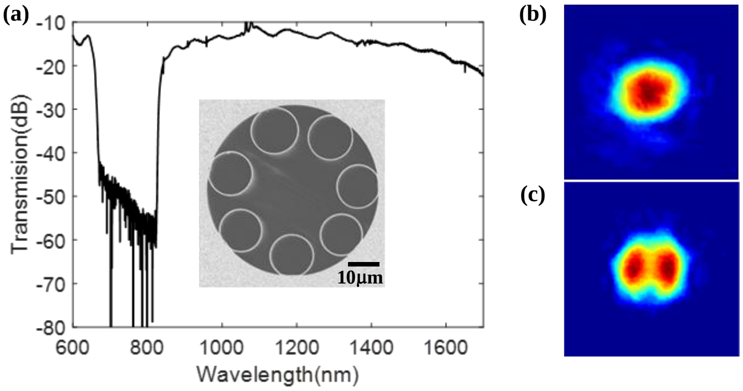

Figure 4.9. The transmission spectrum and the optical mode of AR-HCF used in the experiment.

The modal properties of the AR-HCF were studied numerically by using COMSOL Multiphysics. The geometry model is based on the SEM of the AR-HCF used in our experiments and is shown in Fig. 4.10(a). The fiber supports two groups of modes: the LP_{01}-like mode and the LP_{11}-like mode that includes the LP_{11a} and LP_{11b} modes. The calculated mode fields of the LP_{01} at 1550 nm are shown in Figs. 4.10(b) and (c) while the mode fields of the LP_{11} are shown in Figs. 4.10(d)-(g). The RI difference between LP_{01} and LP_{11} is $\sim 1.2 \times 10^{-3}$.

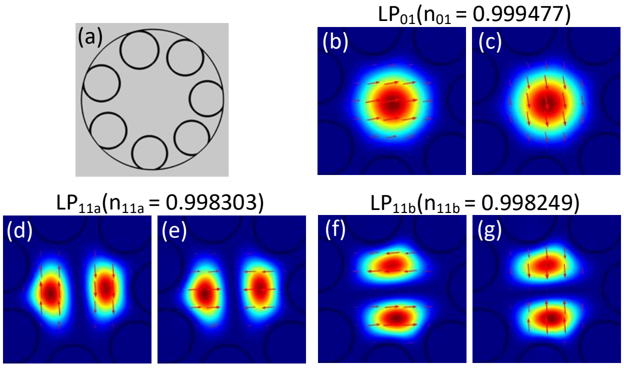

Figure 4.10. The optical modes in the AR-HCF. (a) The geometry used for mode analysis. (b-g) The optical modes supported by the AR-HCF.

The basics of MPD-PTS may be explained intuitively by using the illustrations in Fig. 4.11. A modulated pump laser beam propagating in a dual-mode AR-HCF is absorbed by trace molecules in the hollow core, which heats up the gas and perturbs the RI distribution. The heating profile follows the intensity distribution of the pump, which depends on the fractional power of the pump in the two modes. The intensity would have an approximate Gaussian distribution for the LP_{01} mode and a two-lobe distribution for the LP_{11} mode. Fig. 4.11(a) shows a general scenario where the LP_{01} and LP_{11} modes are both present in the HCF. The pump intensity, the temperature (and hence the RI) distribution in the hollow core varies periodically along the HCF due to coherent mixing of the two modes and the spatial period equals to the modal beat length. Figures. 4.11(b) and (c) show respectively the variations of pump intensity and temperature along the HCF. If a probe laser beam is now propagating simultaneously in the HCF, it will be modulated by the RI change. The probe also has LP_{01} and LP_{11} modes. The photothermal phase modulations for the two modes are different, depending on the overlap integral of the mode fields with the RI perturbation, as shown in Fig. 4.11(c). The differential photothermal phase modulation is proportional to gas concentration C and given by

$$\delta\phi = \Delta\phi_{01} - \Delta\phi_{11} = k^{*}(\eta, f)\alpha_A(\lambda_P)CLP_P \tag{4.8}$$

where $\Delta\phi_i$ (i = 01 or 11) represents phase modulation for LP_{01} or LP_{11} mode of the probe, $\alpha_A(\lambda_P)$ is the peak absorption coefficient for a relative concentration of 100%, λ_P the wavelength of pump, L the length of the sensing HCF, P_P the average pump power over L, η the fractional pump power in the LP_{01} mode, and f pump modulation frequency. The differential phase modulation coefficient k^* is a function of η and f. For $\eta = 0.9$ and $f < 11\ kHz$, k^* is determined to be 1.63(±0.14)×10^{-7} rad·cm·ppm^{-1}·m^{-1}·mW^{-1} for balance gas of argon. It is about 20% of the phase modulation coefficient of the fundamental mode for the AR-HCF. This means that the MPD is still quite sensitive to gas concentration, which is a result of different mode fields overlapping with the non-uniform heating profile. The variation in the MPD can be conveniently detected by using a simple in-line dual-mode fiber interferometer, as shown in Fig. 4.11(d).

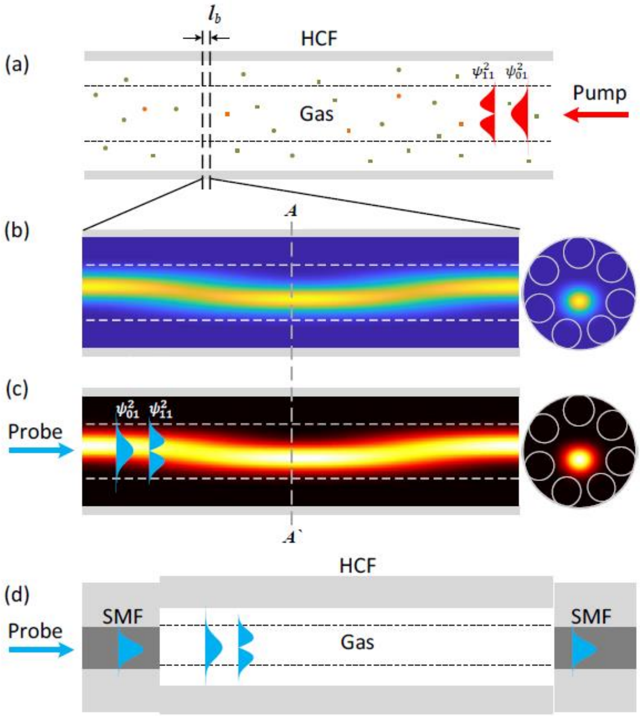

Figure 4.11. The basic principle of MPD-PTS. (a) The schematic diagram of a HCF filling with gas. (b) A period of the beating pump intensity field. With modal beating length $l_b \approx 1.3\ mm$. The panel on the right shows the intensity at the cross-section A-A'. (c) A period of the temperature distribution. The panel on the right shows the temperature distribution over the cross-section A-A'. The probe intensity profiles of the two modes are superimposed onto the temperature profile to show the different overlap between them. (d) A SMF-HCF-SMF modal interferometer for detecting variation in the MPD.

Although the AR-HCF supports the LP_{01} as well as LP_{11a} and LP_{11b} modes. Only one of the LP_{11} mode (e.g., LP_{11a}) is excited in the experiment. The normalized mode fields of the LP_{01}

and the LP11 modes are labelled as $\psi_{01}(x, y)$ and $\psi_{11}(x, y)$, which satisfies $\langle\psi_i, \psi_i\rangle = 1$ (i = 01 or 11) with "$\langle\,\rangle$" represents the overlap integral over the fiber cross-section. The coordinates 'x' and 'y' in mode filed ψ_i are omitted in later equations for simplicity. The pump intensity along the HCF ($i.e.$, z-direction) may be expressed by

$$I_P = P_P\left[\eta\psi_{01}^2 + (1-\eta)\psi_{11}^2 + 2\sqrt{\eta(1-\eta)}\psi_{01}\psi_{11}cos(k_P\Delta nz)\right] \tag{4.9}$$

where k_p is the angular wavenumber of the pump, $\Delta n(= n_{01} - n_{11})$ the differential mode index between LP_{01} and LP_{11}. Now we consider the WMS in which the pump wavelength is modulated sinusoidally at frequency $\omega = 2\pi f$ with a modulation depth of m. The harmonic modulation of the pump wavelength results in a series of harmonic heat sources at multiples of the modulation frequency. In our experiment, we concern on the second harmonic (2*f*) heat source. Since the spectroscopic gas detection is carried out at atmospheric pressure and room temperature, the gas absorption lineshape can be regarded as Lorentzian. The heat source at $2f$ may be expressed

$$\tilde{Q} = H_2\alpha_{\mathrm{A}}CI_pe^{j2\omega t} = Qe^{j2\omega\mathrm{t}} \tag{4.10}$$

where α_{A} is the peak absorption coefficient that equals to $1.051\ cm^{-1}$ for the P(13) line of $\mathrm{C_2H_2}$ at 296 K and 1 atm, *C* the gas concentration of C_2H_2 and 2ω is the angular frequency of the second harmonic wave. In our experiment, the amplitude of wavelength modulation is 2.2 times of the absorption linewidth, giving the maximum value of $H_2 = 0.343$.

Under the assumption that absorption is weak and thermal conduction is the dominating heat dissipation process, the heat conduction in the HCF may be studied by using

$$j\omega\rho c_p\tilde{T} - \kappa\nabla^2\tilde{T} = \tilde{Q} \tag{4.11}$$

where ρ, c_p and κ are respectively the density, the heat capacity at constant pressure, the thermal conductivity of the balance gas or silica. $\tilde{T}$ is the harmonic perturbation of the temperature distribution. The inner wall of the silica outer cladding is regarded as the boundary with constant temperature. Since the gradient of heat source along the z-direction is much smaller than that in the radial thermal directions, we may ignore the heat conduction along the z-direction and replace ∇^2 by the transverse operator ∇_T^2. Under this assumption, the temperature field $\tilde{T}$ could be expressed as

$$\tilde{T} = T_1(x, y)e^{j2\omega t} + T_2(x, y)cos(k\Delta nz)e^{j2\omega t} \tag{4.12}$$

The temperature field varies periodically along the fiber with a spatial period of l_b~1.3 mm. Using the standard perturbation theory, the perturbation of mode indexes may be calculated by the overlap integral over the fiber cross-section

$$\Delta n_{01}(z,t) = \langle \Delta n(x,y,z), \psi_{01}^2 \rangle \tag{4.13}$$

$$\Delta n_{11}(z,t) = \langle \Delta n(x,y,z), \psi_{11}^2 \rangle \tag{4.14}$$

where

$$\Delta n(x,y,z) = -\frac{n_0 - 1}{T_0}\tilde{T} \tag{4.15}$$

is the perturbation of RI of the gas in the hollow-core and n_0 is the RI of the original balance gas ($n_0 - 1 \approx 2.8 \times 10^{-4}$ for N_2, 2.63×10^{-4} for Ar), and T_0 the ambient temperature. Here we have ignored the change of RI of silica because the optical modes are almost completely in the air-core (less than 3×10^{-4} of power in silica for the AR-HCF used in the experiment). The overall perturbation of the MPD between the two modes is

$$\Delta\phi = k_s \int_0^L [\Delta n_{01}(z,t) - \Delta n_{11}(z,t)] dz \tag{4.16}$$

where k_s is the angular wavenumber of probe. From Eqs. (4.13)-(4.16) we could figure out that, over the integer multiples of the modal beam length, the second term on the right side of Eq. (4.12) would have negligible contribution to the overall change of the MPD. This term is accumulated over many periods of modal beat length (more than 500 periods) and approaches zero since the PT induced phase modulation in MPD is very small over one period of beat length. Hence, we may approximately calculate the phase change of MPD as

$$\Delta\phi = -\frac{k_s(n_0 - 1)Le^{j2\omega t}}{T_0} \langle T_1(x,y), \psi_{01}^2 - \psi_{11}^2 \rangle \tag{4.17}$$

with $T_1(x,y)$ as the solution of

$$j\omega\rho c_p T_1(x,y) - \kappa \nabla_T^2 T_1(x,y) = H_2 \alpha_{\mathrm{A}} C P_p [\eta \psi_{01}^2 + (1-\eta)\psi_{11}^2] \tag{4.18}$$

The modulation coefficient k^* is then determined as

$$k^*(\eta,\omega) \equiv \frac{|\Delta\phi|}{\alpha_{\mathrm{A}} C L P_p} = \frac{k_s(n_0 - 1)}{T_0} \langle \widehat{T_1}(x,y), \psi_{01}^2 - \psi_{11}^2 \rangle \tag{4.19}$$

where $\widehat{T_1}(x,y)$ is the solution of

$$j\omega\rho c_p \widehat{T_1}(x,y) - \kappa \nabla_T^2 \widehat{T_1}(x,y) = H_2 [\eta \psi_{01}^2 + (1-\eta)\psi_{11}^2] \tag{4.20}$$

Equation (4.20) can be solved by finite-element method. The modulation coefficient k^* shows no significant change at below 22 kHz (85% of the maximum value) and reduces quickly from ~22 kHz to ~215 kHz (20% of the maximum value), and approximately halved at ~59 kHz for argon (~67 kHz for nitrogen) as we shown in Fig. 4.12. For η = 0.96, f = 19 kHz and λ = 1550 nm, k^* is determined to be ~1.6×10^{-7} rad cm ppm^{-1} m^{-1} mW^{-1} and ~1.2×10^{-7} rad cm ppm^{-1} m^{-1} mW^{-1} with argon and nitrogen as the balance gas, respectively.

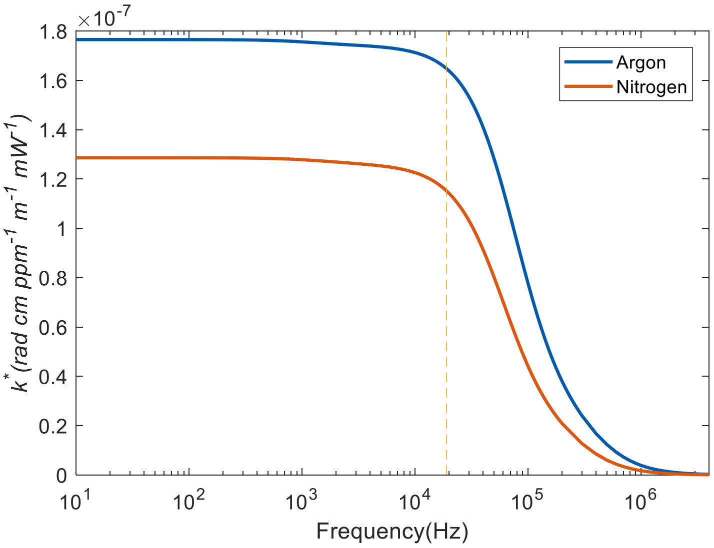

Figure 4.12. Modulation coefficient k^* as a fucntion of second harmoinc frequency. All data are obtained under the condition of ambient temperature and pressure of 1.5 bar. Vertical dashed line indicates the operating frequency of our experiment.

The reduction in k^* may be explained by the thermal conduction in the HCF. Under the condition of the same or similar beam radius (w_p) for the pump and probe beams and ignoring the mutual influence between conduction and convection processes, the thermal conduction velocity may be estimated by [23]

$$v_{cond} = \frac{\kappa}{\rho c_P w_p} \tag{4.21}$$

Under the room temperature and pressure of 1.5 bar argon, in an AR-HCF with beam radius of ~11 μm, the thermal conduction velocity is calculated to be ~1.2 m/s. This would give a thermal conduction time of the order of 10^{-5} s, corresponding to ~100 kHz, during this period the generated heat dissipates outwards radially and approaches the silica wall from the center of core. Similar result is obtained with nitrogen as the balance gas.

In our experiments, the pump and probe are lunched into the AR-HCF from different ends, which means that the pump and the probe could be in the same or different LP_{11} modes. To examine the effect of different combination of the pump and probe modes on the differential photothermal phase modulation, we numerically calculated the differential photothermal phase modulation coefficient for various pump and probe mode combinations for varying factional pump power η in the LP_{01} mode. The results are shown in Fig. 4.13. According to the simulation results, for $\eta > 80\%$, the change of modulation coefficient k^* is within 20% of the maximum value (i.e., the value for $\eta = 100\%$). This means that it is not a big issue whether the pump and the probe are launched into the same or different LP_{11} modes, as long as most of the pump power is in the LP_{01} mode. Figure 4.18 also shows that it is better to launch the pump and the probe into orthogonal LP_{11} mode (i.e., one in LP_{11a} and the other in LP_{11b}) because the dependence on η is much weaker. The best choice is of course to launch all the pump power into the LP_{01} mode (i.e., $\eta = 100\%$), where k^* value is always maximized and around $1.6 \times 10^{-7}\ rad\ cm\ ppm^{-1}\ m^{-1}\ mW^{-1}$. While for probe light, the best choice is that the probe powers collected from LP_{01} mode and LP_{11} mode in HCF are equal.

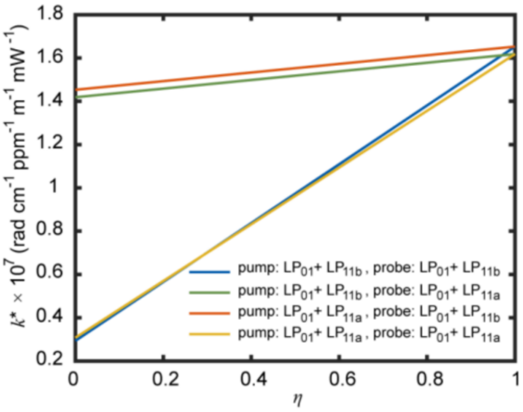

Figure 4.13. Photothermal modulation coefficient k^* as a fucntion of η for different combinations of LP_{01} and LP_{11} modes of pump and probe beam. The results are obtained under the condition of ambient temperature and gas pressure.

4.2.2. Sensitivity of MPD to external temperature and pressure

One of the prominent advantages of MPD detection is the common-noise rejection. In this section, we discuss this feature of MPD using numerical analysis. The sensitivity of the fundamental mode (i.e., LP_{01}) phase and the MPD to external temperature and pressure were studied via the model shown in Fig. 4.14. The model includes an 80-μm polymer coating with radius, a silica outer cladding with diameter of 190 μm and an inner cladding comprising 7 thin rings with a diameter of 56 μm. The parameters used in the simulation are listed in Table 4.2. External temperature and pressure were treated as uniform small perturbations. Under the assumption of small external perturbations, the change of phase is linear to the amplitude of external perturbations and could be described by the phase sensitivity to the perturbations (e.g., temperature, pressure).

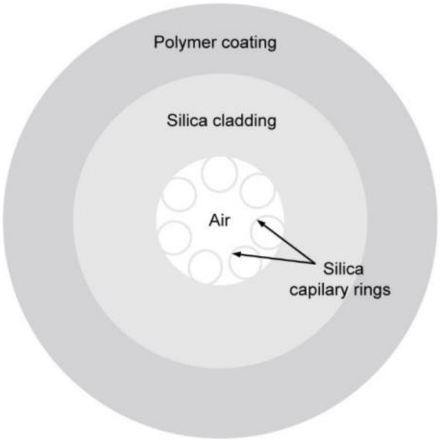

Figure 4.14. The model for numerically calculating the phase sensitivity to external perturbations.

Table 4.2. Parameters used for simulation.

Property	Silica	Polymer	Argon	Nitrogen
Density ρ [kg/m^3]	2203	1190	1.81	1.16
Thermal conductivity κ [W/(m·K)]	1.38	-	0.0174	0.0256
Thermal expansion coefficient α_T [K^{-1}]	5.5×10^{-7}	1.8×10^{-4}	-	-
Ratio of specific heats γ_r	-	-	1.66	1.4
Isobaric specific heat capacity c_p [J/(kg*K)]	703	1420	520	1040
Young's modulus E_Y [GPa]	73.1	0.035	-	-
Poisson's ratio ν_r	0.17	0.40	-	-
Thermo-optic coefficient dn/dT [1/K]	9.5×10^{-6}	-	$-\frac{n_0 - 1}{T_0}$	$-\frac{n_0 - 1}{T_0}$

Firstly, we consider phase sensitivity to the external temperature perturbation. Generally speaking, two kinds of effect need to be taken in account in our simulation if we ignore the PE induced by thermal expansion [24]. First, the RI change of material due to temperature change, or the thermo-optic effect. Second, the longitudinal and transverse thermal expansion. Take the phase sensitivity of LP$_{01}$ to temperature as an example:

$$\frac{\Delta\phi_{01}}{\Delta X} = \frac{2\pi n_{01} L}{\lambda}\left(\frac{1}{n_{01}}\frac{\partial n_{01}}{\partial X} + \frac{1}{L}\frac{\partial L}{\partial X}\right) \tag{4.22}$$

where X refers to temperature here (and also pressure as we will discuss later). The first term on the right hand side (RHS) accounts for change of effective RI induced by the transverse thermal expansion and the thermo-optic effect. The second term on the RHS accounts for the longitudinal expansion of the fiber. The thermal expansion of the fiber could be calculated using the Hooke's Law which relates the strain tensor $\boldsymbol{\epsilon_S}$ and the stress tensor $\boldsymbol{\sigma_S}$:

$$\boldsymbol{\epsilon_S} = \boldsymbol{C_T}\boldsymbol{\sigma_S} + \boldsymbol{\alpha_T}\Delta T \tag{4.23}$$

where $\boldsymbol{C_T}$ is the compliance tensor which is related to the Young's modulus E_Y and the Poisson's ratio ν_r, and $\boldsymbol{\alpha_T}$ is the thermal expansion coefficient which is isotropic and only has the diagonal elements. The parameters used in the simulation are listed in Table 4.2. The phase sensitivity to temperature is closely related to the thermal property of polymer since polymers used for fiber coating usually have a large thermal expansion coefficient when compared with silica. In cylindrical coordinates, only the diagonal elements of $\boldsymbol{\epsilon_S}$ are nonzero for isotropic material (i.e. silica). By following the procedure of Ref. [25], we calculated the longitudinal and transverse thermal expansion numerically using COMSOL Multiphysics. Then the change of effect RI of optical modes is also calculated numerically by taking into account both the thermo-optic effect (parameters listed in Table 4.2) and the transverse thermal expansion.

Secondly, we calculate the phase sensitivity to the external pressure perturbation following the same procedure. The external pressure compressed the fiber and results in longitudinal elongation and transverse deformation. The boundary condition at the outer surface (normal vector $\hat{n}$) of polymer should satisfy

$$\boldsymbol{\sigma_S} \cdot \boldsymbol{\hat{n}} = -P\boldsymbol{\hat{n}} \tag{4.24}$$

where P is the relative external pressure with reference to 1 atm. With Hooke's Law, we could solve the strain field and then the displacement field numerically. The phase sensitivity to external pressure P was calculated using Eq. (4.22). The first and second terms on the RHS is referred to as the change of effective RI induced by transverse deformation and longitudinal elongation, respectively. The analysis discussed above was also performed for the MPD as

$$\frac{\delta\phi}{\Delta X} = \frac{2\pi\Delta n L}{\lambda}\left(\frac{1}{\Delta n}\frac{\partial\Delta n}{\partial X} + \frac{1}{L}\frac{\partial \mathrm{L}}{\partial X}\right) \tag{4.25}$$

where X refers to temperature T or pressure P. We ignore weak contribution of PE in the simulation of effect RI of optical modes [26]. The ratio between the phase sensitivities of Eqs. (4.36) and (4.39) is

$$\zeta = \frac{\Delta\phi_{01}/\Delta X}{\delta\phi/\Delta X} \tag{4.26}$$

which represents the enhancement of system stability against external perturbations (e.g. temperature or pressure). Numerical simulation shows that the values of ζ is ~280 for temperature and ~170 for pressure for the AR-HCF at 1550 nm. In other words, the phase sensitivity to temperature or pressure is about a few hundred times smaller for the MPD than that for LP_{01} mode.

4.2.3. Experiment and discussion

The experimental system is shown in Fig. 4.15(a). The pump source is a 1.53-μm DFB laser and its wavelength is scanned slowly across the P(13) absorption line of acetylene at 1532.83 nm, which is at the same time modulated sinusoidally at the frequency of ~9.5 kHz. The amplitude of wavelength modulation is set to ~2.2 times the linewidth of the P(13) line to maximize the second harmonic (2*f*) signal. The probe source is an external cavity diode laser (ECDL) and its wavelength is tuned to a quadrature point of a dual-mode interference fringe around 1550 nm. The pump and probe beams are launched into the HCF from the opposite directions via two WDMs (WDM1 and WDM2), and the probe beam coming out from WDM2 is detected by a PD. The 2*f* component of the MPD modulation is demodulated by a LIA and recorded by a computer via a data acquisition (DAQ) card for further processing.

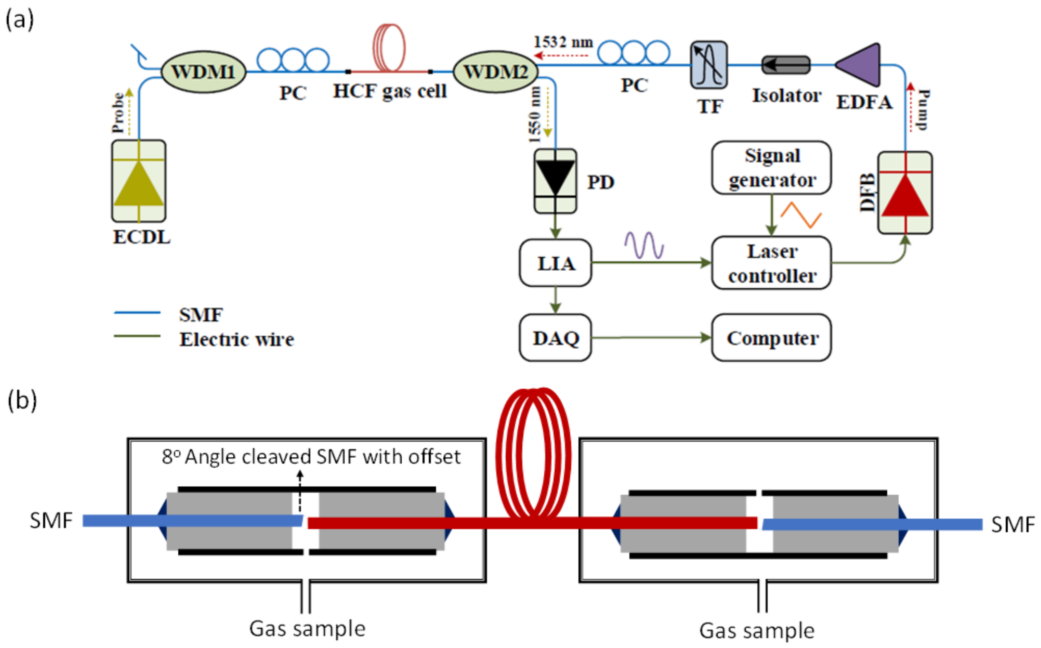

Figure 4.15. The experiment setup for MPD-PTS. (a) The setup for gas detection. (b) Configuration of the HCF gas cell.

Different from the last gas cell shown in Fig. 4.1(b), the AR-HCF gas cell is mechanically spliced to SMF pigtails. The AR-HCF and the SMF are inserted in ceramic ferrules and the two ferrules are fixed by a ceramic sleeve. The ceramic ferrules are made with a small offset. This enables lateral offsets for excitation and collection of light from the LP_{01} and LP_{11} modes to form an in-fiber modal interferometer to probe the MPD. Fibers are inserted into the ceramic ferrule and then assembled with a ceramic sleeve. A small gap of ~5 μm between the butt coupled fibers allows gas flow into/out of the sensing HCF. SMFs cleaved with 8° angle are used to avoid the Fabry-Perot interferometer formed by the reflection on the end-face of SMFs. The coupling loss for each of the joint is 4-6 dB. The mechanical joint is AB glue sealed in a glass tube for gas filling.

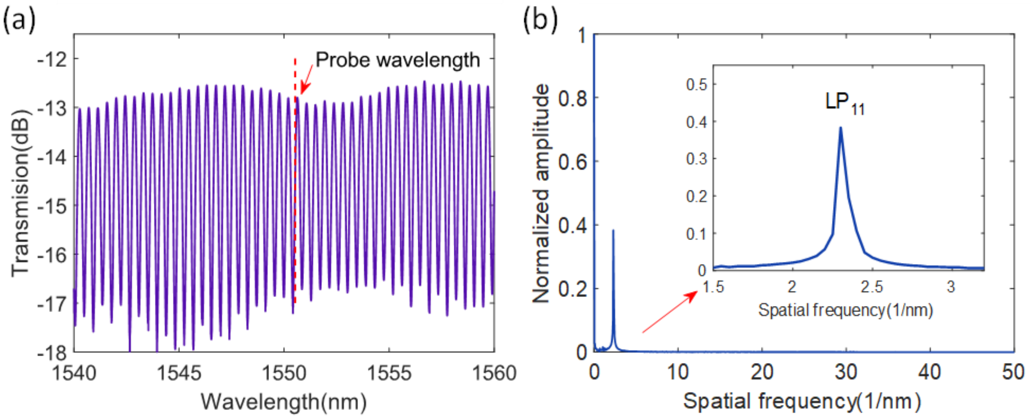

Figure 4.16. The optical property of the AR-HCF gas cell. (a) The transmission spectrum. (b) The Fourier transform of the transmission spectrum.

The transmission spectrum of the AR-HCF gas cell is shown in Fig. 4.16(a) measured by the OSAwith wavelength tuning resolution of 10 pm. The mean insertion loss of the AR-HCF gas cell is ~14.4 dB. This relatively large loss is due to mode field diameter mismatch and the lateral offset between AR-HCF and SMF. The interferogram clearly shows that the AR-HCF supports two orders of optical modes. Figure 4.16(b) shows the Fourier transform of the interferogram that reflects the modal properties of the AR-HCF gas cell. The only peak near 2.4 cm^{-1} is due to the LP_{11} mode and no other higher order modes is observed. The fractional power in the LP_{11} mode is estimated to be ~4% (i.e., $\eta = 0.96$).

Experiments are conducted with the 4.67-m-long HCF gas cell filled with 1 ppm acetylene balanced by Argon. The gas is pressurized into the hollow-core with ~1.95 bar pressure at the input joint while the output joint is open to atmosphere. Fig. 4.17(a) shows the *2f* lock-in output signal when the pump is tuned across the P(13) line of acetylene for different pump power levels delivered to the HCF. The *2f* lock-in output when the pump is tuned away from the absorption line to 1532.57 nm is also recorded and regarded as background noise. The signal increases linearly with pump power, while the standard deviation of the noise remains approximately unchanged, as shown in Fig. 4.17(b). At the pump power of 108 mW, the SNR is ~14804 for a lock-in time constant of 1 second with 18 dB/Oct slope, giving a NEC of ~68 ppt for SNR of unity (i.e., 1σ).

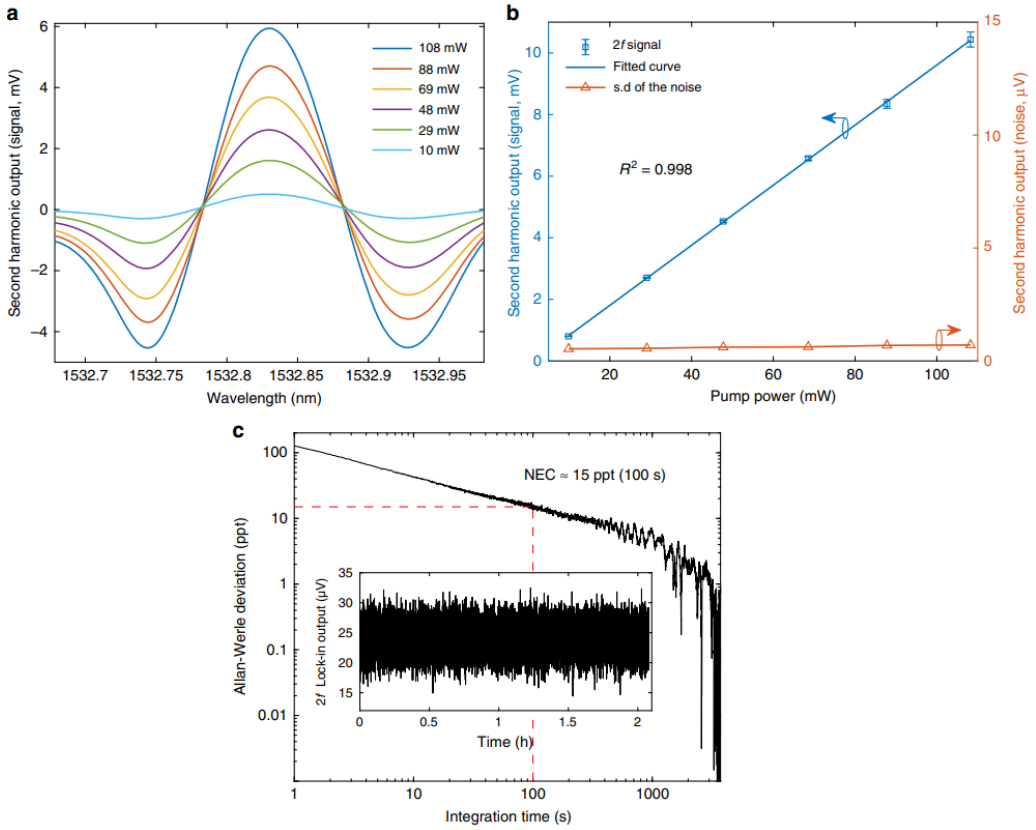

Figure 4.17. The experiment result with 1 ppm acetylene. (a) The second harmonic wave at different pump powers. (b) The power dependence of the second harmonic wave. (c) The Allan variance analysis of the sensitivity of MPD-PTS.

Allan variance analysis was conducted with the noise data over a period of 2 hours [27], and the results are shown in Fig. 4.17(c), the Allan deviation decreases with the integration time linearly on the log-log scale and the 1σ NEC goes down to ~766 ppq for 3630 s integration time. This result is more than three orders of magnitude better than the previous optical fiber gas sensors [12].

The performances of some state-of-the-art spectroscopic laser gas sensors are summarized in Table 4.3. For ease of comparison, we use NEA, which is independent of gas types and absorption strength. The values of NEA can be converted from NEC through equation $NEA = NEC \cdot \alpha_A(\lambda_{pump})$. The NEA of the MPD-PTS is more than three orders of magnitude better than the PTS with a PBG-HCF [12] and between the two most sensitive spectroscopic techniques, i.e., OA-ICOS and NICE-OHMS, but the system is much simpler and in an all-fiber format. The dynamic range is at least one to two orders of magnitude larger than any of the previous techniques. The MPD-PTS system can operate under the condition of ambient pressure and temperature.

Table 4.3. Comparison between several spectroscopic laser gas sensors.

Gas type	Technique [a]	Wavelength(μm)	effective path length (m)	NEA (cm^{-1})
H_2S[28]	TTFMS	1.577	1	5.3×10^{-9}
NO[29]	TDLAS	5.263	210	1.5×10^{-10}
CH_4[30]	OF-CEAS	2.33	~10000	1×10^{-9}
CH_4[31]	CRDS	1.651	~12000	2.3×10^{-11}
C_2H_2[32]	NICE-OHMS	1.534	~13796	2.2×10^{-14}
CO[33]	OA-ICOS	1.565	2700	1.9×10^{-12}
C_2H_2[34]	CERPAS	1.533	0.12	8.4×10^{-11}
C_2H_2[12]	PTS	1.53	10	2.3×10^{-9}
C_2H_2 (this work)	MPD-PTS	1.533	4.67	8.1×10^{-13}

[a] TTFMS, two-tone frequency modulation spectroscopy; OF-CEAS, optical feedback cavity-enhanced absorption spectroscopy; CRDS, cavity ringdown spectroscopy; OA-ICOS, off-axis integrated cavity output spectroscopy; CERPAS, cantilever-enhanced resonant photoacoustic spectroscopy.

In summary, we demonstrated a new MPD-PTS technique and achieved ultra-sensitive gas detection. The detection of MPD minimizes the effect of environment perturbation while maintaining a sufficiently large photothermal modulation signal, enabling orders of magnitude of enhancement of SNR. The broadband transmission of the AR-HCFs [35, 36] in combination of ultra-low noise dual-mode interferometry would enable cost-effective, precision all-fiber sensors with multi-gas detection capability. The common-mode noise-rejection concept could also be applied for liquid-core fiber sensors and other dual-mode waveguide systems.

4.3. Conclusion

In this chapter, we have presented two methods to enhance the sensitivity of PTS with HCFs: intracavity PTS and MPD-PTS.

The intracavity PTS improves the sensitivity of gas detection by placing a gas cell inside a laser cavity. The phase modulation of PTS is enhanced by fully utilizing the power of pump laser. With a 0.62-m-long PBG-HCF, we realize a sensitivity of 176 ppb C_2H_2 with 10 s integration time. Theoretical study shows, by reducing the loss of fiber ring laser cavity, the sensitivity can be enhanced to ppb level with the same length of HCF.

The MPD-PTS improves the sensitivity by reducing the noise in interferometric detection by measuring the phase difference between guided optical modes in AR-HCFs. The common-mode noise in the interferometer is significantly decreased, which results in a much higher SNR for gas detection. With a 4.67-m-long AR-HCF, we realize a sensitivity of ppt level C_2H_2 with 3630 s integration time. The sensitivity of MPD-PTS is comparable with the most sensitive spectroscopic techniques.

Reference of Chapter 4

1. Stewart, G., Atherton, K., Yu, H., & Culshaw, B. (2001). An investigation of an optical fibre amplifier loop for intra-cavity and ring-down cavity loss measurements. *Measurement Science and Technology*, *12*(7), 843.

2. Zhang, Y., Zhang, M., & Jin, W. (2003). Sensitivity enhancement in erbium-doped fiber laser intra-cavity absorption sensor. *Sensors and Actuators A: Physical*, *104*(2), 183-187.

3. Zhang, M., Wang, D. N., Jin, W., & Liao, Y. (2004). Wavelength modulation technique for intra-cavity absorption gas sensor. *IEEE Transactions on Instrumentation and Measurement*, *53*(1), 136-139.

4. Song, Y. W., Havstad, S. A., Starodubov, D., Xie, Y., Willner, A. E., & Feinberg, J. (2001). 40-nm-wide tunable fiber ring laser with single-mode operation using a highly stretchable FBG. *IEEE Photonics Technology Letters*, *13*(11), 1167-1169.

5. Smith, D. A., Maeda, M. W., Johnson, J. J., Patel, J. S., Saifi, M. A., & Von Lehman, A. (1991). Acoustically tuned erbium-doped fiber ring laser. *Optics Letters*, *16*(6), 387-389.

6. Zhang, X., Zhu, N. H., Xie, L., & Feng, B. X. (2007). A stabilized and tunable single-frequency erbium-doped fiber ring laser employing external injection locking. *Journal of Lightwave Technology*, *25*(4), 1027-1033.

7. Hoo, Y. L., Liu, S., Ho, H. L., & Jin, W. (2010). Fast response microstructured optical fiber methane sensor with multiple side-openings. *IEEE Photonics Technology Letters*, *22*(5), 296-298.

8. Okoshi, T., Kikuchi, K., & Nakayama, A. (1980). Novel method for high resolution measurement of laser output spectrum. *Electronics Letters*, *16*(16), 630-631.

9. Richter, L., Mandelberg, H., Kruger, M., & McGrath, P. (1986). Linewidth determination from self-heterodyne measurements with subcoherence delay times. *IEEE Journal of Quantum Electronics*, *22*(11), 2070-2074.

10. Cubillas, A. M., Silva-Lopez, M., Lazaro, J. M., Conde, O. M., Petrovich, M. N., & Lopez-Higuera, J. M. (2007). Methane detection at 1670-nm band using a hollow-core photonic bandgap fiber and a multiline algorithm. *Optics Express*, *15*(26), 17570-17576.

11. Carvalho, J. P., Lehmann, H., Bartelt, H., Magalhães, F., Amezcua-Correa, R., Santos, J. L., ... & Knight, J. C. (2009). Remote system for detection of low-levels of methane based

on photonic crystal fibres and wavelength modulation spectroscopy. *Journal of Sensors*, *2009*.

12. Jin, W., Cao, Y., Yang, F., & Ho, H. L. (2015). Ultra-sensitive all-fibre photothermal spectroscopy with large dynamic range. *Nature Communications*, *6*(1), 1-8.

13. Rothman, L. S., Gordon, I. E., Babikov, Y., Barbe, A., Benner, D. C., Bernath, P. F., ... & Wagner, G. (2013). The HITRAN2012 molecular spectroscopic database. *Journal of Quantitative Spectroscopy and Radiative Transfer*, *130*, 4-50.

14. Xiao, L., Demokan, M. S., Jin, W., Wang, Y., & Zhao, C. L. (2007). Fusion splicing photonic crystal fibers and conventional single-mode fibers: microhole collapse effect. *Journal of Lightwave Technology*, *25*(11), 3563-3574.

15. Kristensen, J. T., Houmann, A., Liu, X., & Turchinovich, D. (2008). Low-loss polarization-maintaining fusion splicing of single-mode fibers and hollow-core photonic crystal fibers, relevant for monolithic fiber laser pulse compression. *Optics Express*, *16*(13), 9986-9995.

16. Xie, S., Pennetta, R., & Russell, P. S. J. (2016). Self-alignment of glass fiber nanospike by optomechanical back-action in hollow-core photonic crystal fiber. *Optica*, *3*(3), 277-282.

17. Stewart, G., Whitenett, G., Vijayraghavan, K., & Sridaran, S. (2007). Investigation of the dynamic response of erbium fiber lasers with potential application for sensors. *Journal of Lightwave Technology*, *25*(7), 1786-1796.

18. Chieng, Y. T., Cowle, G. J., & Minasian, R. A. (1996). Optimization of wavelength tuning of erbium-doped fiber ring lasers. *Journal of Lightwave Technology*, *14*(7), 1730-1739.

19. Uebel, P., Günendi, M. C., Frosz, M. H., Ahmed, G., Edavalath, N. N., Ménard, J. M., & Russell, P. S. J. (2016). Broadband robustly single-mode hollow-core PCF by resonant filtering of higher-order modes. *Optics Letters*, *41*(9), 1961-1964.

20. Barnard, C., Myslinski, P., Chrostowski, J., & Kavehrad, M. (1994). Analytical model for rare-earth-doped fiber amplifiers and lasers. *IEEE Journal of Quantum Electronics*, *30*(8), 1817-1830.

21. Davis, C. C., & Petuchowski, S. J. (1981). Phase fluctuation optical heterodyne spectroscopy of gases. *Applied Optics*, *20*(14), 2539-2554.

22. Ye, J., Ma, L. S., & Hall, J. L. (1998). Ultrasensitive detections in atomic and molecular physics: demonstration in molecular overtone spectroscopy. *JOSA B*, *15*(1), 6-15.

23. Lin, Y., Jin, W., Yang, F., Ma, J., Wang, C., Ho, H. L., & Liu, Y. (2016). Pulsed photothermal interferometry for spectroscopic gas detection with hollow-core optical fibre. *Scientific Reports*, *6*(1), 1-12.

24. Fokoua, E. N., Petrovich, M. N., Bradley, T., Poletti, F., Richardson, D. J., & Slavík, R. (2017). How to make the propagation time through an optical fiber fully insensitive to temperature variations. *Optica*, *4*(6), 659-668.

25. Dangui, V., Kim, H. K., Digonnet, M. J., & Kino, G. S. (2005). Phase sensitivity to temperature of the fundamental mode in air-guiding photonic-bandgap fibers. *Optics Express*, *13*(18), 6669-6684.

26. Pang, M., Xuan, H. F., Ju, J., & Jin, W. (2010). Influence of strain and pressure to the effective refractive index of the fundamental mode of hollow-core photonic bandgap fibers. *Optics Express*, *18*(13), 14041-14055.

27. Werle, P. O., Mücke, R., & Slemr, F. (1993). The limits of signal averaging in atmospheric trace-gas monitoring by tunable diode-laser absorption spectroscopy (TDLAS). *Applied Physics B*, *57*(2), 131-139.

28. Modugno, G., Corsi, C., Gabrysch, M., & Inguscio, M. (1998). Detection of H_2S at the ppm level using a telecommunication diode laser. *Optics Communications*, *145*(1-6), 76-80.

29. Nelson, D. D., McManus, J. B., Herndon, S. C., Shorter, J. H., Zahniser, M. S., Blaser, S., ... & Faist, J. (2006). Characterization of a near-room-temperature, continuous-wave quantum cascade laser for long-term, unattended monitoring of nitric oxide in the atmosphere. *Optics Letters*, *31*(13), 2012-2014.

30. Kassi, S., Chenevier, M., Gianfrani, L., Salhi, A., Rouillard, Y., Ouvrard, A., & Romanini, D. (2006). Looking into the volcano with a Mid-IR DFB diode laser and Cavity Enhanced Absorption Spectroscopy. *Optics Express*, *14*(23), 11442-11452.

31. Crosson, E. (2008). A cavity ring-down analyzer for measuring atmospheric levels of methane, carbon dioxide, and water vapor. *Applied Physics B*, *92*(3), 403-408.

32. Zhao, G., Hausmaninger, T., Ma, W., & Axner, O. (2018). Shot-noise-limited Doppler-broadened noise-immune cavity-enhanced optical heterodyne molecular spectrometry. *Optics Letters*, *43*(4), 715-718.

33. Engel, G. S., Drisdell, W. S., Keutsch, F. N., Moyer, E. J., & Anderson, J. G. (2006). Ultrasensitive near-infrared integrated cavity output spectroscopy technique for detection of CO at 1.57 μm: new sensitivity limits for absorption measurements in passive optical cavities. *Applied Optics*, *45*(36), 9221-9229.

34. Chen, K., Yu, Q., Gong, Z., Guo, M., & Qu, C. (2018). Ultra-high sensitive fiber-optic Fabry-Perot cantilever enhanced resonant photoacoustic spectroscopy. *Sensors and Actuators B: Chemical*, *268*, 205-209.

35. Gao, S. F., Wang, Y. Y., Ding, W., & Wang, P. (2018). Hollow-core negative-curvature fiber for UV guidance. *Optics Letters*, *43*(6), 1347-1350.

36. Yu, F., & Knight, J. C. (2013). Spectral attenuation limits of silica hollow core negative curvature fiber. *Optics Express*, *21*(18), 21466-21471.

Chapter 5 Photoacoustic Brillouin spectroscopy with HCFs

Following the discussion in Chapter 3, we study the photoacoustic effect in HCFs induced by optical absorption and present a new method of gas sensing named PABS with gas-filled HCFs. The principles of PABS are explained theoretically. The spectroscopy of C_2H_2, as well as spectroscopy of the microstructure of HCFs, are demonstrated experimentally. The potential of gas sensing with PABS is also discussed with comprehensive modeling.

5.1. Previous work of PAS for gas sensing

PAS is a powerful tool for tracing gas by detecting the acoustic wave generated with optical absorption [1, 2]. Typically, an open-path absorption cell is used for photoacoustic generation and a microphone for acoustic detection. The types of microphones used include quartz-tuning-fork [3], interferometric cantilever [4], fiber-optic microphone [5], etc. The detection sensitivity can be enhanced by using an additional resonant-acoustic-cavity [6] and ppb level detection has been demonstrated for a variety of gases [7-11]. To the best of our knowledge, PAS has not been implemented in HCFs before.

Previously, forward Brillouin scattering (FBS) in HCFs has been studied [12-14]. Recently, intense backward stimulated Brillouin scattering was also observed at high gas pressures and was used for lasing and distributed temperature sensing [15]. However, FBS at atmospheric pressure is extremely weak in HCFs, and no useful application has been reported.

5.2. Principle of PABS with gas-filled HCFs

5.2.1. Acoustic mode and optical mode in HCFs

Figure 5.1(a) shows a SEM image of the AR-HCF used in the experiment. It consists of an air-core and seven suspended silica capillaries of slightly different sizes. FEM analysis based on the thermo-viscous acoustic model shows that the fiber supports a few coupled acoustic modes in the frequency range up to 8 MHz. In general, the resonant frequency of acoustic mode in HCFs are related to the acoustic out-of-plane wavevector. The acoustic out-of-plane wavevector describe the propagation of acoustic mode along the fiber. An acoustic mode is said to be cutoff when it does not propagate along the fiber (i.e., out-of-plane wavevector is zero). However, for PABS in HCFs, the acoustic modes are close to cutoff, which means their resonant frequencies can be approximated by the cutoff frequency.

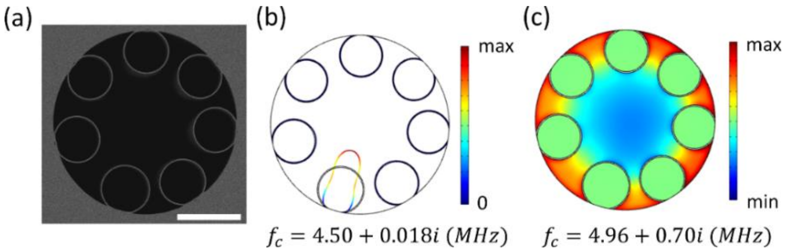

Figure 5.1. The SEM of AR-HCF and the acoustic modes in the fiber. (a) The SEM of AR-HCF. The white bar is 20 μm. (b) The capillary mode of AR-HCF. (c) The air mode of AR-HCF.

Intuitively, the structure of a gas-filled AR-HCF supports acoustic modes in air (termed as air mode) and silica capillaries (termed as capillary modes). They form hybrid acoustic modes. The air mode is described by the density change (ρ), which accounts for both pressure change and temperature change. The capillary mode is described by the displacement of the silica capillary (w).

As examples, Fig. 5.1(b) shows a capillary mode (the first-order wine-glass-like mode w_1) with an eigenfrequency of 4.50 + 0.018i MHz. The imaginary part of the eigenfrequency accounts for the loss of the mode. The quality factor is about 120. The loss of the capillary mode is dominantly due to air damping. Fig. 5.1(c) shows an air mode (the first-order radial-like mode R_{01}) with an eigenfrequency of 5.15 + 0.70i MHz, which is more lossy compared with the capillary mode. There are 7 similar capillary modes, corresponding to the number of the capillaries. The different sizes of capillaries reduce their coupling to the air mode, and also reduce the loss of capillary modes.

Table 5.1. Parameters of AR-HCF estimated from SEM [a].

Label	Inner diameter (μm)	Thickness (nm)	Center of capillary (μm, μm)
1	15.10	406	(-6.5, -22)
2	14.26	439	(-22.4, 5.6)
3	13.78	459	(-18.2, 14.9)
4	13.89	443	(0.4, 23.4)
5	13.70	395	(18.3, 15.3)
6	13.90	428	(23.3, -2.5)
7	14.28	413	(12.5, -19.7)

[a] The diameter of the whole hollow region is 60.5 μm and its center is set at (0, 0).

Different from the commonly used excitation methods of FBS, here an acoustic mode is excited via the photoacoustic effect by gas absorption of a modulated pump laser beam propagating in the gas-filled AR-HCF. The wavelength (λ_P) of the pump is tuned to an absorption line of the gas and the modulation frequency ($f = \Omega/2\pi$) of pump to the frequency of an acoustic mode. At low frequency of several MHz, the acoustic mode is very close to cut-off and almost transverse, the eigenfrequency may be approximated by the cut-off frequency f_c.

Considering a simplified two-level system, the amplitude of the acoustic signal is proportional to the optical absorption induced harmonic heat source $\tilde{Q} \propto \alpha_A C P_P/\sqrt{\Omega^2\tau^2+1}$, where P_P is the pump power and τ is the thermal relaxation time of the system. For many gases or gas mixtures, the values of τ is in the range of micro to nano second [16] and hence the photoacoustic effect is particularly suited for exciting the lowest order capillary and air acoustic modes of the AR-HCF, which is in the frequency range of megahertz. The capillary mode usually dominates at atmospheric pressure or lower pressures while the air mode dominates at high pressures.

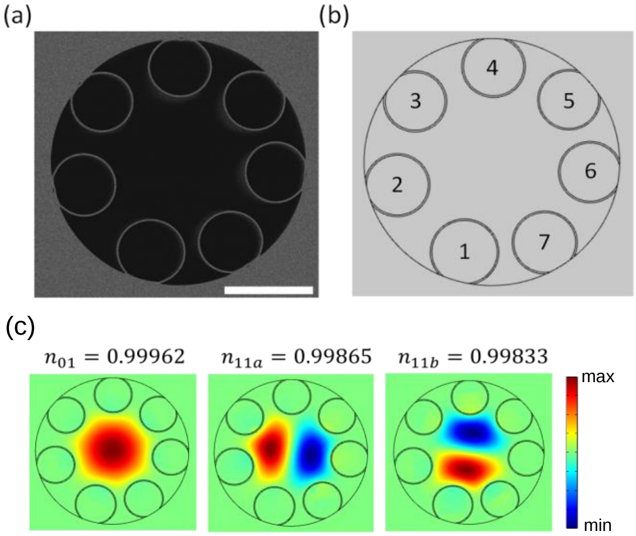

Figure 5.2. The geometry used for simulation and the optical modes supported by the fiber. (a) The SEM image of the AR-HCF. (b) The geometry built from the SEM image for simulation. (c) The simulated optical modes.

The geometry model of AR-HCF used for simulation is precisely built from the SEM of the fiber. SEM image of fiber A and its geometry used for simulation are shown in Figs. 5.2(a) and (b), respectively. The simulated electric field ψ_i (i = 01, 11a and 11b) of the guided optical modes is shown in Fig. 5.2(c).

5.2.2. Excitation of acoustic mode

We focus on the P(13) of $\nu_1 + \nu_3$ band of C_2H_2 at 1532.83 nm. Foreign gas broadening affects the absorption coefficient (α_A) of acetylene (C_2H_2). For simplicity, we assume nitrogen has the same foreign broadening coefficient as that of air. The normalized absorption coefficients of C_2H_2 versus gas pressure are shown in Fig. 5.3. They are calculated based on Eq. (2.7) in Chapter 2. In the Doppler broadening regime of gas molecules (i.e. pressure less than 1 kPa), the wall collisional broadening in AR-HCF estimated with hard sphere model is about 7 MHz [16, 17], which is much smaller than the Doppler linewidth and hence is ignored in the simulation.

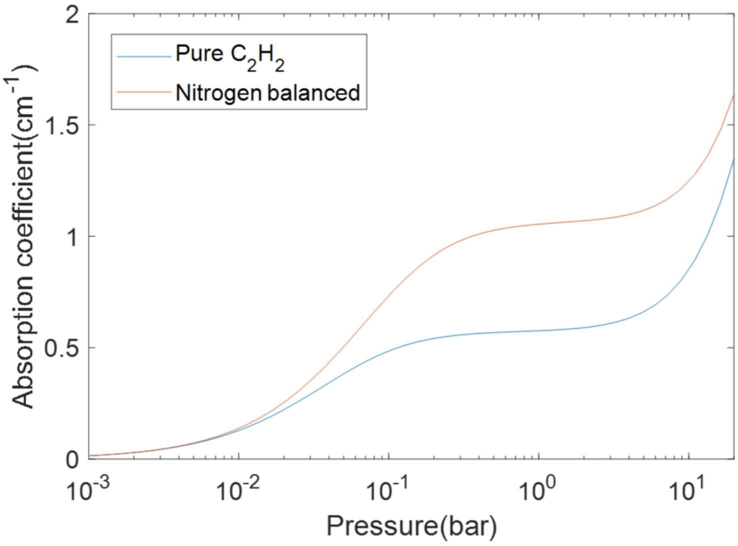

Figure 5.3. The normalized absorption coefficient (α_A/C) of acetylene with different pressures.

AR-HCF mainly supports two sets of LP-like optical modes as shown in Fig. 5.2(c). It is calculated with COMSOL Multiphysics. The intensity of pump is modulated by a frequency of Ω. The optical intensity of pump is

$$I_P = I_0 + \tilde{I} \tag{5.2}$$

$$I_0 = P_P[\Psi_1 + \Psi_2 \cos(kn_r z)] \tag{5.3}$$

$$\tilde{I} \approx P_P[\Psi_1 + \Psi_2 \cos(kn_r z)] \exp(-j\Omega t) \tag{5.4}$$

where $\Psi_1 = \eta\psi_{01}^2 + (1-\eta)\psi_{11}^2, \Psi_2 = 2\sqrt{\eta(1-\eta)}\psi_{01}\psi_{11}$, and ψ_i are the power normalized electric field of LP_{01} and LP_{11}-like modes, η the fractional power in LP_{01}, z the direction of light propagation, k_P the angular wavevector of pump light, $n_r = n_{01} - n_{11}$ the differential mode index between LP_{01} and LP_{11} and $\Omega = 2\pi f$ is the angular frequency of pump modulation. For AR-HCFs, more than 99.9% power of light is in the gas ($n_{gas} \approx 1$) and hence it is a good approximation to normalize that $\int \psi_i^2 dA = 1$ over the fiber cross-section. For modulation frequency of a few MHz and fiber length of tens of millimeters, the phase term of optical intensity can be calculated as $qL \approx 2\pi f L/c \ll \pi$ (where L is the length of fiber) and could be ignored (the effective mode indices are all very close to unity). For simplicity, the heat source is estimated with a two-level model and is expressed by

$$Q = Q_0 + \tilde{Q} \tag{5.5}$$

$$Q_0 = \frac{\alpha_A C I_0}{\sqrt{\Omega^2 \tau^2 + 1}} \tag{5.6}$$

$$\tilde{Q} = \frac{\alpha C \tilde{I}}{\sqrt{\Omega^2 \tau^2 + 1}} \exp(j\varphi) \tag{5.7}$$

where Q_0 is the background heat source, $\tilde{Q}$ the harmonic heat source, C the concentration of C_2H_2 and $\varphi = \tan^{-1}(\Omega\tau)$ is the phase angle.

Table. 5.2. Parameters used for acoustic simulation.

Symbol	Description	Value at T_0	
		N_2	C_2H_2
η_0	Dynamic viscosity	1.8×10^{-5} Pa s	1.0×10^{-5} Pa s
η_B	Bulk viscosity	1.4×10^{-5} Pa s	7.0×10^{-4} Pa s
c_P	Isobaric specific heat capacity	1.0×10^{3} J/(kg K)	2.2×10^{3} J/(kg K)
κ	Thermal conductivity	0.026 W/(m K)	0.024 W/(m K)
c_s	Speed of sound	348 m/s	343 m/s
ρ_0	Gas density at 1 atm	1.165 g/L	1.092 g/L
n	RI at 1 atm	$1+2.8 \times 10^{-4}$	$1+5.5 \times 10^{-4}$
γ_r	Ratio of specific heat capacity	1.4	
β_T	Isothermal compressibility	$\gamma_r/(\rho_0 c_s^2)$	
T_0	Ambient temperature	293.15 K	
α_P	Isobaric thermal expansion coefficient	$1/T_0$	
ρ_S	Density of fused silica	2203 kg/m^3	
E_Y	Young's modulus	73.1 GPa	

For simulation of acoustic problems in small dimension, viscous and thermal dissipation at the boundary play an important role and a thermo-viscous acoustic model is often used [18, 19]. Meanwhile, we need to consider the coupling between the thermo-viscous acoustics and the silica capillaries [20]. The thermoviscous model and the solid mechanics model are used for simulation in COMSOL Multiphysics. The parameters used in the simulation is listed in Table. 5.2 [21-25]. The density of gas is assumed to be linear dependent on gas pressure. The thermo-viscous acoustic model is coupled with the solid mechanics model with an isothermal boundary condition. For low concentration of C_2H_2 in nitrogen, parameters of N_2 is used for simplicity. The heat generated by pump absorption results in local temperature change and leads to generation of acoustic wave. The acoustic wave propagates in the air region of HCF and reflects at the silica-air boundary. The reflection of acoustic wave also results in vibration of the silica capillary. This is the so-called vibro-acoustic system.

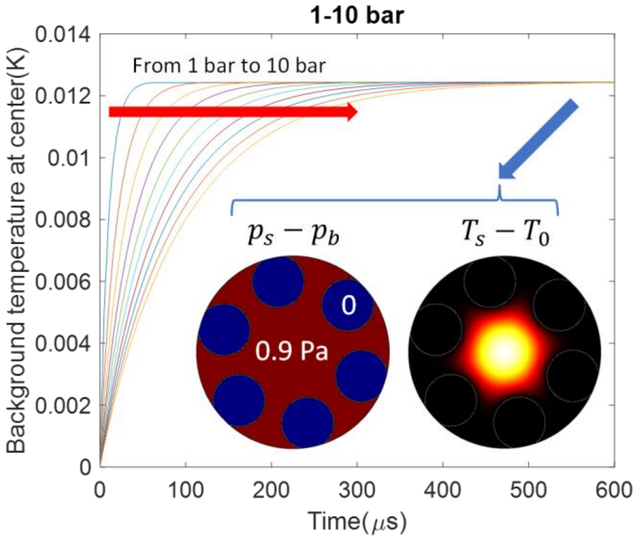

Figure 5.4. The transient response of the pressure and the temperature. The simulation is done with parameters $\alpha_A = 1.06\ cm^{-1}$, $C = 106\ ppm$ *and* $P_P = 162\ mW$.

The background temperature and pressure need to be considered when we calculate harmonic perturbations. It can be approximated by the steady state of temperature and pressure under the background heat source Q_0. For simplicity, we ignore the deformation of the fiber geometry at steady state and only consider the steady state temperature field T_s and pressure field p_s. Figure 5.4 shows the transient response of the AR-HCF. The system reaches the steady state within a time of 500 μs. The steady state of pressure and temperature is shown in the inset of Fig. 5.4. By increasing the gas pressure, as indicates by the red arrow, it takes a longer time to reach the steady state but the distribution of pressure and temperature at steady state are almost the same at different pressures. Then we calculate the harmonic perturbation in the frequency domain. The harmonic perturbation is accurate only when the harmonic perturbations of pressure, temperature and density are much smaller than their steady state values. Since the variation of heat source along z-axis is much smaller than that in the fiber cross-section, the simulation is performed with a 2-D model for simplicity. We have

$$\rho = [\rho_1 + \rho_2 \cos(kn_r z)]\exp(-j\Omega t + \varphi) \tag{5.8}$$

$$w = [w_1 + w_2 \cos(kn_r z)]\exp(-j\Omega t + \varphi) \tag{5.9}$$

where ρ_1 and w_1 are the harmonic solutions when only the first term of $\tilde{Q}$ on the RHS of Eq. (5.4) is applied, ρ_2 and w_2 are the harmonic solution when only the last term of $\tilde{Q}$ on the RHS of Eq. (5.4) is applied.

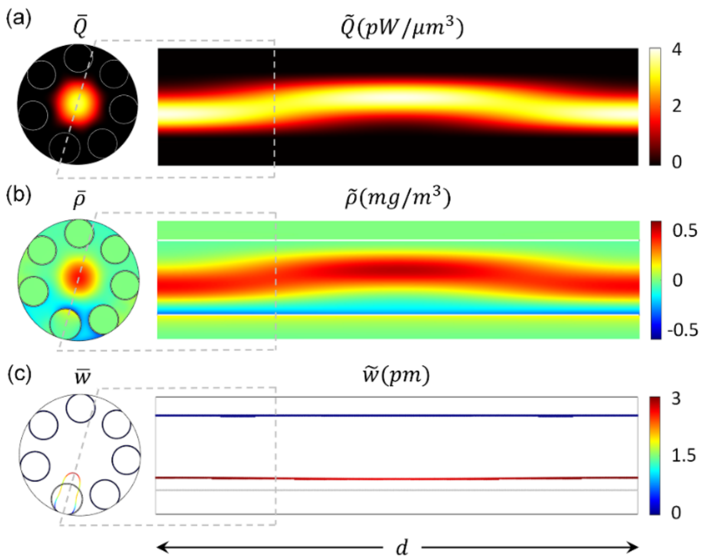

Figure 5.5. The modal interference induced periodical distribution of harmonic heat source $\tilde{Q}$, *density change* $\tilde{\rho}$, *and displacement of capillary* $\tilde{w}$ *with parameters* $\alpha_A = 1.06\ cm^{-1}$, $C = 106\ ppm$ *and* $P_P = 162\ mW$. *The displacement in the figure is enlarged by* 2×10^6 *times for clarity. The slice long the fiber is plotted along the dash line of the fiber cross-section.*

As demonstrated in Fig. 5.5, the modal interference gives a periodical optical intensity distribution $I_P = I_P^0 + \tilde{I}_P e^{-j\Omega t}$ (and hence the heat source distribution $Q = Q_P^0 + \tilde{Q}e^{-j\Omega t}$ as shown in Fig. 5.5(a)) along fiber with a period of $d = \lambda_P / n_r \approx 1.6\ mm$. The periodical heat source results in a periodical distribution of acoustic field, which is described by the density change $\rho = \rho_0 + \tilde{\rho}\, e^{-j\Omega t}$, and the displacement of capillary $w = w_0 + \tilde{w}e^{-j\Omega t}$. In our experiment, $L/d \gg 1$ and hence the total phase modulation is equivalently induced by the equivalent acoustic fields $\bar{\rho} = \rho_1$ and $\bar{w} = w_1$. The cosine terms in Eqs. (5.8) and (5.9) are average out. The acoustic fields $\bar{\rho}$ and $\bar{w}$ are induced by an equivalent harmonic pump $\bar{Q}$. The equivalent fields ($\bar{\rho}$, $\bar{w}$, etc.) are equal to the fields at 1/4 period.

The basic principle of the phase modulation of probe has been discussed in Chapter 3. The probe light in the AR-HCF experiences phase modulation (or change of mode index n_m) due to shifting boundary (SB), gas density change (GD) and photoelasticity (PE):

$$\frac{dn_m}{dx} = \left.\frac{dn_m}{dx}\right|_{SB} + \left.\frac{dn_m}{dx}\right|_{GD} + \left.\frac{dn_m}{dx}\right|_{PE} \tag{5.10}$$

where x is an infinitesimal perturbation (i.e. a normalized equivalent harmonic heat source $\bar{Q}/\alpha C P_P$) and subscript m refers to the label of optical modes (e.g. LP_{11b}). Since we only care about the harmonic phase modulation near the steady state, we only consider the phase modulation due to harmonic perturbations. Considering the pump depletion due to optical absorption and ignoring the fiber loss, the phase modulation is calculated by

$$P(z) = P_P \exp(-\alpha_A C z) \tag{5.11}$$

$$\Delta\phi_m = \frac{\alpha_A C \omega_L}{c} \int_0^L dz\, P(z) \frac{dn_m}{dx} \tag{5.12}$$

where L is the length of AR-HCF and dn_m/dx is independent of z when considering a normalized equivalent heat source $\bar{Q}/\alpha_A C P_P$. Hence from Eqs. (5.11) and (5.12) we have,

$$\Delta\phi_m \approx \frac{P_P \omega_L}{c} (1 - e^{-\alpha_A C L}) \frac{dn_m}{dx} = \frac{\alpha_A C P_P L_{eff} \omega_L}{c} \frac{dn_m}{dx} \tag{5.13}$$

$$L_{eff} = \frac{1 - e^{-\alpha_A C L}}{\alpha_A C} \tag{5.14}$$

where L_{eff} is the effective absorption length and it approximates the length of fiber L when $\alpha_A C L \ll 1$. The change of mode index is related with change of frequency of optical mode by

$$\frac{dn_m}{dx} = -\frac{n_m^g}{\omega_L} \frac{d\omega}{dx} \tag{5.15}$$

where $n_m^g = n_m + \omega_L dn_m/d\omega$ is the group RI and ω_L is the angular optical frequency of probe. The shifting boundary induced perturbation is calculated as

$$\left.\frac{dn_m}{dx}\right|_{SB} = \frac{n_m^g}{2} \frac{\int ds(\frac{d\boldsymbol{w}}{dx} \cdot \hat{n})\,[\Delta\varepsilon_{12}|\hat{n} \times E_m|^2 - \Delta(\varepsilon_{12}^{-1})|\hat{n} \cdot D_m|^2]}{\iint dS |E_m|^2 \varepsilon} \tag{5.16}$$

where $\hat{n}$ is the normal vector on the interface from silica to gas, E_m the probe electric field, $D_m = \varepsilon E_m$ the probe electric displacement field, $\Delta\varepsilon_{12} = \varepsilon_1 - \varepsilon_2$ and $\Delta(\varepsilon_{12}^{-1}) = \varepsilon_1^{-1} - \varepsilon_2^{-1}$ are the differential permittivity between silica (ε_1) and gas (ε_2). The density change and photoelasticity induced perturbations are calculated by the standard perturbation theory

$$\left.\frac{dn_m}{dx}\right|_{GD} = \frac{n_m^g \gamma_e}{2\rho_0} \frac{\iint dS |E_m|^2 \frac{d\rho}{dx}}{\iint dS |E_m|^2 \varepsilon_r} \tag{5.17}$$

$$\left.\frac{dn_m}{dx}\right|_{PE} = \frac{n_m^g n_{silica}^4}{2\iint dS|E_m|^2\varepsilon_r}\int dS\,(\sum 2Re\{E_{i,m}^* E_{j,m}\}p_{44}\frac{dS_{ij}}{dx} + \\ + \sum |E_{i,m}|^2\left(p_{11}\frac{dS_{ii}}{dx} + p_{12}\left(\frac{dS_{jj}}{dx} + \frac{dS_{kk}}{dx}\right)\right)) \qquad (5.18)$$

where the electrostrictive constant $\gamma_e = 2(n_{gas} - 1) = A\rho_0$ for dilute gas and A is a constant. S_{ij} is the strain tensor and for fused silica, $p_{11} = 0.121$, $p_{12} = 0.27$ and $p_{44} = (p_{11} - p_{12})/2$ [25].

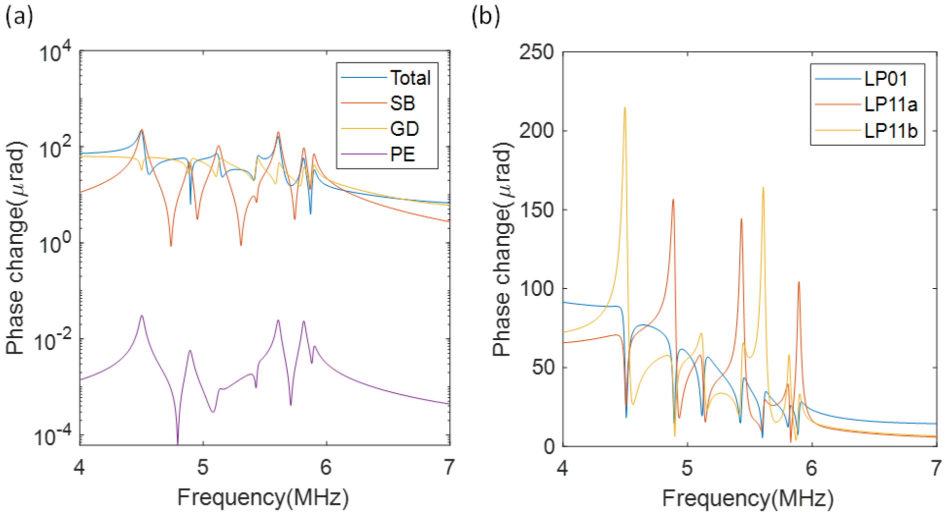

Figure 5.6. The calculated phase modulation of PABS. The parameters are: $P_P = 162\ mW, C = 106\ ppm$ *and* $L = 30\ cm$*. (a) The phase modulation from different mechanisms for* LP_{01} *mode. (b) The phase modulation of different optical modes.*

The phase modulation of modal interferometer (MI) is

$$\Delta\phi_{MI} = \Delta\phi_{01} - \Delta\phi_{11a,b} \qquad (5.19)$$

For example, Fig. 5.6 shows the simulation result with 106 ppm C_2H_2 balanced with nitrogen at a pressure of 1 bar. As shown in Fig. 5.6(a), for optical modes in the gas, the contribution of phase modulation from PE could be ignored. The contributions from gas density change and shifting boundary are comparable. Different optical modes also experience different phase modulation as we shown in Fig. 5.6(b). However, the two polarizations of an optical mode shows little difference as we found in the simulation.

The phase modulation exerts on a probe optical mode results mainly from two contributing factors, the gas density change and the shifting boundary of silica capillaries. The density change includes a non-resonant part due to photothermal phase modulation and the resonant part due to the photo-acoustically excited acoustic resonance. The differential phase modulation may be calculated by using $\Delta\phi = (2\pi/\lambda_L)\int_0^L dz[\Delta n_{01}(z) - \Delta n_{11}(z)]$. The differential phase modulation may be expressed in the form of

$$\Delta\phi(\Omega, \lambda_P) = k_{PA}^*(\Omega)\alpha_A(\lambda_P)CL_{eff}P_P \tag{5.20}$$

where the effective interaction length of AR-HCF approximates the length of fiber when $\alpha_A CL \ll 1$, k_{PA}^* is a photoacoustic phase modulation coefficient that describes the frequency response of the fiber and would become significant around the acoustic resonances. We could define a photoacoustic Brillouin nonlinear coefficient $\gamma_{PA} = k_{PA}^*(\Omega)\alpha_A(\lambda_P)$. Since $\Delta\phi(\Omega, \lambda_P)$ is a function of the modulation frequency $\Omega = 2\pi f$ and the wavelength of pump λ_P, the proposed PABS method may be used for gas spectroscopy via the $\alpha_A(\lambda_P)C$ dependence and for spectroscopy of microstructure via the $k_{PA}^*(\Omega)$ dependence.

5.3. Experiment of PABS

5.3.1. Experiment setup

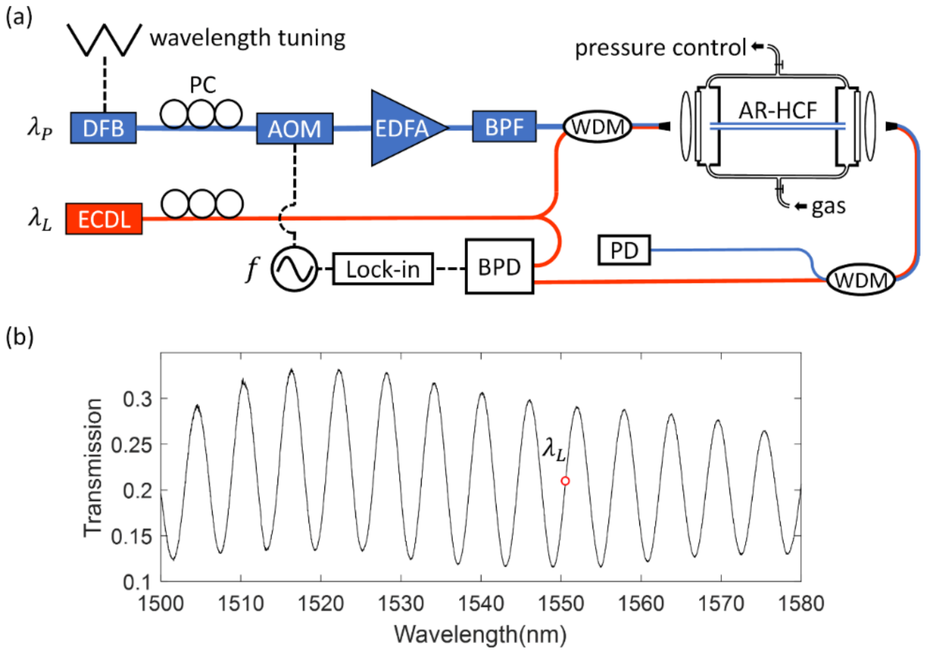

Figure 5.7. The experiment setup of PABS. (a) Detailed experiment setup for PABS. Light is coupled into AR-HCF with optical fiber collimators and optical lenses. λ_P and λ_L, wavelengths of pump and probe laser beams. (b) Transmission spectrum of the SMF/AR-HCF/SMF dual-mode interferometer. The red circle shows the wavelength of the probe at a quadrature point of the interferogram.

The experiment setup is shown in Fig. 5.7(a). The pump laser is a DFB laser with a wavelength at 1532.83 nm, which is near the P(13) absorption line of acetylene. The wavelength of pump is tuned across the absorption line by thermal tuning and the intensity of pump is modulated sinusoidally at the frequency of Ω by use of an AOM. The pump power is further amplified by an EDFA. An optical bandpass filter (BPF) is used to filter out the ASE noise from the EDFA. The 3-dB bandwidth of BPF is about 1-nm. The probe light is from an ECDL and is multiplexed/de-multiplexed with the pump beam by WDMs. Optical lenses are used to couple light into and collect light from the AR-HCF.

The AR-HCF used here primarily supports two groups of optical modes (i.e., LP_{01} and LP_{11}), and due to different overlap with the acoustic modes, the phases of the two optical modes are modulated differently by the acoustic resonances. We choose to use a modal interference method to measure the phase difference between the two optical modes. The index difference between LP_{01} and LP_{11} modes, $\Delta n = n_{01} - n_{11}$, is on the order of 1.0×10^{-3}; and the differential phase is insensitive to external disturbance due to common-path noise cancellation. Compared with the phase modulation of an individual mode, the differential phase is more robust against environment disturbance with enhanced noise rejection ratio on the order of $n_{01}/\Delta n$.

Both LP_{01} and LP_{11} modes are excited in the AR-HCF and combined at the output single-mode-fiber (SMF) to form a dual-mode optical interferometer for the probe beam. The polarization controller (PC) and optical lenses are carefully adjusted to achieve maximum fringe contrast at the interferometer output. Fig. 5.7(b) shows the transmission spectrum of the modal interferometer measured with a broadband light source and an optical spectrum analyzer. The near perfect sinusoidal interference spectrum indicates that only two spatial optical modes (i.e., LP_{01} and LP_{11}) are guided in the AR-HCF. The probe laser wavelength λ_L is then fixed at the quadrature point of an interference fringe. The probe beam is detected by a BPD to reduce the effect of intensity noise. A LIA is used to measure the harmonic signal at the modulation frequency $f = \Omega/2\pi$.

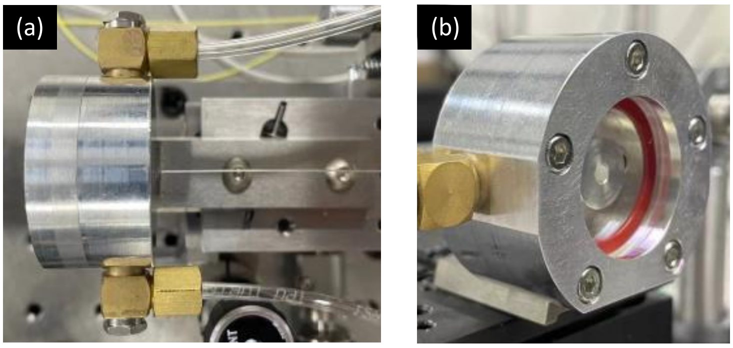

Figure 5.8. The homemade HCF gas cell.

Figure 5.8 shows the HCF gas cell used in the experiment. Different from the last gas cell shown in Fig. 4.15(b), the optical beam is coupled into the HCF via fiber collimator and optical lens as we demonstrated in Fig. 5.7(a). The HCF is inserted into a ceramic ferrule and the ferrule is embedded in the homemade gas cell. The lateral offsets for excitation and collection of light from the LP_{01} and LP_{11} modes is achieved by adjusting the 3-axis translational stages under the gas cell.

5.3.2. Phase calibration of the probe light

The phase modulation of probe is calibrated with the interferogram measured by detuning the wavelength of probe as shown in Fig. 5.9. In the experiments, $V_0 = 0.8\ V$ and $V_{DC} = 1.8\ V$. The LIA measures the RMS voltage of the small harmonic signal (V_{RMS}). Hence, the experimental phase modulation could be calibrated as

$$|\Delta\phi_{expr}| = \frac{1.4V_{RMS}}{V_0} \tag{5.21}$$

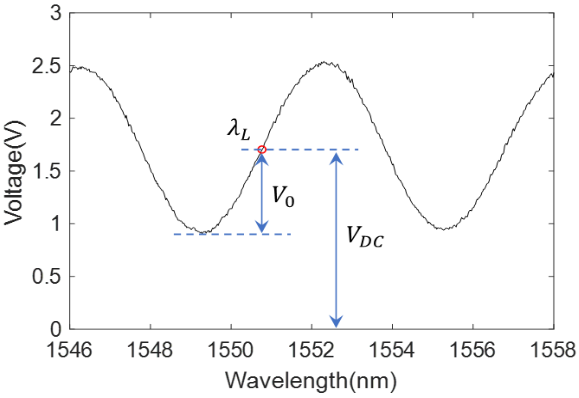

Figure 5.9. The measured interferogram of the modal interferometer. The wavelength of probe is centered at the quadrature point (red dot).

The harmonic modulated pump also generates Raman gain on the probe via the SMF pigtails. The harmonic Raman gain is detected by the LIA and then gives an equivalent background 'phase modulation'. The Raman gain with a frequency difference $\Delta\nu = \nu_P - \nu_L = 72\ cm^{-1}$ is about 0.14 of its peak value [26]

$$g_R(\Delta\nu) = 0.14 g_{R,peak} \approx 7.8 \times 10^{-15}\ m/W \tag{5.22}$$

In the experiment setup, the harmonic pump power is about $P_P = 162\ mW$. The length of SMF pigtails is about $L_{SMF} = 25\ cm$ and the effective cross-section of SMF is about $A_{eff} = 76\ \mu m^2$. The Raman gain on probe is about

$$G_R = g_R(\Delta\nu)\frac{P_P}{A_{eff}} L_{SMF} \approx 4.2 \times 10^{-6} \tag{5.23}$$

The Raman gain induced equivalent background 'phase modulation' is

$$|\Delta\phi_R| = \frac{1.4 G_R V_{DC}}{V_0} \approx 13\ \mu rad \tag{5.24}$$

Since the Raman induced background $\Delta\phi_R$ is an equivalent phase background, the total phase modulation is simply the sum of the absolute value of the Raman equivalent background 'phase modulation' $|\Delta\phi_R|$ and the phase modulation of modal interference $|\Delta\phi_{MI}|$. The experimental phase modulation $|\Delta\phi_{expr}|$ is compared with the total phase modulation

$$|\Delta\phi_{tot}| = |\Delta\phi_{MI}| + |\Delta\phi_R| \tag{5.25}$$

5.3.3. Measurement of the thermal relaxation time

Since PABS working in the frequency range of a few megahertz, as we have discussed in Chapter 2.4, the speed of heat generation limited by thermal relaxation time (τ) have considerable impact on the efficiency of generating a harmonic heat source in the megahertz regime. For C_2H_2, it is determined by the V-R/T relaxation process and is inversely proportional to gas pressure p. We measure the transient response of the thermal relaxation process by generating a pulsed pump using the AOM. As shown in Fig. 5.10, we measure the thermal relaxation processes in AR-HCF with a 10-ns optical pulse and 1% C_2H_2 in nitrogen. The rising edge in the curve yields a thermal relaxation time:

$$p\tau \approx 74\ ns \cdot atm\ (N_2\ balanced\ C_2H_2) \tag{5.26}$$

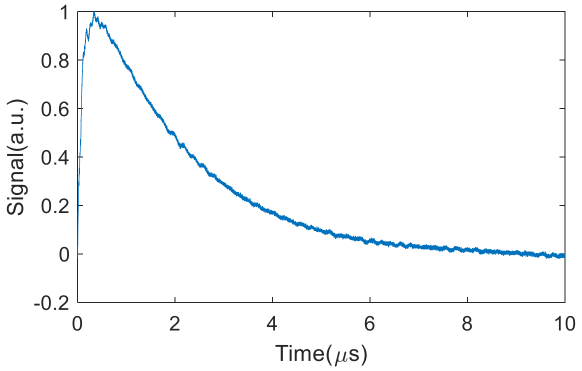

Figure 5.10. The transient response of thermal relaxation and thermal conduction in AR-HCF.

5.3.4. Basic experiments of PABS

In this section, we study the basic properties of PABS under different condition or parameters, including different pump wavelengths, probe optical modes, length of HCF, and curvature of HCF. This will be basics for further applications of PABS.

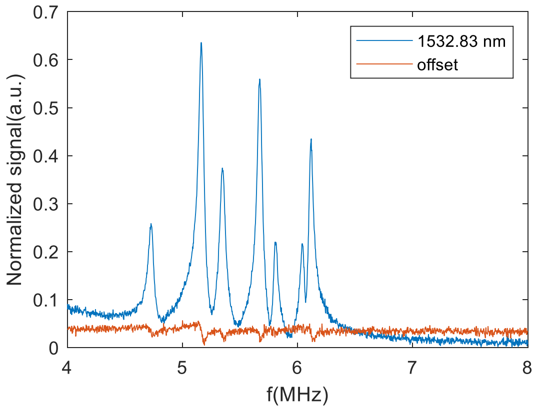

Figure 5.11. The PABS spectrum due to the photoacoustic effect and the optical force.

Figure 5.11 shows the PABS spectrum with different pump wavelengths measured with 106 ppm C_2H_2 in nitrogen. The blue curve shows the spectrum when the pump is centered at the peak of the absorption line. And the red curve shows the spectrum when the pump is detuned away from the absorption line. The residual resonances of the red curve is believed to be induced by the optical force (i.e., electrostriction, radiation pressure). Figure 5.12 shows the PABS spectrum with different LP_{11} modes of the probe light measured with 106 ppm C_2H_2 in nitrogen. The different LP_{11} modes of probe can be selectively excited and collected by adjusting the 3-axis translation stages. LP_{11a} and LP_{11b} have different distribution of electric field near the capillaries. Hence, their sensitivity on different capillary modes are not the same.

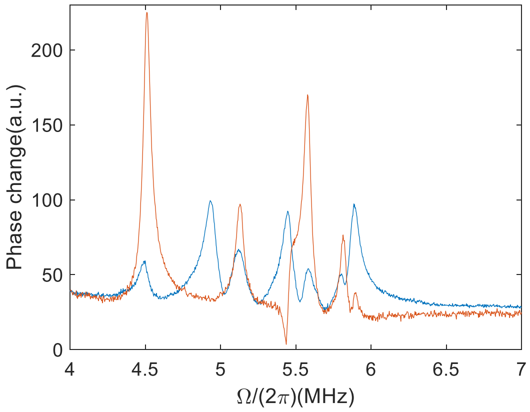

Figure 5.12. The PABS spectrum with different LP_{11} modes of the probe light.

We also do experiment with 106 ppm C_2H_2 in nitrogen to verify the influence of the fiber length and the bending radius at a pressure of 1 bar. In Fig. 5.13(a), It was revealed that the straight fiber and the curved fiber have almost the same PABS spectrum. The bending radius of the curved fiber is about 15 cm. The spikes near 1.6 MHz and 3 MHz are because of the electric instability of the LIA and the signal generator when we slowly sweep the modulation frequency. Figure 5.13(b) shows the normalized PABS spectrum with different lengths of fiber. The quality factor of the capillary mode decreases when the length of fiber increases from 0.3 m to 1.7 m. However, the quality factor is almost the same for the 1.7-m-long fiber and the 3.0-m-long fiber. From Fig. 5.13 we can know that the photothermal signal reduces quickly with increasing pump modulation frequency and becomes neglegible above 4 MHz. However, the photoacoustic signal can be much larger at some acoustic resonances, although it is still smaller than the photohermal signal at low frequencies. As we observed in the experiment, with 0.3-m-long fiber, the strongest acoustic resonances around 7 MHz is about 1/7 of the photothermal signal at 20 kHz at a pressure of 1 bar.

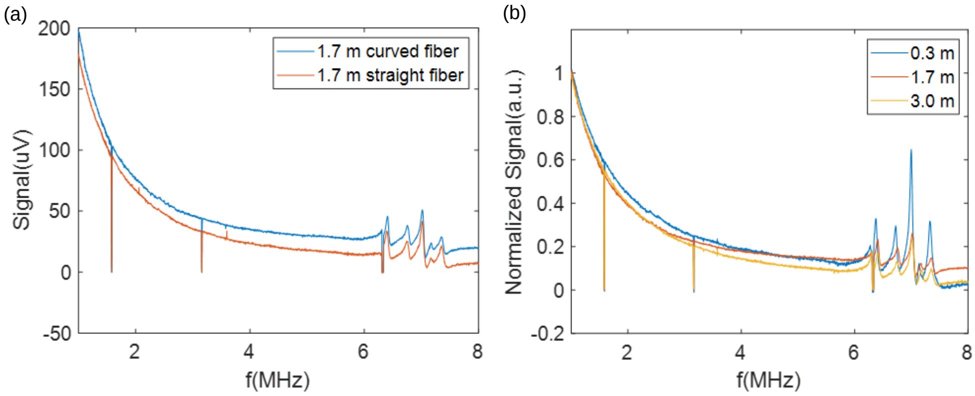

Figure 5.13. The PABS spectrum with different states of the fiber. (a) Experiment results with straight fiber and curved fiber. (b) Experiment result with different lengths of fiber.

5.3.5. Spectroscopy of the microstructure of HCFs

The highly tailorable microstructure of HCFs gives them intriguing acoustic properties. It has been a challenge to characterize the delicate microstructure of HCFs non-invasively. Recently, measurement of the capillary sizes of AR-HCFs by using whispering gallery mode spectroscopy has been reported [27]. PABS of HCFs provides an alternative method to characterize their microstructure.

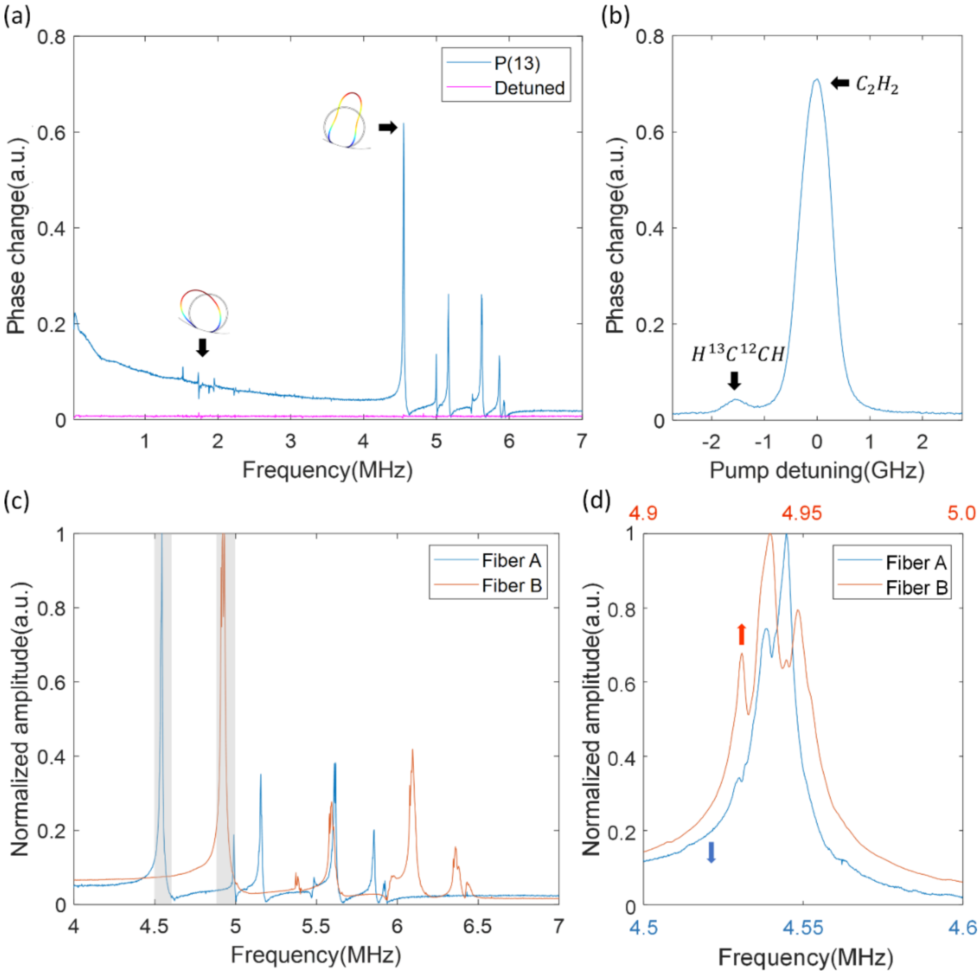

Figure 5.14. The PABS spectrums of 30-cm-long AR-HCFs filled with 10 mbar pure C_2H_2. (a) The frequency response of fiber A. The blue and red curves are measured by tuning the pump to the P(13) absorption line and away from P(13) to 1532.7 nm, respectively. (b) The absorption spectrum of C_2H_2 measured with PABS with sample A with pump modulation frequency fixed at 4.545 MHz. (c) Comparison of the frequency response of two 30-cm-long AR-HCF samples (fiber A and B). (d) A closer look of the grey regions in Fig. 5.13(c) with their frequencies shown on the bottom (blue) for fiber A and on the top (red) for fiber B, respectively.

We measured the PABS signal of a 30-cm-long AR-HCF (fiber sample A) filled with pure C_2H_2 at a pressure of 10 mbar. Figure 5.14(a) shows the probe phase modulation in the frequency range from 25 kHz to 7 MHz when the pump is tuned to the P(13) absorption line of the $\nu_1 + \nu_3$ band of acetylene (blue trace). Seven strong resonances are observed around 5 MHz, corresponding to the seven capillaries of the AR-HCF. The capillary modes are stimulated by optical absorption. Because the air damping of capillary modes is significantly reduced at low pressures, the photoacoustic signal at a few megahertz can be much larger than the photothermal signal at low frequencies as we have shown in Fig. 5.14(a). When the pump wavelength is tuned away from the absorption line, the phase modulation reduces to nearly zero (red trace). The small background signal is believed to due to stimulation of the optical force effect of the pump beam, which is about 200 times weaker than the largest PABS resonance. We also measured the gas absorption spectrum with pump modulation frequency fixed at an acoustic resonance while sweeping the pump wavelength across the P(13) absorption line of acetylene around 1532.83 nm. A Doppler limited lineshape is observed and an isotope of C_2H_2 is resolvable, as shown in Fig. 5.14(b).

For comparison, we conducted experiment with another piece of 30-cm-long AR-HCF (labeled as fiber sample B) from the same fiber drawing process. As shown in Fig. 5.14(c), the two samples show similar acoustic responses but the response for fiber B is upshifted by about 8%. The upshift is due to the scaling of the fiber structure during the drawing process. The blow-up of one of the capillary modes near 4.55 MHz and 4.95 MHz is shown in Fig. 5.14(d). The measured Q-factors of the capillary mode of samples A and B are, respectively, about 480 and 256, which is smaller than the calculated Q-factor limited by gas damping of C_2H_2 (about 940). The multi-peak spectrums are due to the inhomogeneity of the capillary along the fiber over a length of $L_{eff} = 76\,mm$, the effective absorption distance for pure acetylene at 10 mbar. For fiber A, the frequency difference between the two peaks is about $\Delta f = 6$ kHz. FEM analysis shows that such a frequency difference is equivalent to a thickness variation of $0.5\,nm$ or a diameter variation of $28\,nm$, corresponding to an inhomogeneity of 1.6%/m in the wall thickness or 2.4%/m in the capillary diameter. This value is quite close to the inhomogeneity estimated by the relative change of the resonant frequency $\Delta f/(f_c L_{eff}) = 1.7\%/m$. For fiber B, the inhomogeneity is estimated to be 2.3%/m in the wall thickness or 3.6%/m in the capillary diameter.

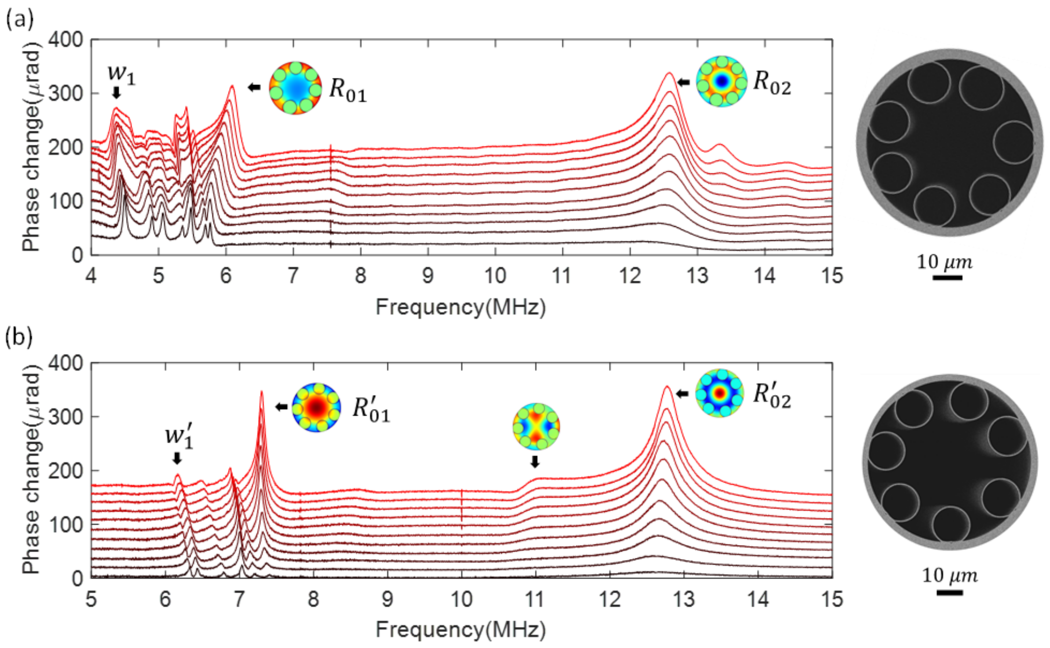

Figure 5.15. The pressure dependence of the Brillouin spectrum measured by PABS with different AR-HCFs.

As shown in Fig. 5.15, we measure the photoacoustic Brillouin spectrum of two different AR-HCFs with a gas pressure from 1 bar to 11 bar. The insets in the figure show the SEM of the AR-HCFs and their acoustic modes. The fiber is filled with 106 ppm C_2H_2 balanced with nitrogen. The phase modulation due to different acoustic mode with different gas pressures is shown in Fig 5.16. The phase modulation due to the radial air mode is almost proportional to the gas pressure. The shift of the resonances is due to the coupling between the capillary mode and the air mode.

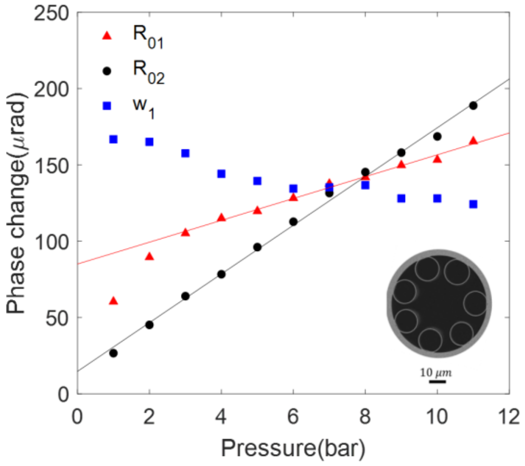

Figure 5.16. Phase modulation due to different acoustic mode with different gas pressures.

The comparison of experimental results and simulation are shown in Fig. 5.17(a). At a pressure of 11 bar, the air mode dominates and the first-order radial-like mode is observed. The frequency shift of the capillary modes is due to the coupling with the air mode. The coupling between capillary mode and the air mode gives them a complicated dependence on the gas pressure. We numerically calculate the phase modulation and the result matches well with our experiment. As shown in Fig. 5.17(b), at a pressure of 1 bar, the signal detected consists of the phase modulation induced by the shifting boundary, the gas density change, and the Raman gain of SMF pigtails. For air mode dominated situations, for example, the radial air mode (R_{01} , etc.), they are proportional to the gas pressure. The small compressibility of gas at high pressure reduces the acoustic attenuation in gas, which results in a higher amplitude of the air mode. However, the irregular silica-air boundary of AR-HCF introduces additional viscous and thermal dissipation at the boundary.

We have also performed PABS of several different HCFs and the results are shown in Fig. 5.18. For AR-HCFs in Fig. 5.18(a-c), both the capillary mode (w_1) and the air mode (R_{01} and R_{02}) are observed. Generally speaking, in AR-HCFs, the air mode is much weaker than the capillary mode due to higher acoustic loss at atmospheric condition. The capillary mode of AR-HCF could be used to characterize the relative sizes as well as the longitudinal inhomogeneity of the capillaries. For photonic bandgap (PBG) HCF in Fig. 5.18(d), only the air mode is observed.

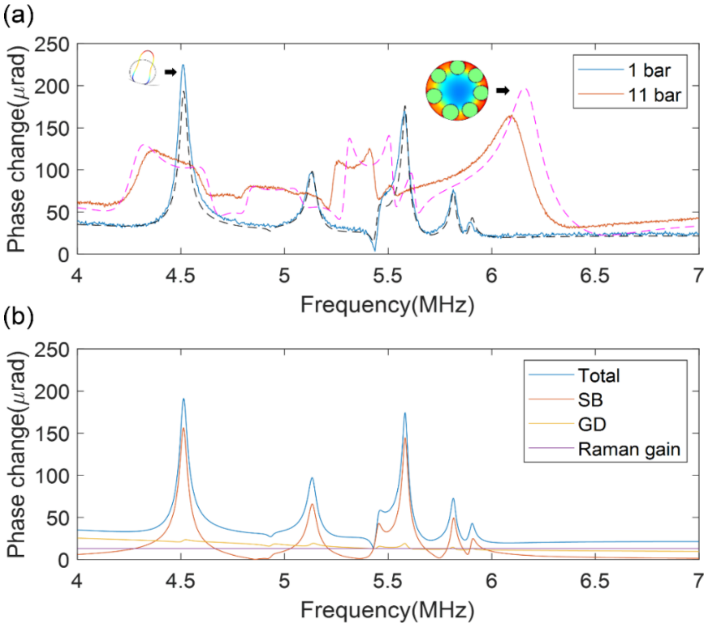

Figure 5.17. The experiment and simulation of PABS spectrum. (a) Frequency dependence of probe phase modulation for fiber sample A at the pressure of 1 bar and 11 bar. The dashed line shows the

simulation results. (b) Contribution of phase modulation due to shifting boundary (SB), gas density change (GD) and the Raman gain of SMF pigtails.

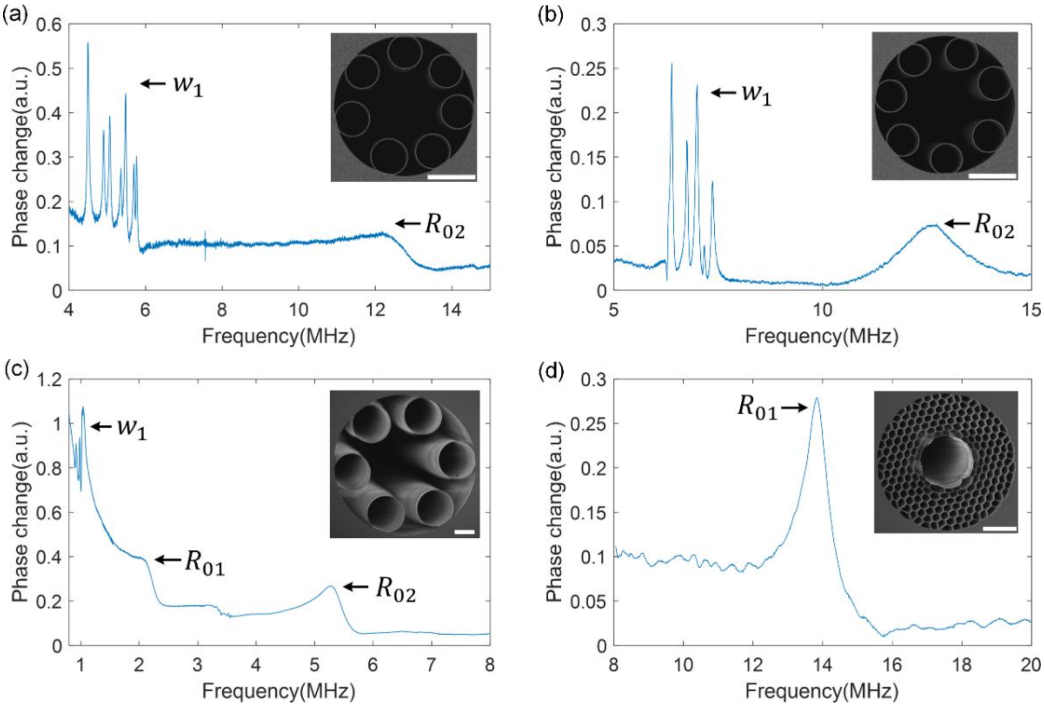

Figure 5.18. PABS of different HCFs at a pressure of 1 bar. The inset shows the SEM image of the HCF. The white bar is 20 μm. The result is measured with a pump power of 162 mW and the 30-cm-long HCFs are filled with 106 ppm C_2H_2. The PABS of PBG-HCF (Fig. 5.18(d)) is measured with a Mach-Zehnder interferometer with the PBG-HCF as one of the arms.

5.3.6. Spectroscopy of acetylene

Gas detection with PABS was performed with fiber A by employing the capillary acoustic mode at 4.51 MHz, which gives a Q-factor about 120 at the pressure of 1 bar. The differential phase modulation of the capillary mode at 1 bar is about 20% larger than that of the strongest air mode (the second-order radial mode) at 11 bar. We measure the absorption spectrum of C_2H_2 by fixing the pump modulation frequency to 4.51 MHz and slowly sweeping the wavelength of pump laser across the P(13) absorption line near 1532.83 nm. The acoustic signal is defined as the amplitude subtracted by the background as shown in Fig. 5.19(a). The background is due to the Raman gain of SMF pigtails. As shown in Fig. 5.19(a), the acoustic signal is enhanced by about 14 times when compared with the non-resonant signal at 4.3 MHz. The absorption spectrum has a Lorentzian lineshape.

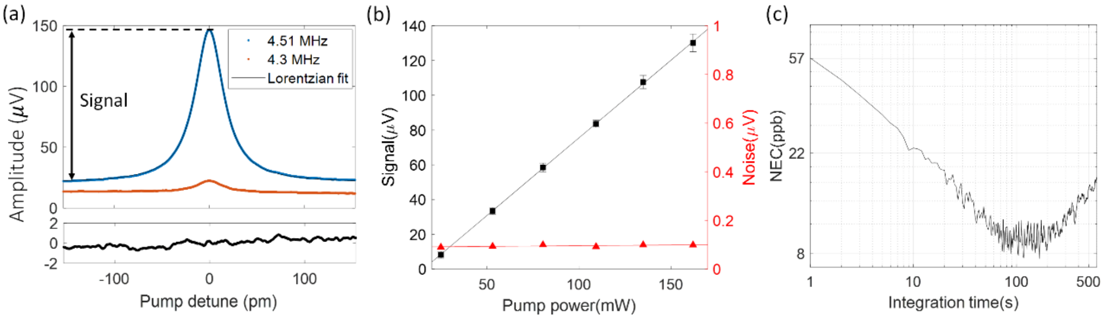

Figure 5.19. Results of gas detection experiment with fiber A filled with 106 ppm C_2H_2 balanced with nitrogen at a pressure of 1 bar. (a) The measured absorption spectrum of P(13) of C_2H_2. The blue and red curves show the spectrum at resonance and off-resonance, respectively. The blue curve can be well fitted to a Lorentzian fit and the residuals is shown as the black curve. (b) The power dependence of photoacoustic signal. The error bar for signal is enlarged for 20 times for clarity. (c) Allan deviation analysis of noise by offsetting the wavelength of pump to 1532.7 nm.

The measured photoacoustic signal is proportional to the pump power as we show in Fig. 5.19(b). The maximum amplitude is about 122 μV. The maximum phase modulation is estimated to be 214 μrad with a 162-mW pump power and 106 ppm C_2H_2, corresponding to a photoacoustic phase modulation coefficient of $k^*_{\mathrm{PA,max}} = 0.39\, rad/W$ or a photoacoustic Brillouin nonlinear coefficient of $\gamma_{\mathrm{PA,max}} = 4.4 \times 10^{-3}\ W^{-1}m^{-1}$ for 106 ppm C_2H_2. Allan analysis is performed based on the measurement data obtained over a period of 3600 second when the pump was tuned away from the absorption line to 1532.7 nm, the results are shown in Fig. 5.19(c). The noise level about 9.1 nV for an integration time of 100 s, giving a signal-noise-ratio of 13406. The noise-equivalent concentration is calculated to be 8 ppb.

5.4. Discussion about the potential of PABS

The approach of PABS we demonstrated here is very different from the traditional methods of PAS. It has unique advantages. First, compared with traditional methods, our approach allows the accumulation of acoustic signal simultaneously in an acoustic mode and along the fiber length. The total acoustic signal is proportional to the Q-factor of acoustic mode and the length of fiber. Second, the detection of differential phase modulation reduces the noise level of PAS and makes it more robust against environmental perturbations. In addition, using a light beam propagating in the same HCF as an acoustic probe avoids the use of an additional microphone, which intrinsically minimizes the disturbance of microphone on the acoustic mode. HCFs may be conveniently integrated into standard fiber-based systems for cost-effective sensors and instrument with compact size and remote detection capability.

Different probe optical mode has different phase sensitivity to the acoustic mode. For the AR-HCF we used, the phases of the high-order modes are more sensitive to the capillary mode since the optical field is stronger in the vicinity of silica-gas boundary. The maximum displacement of the capillary mode w_1 is about $\delta = 2.9\ pm$, corresponding to a sensitivity to the deflection about $|\partial n_{11b}/\partial\delta| \approx 41\ m^{-1}$ for the most sensitive LP_{11b} mode. From another perspective, increasing the sensitivity of probe on acoustic mode is actually equivalent to maximizing the work done by its optical force during an acoustic period. The sensitivity can be enhanced by optimizing the waveguide structure. For example, the parallel evanescent-field-bonding waveguides [28-30] could increase the sensitivity on the acoustic mode significantly. A sensitivity of $\left|\partial n_{eff}/\partial\delta\right| = 64 \times 10^3\ m^{-1}$ has been demonstrated on a dual-nanoweb fiber [30]. In our experiment, the AR-HCF is not designed for high-Q acoustic performance. A well-designed wine-glass mode of silica capillary could reach a Q-factor of a few thousands at atmospheric condition [31] and could be even higher at lower pressures. The length of AR-HCF can also be at least 100 times longer providing that the inhomogeneity is not a problem. A potential enhancement of the PABS signal by several orders of magnitude is possible at atmospheric condition.

The ultimate Q-factor of capillary mode of HCFs might be limited by the surface roughness from the frozen surface capillary wave during the fiber fabrication [32]. In our experiment, the estimated maximum displacement of the capillary is about a few picometers, which is much smaller than the rms surface roughness (about 0.1 nm [33]). By using a short length of AR-HCF or AR-HCF with very good homogeneity, it might be possible to characterize the surface roughness of HCFs, which accounts for an important optical loss mechanism of them. Furthermore, the concept of PAS we demonstrated is not limited to HCFs. It could be applied on other platforms such as opto-mechano-fluidic resonator [34], dual-nano web fiber [30], integrated photonic circuit [29].

Here we show some simulation results with the dual-nano web-like fibers made of silica. The geometry of the fiber [30] and one of acoustic mode it supported are shown in Fig. 5.20. The eigenfrequency is 5.07 + 0.0033 MHz, giving a quality factor of about 760. The quality factor is several times higher than the that of a capillary mode of AR-HCF. The length of the nano-web is about 22 μm and the thicknesses of the two nano-web are about 400 nm and 420 nm, respectively. The center of the web is slightly thicker to confining the optical mode. For a structure like this, the main origin the acoustic loss is the squeezed film effect. In other words, the viscous and thermal acoustic losses in the thin air film. The thickness of the two nanowebs are designed to be different to avoid the strong squeezed film effect when the two webs are resonant at the same frequency. Here we show the asymmetric first-order in-plane bending mode in Fig. 5.20.

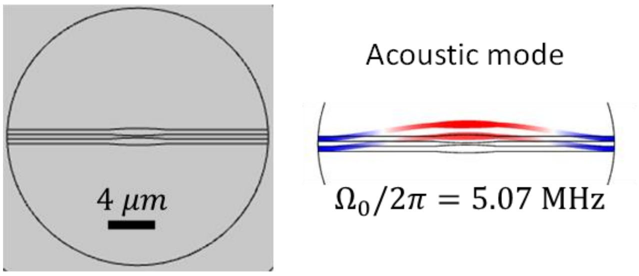

Figure 5.20. The geometry of the dual-nano web-like fibers and its acoustic mode.

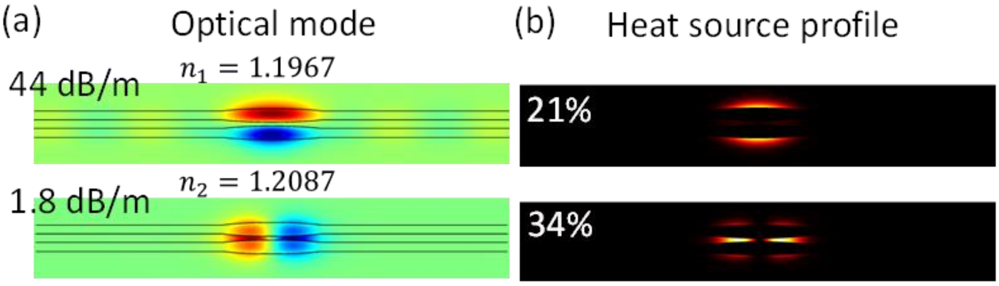

Figure 5.21. The optical mode and the heat source of dual nanoweb fiber.

The optical modes supported by the fiber the corresponding heat source are shown in Fig. 5.21. Figure 5.21(a) shows two optical modes supported by the fiber: the first-order symmetric mode ($n_1 = 1.1967$) and the first-order asymmetric mode ($n_2 = 1.2087$). The optical losses of the two modes are about 44 dB/m and 1.8 dB/m. Since the optical mode propagates in the silica, only the evanescent field of it can interact with the gas molecules. Figure 5.21(b) shows the heat source. For the symmetric optical mode, the heat source is mainly in the outer side of the webs. Hence, the acoustic wave in the air tends to push or drag the web from the outer side. For the asymmetric optical mode, the acoustic wave tends to push or drag from the inner side.

For simplicity, we ignore the optical force (i.e., electrostriction or radiation pressure) in the simulation. In the experiment, the effect of optical force might be reduced by using wavelength modulation technique because the intensity of light is not changed by the modulation. The simulation only consider the optical absorption of acetylene. Figure 5.22 shows the phase modulation near the resonance with different combinations of pump optical mode and probe optical mode. The sensitivity on acoustic mode of this dual nanoweb fiber is about $\left|\partial n_{eff}/\partial \delta\right| = 3.2 \times 10^4\ m^{-1}$, which is nearly 3 orders of magnitude larger than that in the AR-HCF. The phase modulation per unit length due to photoacoustic effect is about 100 times larger than that in the AR-HCF. The maximum displacement δ_{max} of the nanoweb is about 0.5 pm in the nanoweb fiber, which is smaller when compared with the displacement of 2.9 pm in the AR-HCF. This is because of two reasons: first, the proportion of light in the gas is smaller in nanoweb fiber. For example, as we shown in Fig. 5.21(b), the proportion of light in the gas is about 21% and 34% for the two optical modes, respectively. For AR-HCF, this number is almost 100%. Second, the net force applied on the nanoweb by photoacoustic effect is very small due to the symmetric intensity field of pump light.

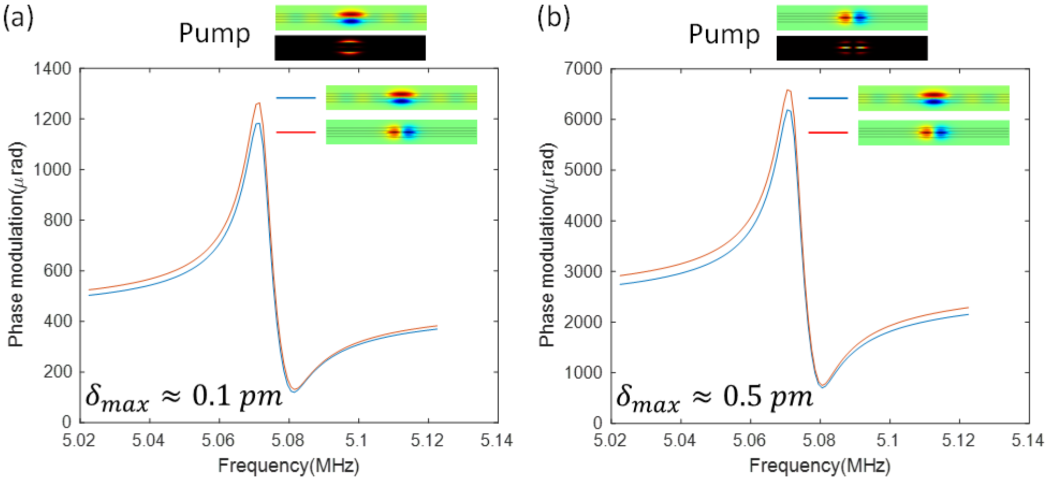

Figure 5.22. The simulation of phase modulation with dual nanoweb fiber. Parameters are: $P_P = 160\ mW, C = 106\ ppm\ C_2H_2, L = 0.1\ m, \lambda_L = 1550\ nm$ *at 1 atm.*

To increase the displacement of nanoweb, we designed a new type of fiber for PABS application. The principle of design follows three reasons: first, separation of the pump and probe light to avoid nonlinear interaction between the strong pump field and the weak probe field; second, introducing an asymmetric force by photoacoustic effect on the nanoweb; third, considering the thermal relaxation of excited molecules, the resonant frequency of acoustic mode should be in the megahertz range or even lower. Figure 5.23 shows the structure of a designed nanoweb fiber for PABS. It supports an acoustic mode with eigenfrequency of 2.615 + 0.0095 MHz, giving a quality factor of 138. The fiber consists of two air-cores with a diameter of 160 μm and a dual nanoweb which is the same as the nanoweb we shown in Fig. 5.20. An air-core of 160 μm can support optical mode in the air with acceptable loss. The pump light can propagate in one of the air core or in both the air-cores with a π-phase shift.

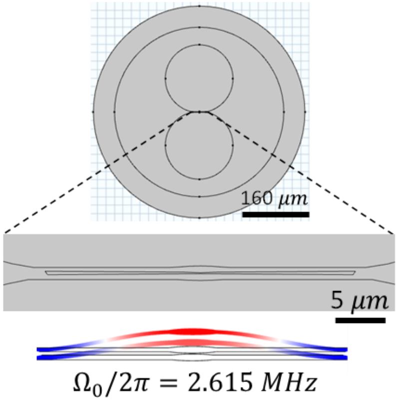

Figure 5.23. The geometry of a designed nanoweb fiber for PABS.

The pump field and the corresponding heat source in the air-core is shown in Fig. 5.24. It excites an acoustic mode in the air. Due to the vibroacoustic coupling, the nanoweb will also vibrate at the same frequency as we shown in the enlarged picture. By using a structure like this, the displacement of the nanoweb will be much larger than it in the dual nanoweb fiber.

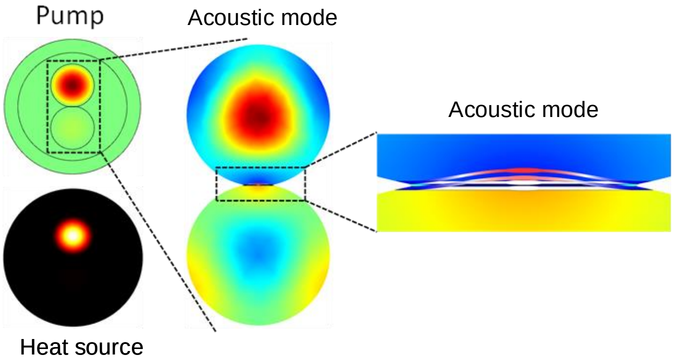

Figure 5.24. The pump field, heat source and the acoustic mode.

The simulation of phase modulation is shown in Fig. 5.25. With the same parameters we used in Fig. 5.22, the phase modulation is about 0.3 rad, which is about 4800 times than the phase modulation of PABS we demonstrated in the experiment. The maximum displacement is about 16 pm. However, the quality factor of the acoustic mode is only about 138 and is smaller than that of the dual nanoweb fiber in Fig. 5.20. Further simulation might be performed to optimize the acoustic loss. If we considering a shot-noise-limited noise of 200-μW probe of about 45 $nrad/\sqrt{Hz}$, the shot-noise-limited sensitivity with 1-s constant of LIA would be 4 ppt C_2H_2.

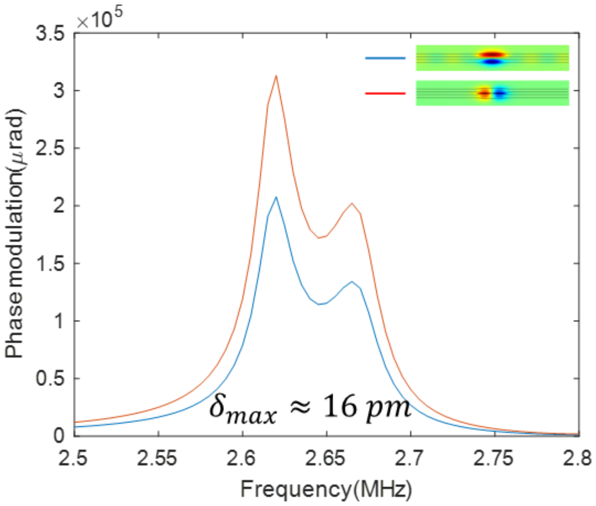

Figure 5.25. The simulation of phase modulation with designed dual nanoweb fiber. Parameters are: $P_P = 160\ mW, C = 106\ ppm\ C_2H_2, L = 0.1\ m, \lambda_L = 1550\ nm$ *at 1 atm.*

In short, we discuss the potential of PABS for gas sensing and fiber characterization. Simulation shows the phase modulation due to photoacoustic effect can be enhanced by several orders of magnitude in these fibers. A preliminary simulation shows the phase modulation of PABS can be 4800 times larger and the shot-noise-limit sensitivity of ppt level could be realized. However, the process of fiber drawing is complicated and difficult. Sometimes, the designed structure cannot be realized in practice. The design of fiber structure must consider the practical fiber drawing process. Further development of PABS might need cooperation with experts in the field of making HCFs.

5.5. Conclusion

We demonstrated PABS of gas-filled HCFs. A study of the acoustic resonances of AR-HCFs reveals its delicate microstructures and allows characterization of inhomogeneity along the fiber. Experiment with fiber samples from the same fiber drawing process reveals longitudinal inhomogeneity of a few percent per meter along the fiber. By employing a wine-glass-like acoustic mode of the silica capillary, we demonstrate a PABS for gas sensing with a sensitivity of 8-ppb C_2H_2. Different from PTS, PABS measures the phase modulation in the frequency of megahertz range. Gas sensors working at a higher frequency may be less affected by the noises such as the intensity noise and phase noise of laser, and the '1/f' noise. The new approach we demonstrated in this Chapter provides a method to further increase the signal amplitude of HCF gas sensing. Numerical simulations show that the shot-noise-limit sensitivity of PABS can be enhanced to ppt level with a well-designed optical fiber.

Reference of Chapter 5

1. Harren, F. J., & Cristescu, S. M. (2006). Photoacoustic spectroscopy in trace gas monitoring. *Encyclopedia of Analytical Chemistry: Applications, Theory and Instrumentation*, 1-29.

2. West, G. A., Barrett, J. J., Siebert, D. R., & Reddy, K. V. (1983). Photoacoustic spectroscopy. *Review of Scientific Instruments*, *54*(7), 797-817.

3. Kosterev, A. A., Bakhirkin, Y. A., Curl, R. F., & Tittel, F. K. (2002). Quartz-enhanced photoacoustic spectroscopy. *Optics Letters*, *27*(21), 1902-1904.

4. Koskinen, V., Fonsen, J., Roth, K., & Kauppinen, J. (2008). Progress in cantilever enhanced photoacoustic spectroscopy. *Vibrational spectroscopy*, *48*(1), 16-21.

5. Wang, Q., Wang, J., Li, L., & Yu, Q. (2011). An all-optical photoacoustic spectrometer for trace gas detection. *Sensors and Actuators B: Chemical*, *153*(1), 214-218.

6. Miklós, A., Hess, P., & Bozóki, Z. (2001). Application of acoustic resonators in photoacoustic trace gas analysis and metrology. *Review of scientific instruments*, *72*(4), 1937-1955.

7. Bernegger, S., & Sigrist, M. W. (1990). CO-laser photoacoustic spectroscopy of gases and vapours for trace gas analysis. *Infrared Physics*, *30*(5), 375-429.

8. Lintel Hekkert, S. T., Staal, M. J., M Nabben, R. H., Zuckermann, H., Persijn, S., Stal, L. J., ... & Parker, D. H. (1998). Laser photoacoustic trace gas detection, an extremely sensitive technique applied in biological research. *Instrumentation science & technology*, *26*(2-3), 157-175.

9. Dong, L., Kosterev, A. A., Thomazy, D., & Tittel, F. K. (2010). QEPAS spectrophones: design, optimization, and performance. *Applied Physics B*, *100*(3), 627-635.

10. Spagnolo, V., Patimisco, P., Borri, S., Scamarcio, G., Bernacki, B. E., & Kriesel, J. (2012). Part-per-trillion level SF 6 detection using a quartz enhanced photoacoustic spectroscopy-based sensor with single-mode fiber-coupled quantum cascade laser excitation. *Optics Letters*, *37*(21), 4461-4463.

11. Tomberg, T., Vainio, M., Hieta, T., & Halonen, L. (2018). Sub-parts-per-trillion level sensitivity in trace gas detection by cantilever-enhanced photo-acoustic spectroscopy. *Scientific Reports*, *8*(1), 1-7.

12. Renninger, W. H., Shin, H., Behunin, R. O., Kharel, P., Kittlaus, E. A., & Rakich, P. T. (2016). Forward Brillouin scattering in hollow-core photonic bandgap fibers. *New Journal of Physics*, *18*(2), 025008.

13. Renninger, W. H., Behunin, R. O., & Rakich, P. T. (2016). Guided-wave Brillouin scattering in air. *Optica*, *3*(12), 1316-1319.

14. Iyer, A., Xu, W., Antonio-Lopez, J. E., Correa, R. A., & Renninger, W. H. (2020). Ultra-low Brillouin scattering in anti-resonant hollow-core fibers. *APL Photonics*, *5*(9), 096109.

15. Yang, F., Gyger, F., & Thévenaz, L. (2020). Intense Brillouin amplification in gas using hollow-core waveguides. *Nature Photonics*, *14*(11), 700-708.

16. Han, J., Freel, K., & Heaven, M. C. (2011). Rotational and vibrational energy transfer in vibrationally excited acetylene at energies near 6560 cm^{-1}. *The Journal of Chemical Physics*, *135*(24), 244304.

17. Couny, F., Carraz, O., & Benabid, F. (2009). Control of transient regime of stimulated Raman scattering using hollow-core PCF. *JOSA B*, *26*(6), 1209-1215.

18. Hirschfelder, J. O., Curtiss, C. F., Bird, R. B., & Mayer, M. G. (1964). *Molecular theory of gases and liquids* (Vol. 165). New York: Wiley.

19. Mason, W. P. (Ed.). (2012). *Physical Acoustics V14: Principles and Methods* (Vol. 14). Elsevier.

20. Dowell, E. H., Gorman Iii, G. F., & Smith, D. A. (1977). Acoustoelasticity: General theory, acoustic natural modes and forced response to sinusoidal excitation, including comparisons with experiment. *Journal of Sound and vibration*, *52*(4), 519-542.

21. Lemmon, E. W., & Jacobsen, R. T. (2004). Viscosity and thermal conductivity equations for nitrogen, oxygen, argon, and air. *International journal of thermophysics*, *25*(1), 21-69.

22. Dukhin, A. S., & Goetz, P. J. (2009). Bulk viscosity and compressibility measurement using acoustic spectroscopy. *The Journal of chemical physics*, *130*(12), 124519.

23. Gu, Z., & Ubachs, W. (2013). Temperature-dependent bulk viscosity of nitrogen gas determined from spontaneous Rayleigh–Brillouin scattering. *Optics Letters*, *38*(7), 1110-1112.

24. Cramer, M. S. (2012). Numerical estimates for the bulk viscosity of ideal gases. *Physics of Fluids*, *24*(6), 066102.

25. Royer, D., & Dieulesaint, E. (1999). *Elastic waves in solids II: generation, acousto-optic interaction, applications*. Springer Science & Business Media.

26. Stolen, R. H., Gordon, J. P., Tomlinson, W. J., & Haus, H. A. (1989). Raman response function of silica-core fibers. *JOSA B*, *6*(6), 1159-1166.

27. Frosz, M. H., Pennetta, R., Enders, M. T., Ahmed, G., & Russell, P. S. J. (2019). Non-invasive real-time characterization of hollow-core photonic crystal fibers using whispering gallery mode spectroscopy. *Optics Express*, *27*(21), 30842-30851.

28. Povinelli, M. L., Lončar, M., Ibanescu, M., Smythe, E. J., Johnson, S. G., Capasso, F., & Joannopoulos, J. D. (2005). Evanescent-wave bonding between optical waveguides. *Optics Letters*, *30*(22), 3042-3044.

29. Li, M., Pernice, W. H. P., Xiong, C., Baehr-Jones, T., Hochberg, M., & Tang, H. X. (2008). Harnessing optical forces in integrated photonic circuits. *Nature*, *456*(7221), 480-484.

30. Butsch, A., Koehler, J. R., Noskov, R. E., & Russell, P. S. J. (2014). CW-pumped single-pass frequency comb generation by resonant optomechanical nonlinearity in dual-nanoweb fiber. *Optica*, *1*(3), 158-164.

31. Pan, Y., Wang, D., Wang, Y., Liu, J., Wu, S., Qu, T., ... & Luo, H. (2016). Monolithic cylindrical fused silica resonators with high Q factors. *Sensors*, *16*(8), 1185.

32. Jackle, J., & Kawasaki, K. (1995). Intrinsic roughness of glass surfaces. *Journal of Physics: Condensed Matter*, *7*(23), 4351.

33. Roberts, P. J., Couny, F., Sabert, H., Mangan, B. J., Williams, D. P., Farr, L., ... & Russell, P. S. J. (2005). Ultimate low loss of hollow-core photonic crystal fibers. *Optics Express*, *13*(1), 236-244.

34. Han, K., Kim, J., & Bahl, G. (2016). High-throughput sensing of freely flowing particles with optomechanofluidics. *Optica*, *3*(6), 585-591.

Chapter 6 Raman spectroscopy of hydrogen with HCFs

In this chapter, we present two high sensitivity techniques for the detection of Raman active gases. They are SRG spectroscopy and Raman PTS (RPTS). For SRG spectroscopy, high sensitivity hydrogen sensing based on forward SRG as well as distributed hydrogen sensing based on backward SRG are implemented with PBG-HCFs. For RPTS, the basic theory are formulated, experimental demonstration of hydrogen detection with AR-HCFs are conducted, potential for further sensitivity enhancement is also discussed.

6.1. SRG spectroscopy of hydrogen

For a chemical bond that absorbs IR light, the vibration of the bond should change the dipole moment of the molecule near its equilibrium position. However, for diatomic molecules, there is no permanent dipole because of the symmetry of the electron distribution. And the vibrational modes of diatomic molecules are not IR active. Hence, for molecules like hydrogen, oxygen, and nitrogen, Raman spectroscopy are often used. Raman scattering is much weaker than the IR absorption, which results in reduced sensitivity of gas detection. We use hydrogen detection as an example. Hydrogen is a useful but dangerous gas with low ignition energy and a wide explosion range. It leaks out easily due to the smallest molecule size. Detection of hydrogen sensitively and selectively is important and in urgent need for safety and other applications.

The strength of Raman scattering is proportional to the intensity of the optical field that interacts with hydrogen. Hence, it benefits greatly from HCFs. The long interaction length, small beam size and hence the higher optical intensity, as well as nearly 100% overlap between optical field and gas sample, make HCF an excellent platform for Raman scattering [5]. Recently, HCF-based Raman gas sensors have been reported [6-11]. For example, Buric et al. demonstrated a Raman gas sensor of O_2, N_2, CH_4, and C_2H_6 based on spontaneous Raman scattering [7]. Doménech et al. demonstrated a Raman gas sensor of CO_2 based on SRG spectroscopy [11]. Compared with free-space system, the sensitivity of the HCF-based sensors can be two to three orders of magnitude higher.

6.1.1. Principle of SRG spectroscopy with HCFs

SRS is a third-order nonlinear process involving a pump photon, a down-shifted Stokes photon and a specific vibrational or rotational mode of molecules. By propagating a pump and a probe beam in a medium and matching their frequency difference to a molecular vibrational or rotational transition frequency of the medium, the intensity of the probe experiences a gain (SRG) and the intensity of the pump experiences a loss (stimulated Raman loss, SRL). This pump and probe detection scheme is often termed the seeded SRS. Usually, the SRL of the pump can be ignored and we recall the steady state Raman gain equation. Under the assumption that the Raman gain is much smaller than 1 ($\Delta I_S \ll I_S$), we have:

$$\frac{\Delta I_S}{I_S} = g_R I_P L \tag{6.1}$$

The SRG of Stokes light can be used to measure the Raman gain coefficient, or in other words, the concentration of hydrogen in the buffer gas. A special attention need to be paid on the Raman gain factor g_R. The Raman gain factor is inversely proportional to the Raman linewidth, and it can be expressed as

$$g_R \propto \frac{C}{\Gamma} \tag{6.2}$$

$$\Gamma = \gamma_{air}(1 - C) + \gamma_{self} C \tag{6.3}$$

where C is the concentration of hydrogen in a buffer gas of nitrogen, Γ the Raman linewidth, γ_{air} and γ_{self} are the air-broadening linewidth and self-broadening linewidth. For gas tracing applications, $C \ll 1$, Equation (6.2) can be simplified as

$$g_R \propto \frac{C}{\gamma_{air}} \tag{6.4}$$

Generally speaking, the foreign gas broadening coefficient of nitrogen is larger than the self-broadening coefficient [12]. Hence, the normalized Raman gain coefficient of nitrogen balanced hydrogen will be smaller than that of pure hydrogen. For example, in our experiment, for the $Q_1(1)$ transition of hydrogen at a pressure of 6 bar, the modulation depth to reach a maximum 2-nd harmonic coefficient for 1% H_2 with N_2 is about 2.6 times of that for pure H_2. This indicates the nitrogen-broadening linewidth is about 2.6 times of the self-broadening linewidth.

In this section, we study the SRG spectroscopy with HCFs. A PBG-HCF (HC-1550-06 from NKT Photonics) is used for hydrogen sensing. As shown in Fig. 6.1, the transmission spectrum of PBG-HCF is usually narrow. Hence, only the rotational transition of hydrogen can be used for sensing.

We employ the Raman transition $S_0(0)$ between rotational level J = 0 and J = 2 of hydrogen molecule. When the frequency difference between the pump and probe matches the rotational Raman shift $\Omega = 354.36\ cm^{-1}$, the intensity variation of the probe (Stokes) beam may be expressed as $\Delta I_S \propto g_R I_S I_P \propto I_S I_P \Delta N_{fi}/\Gamma$ in the steady state. Γ is the Raman linewidth and ΔN_{fi} is the number density difference of hydrogen molecules between J = 0 and J = 2. ΔN is proportional to the hydrogen concentration, which can be recovered by detecting ΔI_S.

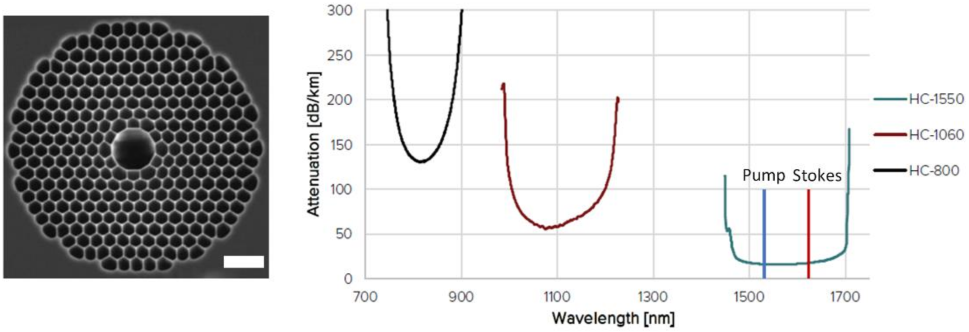

Figure 6.1. HC-1550-06 fiber used for hydrogen sensing. The inset shows the SEM of the fiber. The transmission spectrum is from [13].

The Raman gain factor of hydrogen is polarization dependent. It takes the maximum value when co-propagating pump and probe beams have opposite circular polarizations. The Raman gain coefficient of $S_0(0)$ transition can be expressed by [14]

$$g_R = \frac{8}{5}\frac{\pi^2\omega_S}{c^2 n_S^2}\frac{(J+1)(J+2)}{(2J+1)(2J+3)}\frac{\gamma_{00}^2}{h\Gamma}\Delta N_{fi} \tag{6.5}$$

where n_S is the RI at the Stokes frequency ω_S, and is approximately 1 in HCF. γ_{00} is the off-diagonal element of the anisotropic polarizability [15]. In the PBG-HCF, the pump could travel in the same direction as the probe (forward SRS), or in the opposite direction (backward SRS). The Raman linewidth Γ of the backward SRS is larger due to Doppler broadening [16], resulting in a smaller backward Raman gain factor. However, the forward SRS could not provide the location information needed for distributed sensing. Here, we demonstrate an all-fiber point hydrogen sensor based on forward SRS and a distributed hydrogen sensor based on backward SRS.

The linewidth shows collisional broadening and narrowing (also known as Dicke narrowing [17]) as expected. The backward Raman linewidth of $S_0(0)$ transition of pure hydrogen is 1080 MHz at 1 atm [18]. By use of Eq. (6.5), the forward and backward Raman gain factors were calculated to be 0.1 cm/GW and 4.5 cm/TW, respectively. If we consider the polarization scrambled pump as a natural incident pump light, the Raman gain factor would be 0.059 cm/GW and 2.6 cm/TW, respectively.

6.1.2. Hydrogen sensing with forward SRS

Figure 6.2(a) shows the experiment setup of the point hydrogen sensor. A DFB semiconductor pump laser was modulated by a current controller (CC) at 38.8 kHz and its wavelength was tuned by a temperature controller (TC) around 1531.867 nm. The pump laser is amplified by an EDFA. A optical circulator (OC) and a fiber Bragg grating (FBG) is used to filter out the ASE from EDFA. An ECDL was used as the probe (Stokes) beam with its wavelength fixed to 1619.795 nm. An isolator (ISO) is used to protect the probe laser from the reflection when coupling the laser into the PBG-HCF. The polarization of pump and Stokes are adjusted by two PCs to maximize the Raman gain of hydrogen. The pump and Stokes are combined with a WDM. The differential frequency between the pump and probe beams matches the $S_0(0)$ rotational transition band of hydrogen molecule at atmosphere pressure (354.36 cm^{-1}). WMS with second harmonic lock-in detection was used. The pump and probe (Stokes) beams are co-propagating into PBG-HCF. The pump laser at the output of PBG-HCF is filter out by a pump filter (PF). The PF is a Fabry-Perot type optical filter with a bandwidth of 0.8 nm and an extinction ratio larger than 50 dB. The residual probe laser is detected with a PD. The Raman gain signal is then retrieved by a LIA and a waveform digitizer is used as DAQ.

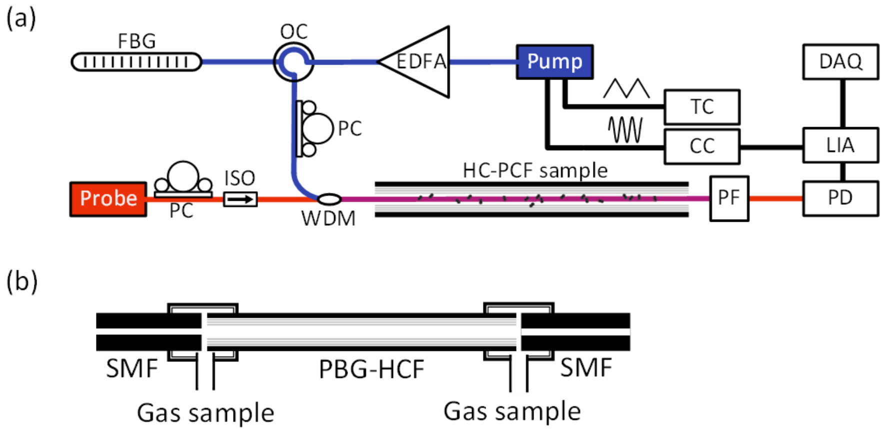

Figure 6.2. The experiment setup of point fiber hydrogen sensor. (a) The experiment setup for hydrogen detection. (b) The configuration of PBG-HCF gas cell.

A 15-m-long PBG-HCF gas cell is used for point hydrogen sensing as shown in Fig. 6.2(b). PBG-HCF samples were fabricated by butt coupling PBG-HCF to standard SMFs (SMFs). The method of butt coupling has been described previously in Fig. 4.15(b). Different from the previous gas cell, there is no lateral offset between SMFs and PBG-HCF and the typical loss the PBG-HCF gas cell is about 6 dB.

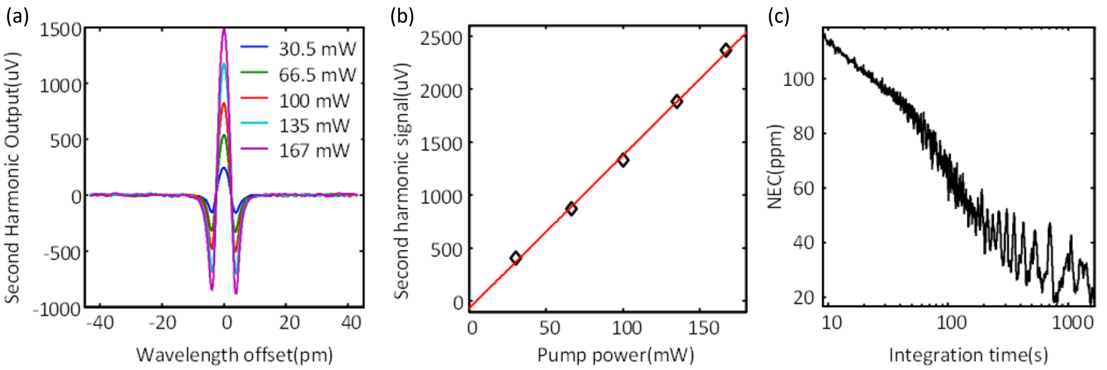

Figure 6.3. Performance of the point hydrogen sensor with a 15-m-long PBG-HCF gas cell. (a) Second-harmonic lock-in output for different pump power levels when the pump wavelength is scanned around 1531.876 nm. The gas concentration used is 4% hydrogen in volume balanced by nitrogen. (b) The peak-to-peak amplitude of the second-harmonic signal as a function of pump power level. (c) NEC as a function of integration time.

Figure 6.3(a) shows the second-harmonic lock-in outputs for different pump power levels delivered to the PBG-HCF. The PBG-HCF was filled with 4% hydrogen in volume balanced by nitrogen. Figure 6.3(b) shows that the peak-to-peak amplitude of the second-harmonic signal is proportional to the pump power delivered to the PBG-HCF. For the pump power of 167 mW, the peak-to-peak amplitude of the second-harmonic signal is 2.37 mV. The standard deviation of noise over a 1000 second period recorded with 1-s lock-in time constant is 7.5 μV, giving a SNR of 316. The noise equivalent hydrogen concentration with different integration time is shown in Fig. 6.3(c). With ~760 second integration time, the NEC is 20 ppm.

6.1.3. Distributed hydrogen sensing with backward SRS

Experiment setup

Figures. 6.4(a) and (b) show the basic principle an all-fiber distributed hydrogen sensor based on backward SRS. The distributed information of hydrogen is obtained by the SRG of probe due to pulsed pump laser at different times. The narrow Raman gain spectrum of $S_0(0)$ transition of hydrogen lies within the wider Raman gain spectrum of fused silica, as shown in Fig. 6.4(c). The Raman gain of the silica SMF pigtails could act as markers to identify the beginning and ending of the PBG-HCF sensing region. The experiment setup for distributed hydrogen sensing is shown in Fig. 6.5. A DFB semiconductor laser was used as the pump laser and an ECDL was used as the probe laser. We use a polarization scrambler (PS) to eliminate the polarization fading effect since SRS is polarization dependent. The pump pulse is generated by using optical intensity modulator (IM) and is further amplified by an EDFA.

Different IMs were used in different experiments. We use an AOM as the IM to generate the 18-ns pump pulses and an electro-optic intensity modulator (EOM) as the IM to generate 1-ns and 2-ns pump pulses. An optical filter centered at the pump wavelength filters out the ASE of EDFA. A PF is a tunable optical filter with a bandwidth of 0.8 nm, which is used before photo-detection to filter out the residual pump light. The time trace of the SRG signal is recorded and averaged with an oscilloscope.

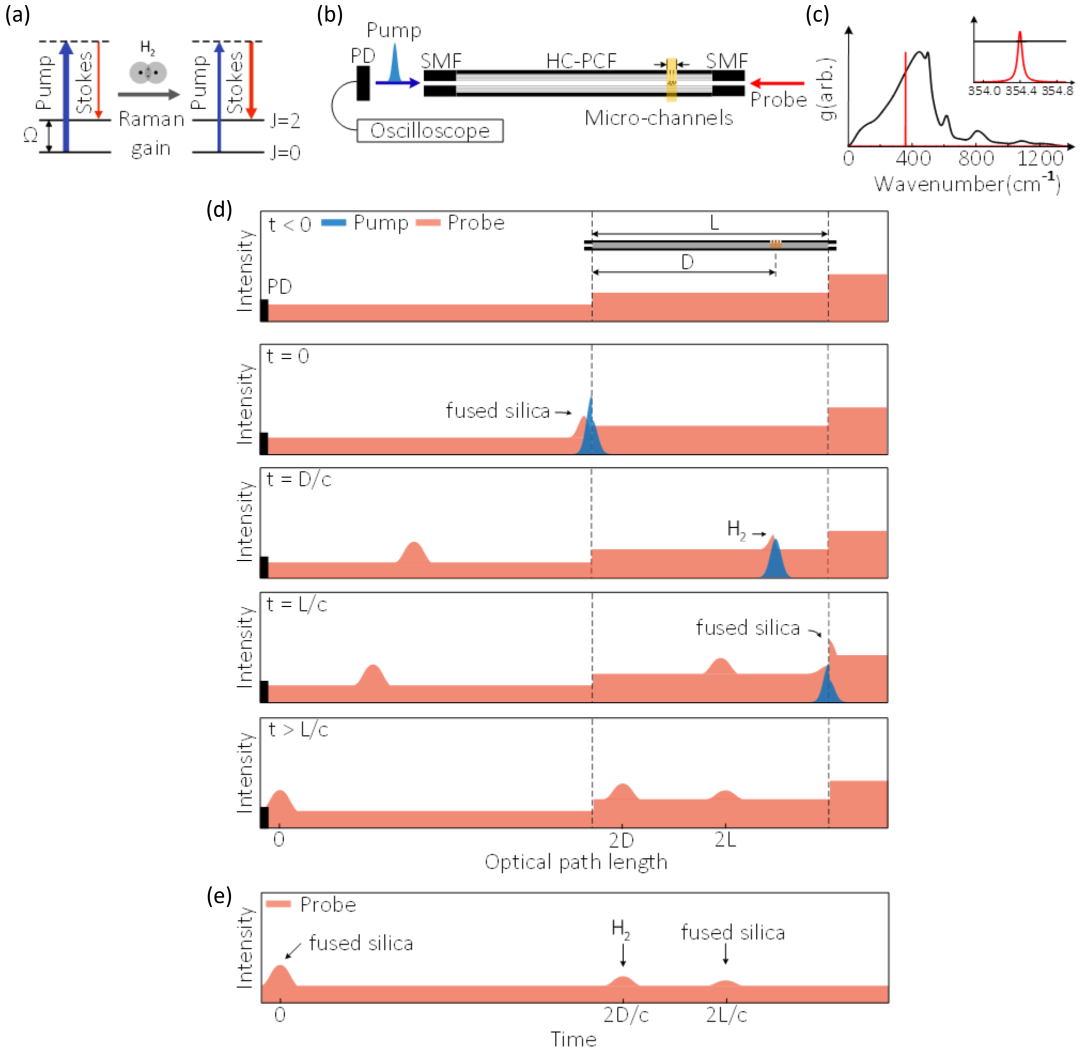

Figure 6.4. Distributed hydrogen sensing with backward SRS in a PBG-HCF. (a) The energy level diagram of $S_0(0)$ transition of hydrogen. (b) Basic setup for distributed hydrogen detection. (c) The backward Raman gain spectrum of $S_0(0)$ transition of hydrogen and fused silica [20]. The inset shows an enlarged view around the $S_0(0)$ transition of hydrogen. (d) Schema showing the principle of distributed hydrogen sensing. (e) SRG signal detected by PD in the time domain.

Raman transition $S_0(0)$ is communication band compatible with the pump located in C band and the Stokes located in L band. We here use a pump around 1532 nm and a probe around

1620 nm, both wavelengths are within the low loss transmission window of the HC-1550-06 fiber (with loss < 30 dB/km from 1490 to 1680 nm). As illustrated in Fig. 6.4(d), as the pump pulse (blue with pulse width τ) travels along the PBG-HCF, it encounters the counter-propagating c.w. probe (red) beam at different locations along the PBG-HCF. The group index of the fundamental mode in the PBG-HCF is ~1 and hence the probe and the pump propagate approximately at the vacuum speed c. The measurement begins when the pump pulse enters the PBG-HCF from the SMF pigtail ($t = 0$). The probe beam experiences firstly the SRG of fused silica. Then, the pump pulse travels in the PBG-HCF and the probe experiences a SRG of hydrogen if there are hydrogen molecules in the PBG-HCF ($t = D/c$). Finally, the pump pulse reaches the output SMF pigtail and the probe experiences the SRG of the output SMF ($t = L/c$). The total optical path length over which the probe beam interacts with the pump pulse is $2L$, corresponding to a duration of $T = 2L/c$ in the time domain. Figure 6.4(e) shows the variation of the detected probe intensity as a function of time, which maps the concentration of hydrogen along the PBG-HCF. The spatial resolution of the SRG measurement would be limited by the pump pulse width τ and given by $\Delta = \tau c/2$.

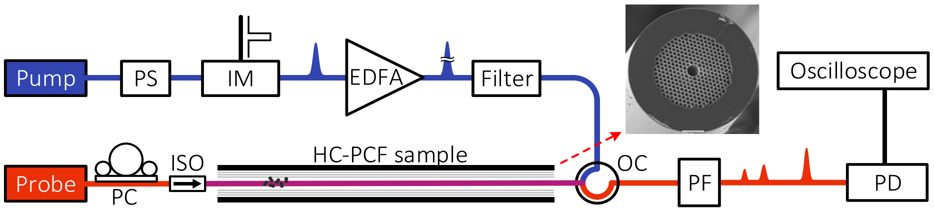

Figure 6.5. Experimental setup for distributed hydrogen sensing. The inset picture shows the cross section of HC-1550-06 fiber.

<u>Test of the lower detection limit</u>

The lower detection limit of the distributed hydrogen sensing system was evaluated with a 100-m-long PBG-HCF gas cell. The gas cell was fabricated by fusion splicing a 100-m-long sensing HC-1550-06 fiber to standard SMF pigtails at both ends, as shown in Fig. 6.6(a). This gas cell is used in the distributed sensing system to test the lower detection limit, response time and dynamic range. For the purpose of gas ingress/egress, 56 pairs of micro-channels (i.e., 112 micro-channels) were drilled over a 2.2-m region around the location 88 m along the 100-m-long sensing PBG-HCF. The region with micro-channels was placed inside a gas chamber with the size of 20 cm × 30 cm × 1 cm. The drilling was done with an 800-nm femtosecond laser micro-machining system [19]. The diameter of the micro-channel is about 8 μm. The separation between the adjacent pairs of micro-channels is ~4 cm, and the spacing between the two channels forming a pair is 200 μm. The total loss of the PBG-HCF sample measured from the input to output SMF pigtail is ~7 dB and ~8.7 dB before and after the drilling of the micro-channels. The average loss of a single micro-channel is estimated to be ~0.015 dB over the wavelength from 1530 to 1620 nm.

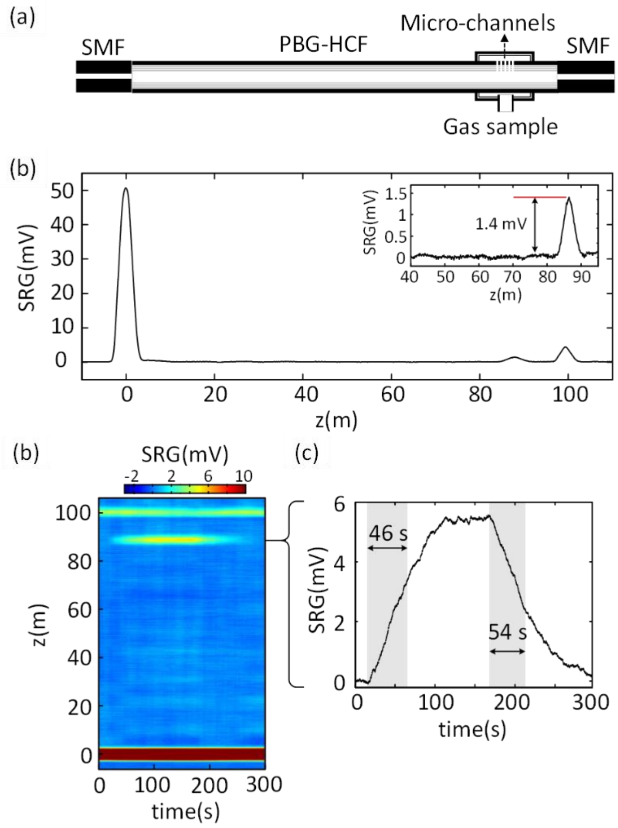

Figure 6.6. SRG trace along a 100-m-long PBG-HCF. (a) The configuration of the PBG-HCF gas cell. (b) The measured SRG trace along the 100-m-long sensing PBG-HCF with 18-ns pump pulse. (c) The distributed Raman gain trace as a function of time of the hydrogen filling and recovering process. The number of averages is 200. (d) SRG signal at the position of 88 m. The shaded regions show the filling and recovering process, which define the e^{-1} response (rising and recovering) time.

The region with micro-channels is exposed to 4% of hydrogen balanced with nitrogen at a pressure of 1 atm. The pump pulse has a duration of 18-ns and the peak power delivered to the PBG-HCF sample was ~30 W, corresponding to a peak pump intensity of 110 MW/cm^2. The power of c.w. probe beam is 100 µW measured before the PD, which is much smaller than that of the pump pulse. Therefore, SRL of the pump pulse is small and need not to considered in our experiment. Figure 6.6(b) shows the measured SRG signal over the 100-m-long PBG-HCF sample. The frequency difference between the pump and probe was tuned to the $S_0(0)$ rotational Raman transition of hydrogen(on-resonance). The inset shows the enlarged SRG signal around 88 m. The number of averages used in the oscilloscope is 12,000. The gain peaks at 0 m and 100 m are due to SRG of silica SMF pigtails. It gives the information about the beginning and ending of the PBG-HCF. The gain peak around 88 m is due to the SRG of hydrogen, which has an amplitude of 1.4 mV. The standard deviation of the noise from 40 to 80 m is 29 µV, giving a NEC of 833 ppm. This detection limit is ~50 times lower than the 4% lower explosive limit of hydrogen.

Test of the response time

To test the response time of the distributed hydrogen sensor, the gas chamber was initially filled with pure nitrogen and then 20% hydrogen balanced with nitrogen was filled into the gas chamber. At last, after the SRG signal of hydrogen reached a steady value, the gas chamber was purged with pure nitrogen. Figure 6.6(b) shows the SRG distribution along the 100-m-long HCF as a function of time. The two Raman gain peaks at the position of 0 and 100 m are the SRG of the SMF pigtails. The SRG signal of hydrogen at ~88 m as a function of time is shown in Fig. 6.6(c). The response time, defined as the rising time to e^{-1} of the steady state after exposing to hydrogen, is 46 s. The recovery time, defined as the falling time to $1-e^{-1}$ of the steady signal after purging with pure nitrogen, is 54 s.

Test of the dynamic range

The dynamic range of distributed SRG gas detection system was tested with the same 100-m-long PBG-HCF sample. SRG signal was measured when the 2.2-m-long region with micro-channels was filled with different concentrations of hydrogen. The HCF sample was placed inside a gas chamber, which was filled initially with pure nitrogen and then a mixture of pure hydrogen and nitrogen of different ratios.

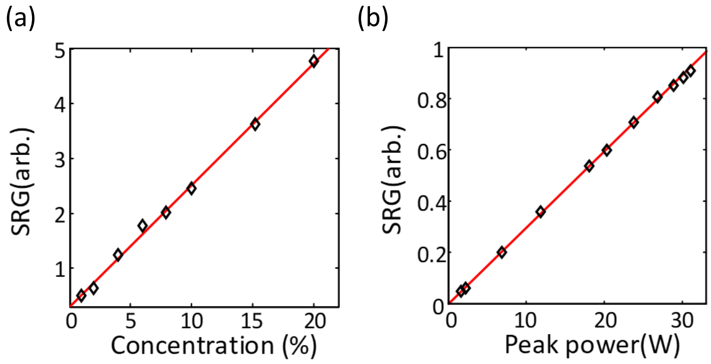

Figure 6.7. Experiment results of dynamic range and linearity. (a) SRG signal for different concentrations of hydrogen balanced with nitrogen. The pump pulse width is 18-ns, the peak power delivered to the PBG-HCF is 30 W. SRG signal was obtained by use of an oscilloscope with 200 averages. (b) SRG of pure hydrogen as a function of peak power level of 18-ns pump pulse.

The results are shown in Fig. 6.7(a) and a good linear relationship is obtained for hydrogen concentration up to 20%. The slope of the linear fit is 22 nV/ppm. The SRG signal of pure hydrogen was also measured and is 17.3 mV, which is ~21% smaller than the value predicted by the linear fit. It shows that our system could be used to detect hydrogen from low concentration to pure hydrogen. The lower detection limit in terms of NEC is 833 ppm, giving a dynamic range of over three orders of magnitude (from 833 ppm to ~100%). The SRG signal as function of peak pump power level is shown in Fig. 6.7(b). The signal amplitude is linearly proportional to the peak pump power, indicating that further enhancement is possible by simply increasing the peak power of the pump.

Test of the spatial resolution

To demonstrate distributed hydrogen detection with a higher spatial resolution, we used a 15-m-long PBG-HCF sample shown in Fig. 6.8(a) and 1-ns pump pulse. The PBG-HCF sample is formed by two pieces of 7.5-m-long PBG-HCFs and two SMF pigtails. The PBG-HCFs and SMFs are connected by butt coupling as we have described in Fig. 6.2(b).

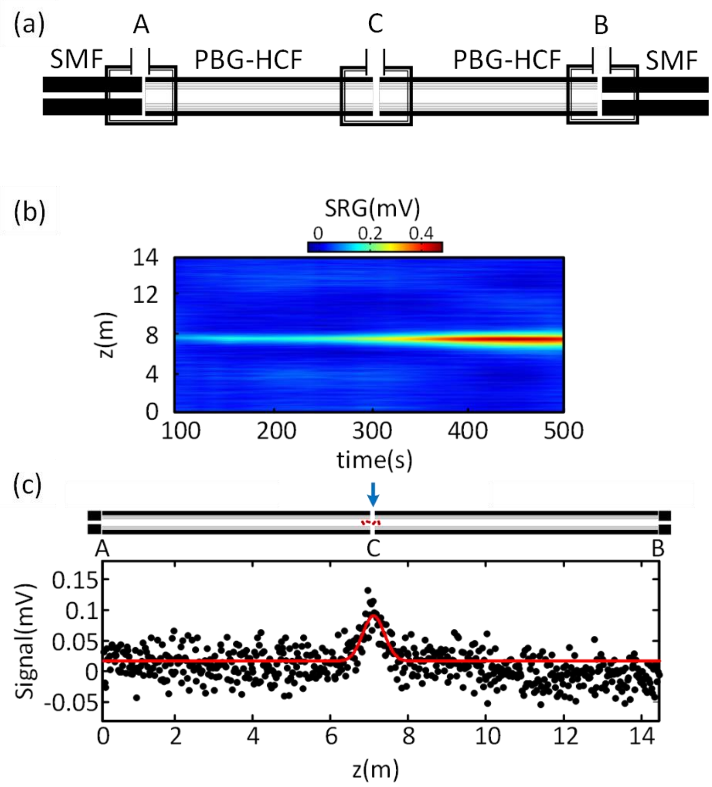

Figure 6.8. Experiment result for testing the spatial resolution. (a) The configuration of the 15-m-long PBG-HCF gas cell. (b)The Raman gain trace as a function of time during the hydrogen loading process. The peak power of pump is ~10 W in the PBG-HCF. (c) Schema of the PBG-HCF sample and the SRG trace at 18 s showing the hydrogen gain signal around z = 7.5 m.

As shown in Fig. 6.8(b), pure hydrogen was pressurized into the PBG-HCF through the air-gap at joint C with a pressure of ~0.7 bar above the atmosphere. The measured SRG distribution along the sensing HCF as a function of time is shown in Fig. 6.8(b). SRG signal of hydrogen is clearly observable around z = 7.5 m and increases with gas loading time. The gain trace at 18 s is shown in Fig. 6.8(c) and the FWHM of the gain peak around z = 7.5 m is 75 cm. This value is larger than the spatial resolution calculated with $\Delta = \tau c/2 = 15$ cm and is believed to be mainly determined by the length of HCF that is filled with hydrogen. Further increase in the pump power level would enhance the gain signal and allow measurement to be performed at an earlier stage (i.e., shorter gas filling length) to demonstrate pump pulse-width limited spatial resolution.

It should be stated that for the 18-ns pump pulse, the SRG can be determined by the gain factor in the steady-state regime. For short pump pulse (e.g., 1 ns), the coherence dephasing needs to be considered and SRG should be described by the backward Maxwell-Bloch equations [21]. For $S_0(0)$ transition of pure hydrogen, the dephasing time is ~3.3 ns at 1 atm. However, the spatial resolution of our distributed gas sensor is not limited by the dephasing time and could be further improved by using shorter pump pulses.

Distributed gas pressure measurement

The distributed sensing system was also tested for the measurement of gas pressure distribution along the PBG-HCF. To determine the gas pressure from the Raman linewidth, we measured the backward Raman linewidth of hydrogen with a 15-m-long PBG-HCF filled with different concentrations of hydrogen. The PBG-HCF gas cell was described in Fig. 6.2(b). The two butt coupling joints were sealed respectively in T-shaped tubes being connected to pressurizing devices. The gas sample was pressurized into the PBG-HCF through the T-shaped tube. Figures 6.9(a) and (b) show respectively the backward Raman linewidth and line shift measured with the HC-1550-06 fiber sample filled with gases with different hydrogen concentrations and pressure levels.

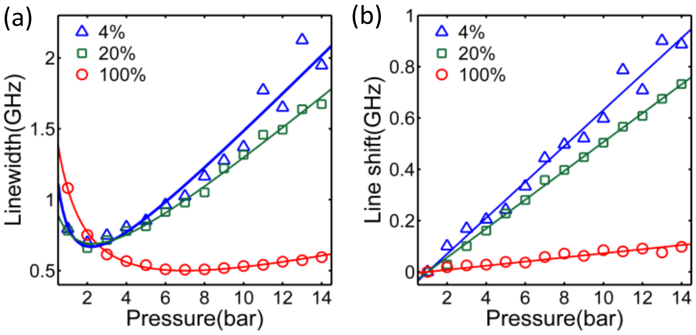

Figure 6.9. Measured backward Raman linewidth and line-shift at 296 K. (a) SRS linewidth as functions of gas pressure for three different hydrogen concentrations. (b) Measured pressure induced Raman shift for different hydrogen concentration.

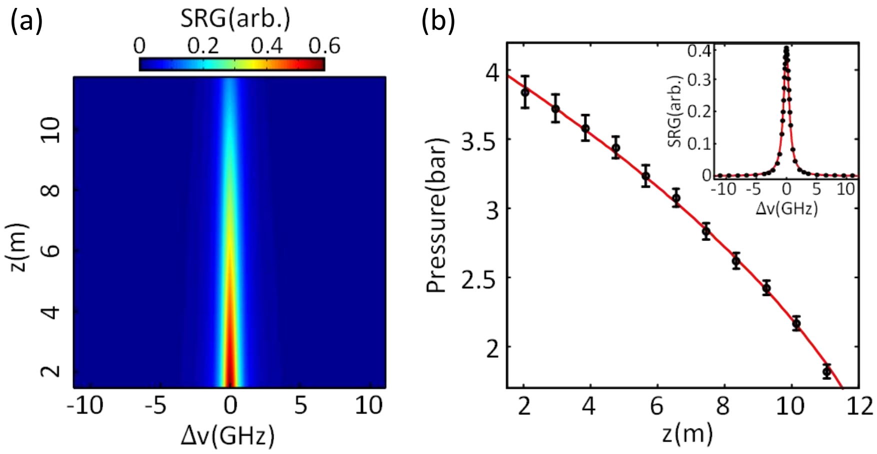

Figure 6.10. Results of distributed gas pressure measurement. (a) The measured backward SRG spectrum along the PBG-HCF. (b) The pressure distribution recovered from the SRG linewidth and the theoretical calculation based on Eq. 6.6 with $P_A = 4.2\ bar$ *and* $P_B = 1\ bar$. *The inset shows a measured SRG spectrum (dot) around z = 7 m and Lorentzian fit (line).*

A 13-m-long PBG-HCF gas cell was used as the sensing gas cell. The gas cell is the same as the gas cell shown in Fig. 6.2(b), except for the length of PBG-HCF. The two ends of the HCF sample were applied with gas pressure of ~4 bar and 1 bar. The measurement was conducted after the pressure gradient in the HCF reaches equilibrium. The wavelength of pump laser is tuned across the Raman gain spectrum of hydrogen while we keep the probe wavelength unchanged. The peak power of pump pulse is 30 W with a pulse width of 18-ns. The SRG spectrum data were recorded by an oscilloscope with 200 averages. The distributed SRG signal decreases as the wavelength of pump laser was tuned away from the Raman gain spectrum of hydrogen, as shown in Fig. 6.10(a). In inset of Fig. 6.10(b) shows the measured SRG spectrum around z = 7 m. The gain spectrum of pure hydrogen can be fitted with a Lorentzian lineshape, from which the SRG linewidth can be determined. The confidence interval of the curve fit is shown as the error bar in Fig. 6.10(b). The backward SRG linewidth was used to decode the pressure distribution according to the linewidth we measured at different pressure (Fig. 6.9(a)). The results are shown as the solid dots in Fig. 6.10(b). Theoretically, the pressure distribution *P* along the HCF with different gas pressure at the ends may be described by [22]

$$P(z) = \sqrt{P_A^2 + \frac{z}{L}(P_B^2 - P_A^2)} \tag{6.6}$$

where *L* is the length of PBG-HCF, $P_{A,B}$ the gas pressure at the ends of PBG-HCF (‘A’ and ‘B’), and *z* the position respect to ‘A’. The experimental result fits well with the theoretical calculation, as shown in Fig. 6.10(b). However, due to interference of the SRG of SMF pigtails, the SRG spectrum of $S_0(0)$ transition is not accurately acquired near the ends of the PBG-HCF sample.

Monitoring the gas filling and purging process

The gas filling and purging process can also be monitored using our distributed hydrogen sensing system. The experiment setup is similar to that shown in Fig. 6.5, but we use a PC instead of a PS. First, we monitored the gas filling process of the 15-m PBG-HCF sample (Fig. 6.2(b)) with 18-ns pump pulses. The 15-m PBG-HCF sample was initially filled with air. We then load pure hydrogen with a pressure of 2 bar at one end of the PBG-HCF, and the other end of the PBG-HCF was exposed to atmosphere. As shown in Fig. 6.11(a), the hydrogen gradually fills the whole PBG-HCF sample. The SRG signal shows a gradient due to the pressure gradient and hydrogen concentration gradient along the PBG-HCF. After the filling process reached equilibrium, both ends (i.e., points A and B) of the PBG-HCF were exposed to atmosphere at around t ≈ 15,000 s. As shown in Fig. 6.11(a), the SRG signal reduces quickly and becomes almost the same along the entire PBG-HCF within a short period of time.

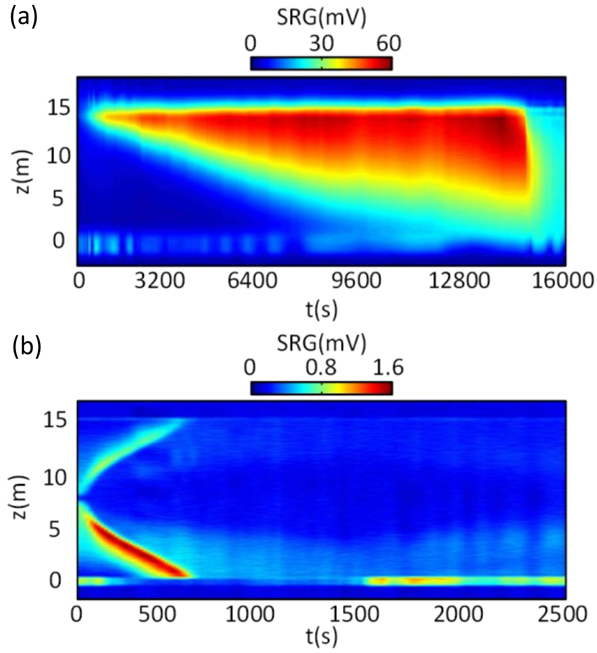

Figure 6.11. Monitoring the gas filling and purging process. (a) The measured hydrogen filling process with an 18-ns pump pulse and the 15-m-long PBG-HCF sample shown in Fig. 6.2(b). (b) The measured hydrogen purging process with a 2-ns pump pulse and the PBG-HCF sample in Fig. 6.10(a).

Second, we monitored the gas purging process using the 15-m-long PBG-HCF sample shown in Fig. 6.8(a), with a pump pulse width of 2-ns. The PBG-HCF sample was initially filled with pure hydrogen. We then loaded pure nitrogen with a pressure of 4 bar at point C, and points A and B were exposed to atmosphere. As demonstrated in Fig. 6.11(b), the nitrogen ‘pushes’ out most of hydrogen in the PBG-HCF in ~600 s. The SRG signal of hydrogen initially increased after we applied nitrogen with a pressure of 4 bar. The main reason for this is that the higher-pressure nitrogen compresses the hydrogen in the PBG-HCF from 1 atm to a higher pressure. The SRG peak moved toward the two ends (i.e., points A and B) and eventually almost disappeared after 600 s, showing most of the hydrogen inside the PBG-HCF has been pumped out by the higher pressure nitrogen gas.

6.1.4. Discussion of SRG spectroscopy

We have demonstrated all-fiber, label-free optical hydrogen sensors with point and distributed sensing capability. For the point sensor, a NEC of ~20 ppm was achieved. For the distributed hydrogen sensor, a NEC of 833 ppm with 2.7 m spatial resolution was demonstrated over a sensing length of 100 m at atmospheric pressure. The response time of the distributed gas sensor is less than 60 s with a dynamic range of more than three orders of magnitude. A higher spatial resolution of 75-cm was demonstrated over a sensing length of 15 m. It has high detection sensitivity and selectivity, large dynamic range, long sensing range and high spatial resolution.

Within the transmission window of the HC-1550-06 fiber, the Raman transitions of several gases such as H_2, O_2 and N_2 are accessible, enabling multi-component gas detection. By using a HCF (e.g., Kagome [26] or single-ring anti-resonant fiber with broader transmission band, vibrational or rotational Raman transitions of a wider range of gases may be accessed, and allowing the detection of many gases with Raman active transitions.

As shown in Fig. 6.7(b), the amplitude of SRG is proportional to the peak power of pump pulse and hence further enhancement of SRG signal is possible by simply increasing the peak power level. Numerical analysis using finite-element analysis shows that most of the light power of the fundamental mode in the commercial HC-1550-06 fiber is in the hollow core and cladding holes, and only a very small fraction (~0.4%) of the light is in the glass part. This results in a much higher threshold for nonlinear effects and optical damage, and allows the use of higher pump power to achieve higher detection sensitivity.

SRS is a very fast process that could enable a sampling rate of tens of megahertz. It is theoretically limited by the dephasing and depopulation times of hydrogen, which is on the order of nanoseconds at 1 atm [27]. In our experiments, we demonstrated an effective sampling rate of 6 Hz over a sensing length of 100 m, limited by the sampling rate of oscilloscope and the number of averages used to improve the SNR of SRG signal. With a higher power pump, a sufficiently high SNR could be achieved without the need for many averages. This would allow significantly higher sampling rate, which would enable fast dynamic fluidic analysis in the PBG-HCF.

We demonstrated distributed hydrogen sensing over a 100-m-long PBG-HCF with micro-channels drilled over a length of 2.2 m. It is feasible to fabricate a large number of micro-channels along the entire length of the PBG-HCF for real time distributed gas detection. With a femtosecond laser, we have demonstrated the fabrication of hundreds of micro-channels with an average loss below 0.01 dB per channel [19]. Observation of the fabrication process showed that most of the micro-channels have negligible contribution to the fiber loss and a few poorly made micro-channels raised the level of the average loss, which is believed caused by the scrap generated during the femtosecond laser drilling process. By improving and automating the fabrication process, mass production of micro-channels with lower loss is possible, which would enable fast distributed gas sensing over the entire length of the fiber. With the newly developed AR-HCFs, which have a simpler structure and better mode quality, micro-channels or lateral cut along the entire length of the fiber could be made easily with negligible loss added to the fibers [28].

6.2. Raman photothermal spectroscopy

In the last section, we discussed about the SRG spectroscopy which measures the relative Raman gain of the Stokes light. However, limited by the saturation power of PD, the power of Stokes light is usually limited to a few milliwatts. Hence, the SRS is relatively weak since it is proportional to the product of pump intensity and Stokes intensity. Similar to the PTS, the hydrogen molecules can be excited to a higher energy level by SRS and then the relaxation of the molecules leads to heat generation. We can also trace hydrogen by measuring the heat generated by SRS. Since we are measuring the SRS indirectly, the optical intensity of pump and Stokes can both be higher to achieve a stronger SRS in HCFs.

As we have discussed in Chapter 2 and Chapter 3, the heat source of SRS (Q_H) with wavelength modulation can be expressed as

$$Q_H = \nu_R \frac{\Delta N_{fi}}{\Delta \nu_R} \frac{32\pi^4}{\pi h c_0^2} \langle (\alpha_{\rho\sigma})_{fi}^2 \rangle P_P P_S |\psi_P \psi_S|^2 \left(H_0 + \sum_{n=1}^{\infty} \frac{H_n e^{-j(n\omega t - \varphi_n)}}{\sqrt{(n\omega\tau_1)^2 + 1}} \right) \tag{6.7}$$

The pump frequency dependence of the polarizability tensor $\alpha_{\rho\sigma}$ can usually be ignored since the frequency of pump light is usually far from any electronic energy level. Take the $Q_1(1)$ transition of hydrogen as an example, if we use a 940-nm pump light, the relative error of the heat source by ignoring the pump frequency dependence of $\alpha_{\rho\sigma}$ is only about 3%. This result is estimated by using Eq. (2.22). Hence, we can make an important conclusion from Eq. (6.7): RPTS is only weakly dependent on the pump frequency. Although the Raman gain coefficient is dependent on the pump frequency, the heat source generated by SRS is only related to the Raman frequency shift ν_R. The Raman frequency shift of the vibrational band is typically much larger than the pure rotational band. Therefore, the vibrational band (i.e., $Q_1(1)$) is more suitable for RPTS.

6.2.1. Principle of RPTS in HCFs

The basic principle of RPTS is demonstrated in Fig. 6.12. A pump light with a fixed wavelength and a Stokes light with a modulated wavelength are incident in an AR-HCF. The wavelength of Stokes light is modulated at a frequency of ω. Another probe light is also incident in the fiber to measure the temperature change due to Raman effect induced photothermal effect. The gas temperature changed by the photothermal effect and induces a phase modulation to both the LP_{01} and LP_{11} modes of the probe light. By measuring the phase difference between the two optical modes of the probe, we can determine the temperature change in the HCF and also the concentration of hydrogen.

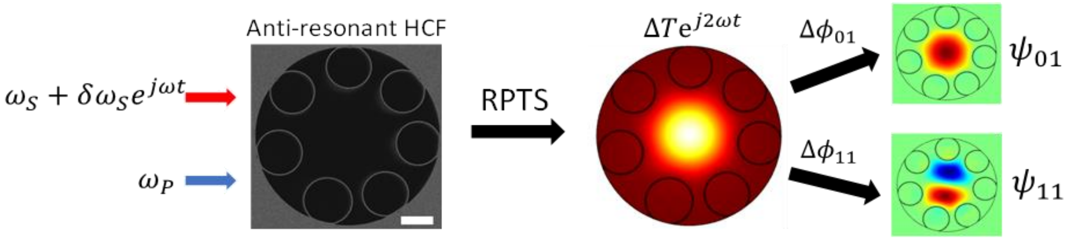

Figure 6.12. The basic principle of RPTS.

We first give an intuitive picture of Raman photothermal effect in AR-HCF by only considering the fundamental optical mode. The heat source under this assumption is already given in Eq. (3.19). Then the phase modulation can be calculated by

$$\phi_{01} = -\frac{k_L L}{T_0}(n_0 - 1)e^{j2\omega t}\langle T_{1,2}(x,y), \psi_{01}^2\rangle \tag{6.8}$$

$$n_0 - 1 = A\rho_0 \tag{6.9}$$

where k_L is the propagation constant of the probe light in vacuum, L the length of HCF, T_0 the ambient temperature, n_0 the RI of the gas in HCF, $T_{1,2}$ the first-order perturbation of temperature at the 2-nd harmonic frequency, and A is a constant for the gas in HCF. As we have mentioned in Eq. (6.7), an important parameter is the VRT τ. It has been studied in pure hydrogen or in hydrogen-rare-gases mixtures [29-32]. For pure hydrogen, $p\tau \approx 385\ \mu s \cdot atm$. However, we found no study about the VRT of hydrogen-nitrogen mixture. The vibrational relaxation in hydrogen-nitrogen mixture is believed to be faster than that in pure hydrogen because nitrogen has introduced additional relaxation channels (e.g., V-V or V-R exchange process of hydrogen and nitrogen).

6.2.2. MPD-RPTS in AR-HCFs

The Raman frequency shift of strongest vibrational transition $Q_1(1)$ is about $4155\ cm^{-1}$. To enable the $Q_1(1)$ Raman transition in HCFs, the transmission of HCF should cover both the pump light and the Stokes light. Limited by the bandwidth of the bandgap structure, typical transmission band of PBG-HCF is about a few hundred nanometers, which is insufficient for the vibrational Raman scattering. Different from PBG-HCF that confines light by a photonic bandgap, the guidance of light in an AR-HCF is enabled by the inhibit coupling between the core mode and the cladding mode that have the same effective mode index [33, 34]. Figure 6.13 shows the SEM of the AR-HCF used for RPTS and the transmission spectrum of a 10-m-long AR-HCF. The AR-HCF mainly supports two groups of optical modes (i.e., LP_{01} and LP_{11}). Hence, it is necessary to use a multi-mode model to analyze the SRS in AR-HCF.

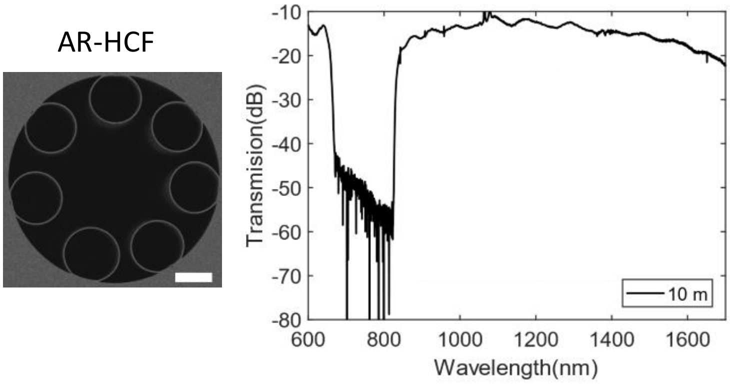

Figure 6.13. The AR-HCF used for RPTS. The white bar is 10 μm.

The electric field of the optical mode can be treated independently in the transverse plane and in the longitudinal direction. In a multimode optical fiber, SRS is described by scattering involved with the combination of four optical modes, which are labeled as $\sigma, \upsilon, \zeta, \eta$. The electric field of mode σ is expressed as

$$e_{\sigma,l}(x, y, z, t) = E_{\sigma,l}(z, t)\psi_\sigma(x, y)q_{\sigma,l} \tag{6.10}$$

$$q_{\sigma,l} = \exp(-i\beta_\sigma(\omega_l)z) \tag{6.11}$$

where ψ_σ is the normalized mode field ($\sigma = 1{,}2$ stands for the LP_{01} and LP_{11} mode, respectively) that satisfies $\langle\psi_\sigma, \psi_\sigma\rangle = 1$ and $E_{\sigma,l}$ is the amplitude of electric field. The subscript $l = -1{,}0{,}1$ refers to the first-order Stokes light, pump light and the first-order anti-

Stokes light. The propagation constant can be calculated by $\beta_\sigma = 2\pi n_\sigma(\omega_l)/\lambda_l$, where n_σ is the effective mode index of optical mode σ. For simplicity, the mode field is assumed to be the same for different wavelengths. FEM simulation shows that this is a good approximation for wavelengths not in the edges of the transmission band of AR-HCF. The amplitude of electric field is approximated by using the effective optical intensity as

$$I_{\sigma,l}^{eff} = \frac{\varepsilon_0 c}{2}\left|E_{\sigma,l}\right|^2 \tag{6.12}$$

$$I_{\sigma,l}^{eff} = \frac{P_{\sigma,l}}{A_\sigma^{eff}} \tag{6.13}$$

The effective mode area is defined as

$$A_\sigma^{eff} = \frac{(\iint |\psi_\sigma|^2 dA)^2}{\iint |\psi_\sigma|^4 dA} \tag{6.14}$$

where the integral is calculated over the fiber cross-section. The Maxwell-Bloch equations can be rewritten in a multi-mode form as [35]

$$\begin{aligned}\left(\frac{\partial}{\partial z} + \frac{n_{\sigma,l}}{c_0}\frac{\partial}{\partial t}\right)E_{\sigma,l} = -j\kappa_{2,l}\frac{\omega_l}{\omega_{l-1}}\sum_{\upsilon\zeta\eta}\frac{S_{\sigma\upsilon\zeta\eta}}{S_{\upsilon\zeta}}Q_{R,\upsilon\zeta}E_{\eta,l-1}q_{\eta,l-1}q_{\sigma,l}^*\\ -j\kappa_{2,l+1}\sum_{\upsilon\zeta\eta}\frac{S_{\sigma\upsilon\zeta\eta}}{S_{\upsilon\zeta}}Q_{R,\upsilon\zeta}^*E_{\eta,l+1}q_{\eta,l+1}q_{\sigma,l}^*\end{aligned} \tag{6.15}$$

$$\frac{\partial}{\partial t}Q_{R,\upsilon\zeta} = -\frac{Q_{R,\upsilon\zeta}}{\tau_2} - \frac{j}{4}S_{\upsilon\zeta}\sum_l \kappa_{1,l}E_{\zeta,l}E_{\upsilon,l-1}^*q_{\zeta,l}q_{\upsilon,l-1}^* \tag{6.16}$$

where the coupling coefficients are defined as

$$\kappa_{1,l} = \sqrt{\frac{2g_{R,l}c^2\varepsilon_0^2}{N\tau_2\hbar\omega_{l-1}}} \tag{6.17}$$

$$\kappa_{2,l} = \frac{N\hbar\omega_{l-1}\kappa_{1,l}}{2\varepsilon_0 c_0} \tag{6.18}$$

The overlap integral $S_{\upsilon\zeta}$ defines the efficiency of generating a coherent wave from a pump mode ζ and a Stokes mode υ. And the overlap integral $S_{\sigma\upsilon\zeta\eta}$ defines the efficiency of Raman scattering from the pump mode η to the Stokes mode σ due to the coherent wave $Q_{R,\upsilon\zeta}$. The overlap integrals are defined as [35, 36]:

$$S_{\sigma\upsilon\zeta\eta} = \frac{\iint \psi_\sigma^* \psi_\upsilon \psi_\zeta^* \psi_\eta dA}{\left(\iint |\psi_\sigma|^2 dA \iint |\psi_\upsilon|^2 dA \iint \left|\psi_\zeta\right|^2 dA \iint \left|\psi_\eta\right|^2 dA\right)^{\frac{1}{2}}} A_{01}^{eff} \tag{6.19}$$

$$S_{\upsilon\zeta} = \frac{\iint |\psi_\upsilon|^2 \left|\psi_\zeta\right|^2 dA}{\left(\iint |\psi_\upsilon| \left|\psi_\zeta\right| dA\right)^2} A_{01}^{eff} \tag{6.20}$$

The overlap integral is normalized by the effective mode area of LP_{01}. Table 6.1 and Table 6.2 show the values of overlap integral $S_{\upsilon\zeta}$ and $S_{\sigma\upsilon\zeta\eta}$ for different combinations of optical modes, respectively.

Table 6.1. The overlap integral $S_{\upsilon\zeta}$.

$S_{\upsilon\zeta}$	01	11
01	1	0.8
11	0.8	1.06

Table 6.2. The overlap integral $S_{\sigma\upsilon\zeta\eta}$.

$S_{\sigma\upsilon\zeta\eta}$	01,01	01,11	11,01	11,11
01,01	1	0	0	0.67
01,11	0	0.67	0.67	0
11,01	0	0.67	0.67	0
11,11	0.67	0	0	1.06

In the above equations, the probability of the hydrogen occupying the upper energy level is assumed to be much smaller than 1. Hence, the occupational probabilities w_R is approximated as -1 in Eqs. (6.15) and (6.16). Then we can calculate w_R by

$$\frac{\partial w_{\sigma\upsilon\zeta\eta}}{\partial t} = -\frac{w_{\sigma\upsilon\zeta\eta} - w_{R,0}}{\tau_1} + \frac{S_{\sigma\upsilon\zeta\eta}}{S_{\upsilon\zeta}} Im\left\{\sum_l \kappa_{1,l} Q_{R,\upsilon\zeta}^* E_{\eta,l} E_{\sigma,l-1}^* q_{\eta,l} q_{\sigma,l-1}^*\right\} \tag{6.21}$$

$$w_R - w_{R,0} = \sum_{\sigma\upsilon\zeta\eta} \left(w_{\sigma\upsilon\zeta\eta} - w_{R,0}\right) \tag{6.22}$$

where w_0 is the occupational probabilities in thermal equilibrium and $w_{\sigma\upsilon\zeta\eta}$ represents the occupational probability with a transverse profile of $|\psi_\sigma \psi_\upsilon \psi_\zeta \psi_\eta|$. The Raman heat source Q also have the same profile and can be expressed as

$$Q_{\sigma\upsilon\zeta\eta} = h\nu_R N \frac{w_{\sigma\upsilon\zeta\eta} - w_{R,0}}{2\tau_1} \tag{6.23}$$

$$Q = \sum_{\sigma\upsilon\zeta\eta} Q_{\sigma\upsilon\zeta\eta} \tag{6.24}$$

Actually, Eqs. (6.15), (6.16) and (6.21) are quite general that they can used to describe the most situations of Raman scattering in HCFs. A MATLAB code for this multi-mode SRS model is provided in the Appendix.

First, we study the RPTS in a simple situation by only considering SRS of fundamental optical mode. From Eq. (6.7), we know that the phase modulation of RPTS is strongly dependent on the gas pressure. The Raman gain coefficient of $Q_1(1)$ of hydrogen increases with the gas pressure and saturates around a pressure of 15 bar. The simulation of the RPTS of pure hydrogen is performed with parameters: $L = 3.9\ m$, $P_P = 800\ mW$, $P_S = 400\ mW$. Figure 6.14(a) shows the pressure dependence of phase modulation, and Fig. 6.14(b) shows the frequency dependence of the phase modulation in RPTS at a pressure of 6 bar. The phase modulation for pure hydrogen on the orders of tens milli-rad. As expected, the phase modulation in the MPD (blue curve) scheme is a few times smaller than that of LP_{01} mode (red curve). The 3-dB roll-off frequency of RPTS is about 10 kHz. Figure 6.15 shows the temperature change weighted by the mode field of LP_{01} mode ($\langle T, \psi_{01}^2 \rangle$ refers to the overlap integral over the fiber cross-section). The temperature change increases rapidly with the increasing of gas pressure and then gradually saturates for pressure larger than 8 bar. The maximum temperature change is about a few milli-Kelvin.

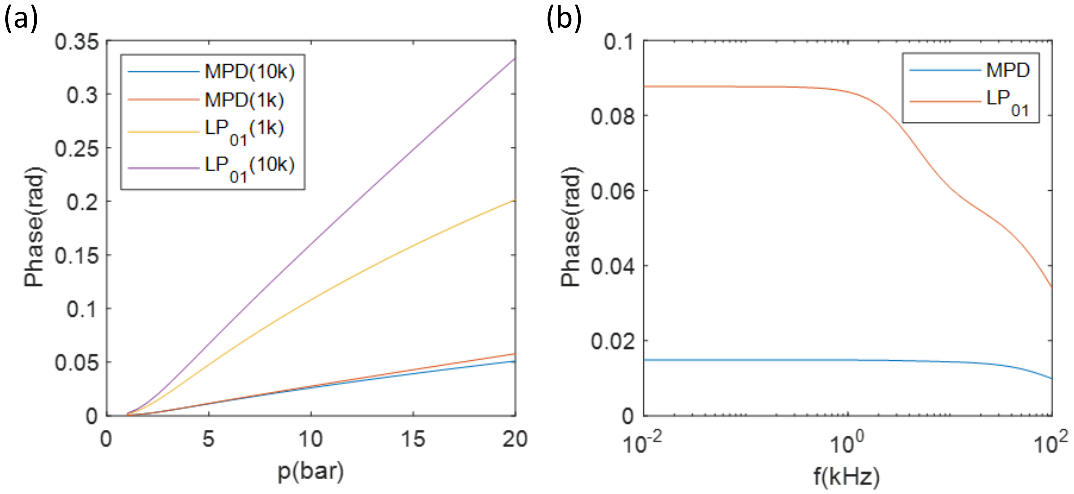

Figure 6.14. The phase modulation in RPTS with only the LP_{01} pump mode. (a) The pressure dependence of phase modulation for MPD and the LP_{01} mode. (b) The frequency dependence of the phase modulation at a pressure of 6 bar.

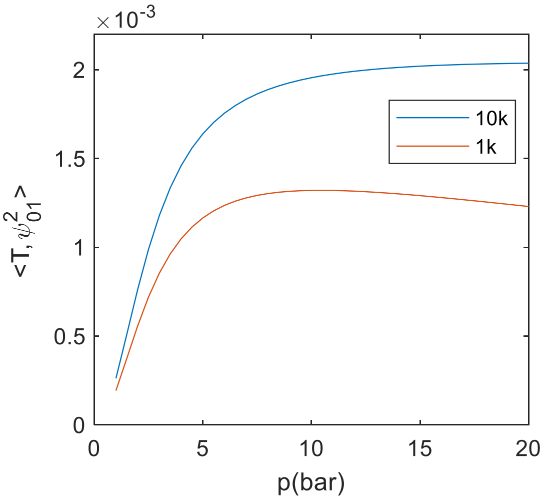

Figure 6.15. The weighted temperature change at modulation frequencies of 1 kHz and 10 kHz.

Then we do an accurate simulation of RPTS by considering the heat source due to intermodal Raman scattering. At steady state, and ignoring the depletion of pump and Stokes due to SRS or fiber loss, the Raman heat source can be obtained by using Eqs. (6.15), (6.16), (6.21) and (6.23):

$$Q_{\sigma\upsilon\zeta\eta} = \frac{\nu_R}{\nu_S} g_R H_{WMS}(\omega) S_{\sigma\upsilon\zeta\eta} Im\left\{\frac{j}{4} c^2 \varepsilon_0^2 E_{\sigma,-1}^* E_{\upsilon,-1} E_{\zeta,0}^* E_{\eta,0} q_{\sigma,-1}^* q_{\upsilon,-1} q_{\zeta,0}^* q_{\eta,0}\right\} \tag{6.25}$$

$$H_{WMS}(\omega) = H_0 + \sum_{n=1}^{\infty} \frac{j}{n\omega\tau_1 + j} H_n e^{-jn\omega t} \tag{6.26}$$

where the subscripts ‘0’ and ‘-1’ stand for the pump and the Stokes, respectively. There are eight different heat sources that are nonzero as we can derive from Eq. (6.25). These heat sources can be treated independently since the thermal conduction equation is linearized near its equilibrium. Some of them have the same distribution. Figure 6.16 shows all three kinds of distribution of heat source of RPTS. However, as we are measuring the accumulated phase modulation over a long length (e.g., a few meters), some of these heat source has no contribution to the accumulated phase modulation.

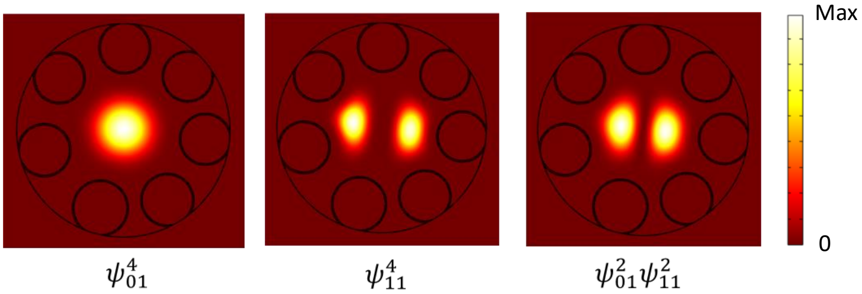

Figure 6.16. The distribution of the heat sources of RPTS.

For example, Fig. 6.17 shows the three kinds of integrated heat source along the fiber. The integrated heat source is the integral of heat source over the fiber cross-section. As we can see, the sum of Q_{1212}-like heat source is periodical along the fiber. In principle, only four heat sources are not periodically along the fiber. The effective heat source can be expressed as

$$Q_{eff} = \underbrace{Q_{1111} + Q_{2222}}_{Intra-modal} + \underbrace{Q_{1122} + Q_{2211}}_{Inter-modal} \tag{6.27}$$

The first two parts in Eq. (6.27) come from the intra-modal Raman scattering and the last two parts come from the inter-modal Raman scattering. For example, Q_{1212} represents the heat source generated by scattering LP_{11} pump mode to LP_{01} Stokes mode due to the coherent wave generated by LP_{01} pump mode and LP_{11} Stokes mode.

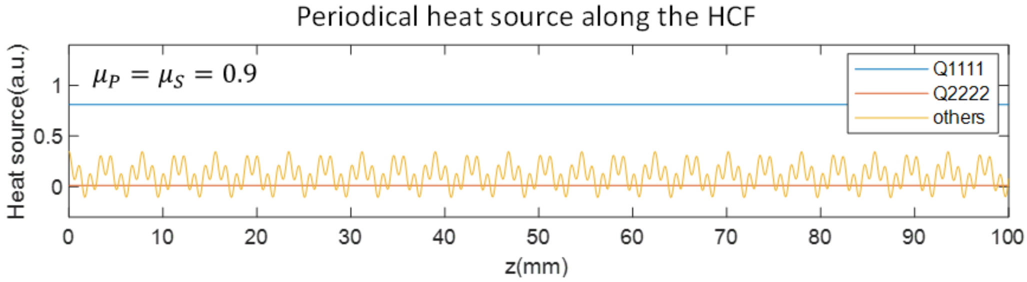

Figure 6.17. The integrated heat source over the fiber cross-section along the fiber.

We can then define a Raman photothermal (RPT) phase modulation coefficient for MPD by

$$k_R^* = \frac{|\Delta\phi_{01} - \Delta\phi_{11a}|}{P_P P_S g_R C L} \tag{6.28}$$

It has a unit of $rad/(W^2 \cdot cm/GW \cdot m)$. This coefficient describes the phase modulation per meter induced by unit pump and probe power, which is normalized by the Raman gain coefficient and the hydrogen concentration. Figure 6.18 shows the simulation of RPT modulation coefficient for all three distributions of heat source. The simulation is done with an AR-HCF filling with 1% hydrogen balanced with nitrogen. The inset shows the SEM of the AR-HCF. The white bar is 10 μm.

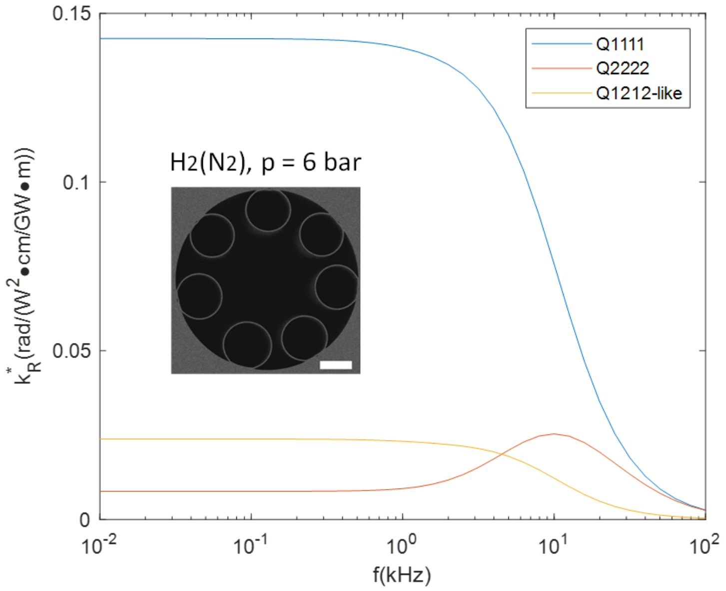

Figure 6.18. RPT modulation coefficient of all three distributions of heat source.

The launched pump and Stokes power in AR-HCF can vary with different coupling conditions. The effective RPT phase modulation coefficient can be calculated using the linear superposition principle:

$$k_{R,eff}^{*} = \sum_{\sigma\eta}^{4} \mu_{P,\eta}\mu_{S,\sigma}k_{R,\sigma\sigma\eta\eta}^{*} \tag{6.29}$$

where $\mu_{P,\eta}$ and $\mu_{S,\sigma}$ are the fractional power in LP_{01} for pump light in mode η and Stokes light in mode σ. Figure 6.19(a) shows the effective RPT modulation coefficient. The grey region shows the prediction region by varying the fractional power in LP_{01}. And the red dots show experiment result, which will be discussed in the next section. There is a solution of μ_P and μ_S that can match the experiment and the simulation. Figure 6.19(a) also demonstrates that $k_{R,eff}^{*}$ can vary in a large region with different fractional power. The power in LP_{11} mode will result in a smaller phase modulation due to RPT effect. At low modulation frequencies when $k_{R,eff}^{*}$ reaches a stable platform (i.e., $f < 1\ kHz$), the dependence of $k_{R,eff}^{*}$ on the fractional powers is shown in Fig. 6.19(b). This figure shows that the fractional power μ_P and μ_S are preferred to be close to unity for a larger RPT phase modulation. Figure 6.20 shows the pressure dependence of phase modulation when $\mu_{P,1} = 0.9$. For 1% hydrogen balanced with nitrogen, and by using AR-HCF with a 400-mW pump and a 400-mW Stokes, the temperature change is about a few micro-Kelvin as shown in Fig. 6.20(a). The weighted temperature ($\langle T, \psi_i^2 \rangle$) refers to the overlap integral between temperature field and the normalized optical modes. The phase modulation is about a few hundred microrads as shown in Fig. 6.20(b). The phase modulation of MPD is smaller than that of the fundamental mode. Therefore, the phase modulation of RPTS can be increased by using Mach-Zehnder interferometer or other interferometers on the cost of the noise performance and stability.

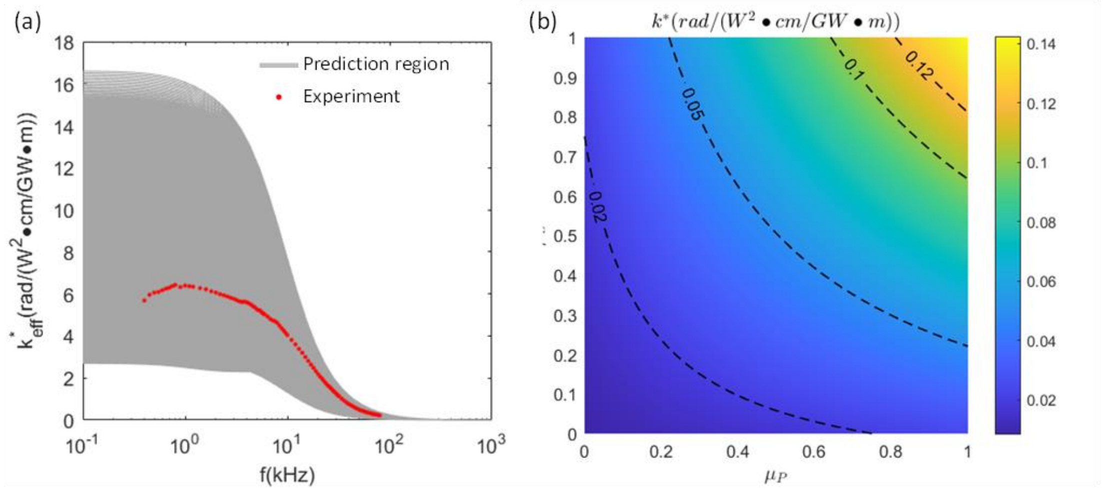

Figure 6.19. The RPT modulation coefficient. (a) The effective RPT modulation coefficient at different frequencies. (b) The effective RPT modulation coefficient at 1ow modulation frequencies (less than 1 kHz).

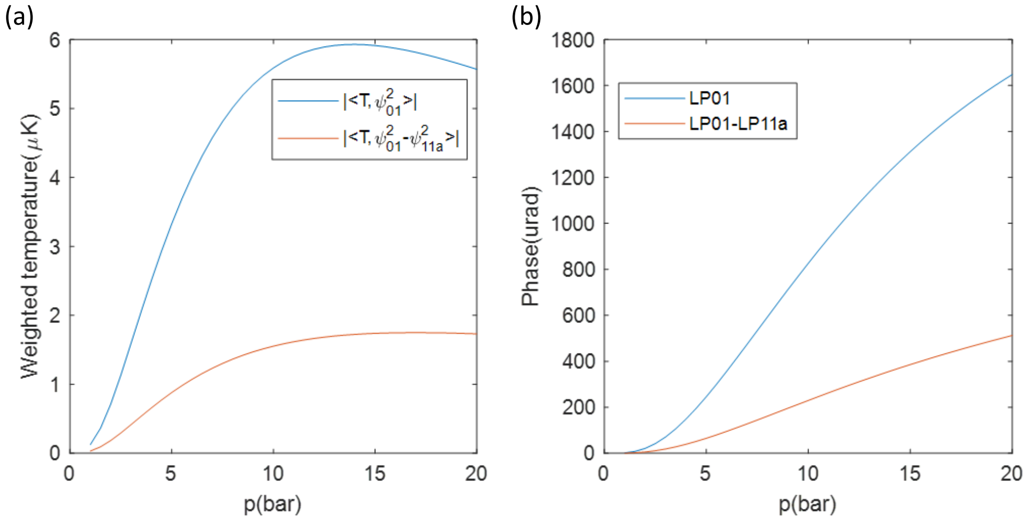

Figure 6.20. The pressure dependence of RPTS. (a) The pressure dependence of the weight temperature. (b) The pressure dependence of the phase modulation.

6.2.3. Experiment and result

Figure 6.21(a) shows the experiment setup of the hydrogen gas sensor with RPTS. A 940-nm pump laser (TA PRO 940 from TOPTICA Photonics) and a 1542-nm Stokes laser (DFB laser) are used to generate a Raman heat source in the AR-HCF. The polarization of the pump laser is linear polarized. The polarization of Stokes laser is adjusted by a PC to make it parallel to the polarization of pump laser. The current of Stokes laser is modulated to generate a wavelength modulation. A 1550-nm fiber laser (from Connect Fiber Optics) with a piezo-feedback is used as the probe laser. The Stokes light is amplified by an EDFA and then is combined with the probe light by a WDM. These two lights in the optical fiber are then combined with the 940-nm laser using a fiber collimator and a dichroic mirror (DM). The lasers are coupled into the AR-HCF using an optical lens. The 3.9-m-long AR-HCF gas cell is homemade and is connected to the test gas and the vacuum pump. The fabrication of the gas cell has been described previously in Fig. 5.8.

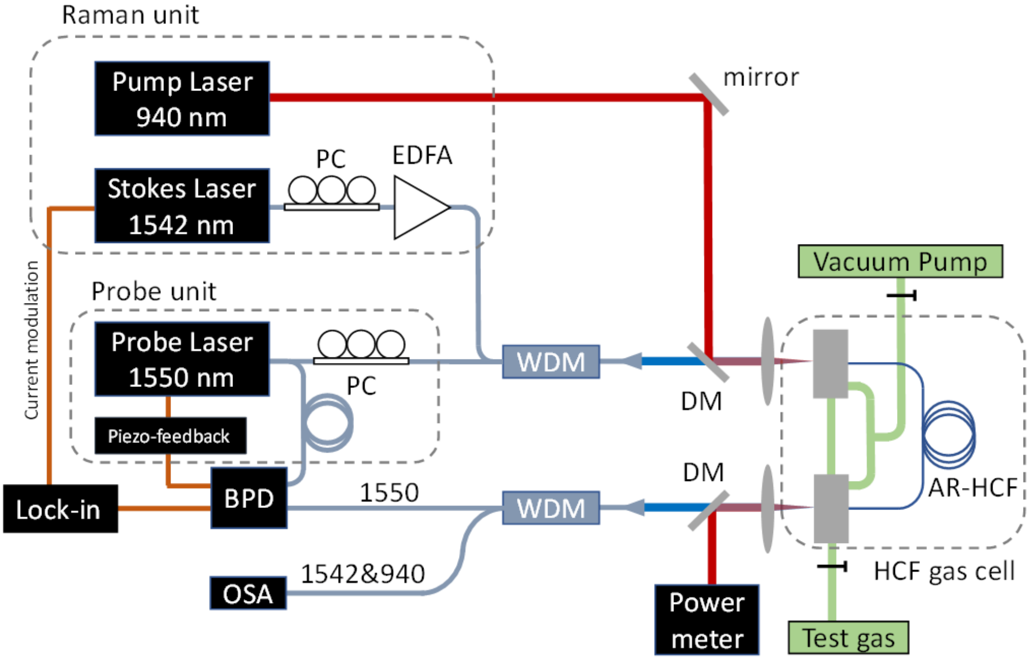

Figure 6.21. The experiment setup of RPTS. (a) The setup for tracing hydrogen. (b) The spectrum of pump and probe lasers measured by the OSA.

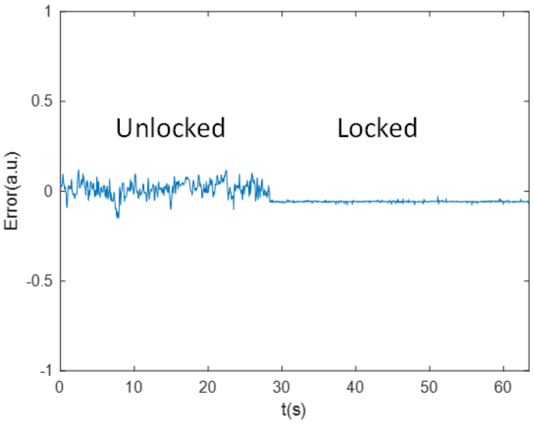

Figure 6.22. The feedback locking of the probe laser.

Most of the pump power at the output of the gas cell is filter out using a DM. The optical power of pump or probe is monitored by using a power meter. Then the light is coupled into a SMF. A specially made WDM is used to filter out the residual pump and Stokes. The 1542-nm Stokes and the residual 940-nm pump can be monitored by an OSA. Figure 6.21(b) shows the optical spectrum measured by the OSA. An auto-BPD detects the power of probe. The monitor port of BPD is used as feedback to lock the probe laser to the quadrature point of the modal interferometer. Figure 6.22 shows the error signal before and after the locking of the probe laser. At last, the weak signal of RPTS is recovered by a LIA.

We firstly measure the frequency response of the phase modulation of RPTS. Figure 6.23 shows the 2-nd harmonic signal recovered by the LIA at different modulation frequencies. The experiment is done with 1% hydrogen balanced with nitrogen at a total pressure of 6 bar. The power of pump and Stokes are about 277 mW and 250 mW, respectively. The phase modulation drops quickly when the frequency increases. The error bar in Fig. 6.23 shows the standard deviation of the phase modulation over 5 measurements and becomes smaller as we increase the modulation frequency. Simulation shows that the phase modulation approaches a constant at low frequencies. However, as we decrease the modulation frequency below 1 kHz, the phase modulation becomes smaller. This phenomenon is hard to explain by the simulation. The phase modulation due to heat source Q_{2222} reaches its maximum around 10 kHz and then becomes smaller at lower frequencies. The heat source Q_{2222} might be a reason for the frequency response around 1 kHz as we observed in the experiment. The corresponding 3-dB roll-off frequency of RPTS with hydrogen is about 14 kHz, which is much smaller than that for PTS with acetylene. For example, by using the same fiber, the roll-off frequency of PTS is about 40 kHz. This indicates that the vibrational relaxation of hydrogen plays a role in the small 3-dB roll-off frequency of RPTS.

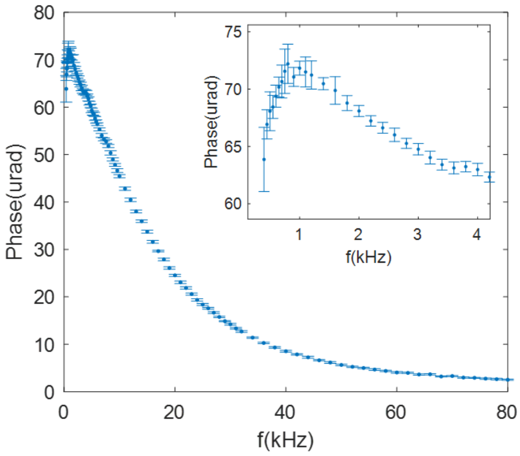

Figure 6.23. The 2-nd harmonic phase modulation at different frequencies.

Then we investigate the power dependence of the 2-nd harmonic wave. The current modulation frequency of Stokes laser is fixed at 3 kHz, corresponding to a 2-nd harmonic frequency at 6 kHz. We first fix the pump power at 277 mW and then adjust the Stokes power. Figure 6.24(a) shows the 2-nd harmonic wave by varying the Stokes power from 0 to 250 mW. The amplitude of 2-nd harmonic is linear dependent on the Stokes power as we demonstrated in Fig. 6.24(b). The error bar in the figure refers to the standard deviation of 6 measurements. Then we fix the Stokes power at 250 mW and then adjust the pump power. Figures 6.24(c) and (d) show the 2-nd harmonic wave by varying the pump power from 0 to 260 mW. It also shows a linear response on the pump power. We can also plot a figure with respect to the product of pump and Stokes powers. As demonstrated in Fig. 6.25, the 2-harmonic signal of RPTS shows a good linear dependence on the product of powers. ‘X’ and ‘R’ in Figs. 6.24 and 6.25 refer to the X-output and R-output of LIA, respectively. By adjusting the phase of LIA at the Raman line center, the R-output is simply the absolute value of the X-output.

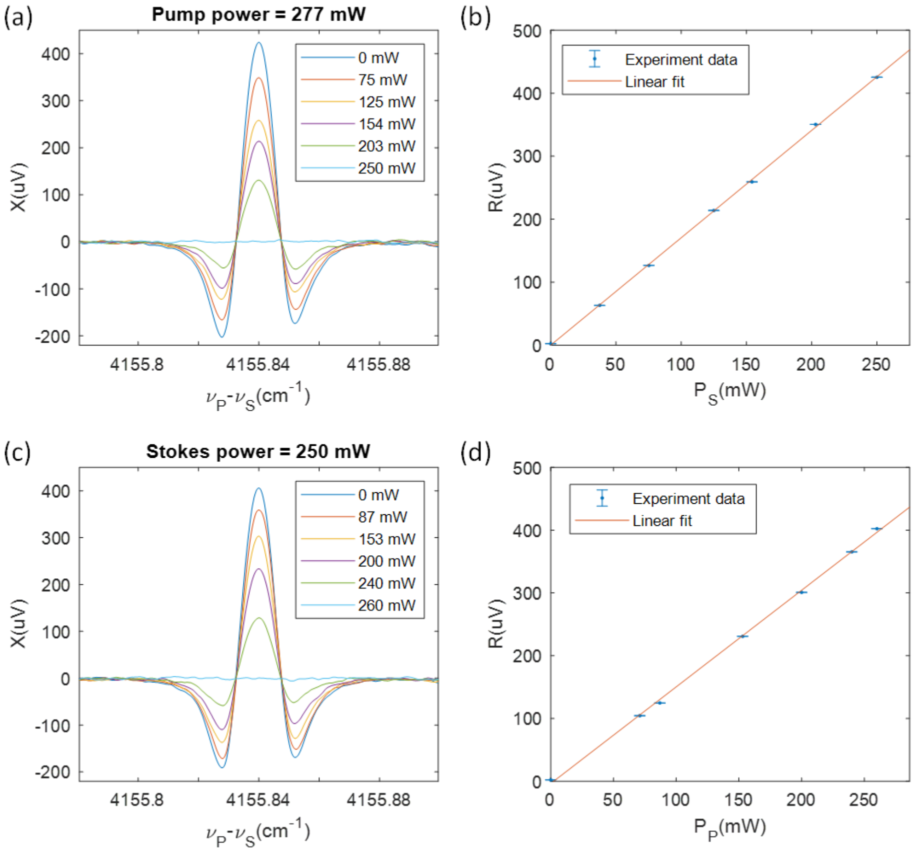

Figure 6.24. The 2-nd harmonic output of LIA with different optical powers. (a) The 2-nd harmonic output of LIA with different Stokes powers. (b) The Stokes power dependence of the 2-nd harmonic output of LIA. (c) The 2-nd harmonic output of LIA with different pump powers. (d) The pump power dependence of the 2-nd harmonic wave.

We measure the noise of the system by detuning the wavelength of Stokes away from the Raman transition. By setting the time constant of the LIA to 1 s, the standard deviation of the noise is about 2.9 μV. The amplitude of 2-nd harmonic wave is about 424 μV, corresponding to a signal-noise-ratio of about 144 and a NEC of 69 ppm.

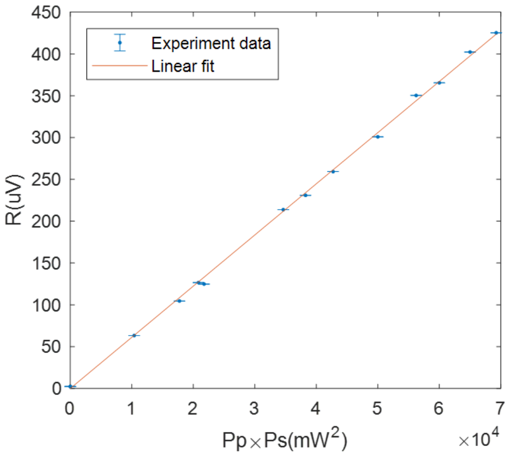

Figure 6.25. The 2-nd harmonic output of LIA with respect to the product of pump and Stokes powers.

We also measure the several vibrational Q_1 transitions of hydrogen by tuning the wavelength of pump laser. As shown in Fig. 6.26, the $Q_1(0)$-$Q_1(4)$ transitions of hydrogen are measured by RPTS at a pressure of 6 bar. These transitions are slightly different in linewidth and hence the amplitudes of 2-nd harmonic signal measured by wavelength modulation are not exactly equal to the amplitude measured by spontaneous Raman scattering.

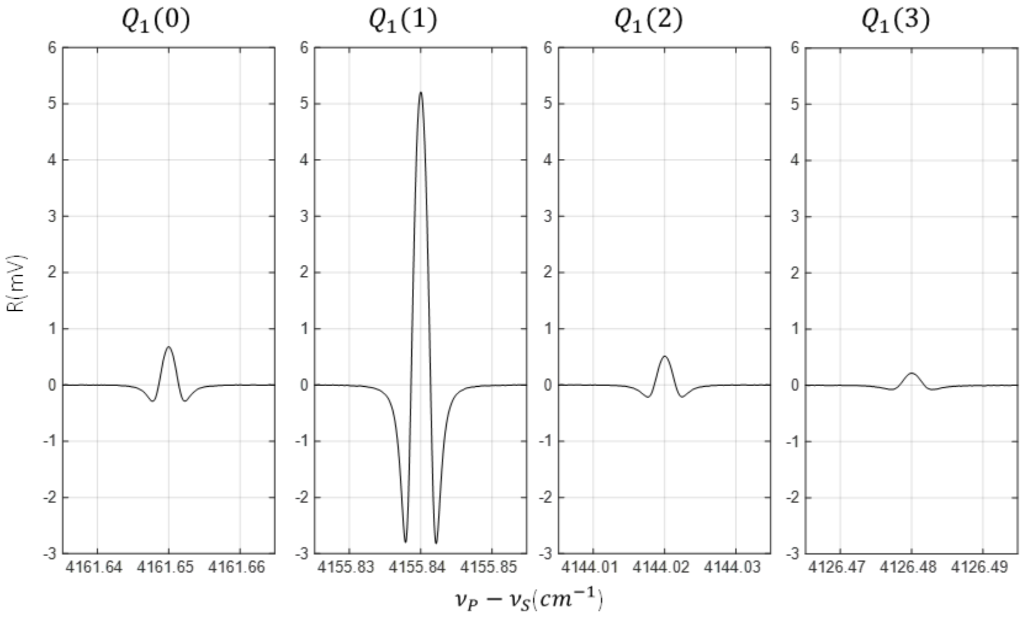

Figure 6.26. The measured vibrational band of pure hydrogen.

To investigate the sensitivity of our RPTS, we do Allan variance with the noise of the system. The noise is measured by detuning the wavelength of Stokes away from the Raman transition and is recorded for more than 10 hours. Figure 6.27 shows the Allan plot of the noise. It indicates the sensitivity of the system can be further increased by using a longer integration time. The ultimate sensitivity of our system is about 3.2 ppm hydrogen with an integration time of 1627 s.

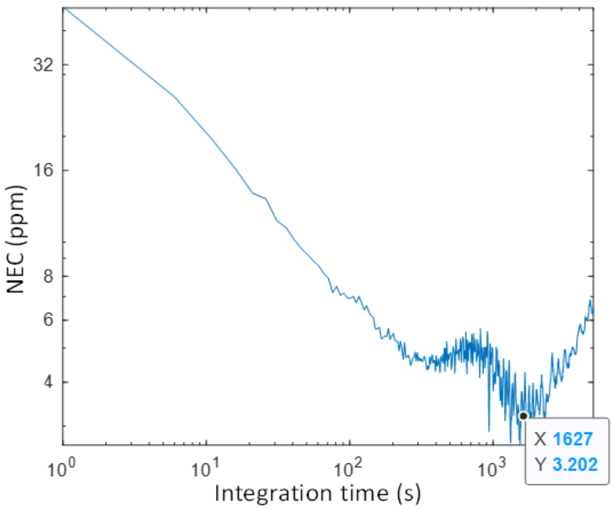

Figure 6.27. The Allan plot for analysis of the sensitivity of RPTS.

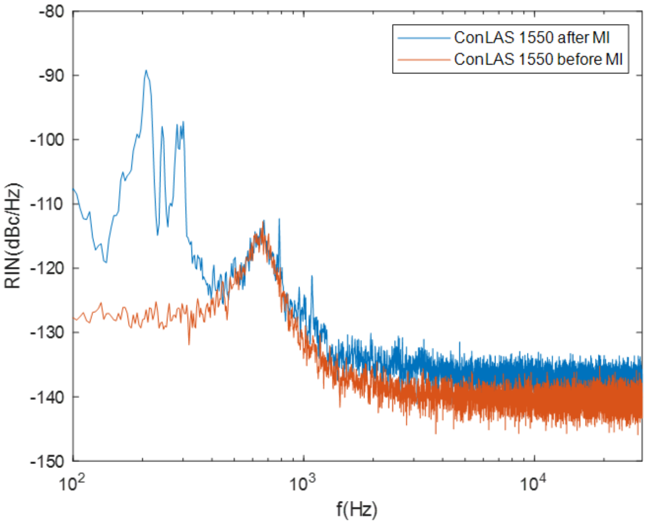

Figure 6.28. PSD of the noise in the system.

We also investigate the source of noise in our system. In the experiment, we use a fiber laser (ConLAS-1550 from Connect Fiber Optics) as the probe. The fiber laser has a relative intensity noise (RIN) of -140 dBc/Hz at 6 kHz. Figure 6.28 shows the measured RIN spectrum. The red curve shows the noise measured before the modal interferometer (MI). The red curve is actually the RIN of the fiber laser. A relaxation oscillation peak can be clearly observed near 0.7 kHz. The relaxation oscillation peak also explains the instability of the 2-nd harmonic signal around 1 kHz that was observed in Fig. 6.23. The blue curve shows the RIN spectrum measured after the MI, which is about 2 times of the RIN of probe laser. Hence, the noise of our system mainly comes from the noise of optical interferometer due to the environment (e.g., vibration of the HCF, lens, etc.).

6.2.4. Discussion of RPTS

For the first time, a new spectroscopic hydrogen sensor based on the PT effect of SRS is demonstrated in an AR-HCF and achieved a sensitivity of 3.2 ppm hydrogen. The sensitivity is comparable to the state-of-the-art hydrogen sensors [6, 37].

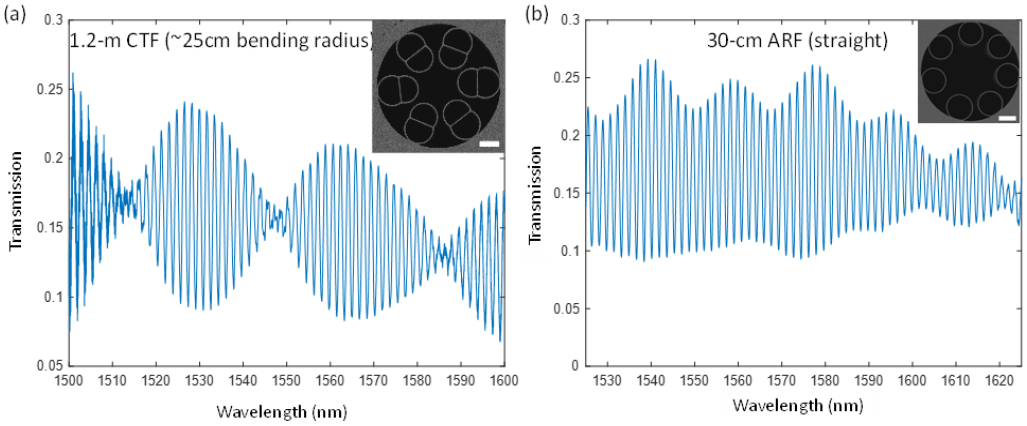

Figure 6.29. The transmission spectrum of the SMF-HCF-SMF structure.

The sensitivity can be further enhanced by using HCFs with lower loss. In our experiment, the transmission of the AR-HCF is estimated to be about 1.6 dB/m. The loss of LP_{11} mode is even higher. Simulation shows the confinement loss of LP_{11} mode is about 1.8 dB/m~4.2 dB/m, which depends on which LP_{11} mode is excited. The high loss of LP_{11} mode is detrimental to the modal interferometer (e.g., smaller contrast of interferogram). We do experiment with two different kinds of AR-HCF. Fig. 6.29 shows the transmission spectrum of the SMF-HCF-SMF structure of two different AR-HCFs. The transmission spectrum of 1.2-m-long conjoined-tube AR-HCF (CT-AR-HCF or CTF) [38] is shown in Fig. 6.29(a). It also supports both the LP_{01} and LP_{11} modes. Figure 6.29(b) shows the transmission spectrum of a straight 0.3-m-long AR-HCF. The average transmission and the contrast of interferogram of two samples are almost the same but the AR-HCF is much shorter than the CTF (even the CTF is bent with a radius of 25 cm). This indicates the loss of LP_{11} in CTF is about 0.25 times of that in AR-HCF. Hence, by using a CTF, the performance of RPTS might be improved.

It needs to mention that we have attempted to do RPTS with the rotational transition $S_0(0)$ of hydrogen but no signal is observed even for pure hydrogen. Here we compare $S_0(0)$, $S_0(1)$ and $Q_1(0)$, $Q_1(1)$ transitions of pure hydrogen at room temperature (298 K) and different pressures. First, we compare the Raman linewidth with a Lorentzian lineshape, the forward FWHM linewidth $\Delta\nu_R$ can be expressed by [39]

$$\Delta\nu_R = \frac{A}{\rho} + B\rho \tag{6.30}$$

where ρ is the density in amagat and the coefficients A and B are given in Table 6.3 [39, 40]. The Raman gain coefficient can be derived using Eq. (2.15):

$$g_R\big(S_0(J)\big) = \frac{32\pi^3\nu_S}{c_0^2}\frac{\Delta N_{fi}}{h\Delta\nu_R}\frac{1}{5}\frac{(J+1)(J+2)}{(2J+1)(2J+3)}\gamma_{00}^2 \tag{6.31}$$

$$g_R(Q_1(J)) = \frac{32\pi^3\nu_S}{c_0^2}\frac{\Delta N_{fi}}{h\Delta\nu_R}\left(a_{10}^2 + \frac{4}{45}\frac{J(J+1)}{(2J-1)(2J+3)}\gamma_{10}^2\right) \tag{6.32}$$

Equation (6.31) gives the Raman gain coefficient of S_0 band of hydrogen with opposite circular polarizations and is exactly Eq. (6.6). Equation (6.32) gives the Raman gain coefficient of Q_1 band of hydrogen with parallel linear polarizations. The polarizability $\gamma_{00}, \gamma_{10}, a_{10}$ are weakly dependent on the pump wavelength and are approximated to be $3.0 \times 10^{-25}\ cm^3$, $0.87 \times 10^{-25}\ cm^3$ and $1.0 \times 10^{-25}\ cm^3$ for pump wavelength in the near IR (the relative change of polarizability is less than 4% for wavelengths from 800 nm to 2000 nm) [41, 42].

Table 6.3. Coefficients A and B at room temperature (298 K).

Transition	A (MHz amagat)	B(MHz/amagat)
$S_0(0)$	1.87	77
$S_0(1)$	6.15	114
$Q_1(0)$	257	76.6
$Q_1(1)$	309	52.2

Then we calculate ΔN_{fi} between the initial state and the final state. For the pure rotational Raman transition $S_0(J)$, the initial state i is $v^i = 0, R^i = J$ and the final state f is $v^f = 0, R^f = J + 2$. The number density difference can be calculated as

$$\Delta N_{fi} = N\big(v^i R^i\big) - \frac{2J+1}{2J+5}N\big(v^f R^f\big) \tag{6.33}$$

where $N(vR)$ is the population density in the energy level vR. Considering the spin degeneracy of hydrogen, the population density can be given by the Boltzmann distribution:

$$N(vR) = \frac{(2J+1)g_{nuc}e^{-\frac{E(vR)}{k_BT}}}{\sum_J (2J+1)e^{-\frac{E(vR)}{k_BT}}} N_{tot} \tag{6.34}$$

where $E(vR)$ is the energy of the energy level vR, $N_{tot} = p/k_BT$ the total number density of molecules and g_{nuc} is the spin degeneracy. At room temperature, g_{nuc} is taken to be 3 or 1 for ortho-H$_2$ with odd J levels or para-H$_2$ with even J levels, respectively. For the pure rotational transitions $S_0(0)$ and $S_0(1)$, $\Delta N_{fi} \approx 0.11N_{tot}$ and $0.62N_{tot}$, respectively. And for the vibrational transitions, since the energy of vibrational transition is much larger than k_BT, the number density on the vibrational energy level $N(v^f R^f)$ can be ignored. Hence, for the vibration transitions $Q_1(0)$ and $Q_1(1)$, $\Delta N_{fi} \approx 0.13N_{tot}$ and $0.658N_{tot}$, respectively. The fractional number density difference is sometimes called the Boltzmann population factor ($K_B = 0.13\ or\ 0.658$).

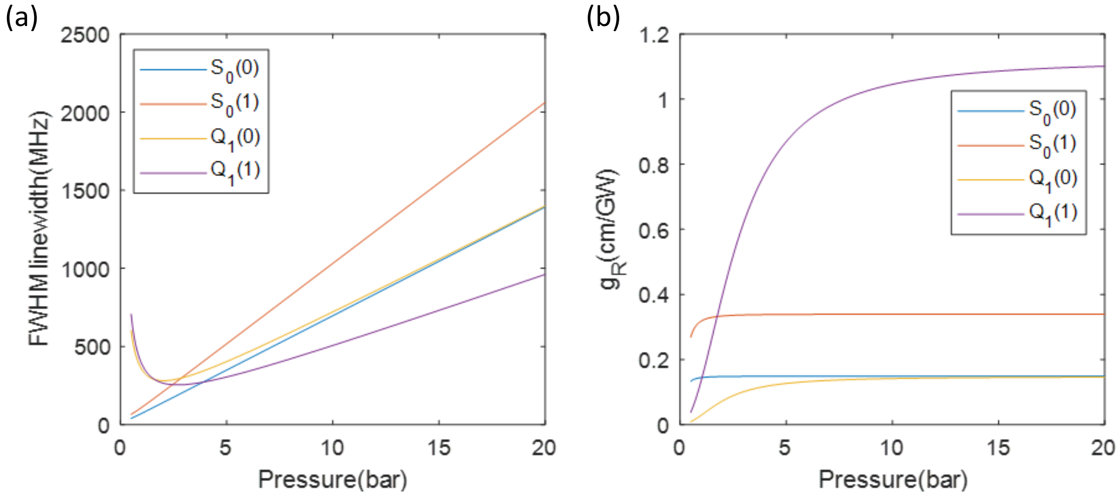

Figure 6.30. The Raman linewidth and the Raman gain coefficient of the rotational and vibrational band of pure hydrogen.

Figure 6.30 shows the Raman linewidth and the Raman gain coefficient of $S_0(0)$, $S_0(1)$, $Q_1(0)$, $Q_1(1)$ transitions when the wavelength of Stokes is 1550 nm. The $Q_1(1)$ transition of hydrogen shows the largest Raman gain coefficient, which is about 3.2 times of that of $S_0(1)$ and is about 7.4 times of $S_0(0)$ for pressures higher than 10 bar.

From Eqs. (6.7) and (6.8) we can derive an approximated indicator of the phase modulation of RPTS:

$$\Delta\phi \propto (n_0 - 1)\nu_R \nu_L \frac{g_R}{\nu_S} \frac{P_P P_S}{A_{eff}} L \tag{6.35}$$

where ν_L is the frequency of probe light. It should note that the factor g_R/ν_S is weakly dependent on the frequency of Stokes. Hence, in RPTS, using shorter pump wavelength to increase the Raman gain does not increase the RPT phase modulation. Previously, we have done experiment of $S_0(0)$ with a 10-μm-core PBG-HCF with a pump power of a few hundred milliwatts and a Stokes power of a few milliwatts. In the earlier experiment, no RPTS signal was observed. Now, by using the $Q_1(1)$ transition and increasing the gas pressure to 6 bar, the factor $(n_0 - 1)\nu_R g_R/\nu_S$ is increased by 455 times. Besides, the product of pump power and Stokes power is also increased by using two high power lasers. Another important parameter is the effective mode area A_{eff}. For the AR-HCF shown in Fig. 6.31(b), $A_{eff} = 441\ \mu m^2$ and for the HC-1550-06 fiber, $A_{eff} = 52\ \mu m^2$. Considering the overall impact of these factors, the total phase modulation of RPTS is increased by a few thousand times. For this reason, we achieve the state-of-the-art sensitivity of hydrogen sensing.

The sensitivity of continuous wave RPTS can be further improved in several aspects: first, the effective mode area can be reduced by carefully designing the AR-HCF or using double PBG hollow-core photonic crystal fiber [43]; second, as we have mentioned, the interference contrast can be improved by reducing the loss of optical modes (especially LP_{11} mode) in AR-HCF. This can be achieved by using CTFs. Furthermore, RPTS can also be performed in a pulsed format. Since the phase modulation of RPTS is proportional to the product of pump power and Stokes power, the power product of two pulsed light can be further improved by several orders of magnitude. By using two pulsed lasers with repetition rate in the kilohertz range, the lock-in detection can also use to realize a narrow detection bandwidth for higher sensitivity.

6.3. Conclusion

In this chapter, we have demonstrated two techniques for Raman gas sensing of hydrogen with HCFs: SRG spectroscopy and RPTS. The sensitivity of Raman gas sensing is enhanced by the high optical intensity in HCFs, as well as the perfect overlap between gas and optical field.

For SRG spectroscopy, we realize a sensitivity of 20 ppm hydrogen with a 15-m-long PBG-HCF. Distributed hydrogen sensing is demonstrated with a 2.7-m spatial resolution, a response time of 50 s, and a sensitivity of 833 ppm over a length of 100 meters. Distributed gas pressure measurement is also implemented by decoding the Raman linewidth of hydrogen.

For RPTS, the sensitivity of Raman gas detection is enhanced by measuring the MPD of photothermal effect induced by SRS. The broad transmission band of AR-HCF enables the $Q_1(1)$ transition of hydrogen, which greatly enhances the heat generated by SRS. Compared with SRG spectroscopy, RPTS could reach a higher sensitivity, but the system is considerably more complex. Hydrogen sensing with a sensitivity of 3.2 ppm is demonstrated by using a 3.9-m-long AR-HCF. The sensitivity of RPTS is comparable with the state-of-the-art hydrogen sensors.

Reference of Chapter 6

1. Owyoung, A. (1978). High-resolution cw stimulated Raman spectroscopy in molecular hydrogen. *Optics Letters*, *2*(4), 91-93.
2. Fink, U., Wiggins, T. A., & Rank, D. H. (1965). Frequency and intensity measurements on the quadrupole spectrum of molecular hydrogen. *Journal of Molecular Spectroscopy*, *18*(4), 384-395.
3. Schweitzer, C., & Schmidt, R. (2003). Physical mechanisms of generation and deactivation of singlet oxygen. *Chemical Reviews*, *103*(5), 1685-1758.
4. Hübert, T., Boon-Brett, L., Black, G., & Banach, U. (2011). Hydrogen sensors–a review. *Sensors and Actuators B: Chemical*, *157*(2), 329-352.
5. Benabid, F., Knight, J. C., Antonopoulos, G., & Russell, P. S. J. (2002). Stimulated Raman scattering in hydrogen-filled hollow-core photonic crystal fiber. *Science*, *298*(5592), 399-402.
6. Hanf, S., Bögözi, T., Keiner, R., Frosch, T., & Popp, J. (2015). Fast and highly sensitive fiber-enhanced Raman spectroscopic monitoring of molecular H_2 and CH_4 for point-of-care diagnosis of malabsorption disorders in exhaled human breath. *Analytical Chemistry*, *87*(2), 982-988.
7. Buric, M. P., Chen, K. P., Falk, J., & Woodruff, S. D. (2008). Enhanced spontaneous Raman scattering and gas composition analysis using a photonic crystal fiber. *Applied Optics*, *47*(23), 4255-4261.
8. Hanf, S., Keiner, R., Yan, D., Popp, J., & Frosch, T. (2014). Fiber-enhanced Raman multigas spectroscopy: a versatile tool for environmental gas sensing and breath analysis. *Analytical Chemistry*, *86*(11), 5278-5285.
9. Yang, X., Chang, A. S., Chen, B., Gu, C., & Bond, T. C. (2013). High sensitivity gas sensing by Raman spectroscopy in photonic crystal fiber. *Sensors and Actuators B: Chemical*, *176*, 64-68.
10. Doménech, J. L., & Cueto, M. (2013). Sensitivity enhancement in high resolution stimulated Raman spectroscopy of gases with hollow-core photonic crystal fibers. *Optics Letters*, *38*(20), 4074-4077.

11. Westergaard, P. G., Lassen, M., & Petersen, J. C. (2015). Differential high-resolution stimulated CW Raman spectroscopy of hydrogen in a hollow-core fiber. *Optics Express*, *23*(12), 16320-16328.

12. Berger, J. P., Saint-Loup, R., Berger, H., Bonamy, J., & Robert, D. (1994). Measurement of vibrational line profiles in H_2–rare-gas mixtures: Determination of the speed dependence of the line shift. *Physical Review A*, *49*(5), 3396.

13. https://www.nktphotonics.com/lasers-fibers/product/hollow-core-photonic-crystal-fibers/

14. Carlsten, J., & Wenzel, R. (1983). Stimulated rotational Raman scattering in CO_2-pumped para-H 2. *IEEE journal of quantum electronics*, *19*(9), 1407-1413.

15. Kol/os, W., & Wolniewicz, L. (1967). Polarizability of the hydrogen molecule. *The Journal of Chemical Physics*, *46*(4), 1426-1432.

16. Maier, M., Kaiser, W., & Giordmaine, J. A. (1969). Backward stimulated Raman scattering. *Physical Review*, *177*(2), 580.

17. Dicke, R. H. (1953). The effect of collisions upon the Doppler width of spectral lines. *Physical Review*, *89*(2), 472.

18. Herring, G. C., Dyer, M. J., & Bischel, W. K. (1986). Temperature and density dependence of the linewidths and line shifts of the rotational Raman lines in N_2 and H_2. *Physical Review A*, *34*(3), 1944.

19. Yang, F., Jin, W., Lin, Y., Wang, C., Lut, H., & Tan, Y. (2016). Hollow-core microstructured optical fiber gas sensors. *Journal of Lightwave Technology*, *35*(16), 3413-3424.

20. Hollenbeck, D., & Cantrell, C. D. (2002). Multiple-vibrational-mode model for fiber-optic Raman gain spectrum and response function. *JOSA B*, *19*(12), 2886-2892.

21. Raymer, M. G., & Mostowski, J. (1981). Stimulated Raman scattering: unified treatment of spontaneous initiation and spatial propagation. *Physical Review A*, *24*(4), 1980.

22. Suda, A., Hatayama, M., Nagasaka, K., & Midorikawa, K. (2005). Generation of sub-10-fs, 5-mJ-optical pulses using a hollow fiber with a pressure gradient. *Applied Physics Letters*, *86*(11), 111116.

23. Sumida, S., Okazaki, S., Asakura, S., Nakagawa, H., Murayama, H., & Hasegawa, T. (2005). Distributed hydrogen determination with fiber-optic sensor. *Sensors and Actuators B: Chemical*, *108*(1-2), 508-514.

24. Wang, D. Y., Wang, Y., Gong, J., & Wang, A. (2011). Fully distributed fiber-optic hydrogen sensing using acoustically induced long-period grating. *IEEE Photonics Technology Letters*, *23*(11), 733-735.

25. Chen, T., Wang, Q., Chen, R., Zhang, B., Chen, K. P., Maklad, M., & Swinehart, P. R. (2012). Distributed hydrogen sensing using in-fiber Rayleigh scattering. *Applied Physics Letters*, *100*(19), 191105.

26. Couny, F., Benabid, F., & Light, P. S. (2006). Large-pitch kagome-structured hollow-core photonic crystal fiber. *Optics Letters*, *31*(24), 3574-3576.

27. Couny, F., Carraz, O., & Benabid, F. (2009). Control of transient regime of stimulated Raman scattering using hollow-core PCF. *JOSA B*, *26*(6), 1209-1215.

28. Belardi, W. (2015). Design and properties of hollow antiresonant fibers for the visible and near infrared spectral range. *Journal of Lightwave Technology*, *33*(21), 4497-4503.

29. Audibert, M. M., Joffrin, C., & Ducuing, J. (1974). Vibrational Relaxation of H_2 in the Range 500–40 K. *Chemical Physics Letters*, *25*(2), 158-163.

30. Dove, J. E., & Teitelbaum, H. (1974). The vibrational relaxation of H_2. I. Experimental measurements of the rate of relaxation by H_2, He, Ne, Ar, and Kr. *Chemical Physics*, *6*(3), 431-444.

31. Ahn, T., Adamovich, I., & Lempert, W. R. (2007). Stimulated Raman scattering measurements of H_2 vibration–vibration transfer. *Chemical Physics*, *335*(1), 55-68.

32. Kreutz, T. G., Gelfand, J., Miles, R. B., & Rabitz, H. (1988). A time domain photoacoustic study of the collisional relaxation of vibrationally excited H_2. *Chemical Physics*, *124*(3), 359-369.

33. Wang, Y. Y., Wheeler, N. V., Couny, F., Roberts, P. J., & Benabid, F. (2011). Low loss broadband transmission in hypocycloid-core Kagome hollow-core photonic crystal fiber. *Optics Letters*, *36*(5), 669-671.

34. Debord, B., Amsanpally, A., Chafer, M., Baz, A., Maurel, M., Blondy, J. M., ... & Benabid, F. (2017). Ultralow transmission loss in inhibited-coupling guiding hollow fibers. *Optica*, *4*(2), 209-217.

35. Mridha, M. (2018). Ultraviolet Raman Scattering in Hollow-Core Photonic Crystal Fiber (Doctoral dissertation, Friedrich-Alexander-Universität Erlangen-Nürnberg (FAU)).

36. Agrawal, G. P. (2000). *Nonlinear fiber optics*. In Nonlinear Science at the Dawn of the 21st Century (pp. 195-211). Springer, Berlin, Heidelberg.

37. Qi, Y., Zhao, Y., Bao, H., Jin, W., & Ho, H. L. (2019). Nanofiber enhanced stimulated Raman spectroscopy for ultra-fast, ultra-sensitive hydrogen detection with ultra-wide dynamic range. *Optica*, *6*(5), 570-576.

38. Gao, S. F., Wang, Y. Y., Ding, W., Jiang, D. L., Gu, S., Zhang, X., & Wang, P. (2018). Hollow-core conjoined-tube negative-curvature fibre with ultralow loss. *Nature Communications*, *9*(1), 1-6.

39. Herring, G. C., Dyer, M. J., & Bischel, W. K. (1986). Temperature and density dependence of the linewidths and line shifts of the rotational Raman lines in N_2 and H_2. *Physical Review A*, *34*(3), 1944.

40. Bischel, W. K., & Dyer, M. J. (1986). Temperature dependence of the Raman linewidth and line shift for the Q(1) and Q(0) transitions in normal and para-H_2. *Physical Review A*, *33*(5), 3113.

41. Bischel, W. K., & Dyer, M. J. (1986). Wavelength dependence of the absolute Raman gain coefficient for the Q(1) transition in H_2. *JOSA B*, *3*(5), 677-682.

42. Kol/os, W., & Wolniewicz, L. (1967). Polarizability of the hydrogen molecule. *The Journal of Chemical Physics*, *46*(4), 1426-1432.

43. Light, P. S., Couny, F., Wang, Y. Y., Wheeler, N. V., Roberts, P. J., & Benabid, F. (2009). Double photonic bandgap hollow-core photonic crystal fiber. *Optics Express*, *17*(18), 16238-16243.

Chapter 7 Conclusions and future works

7.1. Conclusions

In this thesis, spectroscopic gas sensing methods based on HCFs have been studied. Advanced techniques are proposed and studied to enhance the sensitivity of HCF-based gas sensing. The main contributions are categorized into two parts: (1) for gases with strong absorption, advanced techniques of PTS and PAS are studied by employing the new optical and thermodynamic features provided by HCFs; (2) for gases with weak or no absorption, the gas sensing based on Raman spectroscopy is implemented by using different types of HCFs.

For PTS, advanced techniques including intracavity PTS, MPD-PTS are implemented.

The intracavity PTS is demonstrated to enhance the sensitivity of PTS by placing a HCF gas cell inside a fiber laser cavity. The optical power in HCF is enhanced significantly compared with the laser output power. With a 0.62-m-long PBG-HCF, we demonstrated a sensitivity of 176 ppb acetylene (C_2H_2) with 10 s integration time. Theoretical simulation shows that the sensitivity can be further enhanced to ppb level by reducing the optical loss inside the fiber laser cavity.

MPD-PTS is implemented to enhance the sensitivity of PTS by measuring the phase difference between the two optical modes in an AR-HCF. The common-mode noise can be significantly suppressed and hence the MPD-PTS shows a much higher SNR. With a 4.67-m-long AR-HCF, we realize a sensitivity of ppt level C_2H_2 with 3630 s integration time as well as a fast response time of 44 s. The sensitivity of MPD-PTS is comparable with the most sensitive spectroscopic techniques.

We investigated PABS for highly sensitive gas detection. We formulated a theory to study the PABS in HCFs. By employing a wine-glass-like acoustic mode of the microstructure of AR-HCFs, we demonstrate a PABS for gas sensing with a sensitivity of 8-ppb C_2H_2 as well as for characterization of the microstructure of HCFs. Numerical simulations show that the shot-noise-limit sensitivity of PABS can be enhanced by several orders of magnitude to ppt level with a well-designed micro-structured optical fiber.

For Raman spectroscopy, advanced techniques including SRG spectroscopy and RPTS are implemented.

SRG spectroscopy is demonstrated with PBG-HCF. The small air-core of HCF provided a perfect light-gas overlap with high optical intensity, which enhanced the sensitivity of SRG spectroscopy. With a 15-m-long PBG-HCF, a sensitivity of 20 ppm hydrogen has been implemented. And by using the backward SRS with a pulsed laser, a new method of distributed hydrogen sensing is demonstrated with a 2.7-m spatial resolution, a response time of 50 s, and a sensitivity of 833 ppm over a length of 100 meters. Distributed pressure sensing is also demonstrated by decoding the Raman linewidth.

We also demonstrated a new method of Raman gas sensing named RPTS. It is implemented by measuring the MPD due to photothermal effect associated with SRS. We formulated a theory to study the Raman photothermal effect in AR-HCFs. The broad transmission band of AR-HCF enables the $Q_1(1)$ transition of hydrogen, which greatly enhances the heat generated by SRS. By using a 3.9-m-long AR-HCF, a sensitivity of 3.2 ppm hydrogen has been demonstrated. The sensitivity of RPTS is comparable with the state-of-the-art hydrogen sensors. The potential of RPTS by using the newly developed HCFs is also discussed.

7.2. Future works

High sensitivity gas sensing with HCFs has been demonstrated in the thesis. Some suggestions for further improvement of the sensitivity for gas detection, as well as practical applications of HCF based gas sensors, are provided below.

The sensitivity of spectroscopic gas sensor with HCFs can be further improved along the following directions:

1. The phase modulation of PTS or PAS in HCFs can be further enhanced by using a cavity-enhanced technique. Both the pump power (or pump and Stokes light for RPTS) and the phase modulation of probe can be enhanced in an optical cavity.
2. The phase modulation of PABS can be enhanced by several orders of magnitude by using well-designed micro-structured optical fibers or on-chip integrated waveguides. The sensitivity of PABS based gas sensors can hence be further improved.
3. The ultimate sensitivity of HCF gas sensors is limited by the fundamental thermal noise. How do the different noises (e.g., laser intensity noise, phase noise, and environmental noise) interplay and affect the performance of the sensor? Quantitative analysis of these noises might pave the way to further reduce the noise of HCF gas sensors to the fundamental thermal noise limit.
4. The absorption coefficient of common gases (e.g., CH_4, C_2H_2, CO_2, etc.) is much stronger in the mid-infrared. Mid-infrared pump sources can be used to further improve the sensitivity of PTS or PAS in HCFs. Compared with traditional mid-

infrared spectroscopy, PTS or PAS do not need expansive mid-infrared photodetector. The mid-infrared PTS or PAS might be realized with a relatively low cost.

5. Raman scattering is not the only solution for those molecules with weak or no absorption. Quadrupole absorption or electronic absorption can be used to trace important gases such as hydrogen and oxygen. PTS based on the weak absorption lines of hydrogen or oxygen may achieve comparable sensitivity to those with SRS.

The idea of gas sensing with PTS or PAS can be applied to many practical applications. Suggestions along this direction are listed below:

1. The size of the fiber gas sensor head can be very small, which is much smaller than those spectroscopic gas sensors with free-space gas cells. The sensor head can be used for some space-limited applications, such as inside living creatures and batteries for online gas analysis.
2. One of the advantages of HCF based gas sensors is remote detection. The HCF sensor head can be placed a few hundred meters or even kilometers from the gas sensing system. This feature can be applied to practical applications such as explosive gas detection under the mine, human breathe analysis with gastroscopy, and multi-point industrial leakage detection.
3. The size and cost of PTS or PAS based gas sensors can be further reduced by using on-chip integrated waveguides. The high thermo-optic coefficient of solid waveguides makes them very sensitive to their temperature change. The highly designable structure of on-chip waveguides also enables further optimization of the efficiency of PT effect or PA effect.